DISS. ETH NO. 26008

Electron solvation and scattering in clusters

A thesis submitted to attain the degree of
DOCTOR OF SCIENCES of ETH ZURICH
(Dr. sc. ETH Zurich)

presented by

Sebastian Hartweg

M. Sc. ETH Zurich
born on 10.12.1988
citizen of Germany

accepted on the recommendation of

Prof. Dr. Ruth Signorell, examiner
Prof. Dr. Gunnar Jeschke, co-examiner

2019

Abstract

The aim of this work is to study electron solvation and scattering processes in molecular clusters using photoelectron velocity map imaging. Photoelectron spectra and photoelectron anisotropies of neutral water clusters of different sizes are used together with a two-step model to describe low-energy electron scattering in liquid water and large water clusters. The two-step model distinguishes two different types of electron scattering processes: the photoionization process itself and electron scattering processes during the transport of electrons through the material. The effect of electron scattering during the photoionization process is retrieved from fully size-resolved photoelectron angular distributions of small water clusters with up to 20 molecules. It is found that the short range scattering potential for this scattering process is readily described by a small cluster of only six water molecules. The properties of this cluster are referred to as "genuine properties". Together with a detailed electron transport scattering model developed previously in our group these genuine scattering properties are used to quantitatively predict electron scattering effects of liquid water. Good agreement between our predictions and experimental data is found.

A second part of the work on low-energy electron scattering is devoted to the study of photoelectrons in large water clusters with average cluster sizes of $\langle n \rangle < 1000$ molecules. Surprisingly, it is found that the decrease of the photoelectron anisotropy due to electron scattering cannot be described by liquid bulk scattering parameters, even though the photoelectron anisotropies reach liquid bulk values for those cluster sizes. The experimental data indicate stronger elec-

tron scattering effects than expected for the liquid bulk. Electron scattering cross sections in between the liquid bulk and the gas phase values produce qualitative agreement between measurements and simulations for large clusters. The increased scattering probabilities in clusters compared with the liquid bulk can be explained by the reduced dielectric screening of the scattering potentials and differences in the intermolecular vibrational modes.

The concentration dependent behavior of solvated electrons in sodium ammonia nanosolutions is studied with photoelectron velocity map imaging. The measurements cover the concentration range where sodium ammonia bulk solutions show their famous transition to a metallic state. We observe characteristic changes in the photoelectron spectrum at these concentrations, indicating corresponding changes in the electronic structure of the solutions. These changes are attributed to a cluster analog of the transition to the metallic state of sodium ammonia bulk solutions - a hypothesis still awaiting its final proof. The relatively small average cluster size of around 160 ammonia molecules for which the metal transition is observed is intriguing since such system sizes are within the reach of modern ab initio techniques.

A first step is taken toward the study of the concentration dependent magnetic properties of small sodium ammonia clusters with one or two sodium atoms and a few ammonia molecules. The final goal is to clarify whether spin paired and unpaired solvated electrons can be distinguished in photoelectron spectra. To this end, a Stern-Gerlach type deflector for paramagnetic clusters is designed and characterized in this thesis. Potential issues with the experiment are identified, and strategies for improvements are suggested.

Zusammenfassung

Das Ziel dieser Arbeit ist die Untersuchung von Elektronensolvatation und Elektronenstreuung in Molekülclustern mittels Photoelektronen-Abbildungs-Spektroskopie. Photoelektronenspektren und Photoelektronenanisotropien von Wasserclustern verschiedener Grösse werden in einem zweistufigen Modell verwendet, um die Streuung von niederenergetischen Elektronen zu beschreiben. Das zweistufige Modell unterscheidet zwischen zwei verschiedenen Arten von Streuprozessen: Einerseits Streuprozesse während der Photoionisation, und andererseits Streuprozesse während des Transports der Elektronen durch die Flüssigkeit. Die Auswirkung der Elektronenstreuung während der Photoionisation wird anhand von grössenaufgelösten Photoelektronen-Winkelverteilungen kleiner Wassercluster mit weniger als 20 Molekülen bestimmt. Es wird beobachtet, dass das lokale Streupotenzial für diese Art Streuprozess durch einen kleinen Cluster mit nur sechs Molekülen beschrieben werden kann. Die Eigenschaften dieses Clusters bezeichnen wir als "genuine Eigenschaften". In einem detaillierten Streuungsmodell, welches früher in unserer Gruppe entwickelt wurde, verwenden wir die genuinen Streueigenschaften, um quantitative Vorhersagen über die Elektronenstreuung in flüssigem Wasser zu machen. Diese Vorhersagen stimmen gut mit experimentellen Messungen überein.

Ein zweiter Teil der Arbeit über niederenergetische Elektronenstreuung widmet sich der Untersuchung von Photoelektronen in grossen Wasserclustern mit durchschnittlichen Grössen bis zu 1000 Molekülen. Überraschenderweise lässt sich die Abnahme der Photoelektronenanisotropie auf Grund von Elektronenstreuung nicht durch die Elektronenstreuquerschnitte von flüssigem Wasser beschreiben,

obwohl die Photoelektronenanisotropien Werte wie in flüssigem Wasser erreichen. Die experimentellen Daten deuten auf grössere Elektronenstreuquerschnitte hin, als man für flüssiges Wasser erwarten würde. Mit Elektronenstreuquerschnitten zwischen den Werten für flüssiges und gasförmiges Wasser, erhält man eine qualitative Übereinstimmung zwischen den Messungen und den Simulationen für grosse Wassercluster. Die erhöhten Streuwahrscheinlichkeiten in Clustern verglichen mit der Flüssigkeit können mit einer reduzierten dielektrischen Abschirmung der Streupotenziale und Unterschieden in den intermolekularen Schwingungsmoden erklärt werden.

Das konzentrationsabhängige Verhalten von solvatisierten Elektronen in nanoskopischen Natrium-Ammoniak-Lösungen wurde mit Photoelektronen-Abbildungs-Spektroskopie untersucht. Die Messungen erstrecken sich über den Konzentrationsbereich, in welchem makroskopische Natrium-Ammoniak-Lösungen ihren berühmten Übergang in eine metallischen Phase zeigen. Wir beobachten charakteristische Veränderungen in den Photoelektronenspektren in diesem Konzentrationsbereich, welche auf entsprechende Veränderungen in der elektronischen Struktur der Lösungen hindeuten. Diese Veränderungen ordnen wir einem Cluster-Analogon dieses Metallübergangs in Natrium-Ammoniak Lösungen zu, auch wenn der endgültige Beweis dieser Hypothese noch aussteht. Die verhältnismässig kleine Clustergrösse von circa 160 Ammoniakmolekülen, für welche wir diesen Übergang beobachten konnten, ist faszinierend, da solche Systemgrössen einer detaillierten theoretischen Behandlung mit modernen ab initio Methoden zugänglich sind.

Für die Untersuchung von konzentrationsabhängigen magnetischen Eigenschaften von kleinen Natrium-Ammoniak Clustern mit einem oder zwei Natriumatomen und einigen Ammoniakmolekülen, haben wir einen ersten Schritt unternommen. Das Fernziel dieser Untersuchung ist es abzuklären, ob spin-gepaarte und ungepaarte Elektronen in Photoelektronenspektren voneinander unterschieden werden können. Zu diesem Zweck wurde in dieser Arbeit ein Stern-Gerlach-Deflektor für paramagnetische Cluster entworfen und charakterisiert. Mögliche experimentelle Probleme wurden identifiziert, und Strategien zu deren Lösung vorgeschlagen.

Acknowledgement

The work described in this thesis was not done by me alone. I see this thesis rather as the product of fruitful collaboration with many people whom I want to thank on this occasion.

First and foremost I want to express my gratitude to Prof. Dr. Ruth Signorell, who gave me the opportunity to work on these exciting projects. The guidance and advice received from you were greatly appreciated, and I thank you for the dedicated support I enjoyed over the last years. Furthermore, I can say that I am grateful for the opportunity to be part of your group. The Signorell group made the last four years a time on which I will always look back with good memories.

Also I would like to thank my co-examiner Prof. Dr. Gunnar Jeschke for reviewing this thesis.

While I am very thankful to the Signorell group as a whole, there are some members that need further mentioning: I thank Dr. Bruce Yoder for his advice during those past years and the many helpful (not only scientific) discussions we had. You did not only help and teach me a lot in the lab, but also invested time in reading the draft of this thesis to make suggestions for improvements. Big thanks also go to Thomas Gartmann for the good collaboration generally and on the large water cluster measurements specifically. I appreciate the honest feedback that I could at any point get from you. I am grateful for having been placed in an office with Bruce and Thomas four years ago and I do not believe that I could have gotten better office mates.

I also want to thank Dr. David Luckhaus for the patient introduction into the

scattering model, for his help with the DFT calculations as well as for providing the code for the MD simulations for the deflector project. I thank Dr. Egor Chasovskikh for being around to solve any laser problem or other technical issue whenever they occurred.

I thank Dr. Adam West for teaching me a lot about the experimental techniques and the setup at the beginning of my PhD. I think your good introduction and the working setup that I took over from you sent me of to a good start. Also I am thankful to Jonathan Barnes, who took over the experimental setup from me, after helping me a lot in the lab during the last year. Furthermore, I am thankful to Loren Ban who worked with Thomas and me on the large cluster measurements as a master student and later joined the group for a PhD project. I enjoy our discussions (that sometimes may sound like arguments or fights to outsiders) about mostly scientific topics and I believe I learn a lot from them. Loren and Jonathan also offered necessary distraction by regularly letting me win ping pong matches.

I also owe thank to Nina Bersenkowitsch who visited our group twice for three months. The first three month period she spent dedicatedly working on the deflector project, measuring and helping to figure out the experimental problems. Big thanks go also to Alexander Malär who did a lot of work on experiments and calculations on sodium-doped DME clusters during his semester project.

I am immensely grateful for the support I received from David Stapfer and Markus Steger from the mechanical and electronic workshops. Rebuilding parts of the setup for the deflector project would have taken much more time without David's help and pulsing hundreds of Amperes of current through the deflector would certainly not have been possible without Markus' dedicated work. Also the many small issues that come up in the everyday experimental work can only be considered small because David, Markus or other members of the workshops solve them so quickly. I am also thankful to Dani Zindel for always taking care of any chemical problem or concern coming up and for synthesizing the deuterated DME used in the experiments.

I also want to use this opportunity to thank a few people outside the Signorell group who made their contribution to those past years and this thesis in different ways. First of all I want to thank my girlfriend Julia for spending past and future years with me. I owe much of my daily happiness to you and thanks to you, I am looking forward to going wherever we chose to go.

Furthermore I thank my parents and family for their continued support and advice and for always being there for me; not only during the last four, but during the last 30 years. I also thank my parents for always supporting (and possibly also creating) the scientific curiosity that brought me here.

Last but not least I would like to thank the friends that have accompanied me since my studies in Zurich began almost ten years ago. Although not all of them join in for lunch on Mondays and Fridays regularly anymore, we have spent a lot of good times with each other, be it studying, celebrating or vacationing. Thank you Katharina Keller, David Hahn, Lukas Braun, Carl-Philipp Rosenau, Johannes Boshkow, Erik Schrader and Julian Bleich, for offering help, distraction and advice, and for being such good friends.

Contents

Chapter 1
Introduction

This thesis focuses on the processes involving low kinetic energy (<25 eV) electrons in the liquid phase and in clusters. Similar to the situation in crystalline solids, the electronic structure in liquids can be described by a band structure[1–3] (see simplified scheme in Figure 1.1 for liquid water). However, the lack of long range order in liquids and amorphous solids makes a theoretical description much more complicated, since there is no translational symmetry that can be exploited. Electronic properties of a sample can be studied experimentally by photoelectron spectroscopy (PES), which requires working under high vacuum conditions. While generally not causing any difficulties with crystalline or amorphous solids, maintaining high vacuum conditions does pose a problem when working with volatile samples, such as liquid water. Some of these issues can be alleviated by working with liquid microjets. Their use for PES was first demonstrated by Manfred Faubel in 1997.[4] Soon after this pioneering study many PES studies of the liquid phase, especially liquid water, followed.[5–13] More recently, the use of liquid aerosol droplets was demonstrated in our group[14–16] as an alternative approach to the PES of liquids. Droplet and liquid jet measurements can in principle be used to study the electronic structure of liquids or of solutes in liquids. The photoionization of a molecule in liquid water starts with the excitation of an electron into the conduction band of the solvent, where the ensuing transport of the electron through the liquid takes place before it escapes from the sample to be detected (see Figure 1.1). One can distinguish two different types of electron scattering in the course of this process, both of which affect the measured properties of the photoelectron. The first one is scattering of the electron during the photoionization process itself, which depends on the local potential the electron experiences in the molecular

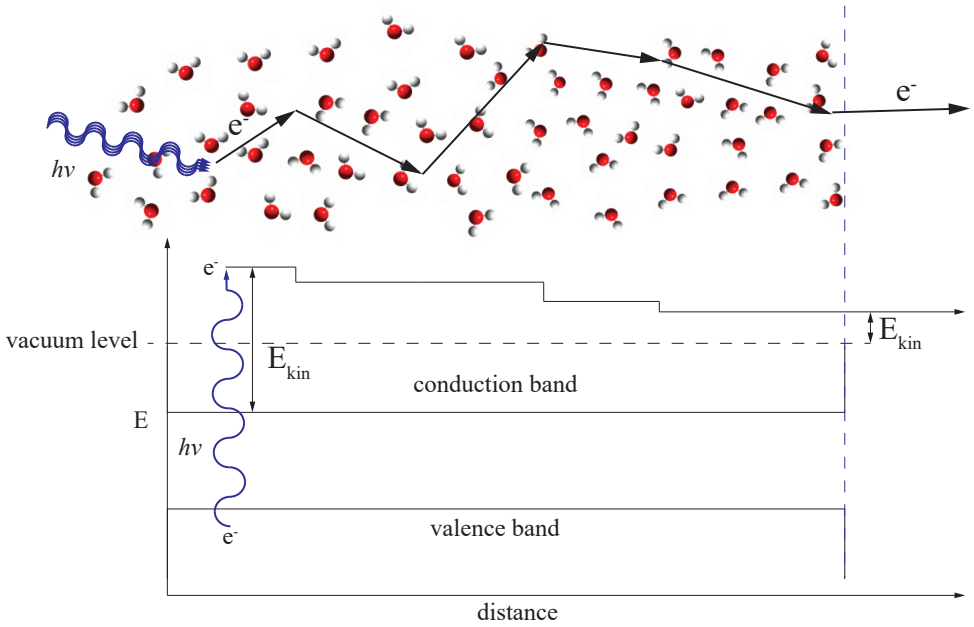

Figure 1.1: Strongly simplified scheme of the band structure of liquid water. The blue arrows indicate the scattering of the electron during the photoionization process itself, i.e. during the excitation of an electron into the conduction band. Afterwards the electron undergoes inelastic and elastic scattering events ("transport scattering", black arrows) on its way out of the liquid.

environment of the remaining solvated ion core. The second occurs during the transport through the liquid bulk material (i.e. "transport scattering"), where the electron is scattered (mainly) by solvent molecules. Both types of electron scattering influence the properties of the photoelectron, e.g. its direction of propagation and its kinetic energy. We will refer to the electron properties before any transport scattering has occurred, as "genuine properties". They hold the information about the electronic structure, orbital character and immediate molecular environment of the ionized species. The transport scattering after the photoionization process, however, can change the kinetic energy and propagation direction of the photoelectron, so that a "direct" experimental determination of genuine properties in a liquid bulk sample is rarely possible. To disentangle the genuine properties from the transport scattering contributions in the measurement, the quantitative analysis of photoelectron data of liquid bulk samples requires a quantitative understanding and an adequate treatment of electron transport scattering in the liquid.

A quantitative description of electron scattering processes is not only needed

for a quantitative analysis of liquid phase photoelectron spectra, but also for understanding and modeling radiation damage to biological tissue.[17,18] It is assumed that ionizing radiation damages DNA molecules not only directly, but also via indirect effects involving slow electrons and the radicals created.[19] The ionizing radiation initially produces high kinetic energy electrons, which lose kinetic energy via inelastic scattering processes. Low kinetic energy electrons can also arise as secondary electrons via electron impact ionization of the solution environment.

Despite many theoretical and experimental studies[12,15,17,20–32] no consistent description of the scattering of low kinetic energy electrons in liquid water has been reached. Thürmer et al.[32] studied effects of electron scattering on the photoelectron angular distributions (PAD) for photoemission of the oxygen 1s orbital of water molecules in a liquid jet. To explain the observed difference of the photoemission anisotropy arising from a gas phase molecule and a liquid jet, they employed a simple model using literature values[33,34] for relative probabilities of elastic and inelastic electron scattering. In the kinetic energy range below 70 eV this led to stark disagreement between their model and the experimental data, indicating an overestimation of the elastic scattering probabilities by more than an order of magnitude. This overestimation can mainly be attributed to the use of electron scattering cross sections for isolated gas phase molecules to explain electron scattering in the liquid bulk phase. Especially in the low kinetic energy range where inter- and intramolecular vibrations and elastic scattering play a significant role, this approach does not work well. In this low kinetic energy range models based on optical properties of water, do not give good results either.[35] Suzuki et al.[20] determined electron attenuation lengths (EAL) for electrons emitted from liquid jets. EALs describe the distance after which an initial electron flux in a given direction has decreased to 1/e of its original value. This quantity does not distinguish between elastic and inelastic scattering, so that EALs do not afford a quantitative understanding of the underlying processes. Michaud et al.[17,27] studied electron scattering in thin films of amorphous ice and determined detailed scattering parameters over a wide range of kinetic energies. They reported differential scattering cross section for various inter- and intramolecular vibrational modes, including angular distributions and energy loss functions for a total of eleven different scattering channels. These results offered the first detailed quantitative understanding of the different processes contributing to low-energy

electron scattering in bulk water. Michaud et al.[17,27] proposed to use amorphous ice as a proxy for liquid water, and suggested that electron scattering in liquid and amorphous solid water was similar - an assumption that became a subject of debate. An argument in favor of it is the vastly different timescale of an electron scattering event compared with the molecular reorganization in liquid water.

To study electron scattering in liquid water quantitatively and to clarify the issue of the transferability of amorphous ice scattering parameters, our group studied photoelectron velocity map images of liquid water droplets[15] and developed a detailed scattering model to analyze the experimental data. The model[12,15] for liquid water is based on a detailed parametrization derived from the results of Michaud et al.[27] for amorphous ice and implemented in a Monte-Carlo approach to simulate large numbers of individual electron trajectories.[33,34,36] The scattering cross sections were adjusted in a fitting procedure, to reproduce the experimental photoelectron velocity map imaging (VMI) data. The effects of electron transport scattering on kinetic energy distributions and angular distributions seem to be well described by the new scattering model for liquid water. In the end, scattering parameters derived from the data given by Michaud et al.[27] for discrete electron kinetic energies in amorphous ice were found to reproduce the experimental VMI data for liquid droplets to within uncertainties ($\pm 30\% - 45\%$). Thereby, the droplet VMI experiments provided a first proof that the scattering of low-energy electrons in the liquid water is virtually identical to that in amorphous ice - at least within current uncertainties - as presumed by Michaud et al.[17,27] Furthermore, the VMI data allowed for the extension of the range of experimental electron scattering parameters for liquid water to even lower electron kinetic energies.

The goal of the present work was to study the scattering of low kinetic energy electrons in water clusters of various sizes, using angle-resolved photoelectron spectroscopy. In a first study (presented in Chapter 4), the key question was whether or not it is possible to determine genuine properties related to the photoionization of liquid water from measurements of small water clusters with less than 20 molecules. Clusters of such sizes are significantly smaller than typical length scales of electron transport scattering, and thus do not yet show prominent electron transport scattering effects. A genuine photoelectron angular distribution offers information on the electronic orbital character of valence electrons in liquid water and on scattering processes during the photoionization process. The

comparison of such genuine properties with those of isolated gas phase molecules could reveal how these properties change upon condensation. Furthermore, the experimental determination of the genuine properties (i.e. scattering during photoionization) allows to predict photoelectron anisotropies of liquid water, using the detailed model for transport scattering. Exploiting these results a second study (presented in Chapter 5) focuses on electron transport scattering in water clusters with average sizes of up to ∼1000 molecules to determine at which cluster size electron transport scattering effects become important. The onset of electron scattering effects gives an estimate of the largest clusters that can be studied without having to account for electron transport scattering. Intimately related to this issue is the question of how large a cluster has to be before transport scattering can be described by liquid bulk parameters. This leads to the importance of finite size effects for electron scattering in clusters. It turns out that cluster size dependent changes in dielectric properties and differences in the intermolecular vibrational modes play an important role (Chapter 5).

The second part of this thesis is devoted to another phenomenon involving quasi-free low kinetic-energy electrons. Here we investigated the concentration dependent behavior of alkali metal ammonia solutions, using photoelectron spectroscopy of sodium-doped ammonia clusters. Sodium ammonia solutions have fascinated chemists ever since their first observation by Sir Humphrey Davy more than 200 years ago.[37,38] Of particular interest is the transition to a metallic state (TMS) occurring at high sodium concentrations and accompanied by the famous change of the intensely colored solutions from dark blue to bronze. In Chapter 6 we investigate if and under which conditions such a transition can be observed in the photoelectron spectra of nanoscale solution droplets. Chapter 7 describes the first steps towards studying yet another aspect of small sodium-doped clusters: the concentration dependent spin pairing effects present in small $Na_m(NH_3)_n$ clusters. Possibilities to experimentally distinguish between solvated electrons in singlet and triplet states in sodium-doped clusters are discussed.

When Sir Humphrey Davy wrote in his laboratory notebook about the fine blue color he observed when heating potassium in gaseous ammonia[37,38] he was not aware that this color was created by electrons solvated in ammonia. The electron was only discovered about 100 years later, and the first interpretation of the "fine blue color" of dilute sodium ammonia solutions as solvated electrons is at-

tributed to Kraus[39,40] and Gibson et al.[41] Since then, electron solvation in sodium ammonia solution has not only been studied for the fascinating physico-chemical processes involved. Solvated electrons in sodium ammonia solutions have also found applications as a strong reducing agent in organic synthesis.[42] Many studies have been performed since Davy, with the results summarized in numerous reviews, e.g. by Edwards,[43] Holton et al.[44] and most recently by Zurek et al.[38] Figure 1.2 summarizes the effects that occur dependent on the alkali metal concentration. At low concentrations, below 10^{-3} mole percent metal (MPM) the solvated electrons and sodium ions behave as simple electrolytes. At higher concentrations up to $5{\cdot}10^{-2}$ MPM the solvated electrons and sodium ions reassociate into ion pairs. In this low concentration regime the equivalent conductance of the solution decreases with increasing concentration. This is typical for electrolytes and signifies the onset of interactions between the solvated electrons and the counter ions. In less dilute solutions interesting electron correlation phenomena occur: At intermediate alkali metal concentrations of up to 1 MPM magnetic measurements have shown that the solvated electrons pair up into spin pairs,[45–47] and metallic clustering is observed. At concentrations between 1 MPM and 10 MPM the transition to the metallic state (TMS) is observed. The exact concentration at which it occurs depends on the solution's temperature and is reported to be accompanied by phase separations. The concentrated, metallic solutions of alkali metals in ammonia show a typical color described as bronze or copper gold. In this concentration range the conductivity increases with increasing sodium (electron) concentrations.

In Chapter 6 we study the TMS in sodium ammonia clusters in more detail. Ammonia clusters doped with single sodium atoms have previously been used in photoelectron VMI studies as model systems for electron solvation.[48–51] Controlling the initial ammonia cluster size distribution and the vapor pressure of sodium in the pickup cell allows for the variation of the sodium concentration over a wide range. Furthermore, varying the ammonia cluster size at a given sodium concentration gives the opportunity to study the influence of system size on the photoelectron spectra of the nanosolutions. It is thus not only possible to determine whether a TMS occurs in clusters and at which sodium concentration, but also the minimum cluster size, for which a TMS can be observed. This could be an important result for theoretical studies of the TMS, since typical bulk systems are not accessible to high level theories.

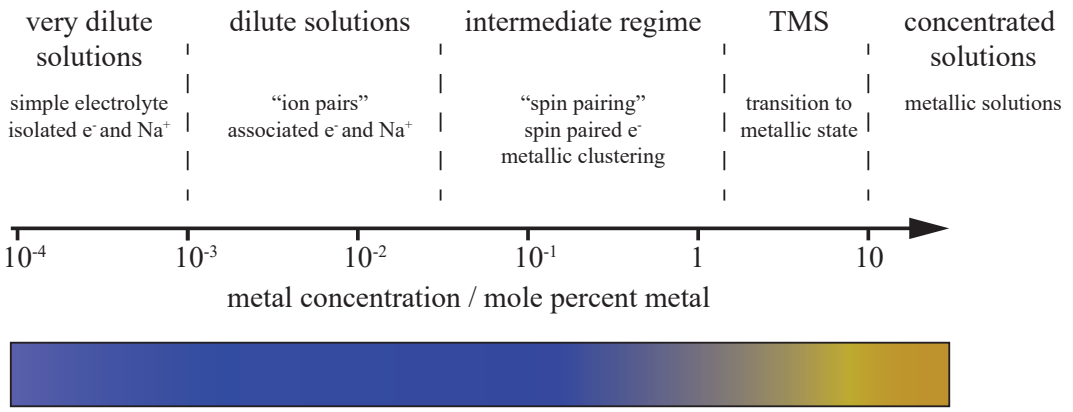

Figure 1.2: Concentration dependent properties of solvated electrons and sodium counter ions in sodium ammonia solutions (adapted from Zurek et al.[38]).

Chapter 7 discusses a possible approach for the characterization of magnetic properties of sodium ammonia solutions in the intermediate concentration range below the TMS. The goal is to build a magnetic deflection experiment that allows for the separation of paramagnetic sodium-doped clusters from diamagnetic clusters in a molecular beam. While single-doped clusters $Na(NH_3)_n$ are expected to be paramagnetic, double-doped clusters $Na_2(NH_3)_n$ can show diamagnetic or paramagnetic behavior, depending on whether the electron spins are paired or not. Using a magnetic deflector it might be possible to distinguish paired (singlet state) from unpaired (triplet state) solvated electrons by comparing photoelectron spectra with the magnetic field on and off, respectively. This would enable us to determine the cluster size and hence the concentration, at which the electron spins start pairing up. This final chapter reports on the first steps toward the realization of such a magnetic deflection experiment to study concentration dependent spin pairing effects in sodium ammonia clusters. This comprises the incorporation of a Stern-Gerlach type deflector into our VMI setup, and the theoretical and experimental characterization of its performance for $Na(NH_3)_n$ clusters with $n < 10$.

Chapter 2
Theory and modeling

2.1 Angle-resolved photoelectron spectroscopy

In angle-resolved photoelectron spectroscopy (ARPES) the photoelectron kinetic energy spectrum is measured as a function of the electron emission direction. Traditionally, this is achieved by using an electron spectrometer with a small acceptance solid angle, that can be moved to different angular positions relative to either the sample or the light polarization. Angular information of photoemission is for example important for measurements of band structures of solids.[52] Since ARPES can measure photoelectron spectra in different directions relative to the crystal lattice, it gives direct access to the band structure of a crystalline solid.[53] Also, for molecular samples the angular data can contain information that is not accessible from energy measurements alone, e.g. on the electronic orbital character. For molecular samples the details of the photoemission direction relative to the molecular axis are only accessible when the molecules are aligned in space. For randomly oriented molecules (in the gas, liquid or solid phase) only information on the emission direction relative to the light polarization can be obtained. Photoelectron spectra with angular resolution can in those cases be obtained either by moving the electron spectrometer relative to the light polarization, or by moving the light polarization relative to the spectrometer. A further method to obtain angular information is electron velocity map imaging (VMI).[54]

VMI records a two-dimensional (2D) projection of the three-dimensional (3D) photoelectron distribution as will be discussed in section 2.1.2. Before that, however, the nature of photoelectron angular distributions (PADs) of ensembles of

randomly oriented gas phase molecules and clusters will be described in section 2.1.1.

2.1.1 Photoelectron angular distribution

The PAD is the photoelectron intensity $I(\theta, \phi)$ as a function of the spatial emission direction, defined by a polar angle θ and an azimuthal angle ϕ. In other words, the PAD is the probability distribution of finding a photoelectron emitted in a given direction. As such, it is possible to describe this probability distribution as the square of a photoelectron wave function Ψ_e, i.e.

$$I(\theta, \phi) = \Psi_e^* \Psi_e. \tag{2.1}$$

The photoelectron wave function can be expanded as a series of partial waves[55]

$$\Psi_e = \sum_{lm} c_{lm} e^{i\delta_l} Y_{lm}(\theta, \phi), \tag{2.2}$$

with partial wave amplitudes c_{lm}, and phase shifts δ_l. $Y_{lm}(\theta, \phi)$ are spherical harmonic functions of order m and degree l. The amplitudes c_{lm} depend on the initial and final states of the sample, as well as on the properties of the light used for photoionization. The phase shifts δ_l influence the interference between individual partial waves and can show pronounced kinetic energy dependence. One can think of these phase shifts as time delays in the formation of different partial waves, that depend on each partial wave's interaction with the scattering potential. By calculation of the coherent square of Ψ_e the PAD is obtained:

$$\begin{aligned} I(\theta, \phi) = \Psi_e^* \Psi_e &= \sum_{lm} \sum_{l'm'} c_{lm}^* c_{l'm'} e^{i(\delta_l - \delta_{l'})} Y_{lm}^*(\theta, \phi) Y_{l'm'}(\theta, \phi) \\ &= \sum_{LM} B_{LM} Y_{LM}(\theta, \phi). \end{aligned} \tag{2.3}$$

It is found that any PAD can be expanded as an infinite series of spherical harmonics.[55] The above equation offers a complete and correct description of photoelectron angular distributions, however, its practical use is limited since for a general PAD an infinite number of coefficients B_{LM} would be necessary. The kinetic energy of a electron, and its propagation direction are both contained in

its momentum vector $\mathbf{k}$. For simplicity, we only consider photoelectrons with a fixed kinetic energy for now. In this way it does not matter whether we define an electron's propagation direction using θ and ϕ or by a wave vector $\mathbf{k}$. The wave function Ψ_e contains all possible emission directions. Upon measurement of a photoelectron's momentum vector $\mathbf{k}$ the wave function Ψ_e collapses to a momentum Eigenstate, i.e. to a plane wave $\Psi_{\mathbf{k}}$. The plain wave with wave vector $\mathbf{k}$ can be expressed as a series expansion of spherical harmonics:[56]

$$\Psi_{\mathbf{k}} = e^{i\mathbf{k}\cdot\mathbf{r}} = 4\pi \sum_{l,m} i^l e^{-i\delta_l} Y^*_{lm}(\hat{\mathbf{k}}) Y_{lm}(\hat{\mathbf{r}}) R_{\mathbf{k}l}(r) \tag{2.4}$$

$R_{\mathbf{k}l}(r)$ is the radial part of the photoelectron wave function, and $\hat{\mathbf{k}}$ and $\hat{\mathbf{r}}$ denote unit vectors in the direction of $\mathbf{k}$ and $\mathbf{r}$, respectively. The probability of creating a photoelectron in a given state $\Psi_{\mathbf{k}}$, which means propagating with a given momentum $|\mathbf{k}|$ in the direction defined by $\mathbf{k}$, is given by the square of the appropriate photoionization matrix element. For the simple case of the photoionization of a hydrogen-like atom with linearly polarized light, this matrix element can be written

$$I(\theta, \phi) = \left| \langle \Psi_{\mathbf{k}} \left| r\cos(\theta) \right| \Psi_i \rangle \right|^2, \tag{2.5}$$

Ψ_i is the wave function of the hydrogen-like atom, and $r\cos(\theta)$ is the dipole operator along the z-axis. Equation 2.5 can be solved analytically. The calculation, which is derived in detail in literature,[56] assumes equal population of magnetic sub levels $m = -l, ..., l$ and uses the fact that only partial waves with $l = l_i \pm 1$ can contribute to the photoelectron wavefunction. The final result shows a cylindrically symmetric angular distribution of the form[57]

$$I(\theta) = \frac{\sigma_{\text{total}}}{4\pi} \left(1 + \frac{\beta}{2} \left(3\cos^2(\theta) - 1 \right) \right), \tag{2.6}$$

where σ_{total} is the total ionization cross section. The parameter β is given by

$$\beta = \frac{l(l-1)\sigma^2_{l-1} + (l+1)(l+2)\sigma^2_{l+1} - 6l(l+1)\sigma_{l+1}\sigma_{l-1}\cos(\delta_{l+1} - \delta_{l-1})}{(2l+1)\left(l\sigma^2_{l-1} + (l+1)\sigma^2_{l+1} \right)}, \tag{2.7}$$

where $\sigma_{l\pm1}$ denote the radial matrix elements

$$\sigma_{l\pm1} = \int_0^\infty R_{nl} r R_{\mathbf{k}l\pm1} \mathrm{d}r. \tag{2.8}$$

The parameter β can take values between -1 and 2 and is sufficient to describe the PAD. A value of $\beta = 2$ corresponds to a pure $\cos^2(\theta)$ form of the PAD, while $\beta = -1$ describes a $\sin^2(\theta)$ form. An isotropic distribution is described by $\beta = 0$ and intermediate β parameters produce linear combinations of the above mentioned cases. The above examples are also shown in Figure 2.1. For the special case of photoionization from an atomic s orbital ($l = 0$) there can only be one contributing partial wave, i.e. one with $l = l_i + 1 = 1$, which is called a p wave. A pure p wave corresponds to a $\cos^2(\theta)$ PAD and is therefore described by $\beta = 2$. For $l_i > 0$ there are always two partial waves contributing, and the resulting β depends on their relative intensities, given by the radial matrix elements as well as on their interference, determined by the relative phase shifts δ_l. Note that those phase shifts may depend strongly on the photoelectron kinetic energy.

The form of equation 2.6 corresponds to truncating the series in equation 2.3 after the second term. In the scope of this work all experimental and simulated PADs will be analyzed assuming this form of equation 2.6. Although the original derivation of equations 2.6 and 2.7 assumed the photoionization of a hydrogen-like atom with linearly polarized light, its general form (equation 2.6) holds also for multi-electron atoms in the same form. For molecules that are randomly oriented

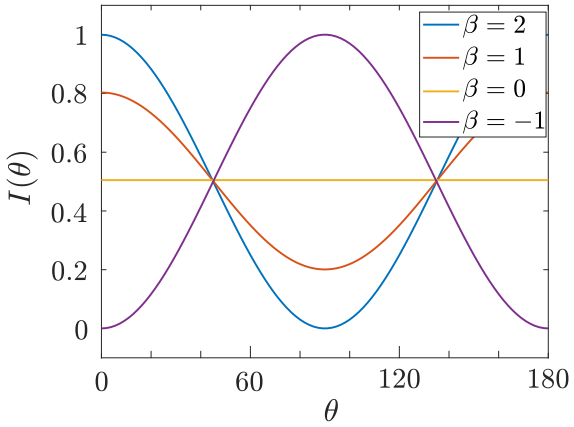

Figure 2.1: Normalized PADs for some typical values of β.

in space the derivation becomes more complicated but the form of equation 2.6 does not change.[55,57] The main difference when considering molecules is that l is not good quantum number anymore, and therefore more than two partial waves need to be considered. As a consequence equations 2.7 and 2.8 cannot be used anymore to determine the β parameter. Note that the simple form of equation 2.6, only holds for single photon ionization (SPI) with linearly polarized light. Multiphoton ionization can result in PADs that have higher order contributions in the expansion of equation 2.3.

2.1.2 Velocity map imaging

Velocity map imaging[54] was invented as an improvement to ion[58] and electron imaging techniques[59] that existed already previously. The descriptions in this section are formulated in terms of photoelectron imaging, the concepts, however, can without modification be applied to ion imaging as well. Photoelectrons emitted with identical kinetic energies from a given point in space are located on a spherical surface in velocity space. The radius of this spherical surface is given by the electron velocity $v_e \propto \sqrt{E_{\text{kin}}}$. The distribution of the electrons on this so called Newton's sphere is described by the PAD discussed above. For isoenergetic photoelectrons that are created at exactly the same position and exactly the same time, this spherical surface in velocity space corresponds directly to a spherical surface in position space at any given time. The radius of this corresponding sphere in position space is given by the electrons' velocity v_e and the time Δt that has passed since the electrons were created. This spherical spatial distribution can be projected by electric fields and imaged on a 2D spatial detector (see Figure 2.2 for clarity). The resulting projection of the full 3D distribution shows a circular shape. Its radius holds information about the velocity and therefore kinetic energy of the electrons, while the angular intensity distribution on the 2D detector holds information on the PAD. In experimental reality there is, however, always a finite spatial ionization volume determined by the overlap of the laser beam and the molecular or cluster beam. This finite volume blurs out the spherical surface in position space, so that the 3D distribution could be described as a superposition of many spherical surfaces with origins all over the ionization region. In VMI a set of electrodes is used to correct for this finite extent of the ionization region. This means all electrons with the same initial velocity vector are mapped to the

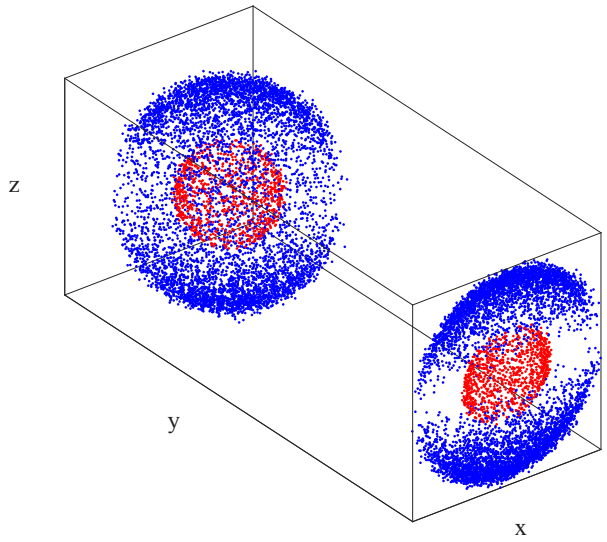

Figure 2.2: Projection of a 3D distribution onto a 2D detector. The 3D distribution is also depicted in Figure 2.3. The radial part consists of two Gaussian peaks, while the angular part is described by $\beta = 2$ for the outer sphere (blue) and by $\beta = -1$ for the inner sphere (red). The symmetry axis is along the z direction.

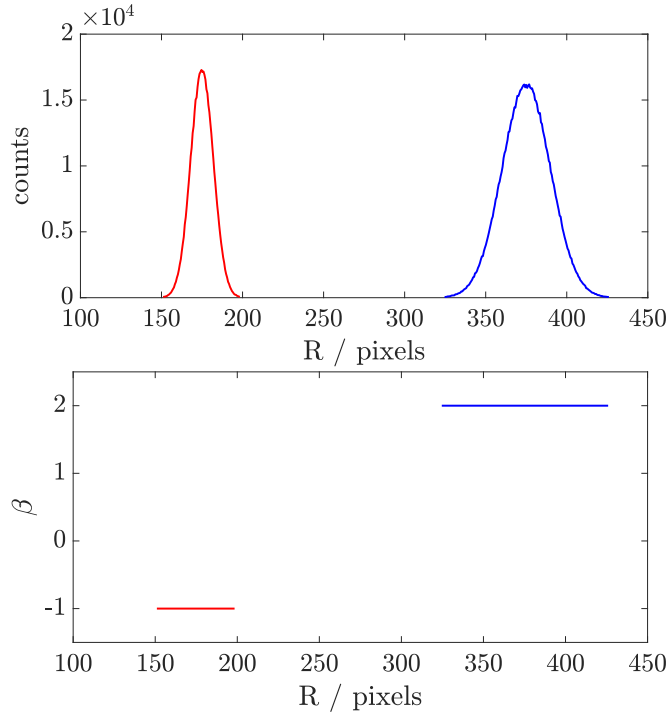

Figure 2.3: Radial part and β parameter for the 3D distribution from Figure 2.2

same position on a two-dimensional detector, irrespective of their point of origin in position space.[54]

For a general 3D velocity distribution the measurement of a 2D projection in position space means a loss of information. However since PADs resulting from single photon ionization with linearly polarized light show cylindrical symmetry according to equation 2.6, it is possible to reconstruct the full 3D velocity distribution from the 2D projection, as long as the polarization axis of the ionizing radiation is parallel to the detection plane. In this work, the term polarization axis refers only to the polarization of the electric field component of the radiation and not to the magnetic field component. Usually this 3D distribution obtained after reconstruction is separated in a radial part and an angular part. The radial part is the so called speed distribution and is linked to the photoelectron spectrum by $E_{\mathrm{kin}} \propto v^2$. The angular part is represented by a β parameter at each radius or kinetic energy. For the 3D distribution in Figure 2.2, the radial part and the β parameters are shown in Figure 2.3.

Although there are other experimental methods to measure angle-resolved photoelectron spectra, velocity map imaging has an advantageous detection efficiency of about 100%. This is because electrons emitted in all directions are detected simultaneously, while retaining their angular information. A magnetic bottle time-of-flight spectrometer[60,61] has a similarly high detection efficiency of 100% but loses all information on the emission direction. Other angle-resolved electron spectrometers detect only electrons that are emitted in a small solid angle.[62,63] The choice of the solid angle range thereby is a trade off between angular resolution and achievable signal levels.

2.1.2.1 Abel and inverse Abel transformation

The description in this section follows the discussion on reconstruction methods in Whitaker's book on "Imaging in Molecular Dynamics".[64] If we consider a 3D spatial distribution of electrons in Cartesian coordinates $I(x, y, z)$, then the 2D projection $p(x, z)$ is given as

$$p(x, z) = \int_{-\infty}^{\infty} I(x, y, z)\mathrm{d}y. \tag{2.9}$$

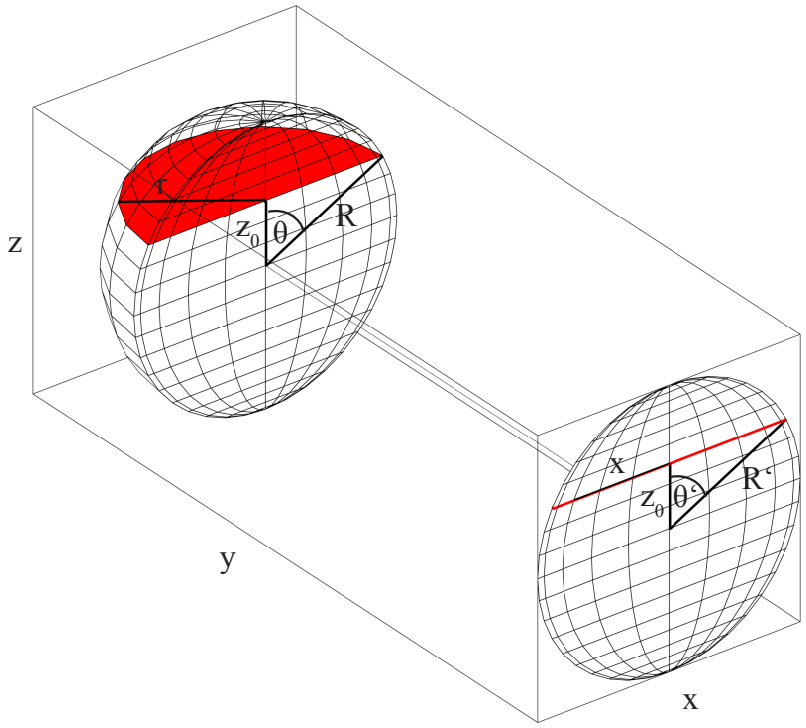

Figure 2.4: Overview of coordinates used in the Abel transforms and polar basis set expansion. Marked in red are a slice of the 3D distribution and the corresponding line in the 2D projection.

We assume that z is the axis of cylindrical symmetry of the system. A single line of the projection (see Figure 2.4) at a constant value of $z = z_0$ can be expressed as

$$p(x, z_0) = 2 \int_0^\infty I(x, y, z_0) \mathrm{d}y. \tag{2.10}$$

The adjustment of the integration borders is possible because of the cylindrical symmetry of the distribution. Due to symmetry it is feasible to express equation 2.10 in polar coordinates with $r^2 = x^2 + y^2$ (see Figure 2.4):

$$p(x, z_0) = 2 \int_x^\infty \frac{I(r, z_0) r}{\sqrt{r^2 - x^2}} \mathrm{d}r \tag{2.11}$$

Equation 2.11 defines $p(x, z_0)$ as the Abel transform of $I(r, z_0)$. To obtain the slice $I(r, z_0)$ of the 3D velocity distribution from its 2D projection $p(x, z_0)$ (both

marked red in Figure 2.4) it is necessary to solve equation 2.11 for $I(r, z_0)$. This way it is possible to go line by line through the projection and build up the 3D distribution slice by slice (see Figure 2.4).

The slice $I(r, z_0)$ of the 3D distribution can be obtained from the inverse Abel transform given as

$$I(r, z_0) = \frac{1}{\pi} \int_r^\infty \frac{\mathrm{d}p(x, z_0)}{\mathrm{d}x} \frac{1}{\sqrt{x^2 - r^2}} \mathrm{d}x. \tag{2.12}$$

There are two problems limiting the use of this analytical solution to the reconstruction problem. The first problem is the singularity of the integrand at $x = r$, which keeps the integral from converging. The second problem is caused by the derivative of the intensity of the projection. Numerically this derivative causes a magnification of noise. Since the end of the 1990's, when VMI became increasingly popular several approaches and algorithms have been developed to circumvent the practical problems with the inverse Abel transform. Methods include onion peeling[65,66] and backtracking algorithms,[67] fitting a set of basis functions to an image[68,69] as well fitting velocity maps directly to the experimental data without using basis functions in maximum entropy methods.[70] All the abovementioned algorithms obtain a 3D distribution from a recorded 2D projection.

In addition to a speed distribution or kinetic energy spectrum, most algorithms also produce a cut through the obtained 3D distribution, parallel to the detection plane. This cut is often referred to as the reconstructed image of the distribution. An example of a simulated photoelectron image and the corresponding reconstructed image for the distribution from Figure 2.3 is given in Figure 2.5. In the following the maximum entropy approach and the polar basis set expansion will be discussed in some detail.

2.1.2.2 Polar basis set expansion algorithms

The idea of the basis set expansion algorithm (Basex) was originally developed by Dribinski et al.,[68] and then later extended by Garcia et al.[69] by using a (polar) symmetry adapted basis set. This polar basis set consists of functions

$$f_{kl}(R, \theta) = e^{-(R-R_k)^2/\sigma} P_l(\cos(\theta)), \tag{2.13}$$

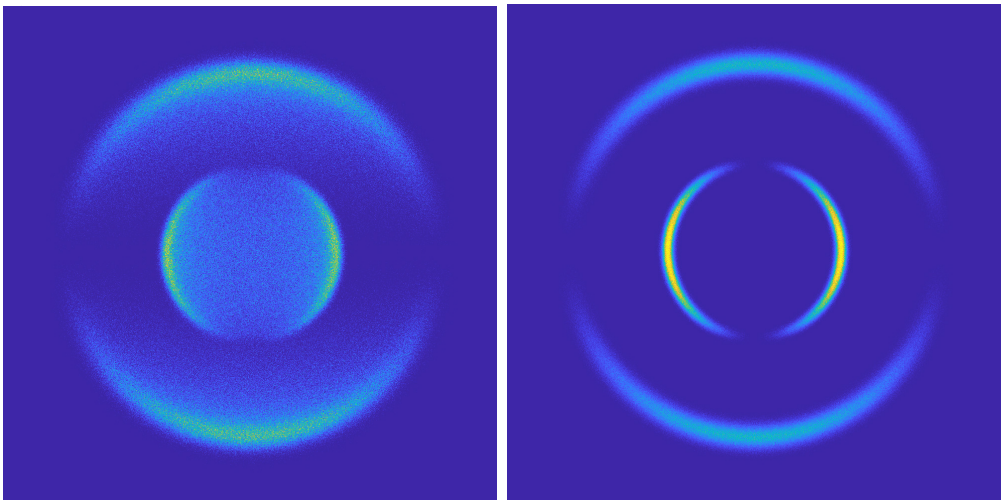

Figure 2.5: Simulated photoelectron image corresponding to the distribution from Figure 2.3 (left) and reconstructed image (right).

where the radial part is described by a Gaussian peak of width σ centered at R_k and the angular part is given by Legendre polynomials $P_l(\cos(\theta))$. The 3D distribution is then represented as

$$I(R,\theta) = \sum_{k=0}^{k_{\max}} \sum_{l=0}^{l_{\max}} c_{kl} f_{kl}(R,\theta), \tag{2.14}$$

where k extends to a $k_{\max}$ large enough to account for the largest radii in the image. The sum over l can typically be truncated already at low values. For single photon ionization using linearly polarized light only terms with $l = 0$ and $l = 2$ need to be taken into account. The basis functions f_{kl} can be Abel transformed according to equation 2.11.

$$g_{kl}(R',\theta') = 2 \int_x^\infty \frac{f_{kl}(R,\theta) r}{\sqrt{r^2 - x^2}} \mathrm{d}r \tag{2.15}$$

The basis functions $g_{kl}(R',\theta')$ can be used to describe the 2D projection of the 3D distribution.

$$p(R',\theta') = \sum_k \sum_l c_{kl} g_{kl}(R',\theta') \tag{2.16}$$

The coefficients c_{kl} are obtained from a fit of the function in equation 2.16 to an experimentally measured image. The coefficients c_{kl} in combination with the

original 3D basis functions f_{kl} reproduce the original 3D velocity distribution. The radial part, i.e. the speed distribution can be calculated as

$$I(R) = R^2 \sum_k c_{k,0} f_{k,0} \tag{2.17}$$

and is therefore represented as a sum of Gaussian peaks. The β parameter trace can be obtained from the coefficients as the ratio

$$\beta(R) = \frac{\sum_k c_{k,2} f_{k,0}}{\sum_k c_{k,0} f_{k,0}}. \tag{2.18}$$

2.1.2.3 Maximum entropy methods

The maximum entropy reconstruction methods for velocity map images were invented by Bernhard Dick.[70] They find the 3D distribution that has the least information content, defined in the computational sense via the entropy S, while still agreeing with the data. The maximum entropy velocity image reconstruction (MEVIR) simulates a reconstructed image ("map") of a 3D distribution, then uses the forward Abel transform to obtain the corresponding 2D projection and then compares this obtained 2D projection to the experimental data. The map is adjusted until it agrees with the experimental data within a given uncertainty threshold. Since the number of pixels in the map is equal to the number of pixels in the image, there are many maps F that result in 2D projections that agree to the experimental data reasonably well. Therefore of those matching velocity maps, the algorithm choses the one that maximizes the entropy function

$$S = -\sum_{J=1}^{N_F} F_J \ln \frac{F_J}{eB_J}, \tag{2.19}$$

where J is an index running over all pixels of the map F and F_J is the intensity value of a given pixel. B_J is a element of a default reference map. The choice of the maximum entropy map to represent the 3D distribution makes sure that there is no information contained in the result that is not necessary to reproduce the data. For extracting the speed distribution and β parameters from the final map,

the distribution is projected onto Legendre polynomials.

$$Q_l(R) = R^2(2l+1)\int_0^\pi P^S(R,\theta)P_l(\cos(\theta))\sin(\theta)\mathrm{d}\theta \tag{2.20}$$

$P^S(R,\theta)$ is the map F transformed to spherical coordinates. The speed distribution is now given by the projection onto the zeroth order Legendre polynomial $Q_0(R)$, while $\beta(R)$ is obtained from the ratio $Q_2(R)/Q_0(R)$. A very similar method, the maximum entropy velocity Legendre reconstruction (MEVELER) does not adjust the map F to reproduce the data, but directly adjusts the $Q_l(R)$. MEVELER therefore uses knowledge about the expected shape of the 3D distribution to reduce the number of fit parameters significantly, and makes the projection onto Legendre polynomials unnecessary.

2.2 Electron scattering and scattering model

2.2.1 General concepts of electron scattering

Electron scattering is the diversion of an electron from its trajectory by a potential created for example by a molecule. The deviation from a trajectory can mean a change in propagation direction, kinetic energy or phase. A phase change corresponds to changing the temporal course of an electron's trajectory, for example by introducing a delay in the electron movement.[71–73] Figure 2.6 displays possible scattering processes. Parts (a) and (b) depict elastic scattering processes, in which the kinetic energy of the electron is conserved, while part (c) and (d) show processes including a change in the electron kinetic energy. Part (a) and (c) include a change of the propagation direction of the electron, while the scattering processes in part (b) and (d) occur in the forward direction. The phase changes occurring with those scattering processes are not shown in Figure 2.6. Since our experiments are not sensitive to the scattering phase shifts, we will not further consider them in this work. Consequently, we will also not further consider elastic forward scattering since the phase is the only quantity that changes in an elastic forward scattering process.

We describe the electrons as an effective flux of discrete classical particles. The scattering of electrons can then be described quantitatively in terms of scattering cross sections. The attenuation of a flux $\Phi_x(E)$ of electrons of a certain kinetic energy E in direction x is described by the differential equation

$$\frac{\mathrm{d}\Phi_x(E)}{\mathrm{d}x} = -n\sigma_{\mathrm{total}}(E)\Phi_x(E), \tag{2.21}$$

where n is the number density of scatterers and $\sigma_{\mathrm{total}}(E)$ is the energy dependent scattering cross section. The resulting exponential decay of the electron flux can also be described by the mean free path λ_{total} given by

$$\lambda_{\mathrm{total}} = \frac{1}{n\sigma_{\mathrm{total}}}. \tag{2.22}$$

The mean free path is the average distance an electron travels in a medium between two successive scattering events. Another quantity that is often used is the electron attenuation length (EAL). The EAL is the distance after which an initial flux in

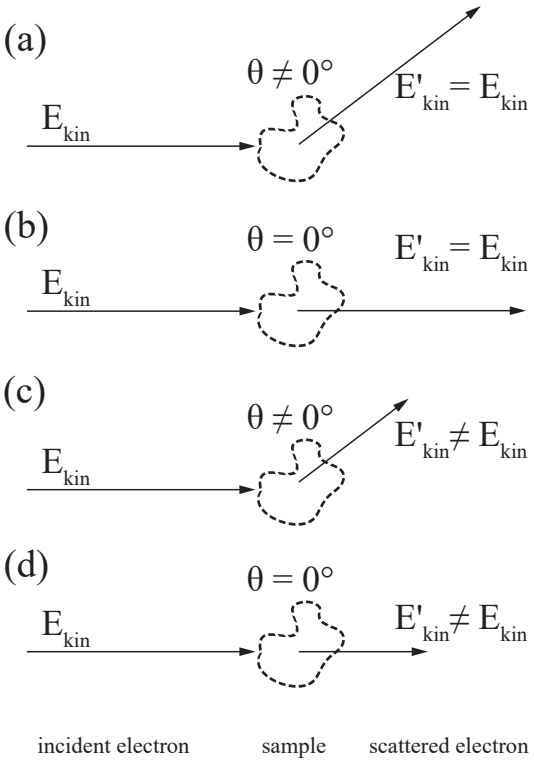

Figure 2.6: Schematic representation of elastic ((a) and (b)) and inelastic ((c) and (d)) scattering processes in forward ((b) and (d)) and random ((a) and (c)) directions.

a given direction has decayed to $1/e$ of its original intensity. Note, however, that the definition of the EAL varies. While an EAL can be easy to measure, it is not of much use for a detailed understanding of the involved processes because it does not distinguish between signal decay due to loss of kinetic energy or loss of signal due to a change in the electron's propagation direction.

The total scattering cross section is often separated into an elastic and an inelastic part

$$\sigma_{\text{total}} = \sigma_{\text{elastic}} + \sigma_{\text{inelastic}}, \tag{2.23}$$

and a similar separation follows for the mean free paths

$$\frac{1}{\lambda_{\text{total}}} = \frac{1}{\lambda_{\text{elastic}}} + \frac{1}{\lambda_{\text{inelastic}}}. \tag{2.24}$$

A further separation of e.g. $\sigma_{\text{inelastic}}$ into cross sections for different scattering channels is possible (see section 2.2.3.1). The change of an electron's propagation

direction and kinetic energy upon scattering is characterized using energy dependent differential scattering cross sections $\sigma(E, \Omega, \Delta_E)$. The $\sigma(E, \Omega, \Delta_E)$ can be thought of, as probability distributions for scattering angles Ω and kinetic energy losses Δ_E. Integrating the differential scattering cross section over all scattering angles and kinetic energy losses provides the energy dependent total scattering cross section

$$\sigma_{\text{total}}(E) = \int_0^E \int_{4\pi} \sigma(E, \Omega, \Delta_E) \mathrm{d}\Omega \mathrm{d}E, \tag{2.25}$$

which is related to the total probability of a scattering event to occur.

The above description of electron scattering assumes a quasi-free electron moving with a propagation direction and kinetic energy. We will refer to scattering processes that occur for such an electron as "electron transport scattering" in the following. A different type of electron scattering is the photoionization process itself, which is described in section 2.1.1. Here one can consider the bound state of an electron as the original trajectory, from which it is diverted after the interaction with light. The new trajectory is described as that of a free photoelectron according to equation 2.4. The probability for the creation of a photoelectron upon interaction with light is described by an energy dependent photoionization cross section $\sigma_{\text{PI}}(h\nu)$. Note that $h\nu$ refers to the photon energy here, not the kinetic energy of the electron. The scattering processes, associated with photoionization are difficult to describe in detail. In this work we will use experimental data to describe the effect of electron scattering during photoionization on the PAD (also referred to as "genuine PAD", see Chapter 4). The transport scattering model described below in section 2.2.3 is then used to describe scattering processes, that have a quasi-free electron as initial state, and their influence on the PAD.

2.2.2 Different energy scales and scattering processes for electrons in water

In this work scattering of electrons with kinetic energies between zero and 20 eV in water is considered. The degree of condensation of water is varied in the experiments and simulations from the gas phase to water clusters of different sizes to the liquid bulk. In this low kinetic energy range, energetically accessible scattering processes for isolated water molecules include excitations of translational and ro-

tational motions, vibrations and electronic excitations. For gas phase water, many theoretical and experimental studies were performed to retrieve cross sections for many different processes, which are summarized by Itikawa and Mason.[74] Since kinetic energy loss due to scattering excitations of translational or rotational motions of gas phase water molecules can typically not be resolved experimentally,[75] these processes are often accounted for in a quasi-elastic scattering cross section. This means elastic scattering cross sections reported for the water gas phase are usually only vibrationally elastic,[74] and are mostly treated in terms of a momentum transfer cross section. This treatment assumes effectively isotropic elastic scattering with a cross section that reproduces the experimentally observed scattering behavior according to equation 2.21. The electron scattering cross sections for vibrational excitations of gas phase water are in general lower than the momentum transfer cross sections, and show a maximum for electron kinetic energies close to the resonant excitation.[74,76–79] Electronic excitations of isolated water molecules start above ∼6 eV electron kinetic energy.[74] Around 6 eV, the first process that occurs is dissociative electron attachment, which does not have a very high cross section. Above 10 eV the electronic excitations contribute significantly to the electron scattering.[74] The two main electronic excitation channels are direct electron impact ionization[80] and electronic excitations leading to formation of OH radicals.[81]

For scattering in condensed water, the most significant change from scattering in the gas phase is the strongly increased density of water molecules (i.e. scatterers). This much higher density of scatterers leads to more pronounced scattering effects. Nevertheless, the scattering probabilities per molecule, i.e. the scattering cross sections, decrease. One reason for the lower scattering cross sections in the condensed phase is the dielectric screening of the scattering potentials by the surrounding water molecules. Further differences become apparent when one considers the available scattering channels in the vapor and in the condensed phase. Condensed water molecules cannot rotate and translate freely. This means there could be significant differences for the quasi-elastic scattering cross sections because some of the contributing processes are changed. In the condensed phase, there are new low frequency intermolecular vibrational and librational (hindered rotations) modes. In this work, we will call the intermolecular vibrational and librational excitations phonons, and treat them as individual inelastic scattering

channels. Depending on the experiment, low frequency phonons can be energetically resolved, making a explicit treatment possible. Also the vibrational scattering may slightly change between the gas and the condensed phase due to coupling between vibrational modes of neighboring water molecules. Electronic excitations are expected not to change significantly.

2.2.3 Electron transport scattering model

To describe electron transport scattering in water we use a probabilistic scattering model that takes into account differential scattering cross sections $\sigma(E, \Omega, \Delta_E)$ for all relevant processes in the kinetic energy range considered. This model was developed in our group[12,14,15] and will be discussed in this section. The model will be used to simulate the effect of electron transport scattering on angle-resolved photoelectron spectra. First, in section 2.2.3.1 the detailed scattering parameters used in the model will be discussed. Second, in section 2.2.3.2 the geometrical setup of typical experiments and simulations will be described. After this the generation of trajectory starting points and the electron propagation will be discussed.

2.2.3.1 Detailed scattering parameters

The availability of scattering cross sections, including angular dependencies and energy loss functions, is a prerequisite for a detailed treatment of scattering. Michaud et al.[27] determined detailed scattering parameters for amorphous ice by analyzing electrons scattered from thin films. They report total inelastic scattering cross sections for 4 different phonon excitations, 5 different vibrational excitations, including combination excitations, and electronic excitations. A total isotropic elastic scattering cross section is reported as well.

For each inelastic scattering process energy loss functions $\sigma(\Delta_E)$ are reported in terms of Gaussian peaks with peak position and width. Electron scattering on electronic excitations of water molecules is treated as a loss of the electron. The angular dependence of the scattering probability is described as a combination of an isotropic term and a $\cos(\theta)$ contribution in the forward direction:

$$\sigma(\theta) = \begin{cases} \sigma_{\text{total}} \cdot \left(\frac{1-\gamma}{2} + \gamma \cdot \cos(\theta)\right) & \text{for } \theta < 90° \\ \sigma_{\text{total}} \cdot \frac{1-\gamma}{2} & \text{for } \theta \geq 90° \end{cases} \tag{2.26}$$

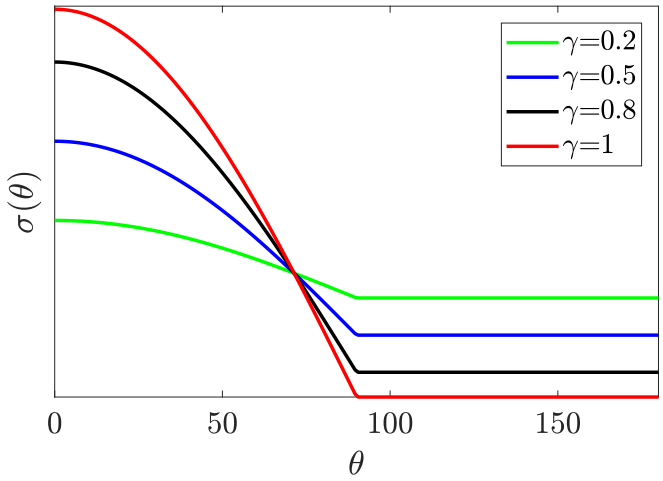

Figure 2.7: Partial scattering cross sections $\sigma(\theta)$ as a function of the scattering angle θ for different values of anisotropy parameter γ.

The energy dependent anisotropy parameter γ can take values between 0 and 1. Some example angular distributions for different values of γ are displayed in Figure 2.7. Anisotropy parameters are reported for each kinetic energy and each process individually. There is no dependence of the differential scattering cross section on the azimuthal angle ϕ because the water molecules in amorphous water ice and liquid water are randomly oriented.

The scattering parameters reported by Michaud et al.[27] were determined for amorphous water ice and not for liquid water. Similar experiments on liquid water are difficult due to its high vapor pressure, and have to our knowledge not been reported yet. Michaud et al. suggested that electron scattering in amorphous ice and liquid water might be similar. One can argue that both phases are unstructured compared with crystalline water ice. Only the molecular dynamics in liquid water are different from the amorphous solid case, meaning the molecules move faster. However, this molecular movement occurs on a femtosecond to picosecond timescale, whereas electron scattering occurs on a timescale below a few femtoseconds.

For liquid water, the first detailed scattering parameters were determined from photoelectron velocity map images of liquid water droplets recorded in our group.[12,15] In this work, photoelectron images with kinetic energies up to 6 eV were simulated applying the model described in the next few sections. The simulated data was fitted to the experimental droplet data by varying the absolute scatter-

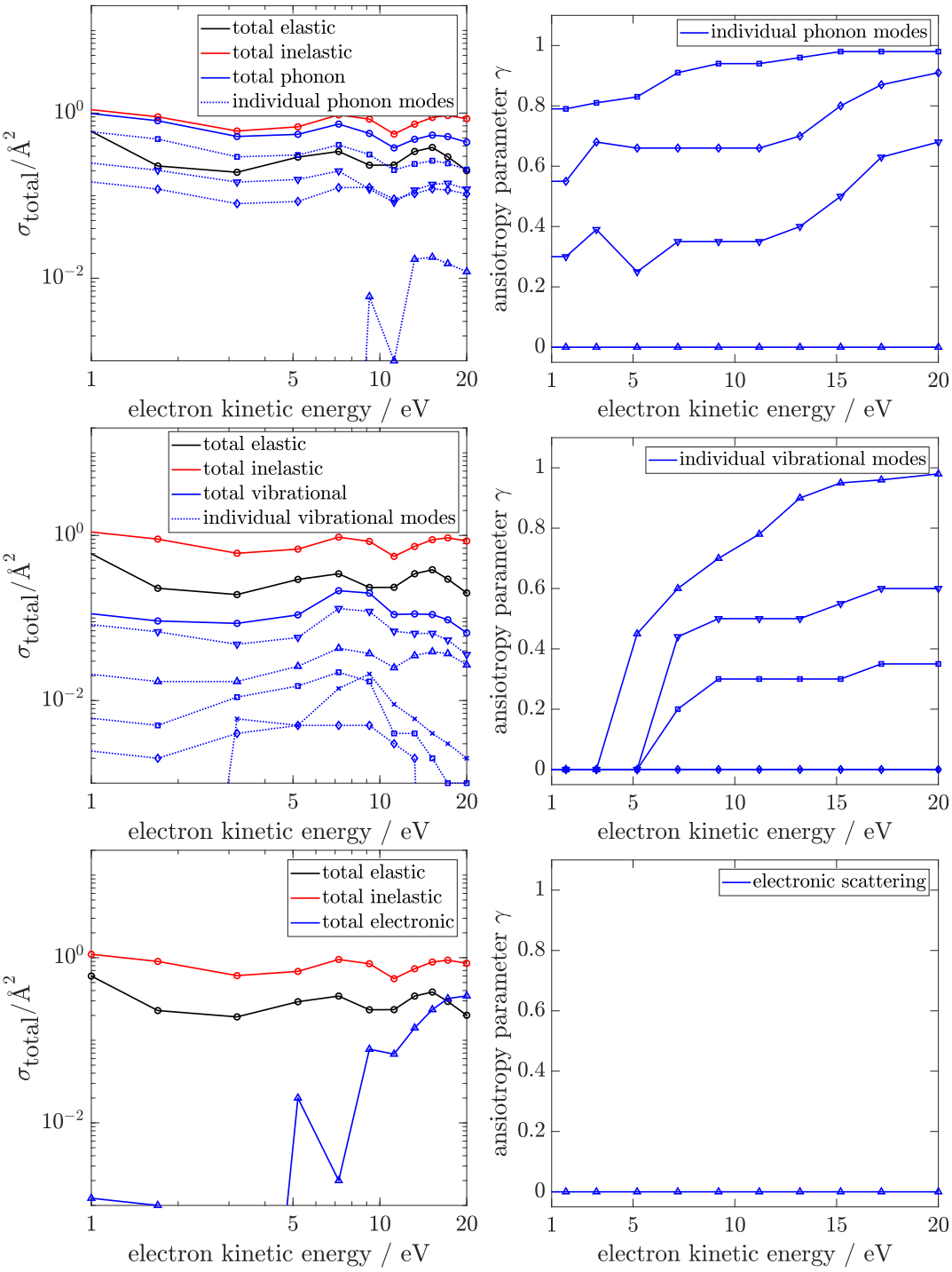

Figure 2.8: Total scattering cross sections (left) and scattering anisotropy parameters (right) for various processes. Phonon scattering is shown in the top panel, vibrational scattering in the center panel, and electronic scattering in the bottom. Total elastic and total inelastic scattering cross sections are shown in all panels for comparison.

ing cross sections at the discrete energies reported by Michaud, while keeping the angular dependencies and energy loss functions constant at the values suggested by Michaud et al. For kinetic energies in between the discrete energies reported by Michaud, the data was described by a double logarithmic function. Furthermore, the data set was expanded towards lower kinetic energies by the above mentioned fitting procedure. The resulting best fit agreed within error bars (30%-45%) with the amorphous solid water data reported by Michaud, thus providing a first proof that electron scattering in amorphous ice and liquid water are indeed very similar. The scattering parameters for liquid water at the discrete energies reported by Michaud, were thus fixed at the values reported by Michaud for amorphous ice. Unpublished data for the energy range between 6 and 20 eV indicate that the similarity between amorphous ice and liquid water holds in this energy range as well. All total scattering cross sections and the corresponding anisotropy parameters γ for liquid water are shown as functions of the electron kinetic energy in Figure 2.8. The marked data points correspond to the values at discrete energies reported by Michaud et al. Note that no anisotropy parameters for elastic scattering are plotted in Figure 2.8 because elastic scattering is effectively isotropic in our model. The energy loss functions for phonon and vibrational scattering are shown in Figure 2.9 for a kinetic energy of 13.2 eV. For different electron kinetic energies the relative weights of the individual Gaussian peaks shift according to the total scattering cross section for the corresponding process. An energy loss function for electronic scattering is not reported since this corresponds to a loss of the electron in the model.

2.2.3.2 Experimental and simulated geometries

The scattering model was used to simulate the effect of electron scattering for two different types of experiments. The first is the measurement of angle-resolved photoelectron spectra from a liquid microjet, and the second one is photoelectron VMI of neutral water clusters. Although both experiments measure photoelectron spectra and PADs (here β parameters), the experimental setup and procedure is different. Since the simulations are intended to be as close to the experiment as possible, the experimental details are included in the simulation procedure.

A typical measurement of an angle-resolved photoelectron spectrum from a liquid jet only detects electrons emitted into a small solid angle and includes

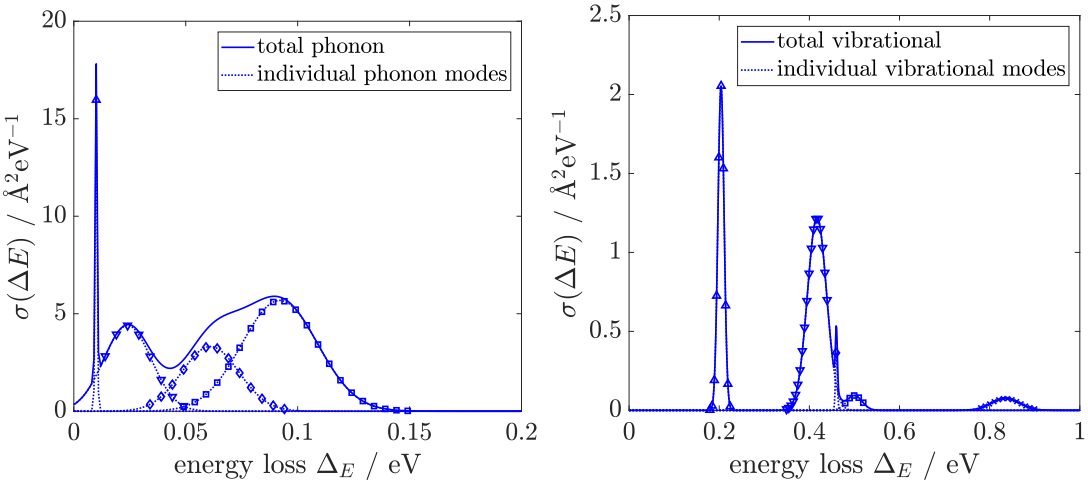

Figure 2.9: Energy loss functions for phonon and vibrational scattering at a kinetic energy of 13.2 eV. The peak areas of the individual Gaussian peaks (blue dotted lines with different symbols) correspond to the total scattering cross sections of the corresponding modes.

measurements of photoelectron spectra for at least two different light polarizations[32,82,83](see Figure 2.10). The anisotropy parameter β is then obtained from

$$\beta = \frac{I_{\parallel} - I_{\perp}}{\frac{1}{2}I_{\parallel} + I_{\perp}}, \tag{2.27}$$

where $I_{\parallel}$ is the electron signal for the polarization parallel to the electron detection direction and $I_{\perp}$ is the electron signal for perpendicular polarization. If more than two polarizations are measured, a curve fit according to equation 2.6 can be used to extract the β parameter. The calculation proceeds exactly in the same way. Both light polarizations are simulated, and the β parameter is determined from equation 2.27. The measurement and simulation scheme is depicted in Figure 2.10. For the liquid jet simulation, the sample volume is chosen as an infinitely long cylinder along the y-axis with a 10 μm diameter. Electron trajectories are started and propagated within this volume. After the escape through the surface of the sample an electron propagates in a straight line and is only detected within a certain solid angle range. In agreement with typical experimental measurements the simulation detects only electrons in a solid angle of $0.9 \cdot 10^{-4}$ sr around the electron detection axis, i.e. the z axis in Figure 2.10. Electrons propagating in a direction outside this solid angle after the escape from the sample are discarded. Experimentally, the solid angle of detection is determined by the distance and size of the detector.

The kinetic energy spectra are obtained as histograms of the kinetic energies of all detected electrons.

For VMI measurements of water clusters (section 2.1.2), a single light polarization perpendicular to the electron detection or projection axis, i.e. parallel to the detector plane, is used. This holds also for the simulations of the scattering effects on VMI images of clusters. Here the sample volume is defined as a sphere of radius r, determined by the number of molecules in a given cluster, the molecular mass of 18 amu and the density of water of 1 g cm^{-3}. The detection scheme of the simulation is an idealized VMI setup. After an electron has escaped from the sample its velocity components perpendicular to the detection axis, i.e. parallel to the detector, are binned onto a two dimensional grid of appropriate resolution, see Figure 2.11. The resulting image is then treated exactly the same way as an experimental image, and the kinetic energy spectrum as well as the angular distribution is obtained from a reconstruction according to section 2.1.2.

2.2.3.3 Electron starting conditions

The first step in the simulations of electron trajectories is the generation of starting conditions. The distribution of starting points contains the initial spatial distribution, the initial angular distribution and the initial kinetic energy distribution of photoelectrons. The initial spatial distribution of photoelectrons is proportional to the distribution of light intensity within the sample volume. In general this light intensity distribution cannot be assumed to be homogeneous. Absorption of light in the sample results in the attenuation of the intensity in the direction of light propagation. Furthermore refraction can lead to nanofocusing of the intensity to the part of a sample that would intuitively be expected to show less intensity.[15] In the case of a liquid jet also the different light polarizations with respect to the liquid jet direction lead to different light intensities within the sample, which must be taken into account. The interplay between real and imaginary parts of the refractive index, sample size, geometry and light wavelength is rather complex. A simple description of these combined effects is not sufficient. In this work the spatial distribution of light intensity is calculated in the framework of the discrete dipole approximation (DDA),[84–86] as implemented by Yurkin and others.[87] The complex refractive indices for the different photon energies are taken from published light scattering measurements.[88] The DDA calculation yields a 3D intensity

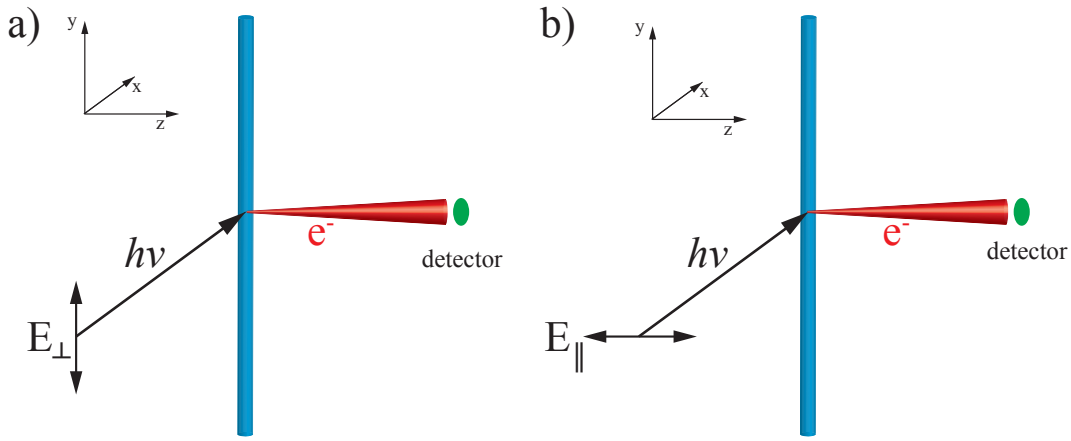

Figure 2.10: Scheme for simulated and experimental measurement of photoemission anisotropy of a liquid microjet. The liquid microjet is shown in blue along the y axis, the red cone along the z axis shows the solid angle of detection. Light of perpendicular (a) and parallel (b) polarization propagates along the x axis.

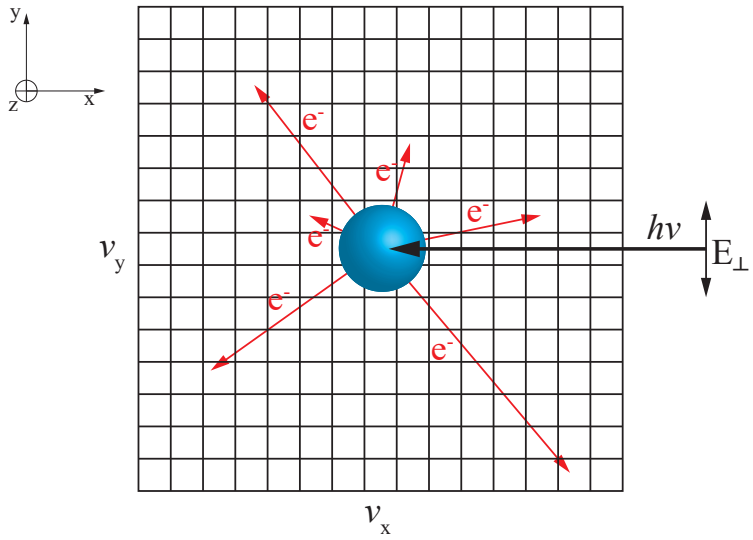

Figure 2.11: Scheme for simulated measurement of VMI of clusters of a certain size. The simulated VMI is a 2D histogram of the x- and y-components of the electrons velocity after the escape from the sample.

distribution for both, the spherical particles and the liquid jet. These specific distributions are used to generate a spatial distribution of trajectory starting points in the given sample.

The electron binding energy spectrum can be taken from published experimental data. From this binding energy spectrum and the photon energy of interest it is straightforward to derive a experimental kinetic energy distribution. The initial kinetic energy distribution created in the simulation is adjusted to fit the experimental kinetic energy distribution after the scattering simulation. In the case of water, the kinetic energy distribution is modeled by the sum of four Gaussian peaks for the three outermost valence orbitals. The experimental spectra for the liquid microjet simulations are taken from reference[5] while the cluster simulations use experimental spectra discussed in chapter 5.

Finally the initial angular distributions of the photoelectrons, the genuine PAD, needs to be determined. This genuine PAD is retrieved from the small cluster measurements described and discussed in chapter 4.

The starting points for the electron trajectories are generated randomly following the spatial, kinetic energy and angular probability distributions discussed above.

2.2.3.4 Electron propagation

After the starting point of a trajectory is determined the electron is propagated through the sample volume. This transport is simulated as a random walk with an exponential step length distribution given by the mean free path λ_{total} according to equation 2.22. Each scattering event changes the kinetic energy and propagation direction of the electron, following the angular and energy loss distributions determined by the differential scattering cross sections. The simulation assumes a flat conduction band, and the Coulomb potential of the remaining positive ion core is not considered. This means in between different scattering events the simulation assumes ballistic quasi-free photoelectrons that have no forces acting on them. Electrons are propagated through the sample volume until they reach the sample surface. At the surface the electrons can transition from quasi-free conduction band electrons to free electrons in the vacuum. However the quasi-free electrons need sufficient kinetic energy to overcome the energy gap E_{gap} between the conduction band edge and the vacuum level. E_{gap} can be deduced from the

difference between the onset of photoconduction and photoemission, leading to a value of about 1 eV.[27] Note that the magnitude of this energy difference between the vacuum level and the conduction band edge is still the subject of active research, and various values can be found in the literature.[1] In the model for the liquid jet, the electron momentum parallel to the surface is conserved upon propagation through the surface. This means electron escape from the sample is only possible if the momentum perpendicular to the surface $p_\perp$ corresponds to a kinetic energy higher than the escape barrier of E_{gap}=1 eV:

$$p_\perp > \sqrt{2m_e E_{\mathrm{gap}}} \tag{2.28}$$

If the momentum perpendicular to the surface is insufficient the electron does not escape from the sample but is reflected back into the interior, and is further propagated through the sample. As soon as the electron kinetic energy drops below the escape barrier, the propagation is stopped and the electron is considered lost, as it can never escape from the sample but will eventually be reabsorbed. The electron changes its propagation direction in the case of an escape from the sample since the momentum parallel to the sample surface $p_\parallel$ is conserved, while $p_\perp$ is reduced by $\sqrt{2m_e E_{\mathrm{gap}}}$. This deflection away from the axis perpendicular to the surface is analogous to Snell's law for light refraction. For the cluster simulations, the escape conditions are similar. The only difference in the procedure is that electrons with insufficient momentum $p_\perp$ perpendicular to the cluster surface are allowed to escape the cluster via inelastic forward scattering if they have sufficient kinetic energy to overcome the barrier. The change of propagation direction is given in this case as a $\cos(\theta)$ in the forward direction, and the energy loss is given by 1 eV. This procedure approximates the effects of the rough cluster surface, which loosens the restrictions for the conservation of the parallel momentum.

2.3 Sodium-doping of clusters

Many experimental cluster studies require knowledge of the cluster size, or cluster size distribution, generated in an experiment. Also the chemical composition of the clusters may be of interest for certain experiments. There are many methods that can in principle be used to obtain size information, or information on the chemical composition of particles. Among those techniques, mass spectrometry offers many advantages. It does not rely on prior knowledge such as a refractive index needed for light scattering methods. Furthermore it does not only give an average cluster size but allows access to the full distribution, and therefore also offers information on the chemical composition of the clusters. The only precondition for a correct measurement of a cluster size distribution with mass spectrometry is the existence of a soft ionization method, that does not lead to cluster fragmentation. This is of course not an issue for the study of charged clusters, that do not need an additional ionization step. For neutral clusters held together by covalent bonds this can also be fulfilled. However, for neutral weakly bound systems, such as clusters of water or of other organic solvents, soft ionization can be difficult to achieve.[89–92] Electron impact ionization for example, is not soft for weakly bound systems, even if low kinetic energy electrons are used.[91–94] Single photon ionization needs photon energies in the VUV range typically above 7-8 eV for most substances. Such photon energies are available from table top laser sources via four-wave-mixing and high harmonic generation (see section 3.1.4), or from synchrotron light sources. However, VUV single photon ionization is not always a soft ionization method,[89,90] since the valence shell ionization of a molecule in a cluster can trigger post-ionization chemistry. If such photoionization-induced chemical reactions are strongly exothermic, or lead to exothermic chain-reactions the result can be strong cluster fragmentation or evaporation. Such fragmentation processes reduce the measured cluster sizes and therefore disguise the original size distribution.[90] A more reliable way to determine the original neutral cluster size distribution is the sodium doping method, first proposed by Buck and coworkers[50,91,92] and further developed by others[51,95] and in our group.[89,90,96] The idea of this method is to dope weakly bound clusters with single sodium atoms in a pickup cell, and then ionize the solvated sodium atom with a single UV photon. Since the vacuum ionization energy of the sodium atom of 5.14 eV[97] decreases significantly upon solvation,[48]

the ionizing UV photon energy can lie far below typical ionization potentials of the solvent molecules. Since the solvent molecules cannot be ionized, only minor structural rearrangements occur leading to no major heat release and therefore no major fragmentation or evaporation.

Sodium-doping of clusters can, however, not only be used for the measurement of cluster size distributions in molecular beams but also for the study of the sodium-doped clusters themselves. Sodium-doped clusters are attractive model systems for electron solvation.[48–51,95,98] Solvated electrons were first observed for sodium ammonia bulk solutions.[37,43,44,99] While PES studies on such bulk solutions are still very challenging,[100] the study of photoelectrons from sodium-doped ammonia clusters offers a promising alternative. Sodium-doped solvent clusters are systems of variable sizes that open up concentration regimes, that cannot be reached in bulk solutions.

Sodium-doped clusters are produced by passing a molecular beam containing clusters through a pick up cell. The doping process is shown schematically in Figure 2.12.[96] To be sure that the sodium doping method is a reliable measure of the original neutral ("undoped") cluster size distribution, it is necessary to understand the size dependencies of the doping process. The sodium atom is picked up by a cluster upon collision in the pickup cell. These collisions are described by a Poisson distribution[96,101] (section 2.3.1). After the collision the atom needs to stick to the cluster on a time scale longer than that of the experiment.[96] Argumentation regarding the sticking probability and possible cluster evaporation due to heating of the clusters is provided in section 2.3.2. After that the ionization and detection efficiencies are discussed (sections 2.3.3 and 2.3.4).

2.3.1 Poisson collision statistics

The collision probability between clusters and sodium atoms follows a Poisson distribution[96,101]

$$P_m = e^{-\langle m \rangle} \frac{\langle m \rangle^m}{m!}, \tag{2.29}$$

where P_m is the probability for m collisions between a cluster and sodium atoms. The average number of collisions $\langle m \rangle$, which is also the width of the distribution,

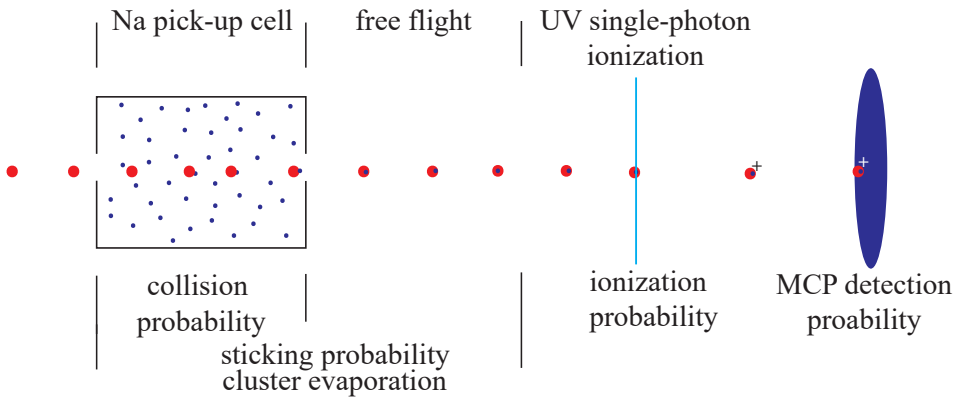

Figure 2.12: Schematic representation of the sodium doping process, with the probabilities that are relevant for the process.

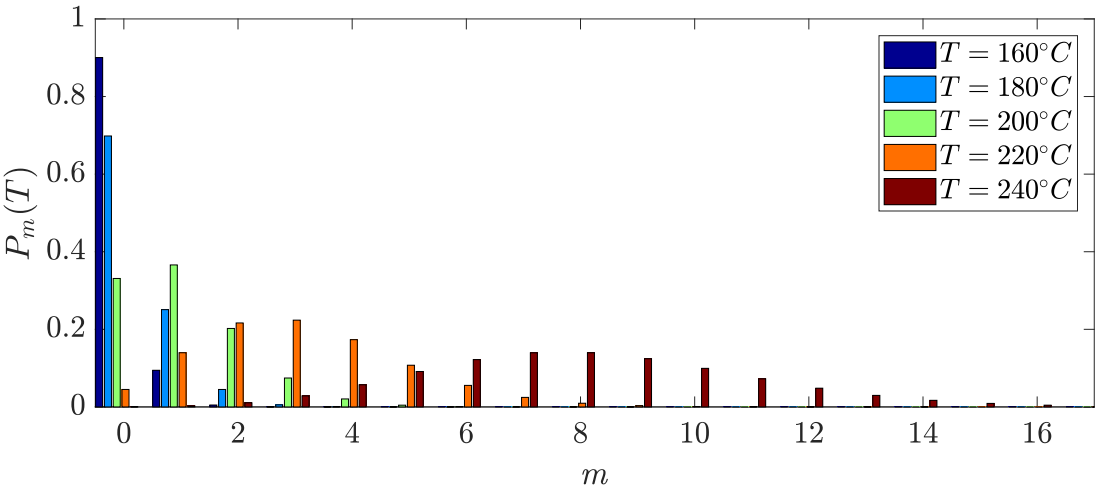

Figure 2.13: Probabilities for doping a cluster of 200 water molecules with m sodium atoms at different oven temperatures.

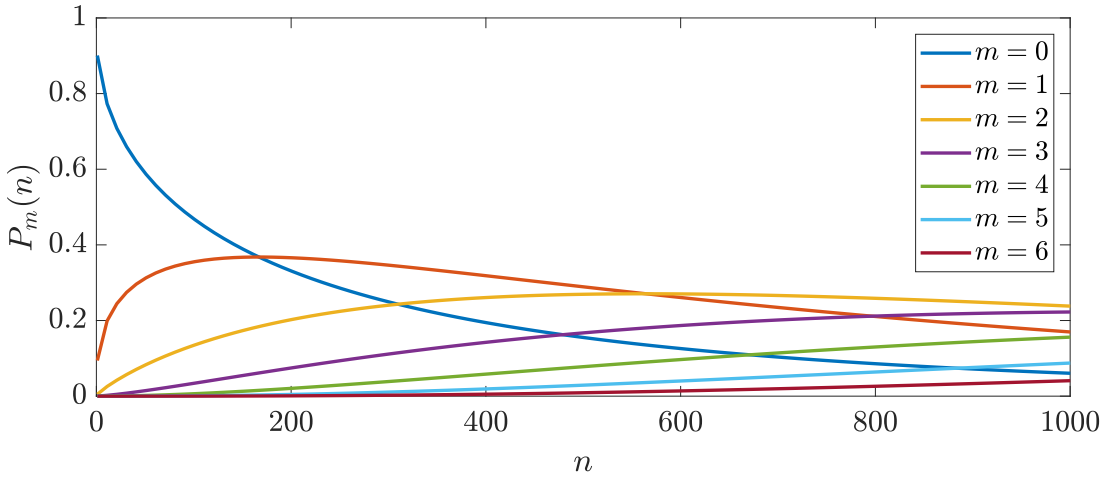

Figure 2.14: Probability for doping a cluster with m sodium atoms depending on the cluster size, for an oven temperature of 200°C .

is given by

$$\langle m \rangle = \bar{n} F L \sigma, \tag{2.30}$$

depending on the number density $\bar{n}$ of sodium atoms, the length L of the pickup cell, the collision cross section σ and a parameter F, that takes into account the velocity of the cluster beam and the velocity distribution of the sodium atoms. F is a function of the velocity ratio $x = v_c/\hat{v}_{Na}$, where v_c is the velocity of the cluster beam and

$$\hat{v}_{Na} = \sqrt{\frac{2k_B T}{m_{Na}}} \tag{2.31}$$

is the most likely velocity of a sodium atom at a given temperature. The functional form of F is given by the equation

$$F(x) = \frac{1}{\sqrt{\pi}} x^{-1} e^{-x^2} + (2 + x^{-2}) \int_0^x e^{-t^2} \mathrm{d}t. \tag{2.32}$$

The number density of sodium atoms $\bar{n}$ is obtained from the vapor pressure of sodium at the given temperature of the pickup cell (oven) (see Fink and coworkers[102]). As the vapor pressure increases exponentially with temperature this introduces a strong temperature dependence of the collision probability, as can be seen from Figure 2.13. A hard sphere collision cross section σ is assumed, with

two spheres of radii r_c and r_{Na} for the clusters and the sodium atoms, respectively,

$$\sigma = \pi(r_{Na} + r_c)^2. \tag{2.33}$$

The radius r_c is determined from the number of molecules and the bulk density of the substance. The van der Waals radius of the sodium atom of 2.27 Å[103] is used for r_{Na}. The collision cross section introduces a cluster size dependence to the collision probability, as can be seen from Figure 2.14. Small clusters have a high probability of not colliding with any sodium atoms (blue line with $m = 0$ in Figure 2.14), while larger clusters have a significant probability to collide with multiple sodium atoms. For very small clusters, the assumption of hard spheres is not well justified. Those collisions would be better described by a Langevin cross section as used for example by Forysinski et al.[104] and Schläppi et al.[96] Such a Langevin collision model takes into account the dispersion and induction interactions as well as the collision energies E. The resulting, energy dependent cross section is given by

$$\sigma_L(E) = \pi \left(\frac{27(C_{disp} + C_{ind})}{4E} \right)^{1/3}. \tag{2.34}$$

The dispersion coefficient C_{disp} depends on the ionization potentials and the polarizabilities of the clusters and the sodium atom, while the induction coefficient C_{ind} depends on the dipole moment of the cluster and on the polarizability of the sodium atom. The Langevin cross sections were not used in this work because reliable calculations for the parameters are missing for the systems of interest.

2.3.2 Sticking probability and cluster evaporation

In an inelastic collision between a cluster and a sodium atom, a part of the total kinetic energy is converted to internal energy of the collision complex. At the moment of the collision this internal energy can be seen as localized in a vibrational mode that could be described by the Na to cluster distance. The sticking probability of the sodium atom is determined by the redistribution of this energy into other degrees of freedom. Clusters consisting of at least a few tens of molecules have enough degrees of freedom to redistribute the collision energy quickly enough to accommodate the metal atom on a time scale of tens of microseconds. Very

small clusters that do not have many degrees of freedom lack the possibility to redistribute the collision energy, leading to high probability for dissociation of the collision complex. A theoretical investigation of small sodium-doped acetic acid (HAc) clusters[104] has shown that complexes formed by collision of the HAc monomer or dimer with sodium atoms dissociate within picoseconds. Complexes formed by collisions of the HAc trimer or tetramer lose one or two HAc monomer units by evaporation, before stabilizing. These results are of course substance dependent, and cannot be directly and quantitatively applied to other substances. Nevertheless, the overall trend is rather general.

$$\mathrm{Na(solv)}_n^* \longrightarrow \mathrm{Na} + \mathrm{(solv)}_n \tag{2.35}$$

$$\mathrm{Na(solv)}_n^* \longrightarrow \mathrm{Na(solv)}_{n-m} + m \cdot \mathrm{solv} \tag{2.36}$$

For very small clusters fast dissociation of the sodium cluster collision complexes is expected, see equation 2.35. For slightly larger clusters the sodium atom can be solvated after redistribution of the collision energy, which may lead to the evaporation of a few monomer units as indicated in equation 2.36. An upper estimate for the number m of evaporated solvent molecules can be obtained from a comparison of typical collision energies with the heat of vaporization of typical solvent molecules. The collision energies for sodium atoms at $\sim$200°C and clusters that are of significantly higher mass than the sodium atom are $\sim$400 meV for perpendicular collisions. For a cluster beam traveling at 1000 m/s, parallel collisions with collision partners moving in opposite directions can be up to 1.5 eV. Typical heats of vaporization are around 220 meV for dimethyl ether (DME) and ammonia and 470 meV for water. For the most likely perpendicular collisions, this gives a number of evaporating molecules m of one or two. Another factor that needs to be considered is the heat of solvation of the sodium atom. The full solvation of the sodium atom (in e.g. ammonia) sets free another $\sim$1.25 eV of energy.[98] This energy would, according to our simple estimation, correspond to the evaporation of $\leq$5 ammonia molecules.

In the models used in this work to describe the doping process, the sticking probability for the sodium atom to a cluster is assumed to be one, and cluster evaporation is neglected. This approach follows the considerations of Schläppi et al.[96]

It is clear that the sticking for very small clusters is far from this assumption, but a reasonable estimation for the smallest clusters is not possible without high level ab initio calculations. For clusters larger than ∼5-10 molecules the assumed sticking probability of unity is expected to represent the situation well because the lifetime of the collision complexes is assumed to be longer than the timescale of the experiment. The cluster evaporation is neglected due to the fact that a difference of a few molecules per cluster is typically well within the accuracy of determined average cluster sizes.

2.3.3 Ionization probability

The ionization cross section σ_{UV} for single photon UV ionization of a sodium-doped cluster is proportional to the number of sodium atoms m in the cluster. This can be explained by the fact that the UV photon can only ionize the sodium atom but not the solvent molecules. Since the doping process is probabilistic, it is convenient to use an average ionization cross section $\langle\sigma_{\mathrm{UV}}\rangle$, which is proportional to the average number of sodium atoms $\langle m\rangle$ and can be calculated according to equation 2.30. As discussed above, the size dependence of the collision probability is determined by the size dependence of the collision cross sections of equation 2.33. As a first approximation ($r_{\mathrm{Na}} << r_{\mathrm{c}}$) the collision cross section scales as ${r_{\mathrm{c}}}^2$. Therefore, $\langle\sigma_{\mathrm{UV}}\rangle$ increases as

$$\langle\sigma_{\mathrm{UV}}\rangle \propto \langle m\rangle \propto r_{\mathrm{c}}^2 \propto n^{2/3}. \tag{2.37}$$

A more detailed analysis including the radius of the sodium atom results in a scaling factor of $n^{0.63}$ instead of $n^{2/3}$. Generally this means larger clusters contain a higher average number of sodium atoms, and are therefore more likely to be probed by photoionization. This creates a size bias in sodium-doped mass spectra that needs to be corrected to retrieve the original cluster size distribution in the molecular beam before sodium doping.

In contrast to the SPI of sodium-doped clusters with UV light, the cross section for VUV single photon ionization σ_{VUV} of a cluster is proportional to the cluster volume and hence to the cluster size n.

$$\sigma_{\mathrm{VUV}} \propto n \tag{2.38}$$

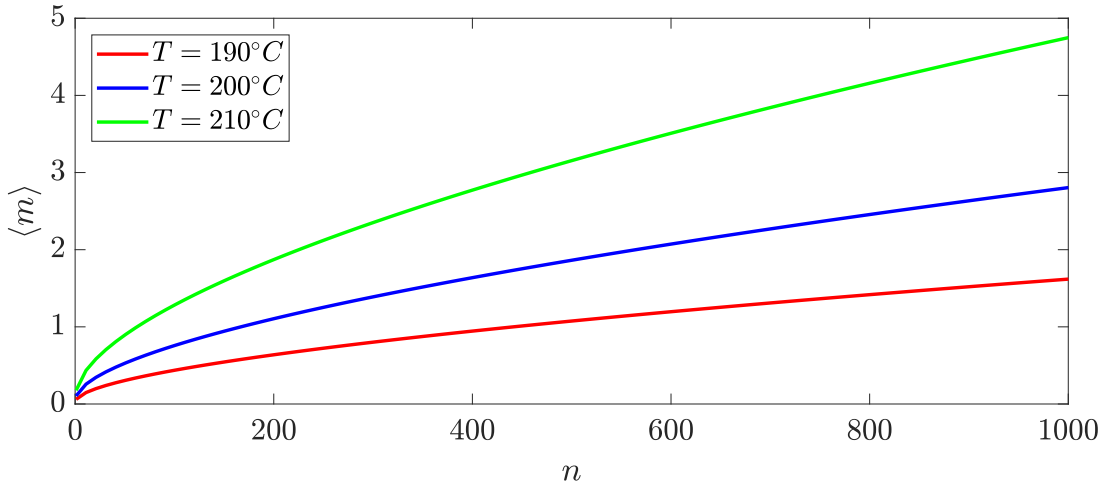

Figure 2.15: Average number of sodium atoms $\langle m \rangle$ as a function of the cluster size, for a fixed oven temperature of 200°C

This is due to the fact that all constituents of the cluster can be ionized by a single photon of the incident light.

Since the ionization efficiencies of both mechanisms depend on the cluster size, it is necessary to correct for resulting mass biases, if mass spectrometry is used to retrieve the original cluster size distribution.

2.3.4 Detection efficiency

The detection efficiency of cluster ions on a microchannel plate (MCP) detector depends on the ion velocity.[96,105] In time-of-flight mass spectrometry, all ions are accelerated to the same kinetic energy. For very heavy ions, the velocity can thus be too low for efficient detection on the MCP detector. Although there is the possibility to correct for such effects[96] it is more convenient to work at high enough extraction voltages to assure that a later correction is not necessary.

2.3.5 Correction of mass spectra

To obtain the original cluster size distribution $P(n)$ before sodium doping, the recorded sodium-doped mass spectrometric signal $I_{\mathrm{UV}}(n)$ needs to be corrected for the ionization efficiency. As discussed above, the ionization efficiency shows the most pronounced cluster size dependence. In this work this is the only correction that is used. Since we are not interested in absolute cluster concentrations, it is

sufficient to use a relative correction:

$$P(n) = \frac{I_{\mathrm{UV}}(n)}{\langle m \rangle (n)} = \frac{I_{\mathrm{UV}}(n)}{n^{0.63}} \tag{2.39}$$

The experiments discussed in Chapter 5 use mass spectrometry of sodium-doped clusters to obtain information on the original cluster size distribution $P(n)$, and then use single photon VUV ionization to study this size distribution with photoelectron spectroscopy. To obtain the size distribution $I_{\mathrm{VUV}}(n)$ as probed by VUV photoelectron spectroscopy an additional correction is necessary:

$$I_{\mathrm{VUV}}(n) = n \cdot P(n) = I_{\mathrm{UV}}(n) \cdot \frac{n}{n^{0.63}} \tag{2.40}$$

Example size distributions $I_{\mathrm{VUV}}(n)$, $I_{\mathrm{UV}}(n)$ and $P(n)$ are shown in Figure 2.16.

It should be noted, that if sodium-doped clusters are studied with UV photoelectron spectroscopy, a correction of the size distribution is not necessary. This is because the mass spectra in this case show exactly the same cluster distribution that is probed by photoelectron spectroscopy. Nevertheless, the Poisson collision model can still be used in those cases to estimate the average sodium concentration of the clusters. To do this one can calculate a concentration in mole-percent sodium (mole-percent metal, MPM) as

$$c(n) = 100 \cdot \frac{\langle m \rangle}{\langle m \rangle + n}. \tag{2.41}$$

The resulting concentration $c(n)$ can be averaged over the size distribution, to obtain an average concentration

$$\langle c \rangle = \frac{\sum_n c(n) \cdot P(n)}{\sum_n P(n)}. \tag{2.42}$$

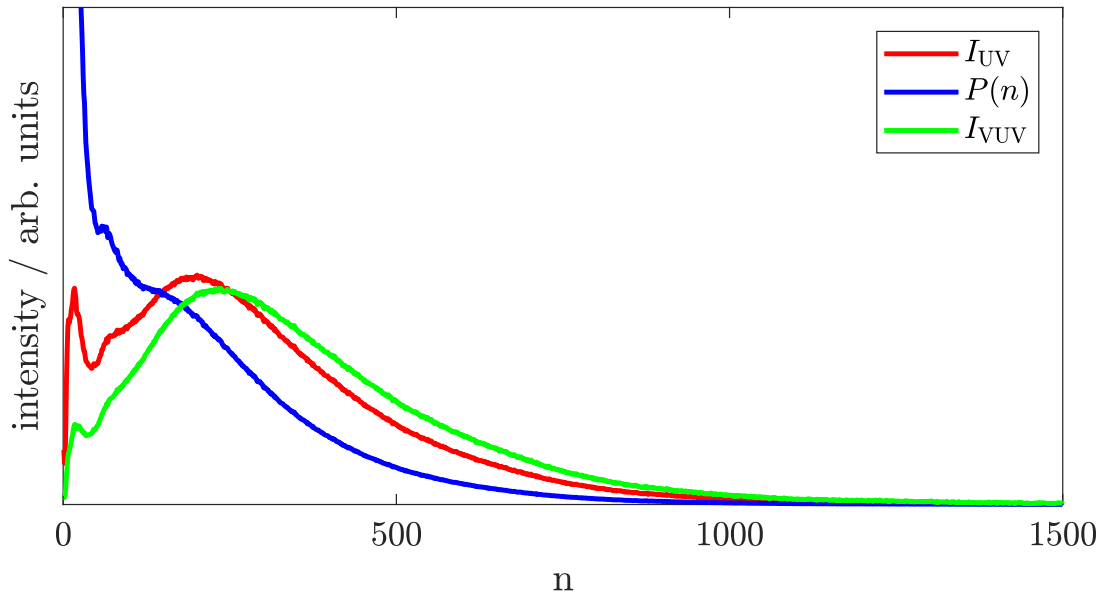

Figure 2.16: Effect of mass spectra correction. The red trace shows the integrated mass spectrometric signal I_{UV} recorded after UV ionization of sodium-doped clusters. The blue trace shows the retrieved original size distribution $P(n)$ of undoped clusters. The black trace shows the size distribution as probed by VUV single photon ionization I_{VUV}. Both, I_{VUV} and $P(n)$ are determined from the recorded trace I_{UV}.

Chapter 3
Experimental

3.1 VMI photoelectron spectrometer at ETH

3.1.1 Overview

The VMI photoelectron spectrometer at the ETH that was used for the work presented in this thesis is the product of development over several years. The earliest designs for the ZEKE (zero electron kinetic energy) photoelectron spectroscopy and mass spectrometry[106,107] with a table top VUV source were soon expanded to offer the capability to dope clusters with sodium atoms.[89,104] In another major development step the design was complemented with the possibility to perform photoelectron velocity map imaging.[108] The final experimental setup is displayed in Figure 3.1 and schematically in Figure 3.2 a). Two implementations of this experimental setup exist in our group, and both were used in this work. The only significant difference between the two setups is the available light sources, and as a result a slightly different detection scheme, as will be discussed in sections 3.1.4 and 3.1.5. The setups consist of three chambers. The source chamber holds the cluster source (see section 3.1.2), and is separated from the oven chamber by a skimmer. This second chamber contains a sodium oven that can be used to dope the clusters with sodium atoms (section 3.1.3). The oven can also be used to create effusive beams of sodium atoms. The last chamber is referred to as the detection or time-of-flight chamber. This is where the cluster beam is ionized (section 3.1.4) and the photoelectrons (section 3.1.5) or ions (section 3.1.6) are extracted and detected. The extraction (ion or electron) optics consist of three equidistant round metal plates of 108 mm outer diameter spaced by 15 mm. In the center of the

plates there are concentric holes through which the cluster beam enters the ionization region and through which either the ions or electrons are extracted. The ionization region, i.e. the overlap between the molecular and light beams, is located between the first (repeller) and the second (extractor) plate (see labels "R" and "E" in Figure 3.2). On the far side of the detection chamber the detector assembly is positioned. It is formed by two microchannel plates in a chevron stack and a phosphor screen. The time of flight and extraction region is shielded from the Earth's and other stray magnetic fields by two concentric μ-metal cylinders.

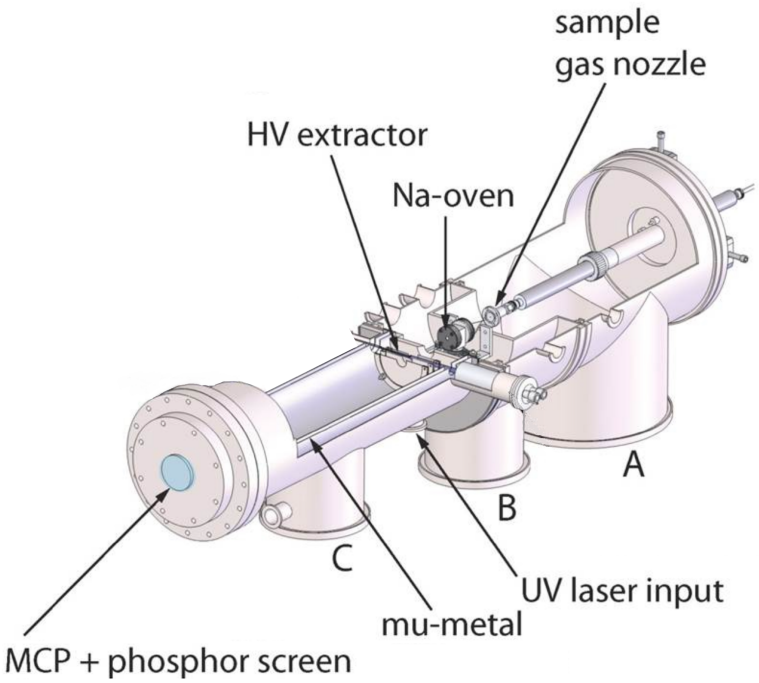

Figure 3.1: 3D view of the experimental setup. A, B and C label the source, oven and detection chamber respectively.

For the experiments described in Chapter 7, the setup was modified significantly. The schematic of this modified experiment is shown in Figure 3.2 b). The main changes are the insertion of an additional chamber to house the deflector, the removal of the μ-metal shield and replacement of the detector. These changes are further motivated and explained in Chapter 7.

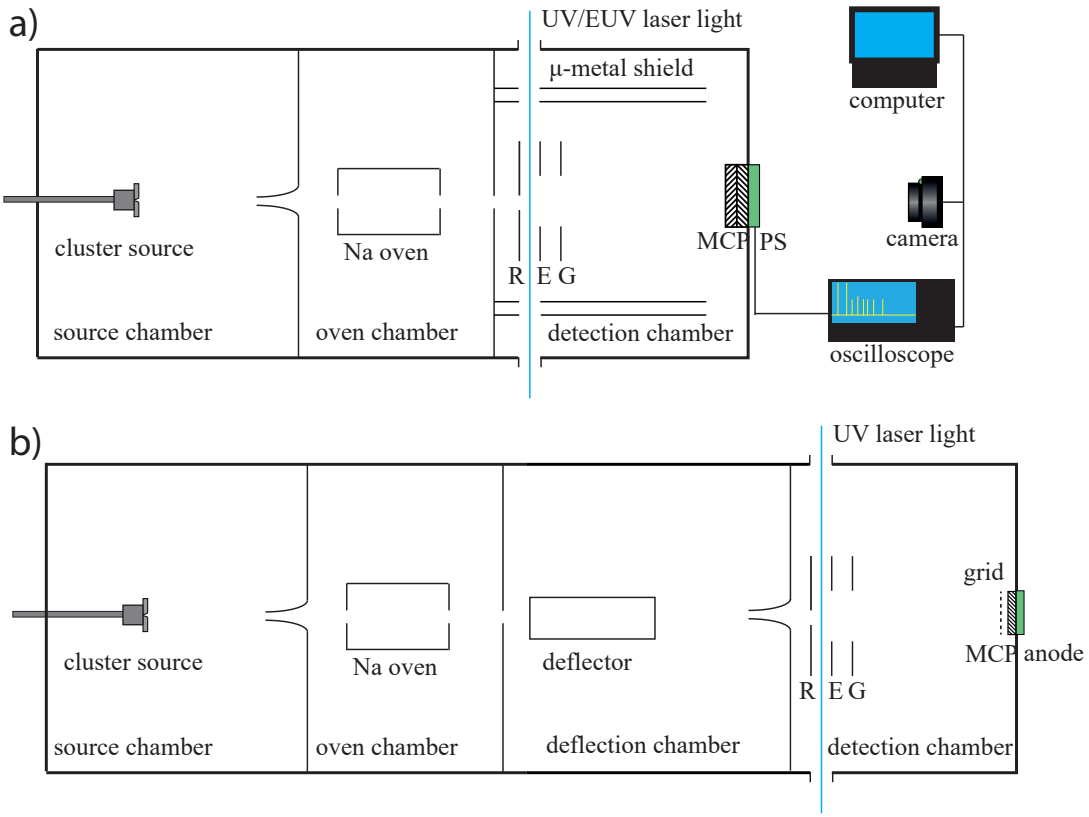

Figure 3.2: Schematic representation of the experimental setup. R, E and G label the repeller, extractor and ground electrodes of the extractor. a) Setup as used in Chapters 5 and 6. MCP and PS label the detector assembly of two multichannel plates and the phosphor screen. b) Setup as used for the work described in Chapter 7, where more details are discussed.

3.1.2 Cluster formation

All cluster sources used in this work are based on supersonic expansions of a neat gas or gas mixture into vacuum. During such an expansion the sample gas is rapidly cooled, as the thermal energy is converted into directed kinetic energy. This rapid cooling can be accompanied by condensation of the sample gas, leading to cluster formation.

In the course of this work several different expansion conditions were used to form clusters. In the following, I will first describe the technical components used for cluster formation, before describing the different controllable parameters and their influence on the resulting cluster size distribution. The pulsed nozzles used for the expansions were an Even-Lavie valve (EL valve) and a general valve from Parker Hannifin (general valve series 9). Both valves are based on a magnetic solenoid mechanism to open the valve. The Parker valve has a maximal repetition rate of 120 Hz, while the EL valve can operate at a rate of up to 1000 Hz. The EL valve is equipped with a heatable nozzle head and can be used at temperatures up to 250°C . The Parker valve is mounted on a temperature controlled copper block, that allows adjustment of the valve temperature between ∼-30°C and ∼80°C by a Peltier element. It can be operated with opening times typically between 250 μs and 1000 μs. The EL valve does not allow to directly control the opening time of the valve, but rather to set the opening amplitude, which determines the opening time. Typically the gas pulses generated by the EL valve are a few tens of microseconds long, which is significantly shorter than those from a Parker valve. The third nozzle used in this work was one for continuous supersonic expansions. This nozzle consists of a small hole of about 50 μm diameter at the end of a gas tube that can be heated to high temperatures.

In addition to the type of nozzle used, the formation of clusters and the resulting cluster size distribution depend on the stagnation conditions and chemical properties of the sample. The parameters to control the stagnation conditions in our experiments were the stagnation pressure, the gas mixture as well as the stagnation temperature (i.e. the nozzle temperature). The gas mixtures were typically produced by passing a flow of the carrier gas, e.g He, Ne, N_2 or Ar, over a liquid surface, or bubbling the carrier gas through a liquid reservoir. The pressure of this carrier gas flow and the vapor pressure of the liquid define the total stagnation pressure as well as the concentration of the condensable gas. To adjust the partial

pressure of the condensable gas, without changing the total stagnation pressure, the vapor pressure of the liquid can be tuned by adjusting the temperature of the liquid reservoir. To truly control the gas mixture, it is necessary for the liquid reservoir to be at the same or a lower temperature than the subsequent gas line and the nozzle. This avoids condensation of the sample gas and consequently a change in the gas composition before the expansion.

To qualitatively explain the dependence of the cluster size distributions on the stagnation conditions, it is sufficient to make two assumptions: The first one is to assume an adiabatic expansion of an ideal gas. The final temperature in such an adiabatic expansion is given by

$$T_f = T_i \left(\frac{p_i}{p_f} \right)^{\frac{1-\gamma}{\gamma}}, \tag{3.1}$$

where $T_{i/f}$ and $p_{i/f}$ are the temperature and pressure before the expansion and after the expansion, respectively. $\gamma = c_p/c_v$ is the ratio of heat capacities. The second assumption is that a lower final expansion temperature increases cluster formation. It is clear that both assumptions are not strictly true. The flow temperature T_f in a free jet expansion is not well defined, and depends on the position in the flow. Furthermore, in such supersonic expansions the translational temperature and the vibrational or rotational temperatures can differ significantly. Also, the assumption that lower flow temperatures lead to increased cluster formation neglects possible limitations due to the limited concentration of the condensable gas. Nevertheless, the simple assumptions can be used to qualitatively explain observed trends.

Minimization of the stagnation temperature and maximization of the stagnation pressure results in cold expansions and thus strong clustering. For neat expansions and expansions with very high concentrations of the condensable gas, the assumption of an ideal gas expanding is not well satisfied. It is observed that they usually form smaller clusters than expansions with a significant amount of carrier gas. This is explained by a more efficient cooling provided by the "ideal" carrier gas expansions. A further experimental observation is that usually longer opening times for pulsed expansions increase the cluster size as well. Continuous expansions tend to form smaller clusters than pulsed ones because of the lower stagnation pressures that are typically used.

3.1.3 Na-doping

The sodium oven is shown in Figure 3.3. The overall height of the oven is 10 cm and the length of the top part is 4.4 cm. The exchangeable entry and exit holes for the molecular beam in the top part were between 4 mm and 10 mm in diameter. The top and bottom parts of the oven are heated separately by one resistive heating coil each, and the temperatures of the two parts were measured by two thermocouples and controlled by two PID (proportional-integral-derivative) controllers. The bottom part holds a reservoir of solid or liquid sodium, depending on the temperature. At sufficiently high oven temperatures the top part fills with sodium vapor. The vapor pressure curve of sodium as a function of temperature is shown in Figure 3.4 based on data reported by Fink and coworkers.[102] A new oven design was used toward the end of the work discussed in Chapter 7, which improved the robustness of the thermal contact of the thermocouples and the heating coils to the oven material. Mass spectrometry signals with good signal-to-noise ratios were usually found for oven temperatures above 150°C , depending on the laser power used for photoionization. At temperatures above 200°C there was usually significant multi-doping observable in the mass spectrum. When the oven was not used to dope clusters, it remained in the chamber, and the chamber acted as differential pumping chamber. The vapor pressures of sodium below its melting point (at 97°C) are low enough not to affect the molecular beam or the chamber pressures.

3.1.4 Light sources

With the experimental setup used for the experiments in Chapters 6 and 7, photoionization was achieved exclusively by the use of pulsed nanosecond UV lasers, operating at a repetition rate of 20 Hz. Light of 266 nm wavelength (4.66 eV photon energy) was generated using the fourth harmonic of a Nd:YAG laser (Quantel Ultra). The polarization was made parallel to the detector plane using a half-wave plate in combination with a Glan-laser prism. The laser power could be adjusted by rotating the polarization via the angle of the half-wave plate with respect to the Glan-laser prism.

Slightly higher energetic light of 212 nm (5.85 eV) was created by tripling the 636 nm output of a dye laser (Radiant Dyes NarrowScan). The dye laser was

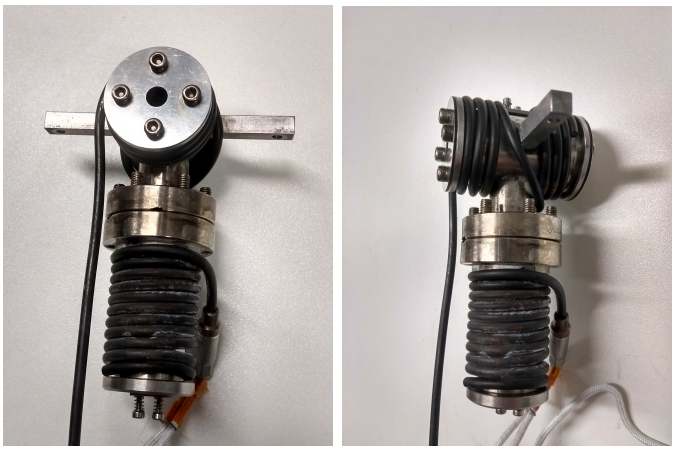

Figure 3.3: Photographs of the sodium oven.

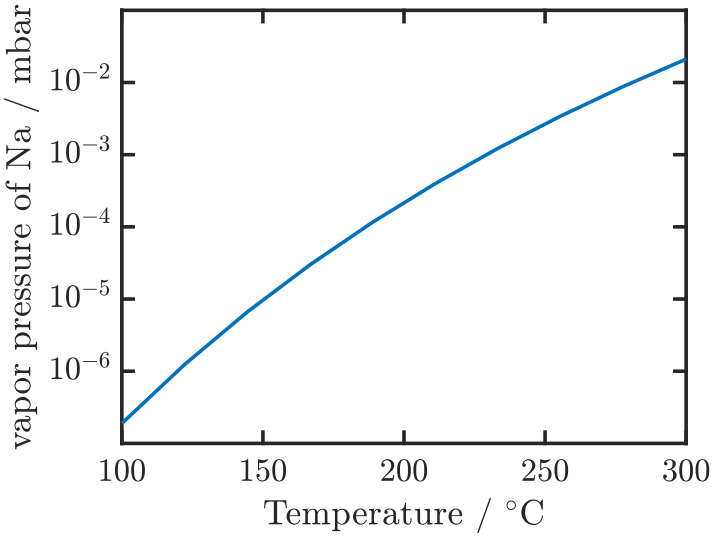

Figure 3.4: Vapor pressure of sodium as a function of temperature.[102]

pumped by the second harmonic (532 nm) of a Nd:YAG laser (Continuum powerlite), and used DCM (4-(Dicyanomethylene)-2-methyl-6-(4-dimethylaminostyryl)-4H-pyran) as a laser dye. Frequency tripling (third harmonic generation) of the fundamental was achieved by first doubling the frequency in a nonlinear crystal, and then performing sum frequency generation (SFG) of the second harmonic and residual fundamental in an additional non-linear crystal. The 212 nm light was separated from the fundamental and the second harmonic, and coupled into the ionization chamber by dielectric mirrors. The polarization was again set by passing the beam through a Glan-laser prism. The laser power was adjusted by detuning the second non-linear crystal and therefore reducing the conversion efficiency.

The optical setup used for the experiments described in Chapter 5 was operated at a repetition rate of 1 kHz. UV light at 280 nm was generated in an optical parametric amplifier (OPA) (Coherent OPerA Solo), which was pumped by a ultrafast Ti:Sapphire laser (Coherent Astrella) centered at a wavelength of 795 nm. The 795 nm fundamental of the Ti:Sapphire laser is used to pump a high harmonic generation[109] (HHG) source for monochromatic EUV (extreme ultraviolet) radiation. The HHG source with subsequent time-preserving monochromator following the design by Poletto and coworkers[110,111] is depicted schematically in Figure 3.5. The polarization-controlled ∼35 fs infrared (IR) pulse from the Ti:Sapphire laser is focused into an argon gas cell by a focusing lens. The created EUV radiation is collimated by a toroidal mirror, diffracted by a grating and focused onto a slit before being collimated again by a third toroidal mirror and coupled into the experiment.

λ / nm	$h\nu$ / eV	f / Hz	Δt
266	4.66	20	∼8 ns
212	5.85	20	∼8 ns
280	4.43	1000	<100 fs
47.1	26.35	1000	<100 fs
61.5	20.15	1000	<100 fs
88.9	13.95	1000	<100 fs

Table 3.1: Overview of used light sources, with the wavelength λ, photon energy $h\nu$, repetition rate f and pulse length Δt.

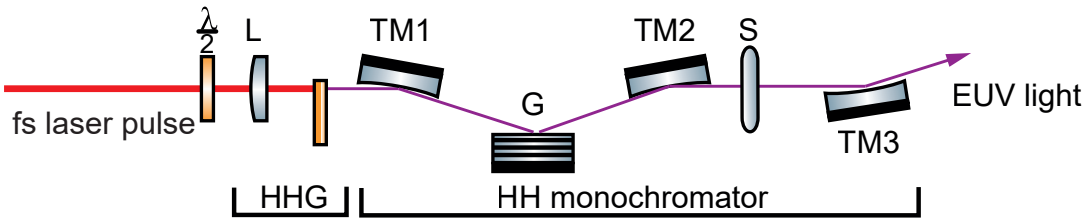

Figure 3.5: Optical layout of the high harmonic laser source and monochromator. $\lambda/2$ half-wave plate, L focusing lens, TM toroidal mirror, G grating and S slit.

3.1.5 Photoelectron velocity map imaging

The theory and the concept behind velocity map imaging, as well as the reconstruction methods to obtain photoemission anisotropy parameters and photoelectron spectra were discussed in section 2.1.2. Therefore, the current section focuses on the experimental details of measuring velocity map images. To accelerate the photoelectrons in the direction of the detector, negative voltages are applied to the repeller and extractor plates (Figure 3.2) in a way that $|V_R| > |V_E|$. To achieve optimal kinetic energy focusing conditions the ratio V_E/V_R has to be set accurately. The exact value of the optimized ratio depends on the length of the flight tube, on the exact laser alignment (i.e. at which position between the extractor and repeller plate the electrons are created). In general, this setting has to be reoptimized if one of these parameters is changed. For optimization of the voltage ratio, it is useful to change the polarities of V_R and V_E to perform photoion velocity map imaging. The optimal voltage ratio for VMI of electrons and ions is identical, and since in general the photoions in such experiments should have near-zero kinetic energy release, it is possible to find optimal voltage settings by minimizing the spatial extent of the ion spot created on the detector. As discussed in section 2.1.2 higher kinetic energies result in larger radii in the velocity map image. When setting the extraction voltages care needs to be taken to make sure that the electrons of highest kinetic energy are still detected on the MCP. Increasing V_R while maintaining a constant V_E/V_R shrinks the electron image by extracting the electrons at higher kinetic energies. In general the repeller voltage V_R is chosen to be as high as necessary and as low as possible, to provide optimal sampling of the photoelectron spectrum by using the full active area of the detector.

The third plate of the extraction optics (labeled G in Figure 3.2) and the first

MCP plate of the detector are maintained at ground, to produce a field-free flight region. In addition to that, the flight region is shielded from the Earth's and other stray magnetic fields by two concentric μ-metal cylinders. The detection of the photoelectrons is synchronized with the ionizing laser pulse to reduce background levels. This means the second MCP plate is only at a high voltage of ∼2300 V during the ∼ 300 ns when photoelectrons created by the laser pulse arrive at the MCP. The rest of the time the MCP voltage is reduced to ∼1800 V, which is enough to reduce the gain of the MCP to essentially zero. The phosphor screen was kept at -6000 V. The fluorescence of the screen is recorded by a CCD (charge-coupled device) or CMOS (complementary metal oxide semiconductor) camera, which is triggered with a short delay after the beginning of the MCP gate. This detection scheme was operated at 20 Hz or at 500 Hz depending on which laser system was used. Note that detection at 1000 Hz was not possible at the time due to the long fluorescence time of the phosphor screen used.

The cameras are connected to a computer that is used to save and sum up the data. In the case of the 20 Hz setup, the single laser shot images (frames) are centroided and summed up in real time by the NuAcq software.[112] Centroiding means that the position of each fluorescence event is calculated. Therefore, the software calculates the center of mass, or centroid, of the multi-pixel event as an intensity weighted average position as depicted in Figure 3.6. In the end those centroided events are summed instead of the original multi-pixel spots. This centroiding step formally doubles the image resolution since each centroid is calculated with an accuracy higher than the image resolution. The main advantage of centroiding is however, that response inhomogeneities in the position sensitive detector can be compensated. For the 500 Hz detection scheme the computational time available per frame is insufficient to perform centroiding on the fly. Therefore, each camera frame (at 500 Hz) is saved and centroiding and summation is performed in a post-processing step. The velocity map images are reconstructed and evaluated using either the MEVIR or pBasex algorithms. The resulting speed distributions $S(r)$ are transformed and calibrated to a kinetic energy spectrum $S(E_{kin})$ according to

$$S(E_{kin}) = \frac{S\left(\frac{r^2 V_R}{C}\right)}{r}, \tag{3.2}$$

where r is the image radius in pixels, V_R is the repeller voltage and C is a setup

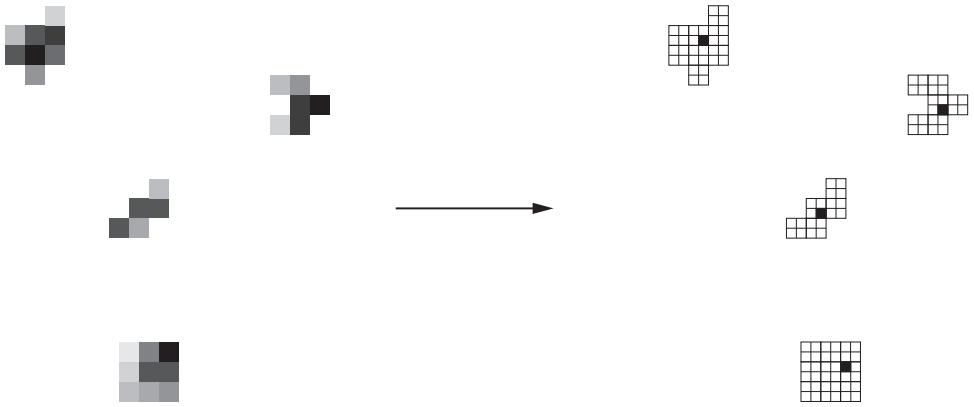

Figure 3.6: Working principle of centroiding. The centroid of multi-pixel event is calculated on a grid with twice the image resolution.

dependent calibration constant. The factor of $1/r$ is needed to account for the nonlinearity in the transformation from space to energy coordinates. C is in general determined from a recorded VMI image of a substance with known ionization potential with a known laser wavelength.

3.1.6 Time-of-flight mass spectrometry

To perform ion time-of-flight (TOF) mass spectrometry the same extraction optics (electrodes) are used. This setup is very similar to the one Wiley and McLaren[113] suggested for ion TOF mass spectrometry. To switch our setup from photoelectron VMI to ion TOF the polarities of the voltages V_R and V_E are switched to positive, and the ratio V_E/V_R is set to ∼0.9. The mass spectrometry conditions are optimized to form ion TOF peaks as narrow as possible. With the setting of V_E/V_R ∼0.9 the ions gain about 90% of their kinetic energy between the extractor and the ground plate. To obtain sufficient detection efficiency also for large clusters (see section 2.3.4), repeller voltages up to 25 kV were used in this work. Similar to the VMI measurements, the first MCP plate was connected to ground to maintain a field-free time-of-flight region. The second MCP plate was set to a constant bias of 2300 V and the phosphor screen, used as an anode here, to ∼2700 V. For detection no cameras are used, but the phosphor screen is connected to

an oscilloscope via a homebuilt capacitative decoupling circuit. This means the phosphor screen acts as a simple anode, that collects the signal current from the MCP. This time-dependent current is transformed to a voltage signal that is displayed on the oscilloscope. The time-of-flight data $I(t)$ is then transformed to a mass spectrum $I(m)$ as

$$I(m) = \frac{I\left(\frac{(t-t_0)^2}{c}\right)}{t}, \tag{3.3}$$

where t_0 is a time offset between the trigger of the oscilloscope and the ionizing laser pulse and c is a setup-dependent calibration constant. The division by the flight time t accounts for the nonlinearity in the transformation. Both t_0 and c are usually determined by fitting the flight times in a mass spectrum to known masses.

3.2 Photoelectron photoion double imaging coincidence spectroscopy

3.2.1 Overview

The technical details of the double imaging photoelectron photoion coincidence spectrometer (i^{2}PEPICO) used in this work (Chapter 4) can be found in the publications by Garcia, Tang and Nahon and coworkers.[114,115] A scheme of the experimental apparatus reproduced from their publications is shown in Figure 3.7. Note that the scheme does not depict all components to scale. The experimental setup is located at the DESIRS (dichroïsme et spectroscopie par interaction avec le rayonnement synchrotron) beamline of SOLEIL synchrotron. This section will focus on the basic features of the spectrometer with respect to the work on small, neutral clusters, and therefore not consider all the technical and scientific possibilities of the instrument.

The basic idea of coincidence spectroscopy is to record information on photoelectrons and photoions simultaneously, in a way that the correlations between ion and electron properties are retained. In other words, every electron remains assignable to the photoion from which it was detached in the photoionization process. This can be achieved experimentally by extracting electrons and ions in opposite directions perpendicular to both the molecular beam and the light beam

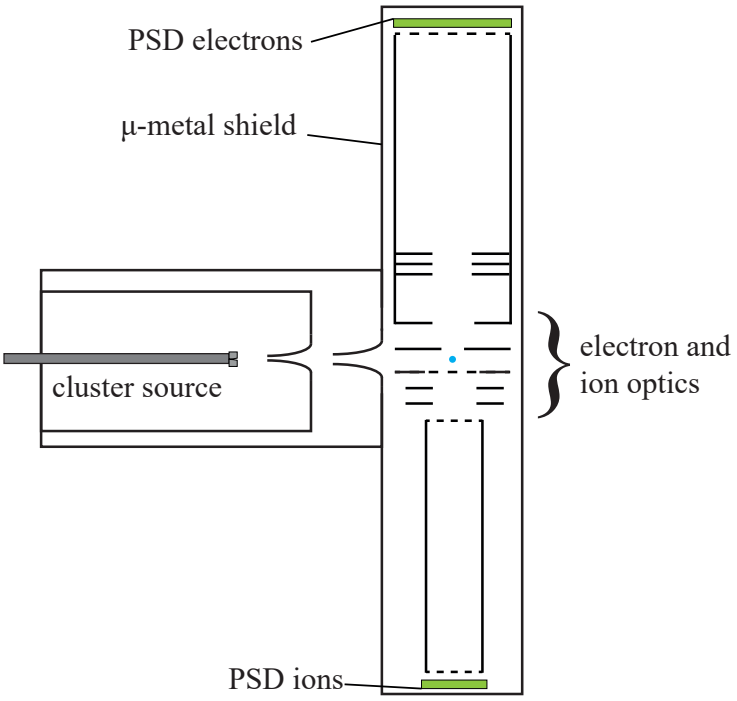

Figure 3.7: Schematic view of the double imaging photoelectron photoion coincidence spectrometer used in this work (reproduced from[114,115]). PSD denotes the position sensitive detectors. Components and chambers are not depicted to scale.

(Figure 3.7). Coincidence detection is only possible if signal levels are low enough to avoid multiple ionization events before the detection of an electron/ion pair is finished. The time needed to finish this detection process is obviously limited by the flight time of the ion. For typical imaging conditions used for non-coincidence experiments in this work, electron detection rates can be as high as 50-80 electrons per laser shot. Such conditions are not practicable for coincidence detection. This is the main reason that coincidence spectrometers usually use high repetition rate or quasi-continuous light sources, so that the high duty cycle can compensate the low signal per shot.

In double imaging photoelectron photoion coincidence spectroscopy, both photoelectrons and photoions are detected on two-dimensional position sensitive detectors (PSD). This allows for simultaneous collection of a correlated electron VMI image, ion image and ion time-of-flight mass spectrum. If the correlation between detected ions and detected electrons was neglected, the results would correspond to recording an electron VMI, an ion image and an ion TOF mass spectrum after each

other on the same cluster size distribution on a setup similar to the one described in section 3.1. The correlation now gives the opportunity to filter the electron image according to ion time-of-flight, and therefore according to ion mass. After filtering the electron images according to ion masses, the result is fully size-resolved VMI images from neutral species. Experimentally these coincidence techniques are limited to relatively small clusters, since otherwise the compromise between high extraction voltages needed to extract higher masses on one side and reasonable electron VMI conditions on the other becomes problematic. The ion image (see example in Figure 3.8) gives the further possibility to filter out background signals by spatial separation. Furthermore, ions of different masses are not only separated in time-of-flight but also spatially on the detector.

3.2.2 DESIRS beamline at SOLEIL Synchrotron

The DESIRS beamline is an undulator based VUV beamline at the French national synchrotron facility SOLEIL.[116] In an undulator, highly-relativistic electrons are forced onto an oscillating trajectory by an alternating magnetic field. The electrons that are accelerated and decelerated on the oscillating trajectory emit radiation of a frequency depending on the strength and spatial period of the magnetic fields and the electron energy. The undulator of the DESIRS beamline is about 10 m long and consists of 14 periods of 640 mm length. The magnetic fields are created by pure electromagnets. The photon energies can be set via the driving currents in the coils to values between 5 eV and 40 eV. Depending on which set of coils is used in the undulator, the polarization can either be set to horizontal or vertical linear polarization, and by using multiple sets of coils with a fixed phase relation circular or elliptical polarizations can be realized. The synchrotron radiation is subsequently put through a rare gas filter to suppress higher harmonics of the desired wavelength created in the undulator, before being sent to a 6.65 m long grating monochromator, with different gratings available. The radiation finally coupled into the experiment has a controlled photon energy between 5 and 40 eV with a bandwidth of down to 1/50'000 (depending on the grating used) and a controlled polarization. In this work, the polarization was always linear (perpendicular to the electron and ion extraction axes) and the photon energies were between 12.5 eV and 35 eV.

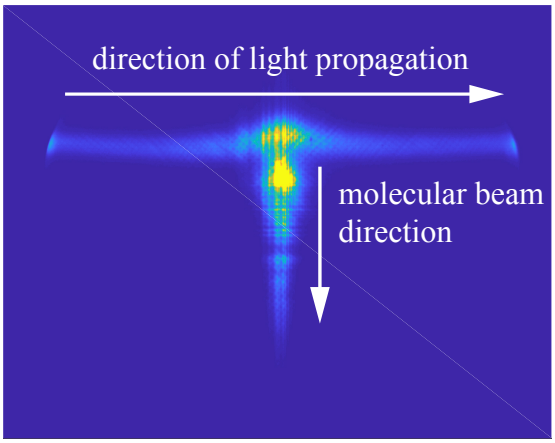

Figure 3.8: Ion image containing ions of all masses present in the molecular beam. The horizontal line originates from background gas, while the signal in the vertical line results from clusters of different sizes in the molecular beam.

Chapter 4

Electron scattering in small water clusters and predictions for the liquid phase

Part of the work presented in this chapter has been published.[117]

4.1 Introduction

The aim of this work is to offer a path to a quantitative description of low energy electron scattering in liquid water, and its effect on photoelectron angular distributions. Angle-resolved photoelectron spectroscopy is well suited to study effects of electron scattering since it gives access to the photoelectron kinetic energy distribution and the photoelectron angular distribution. Both of these quantities are affected by electron scattering in the liquid bulk. PADs are of particular interest for the quantitative understanding of electron scattering in condensed water because of their high sensitivity to electron scattering. A substantial reduction of the β parameter can occur already for one scattering event per electron since a scattering event can pronouncedly change the propagation direction of an electron (see Figure 2.7). In the energy range considered in this work (<25 eV), the average change of kinetic energy per scattering event is small because scattering is dominated by elastic and quasi-elastic scattering. When comparing photoelectron emission from water gas phase molecules and the liquid bulk, one finds more isotropic emission for the liquid bulk.[32,83] This decrease of the β parameter holds information on electron transport scattering in the liquid. Nevertheless, this de-

crease is difficult to analyze quantitatively since electron transport scattering is not the only contribution to it. The PAD without effects of electron transport scattering, i.e. the genuine PAD, is determined by the initial state electronic wave function, the final state electronic wave function and the interaction of the photoelectron with the ion core. Those three determining factors differ significantly between the gas phase and the liquid phase since they are influenced decisively by the molecular environment. We propose to conceptually separate the changes to the PAD into a local photoionization process and electron transport scattering (Figure 4.1). The electron transport scattering can be described appropriately with the electron scattering model introduced in section 2.2.3. Our approach to obtain genuine β parameters for the liquid bulk is to study water clusters $(H_2O)_n$ with $n \leq 20$. Such small water clusters are much smaller than typical mean free paths of electrons in water ($\sim$5 nm[15,27]), therefore it can be assumed that all PADs measured for these clusters are genuine. How many water molecules are needed in a cluster to fully describe the condensation effects on the photoelectron anisotropy is one of the questions we hope to answer in this chapter. After the determination of genuine photoelectron anisotropies it should be possible to use these genuine values and the transport scattering model (section 2.2.3) to obtain β parameters for the liquid bulk. This approach (Figure 4.2) promises the possibility to quantify the different contributions to the decrease of the β parameter between the gas phase and liquid bulk water.

Photoelectron spectra of gas phase water molecules,[62,118,119] water clusters of different sizes[30,120–124] and liquid microjets[5,32,83] have been reported previously.

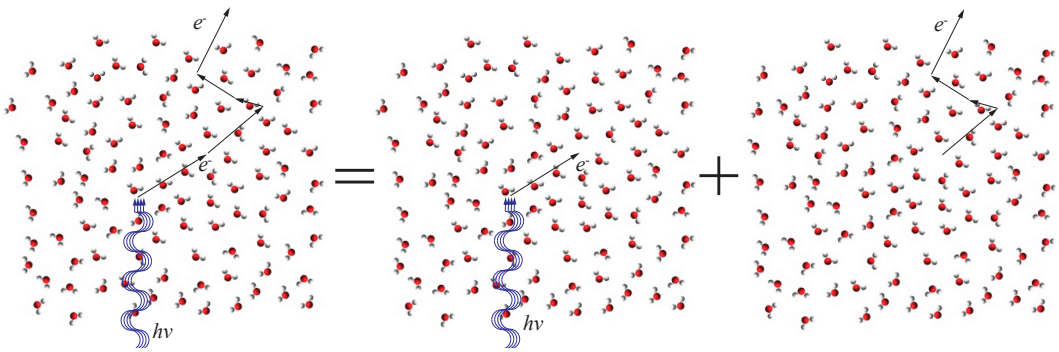

Figure 4.1: Schematic representation of the separation of bulk effects on the PAD (left), into photoionization effects (center) and electron transport scattering effects (right).

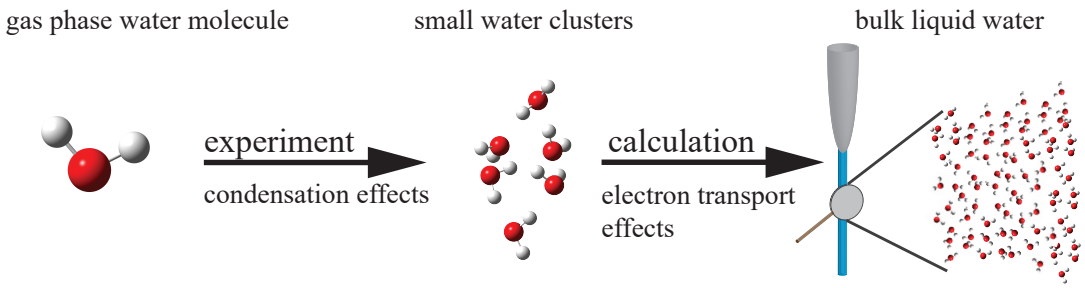

Figure 4.2: Schematic representation of the approach to quantify the different contributions to the decrease of the photoelectron anisotropy between the water in the gas phase and in the liquid bulk.

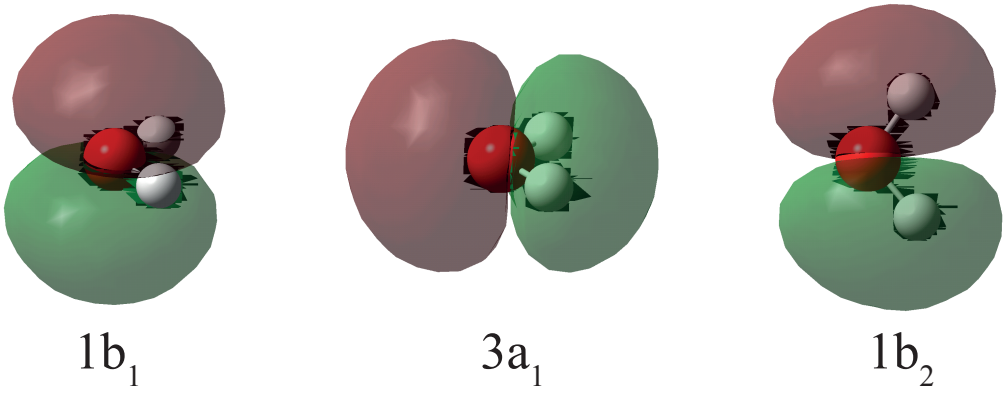

Figure 4.3: Schematic representation of the valence orbitals of the water molecule.

PADs of small water clusters ($n \leq 50$), however, were missing so far. For the gas phase molecule, the valence photoelectron spectrum below binding energies of 25 eV shows photoelectron bands corresponding to photoionization from the three highest-lying occupied molecular orbitals (Figure 4.3). The brief description of the photoelectron spectrum of the water molecule provided below follows the high-resolution experiments and assignments made by Brundle and Turner.[118] The $1b_1$ orbital (HOMO, out-of-plane lone pair) has non-bonding character, i.e. it corresponds to a lone-pair on the oxygen atom, and is therefore visible as a sharp peak at an eBE of 12.6 eV with only a weak vibrational progression of the ν_1 (symmetric stretch) and ν_2 (bending) modes. The $3a_1$ orbital (in-plane lone pair) shows a strong progression of the ν_2 vibration. This hints at the slight H-H-bonding character of this orbital, and therefore at a significant change of the equilibrium geometry upon photoionization from this orbital. The vertical binding energy of ∼14.8 eV corresponds to photoionization accompanied by the excitation of the bending mode with ∼10 quanta. The $1b_2$ orbital with a vertical binding energy of 18.6 eV is the lowest lying orbital considered in this work. It has O-H σ-bonding character, and appears as a complicated progression of all three vibrational modes in the photoelectron spectrum.

In comparison to the gas phase, the cluster spectra show much broader bands that are shifted to lower eBE values. Vibrational structure is typically not resolved in cluster spectra. The widths of the bands as well as the shifts from the gas phase binding energies increase with cluster size. The increasing width of the photoelectron bands can be understood by considering the interactions of the molecular orbitals of the water molecules with those of neighboring molecules. These interactions lead to the formation of "cluster orbitals", as shown schematically for the example of the water hexamer in Figure 4.4. It should be noted that the symmetry of water clusters is not C_{2v} anymore. Nevertheless, we will still refer to the three valence bands as $1b_1$, $3a_1$ and $1b_2$. This approach is commonly used and is suitable although there is some mixing of the molecular orbitals. It is mainly molecular orbitals of the same molecular symmetry interacting with each other to form the cluster orbitals (Figure 4.4).

While the orbital interactions and mixing have an effect on the electron binding energies, it is often thought that the major contributions to the eBE shifts with increasing cluster size are polarization effects. The electric polarization induced

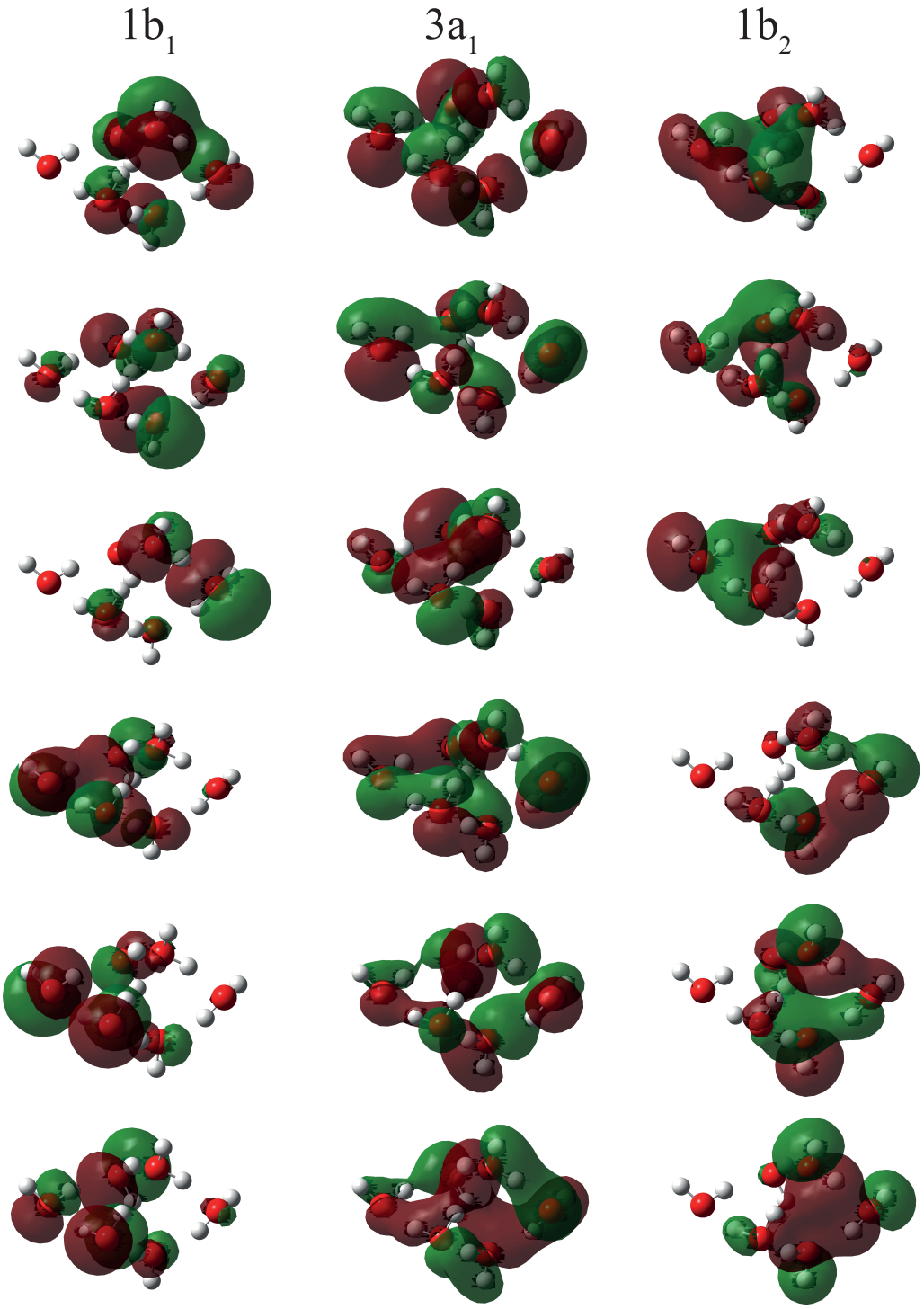

Figure 4.4: Schematic representation of the valence orbitals of the water hexamer in the cage conformation.

by surrounding water molecules stabilizes the positive charge of the final cationic states and therefore reduces the electron binding energies. Even for the largest reported cluster spectra ($\langle n \rangle$ ≈1000 molecules[121]) the eBE values of the liquid bulk spectra (11.16 eV for the $1b_1$ band[5]) are not yet reached. The polarization effects result in a $1/r$ dependence of the eBE on the cluster radius r.

For the water monomer, PADs have been measured over a wide range of photon energies for the three outer valence orbitals.[30,62,83,119] Photoelectron anisotropies for clusters larger than a few ten molecules per cluster were only reported by Zhang et al.[30] They report β parameters for three different cluster size distributions, measured at two different photon energies. The cluster sizes were estimated by empirical scaling laws, relating experimental expansion parameters to average cluster sizes.[92] These scaling laws are in general less reliable than an in-situ size determination, using for example mass spectrometry. Measurements of β parameters on liquid jets are similarly rare, and the only reported data in our photon energy range were reported by Faubel and coworkers,[83] and recently by Nishitani et al.[82]

4.2 Experiments and data analysis

The experimental setup for double imaging photoelectron photoion coincidence spectroscopy was described in section 3.2. It is located at the SOLEIL synchrotron facility in France, where the experiments discussed in this chapter were performed. The cluster source (Figure 3.7) was a continuous molecular beam expansion of water seeded in helium. The water gas mixture was prepared by flowing 3-7 bar of helium over a reservoir of liquid water that was kept at 60-100°C . The nozzle was a home-built, laser-drilled hole (estimated diameter ∼50μm), which was kept at a temperature a few degrees higher than the water reservoir. The experiments were performed with linearly polarized light of photon energies between 12.5 eV and 35 eV. The recorded electron images were filtered according to the ion masses and spatial location of the ions on the detector. Finally, the mass-selected VMI data was reconstructed using the pBasex algorithm (see section 2.1.2.2). Band positions were extracted for a given cluster size, taking into account the measurements at all different photon energies. Therefore, all the spectra of a given cluster size were plotted over each other, and the band center was then determined visually to

agree best with all spectra of a given cluster size. While this is arguably not the most accurate approach, its accuracy is fully sufficient for our purposes. For the monomer, the β parameters were averaged over the FWHM of the three valence bands. The β parameters for the clusters were evaluated by averaging over a 0.8 eV around the peak position for the $1b_1$ orbital, and over a 1.4 eV around the positions of the $3a_1$ and $1b_2$ bands. The chosen energy ranges are slightly smaller than the FWHM. This was done to avoid averaging the β parameters in regions where the bands overlap.

4.3 Results and Discussion

4.3.1 Fragmentation of water clusters upon EUV ionization

The coincidence detection can only be used to obtain mass selected data if there is no significant fragmentation of the created water cluster cations on the timescale of the extraction of the ions into the field free TOF region. The fragmentation of water clusters upon EUV single photon ionization has previously been studied extensively.[90,125,126] Upon EUV SPI of a water cluster a fast proton transfer occurs within a few ten femtoseconds,[127,128] which results in the loss of an OH radical from the cluster:

$$(H_2O)_n \xrightarrow{h\nu} (H_2O)_n{}^+ + e^- \longrightarrow (H_2O)_{n-1}H^+ + OH\cdot + e^-$$

Therefore, all ion masses detected correspond to protonated water cluster cations with n-1 molecules, originating from the neutral water cluster with n molecules. This agrees with the typical mass spectrum displayed in Figure 4.5. Further fragmentation of the protonated water clusters should not occur on the timescale of our experiment. Dong et al.[126] reports maximum rate constants for the unimolecular dissociation

$$(H_2O)_nH^+ \longrightarrow (H_2O)_{n-1}H^+ + H_2O$$

in our cluster size range of $\leq$15'000 s^{-1}. This corresponds to a lifetime of the protonated cluster after loss of the OH radical of $\sim$67 μs. Since this is much

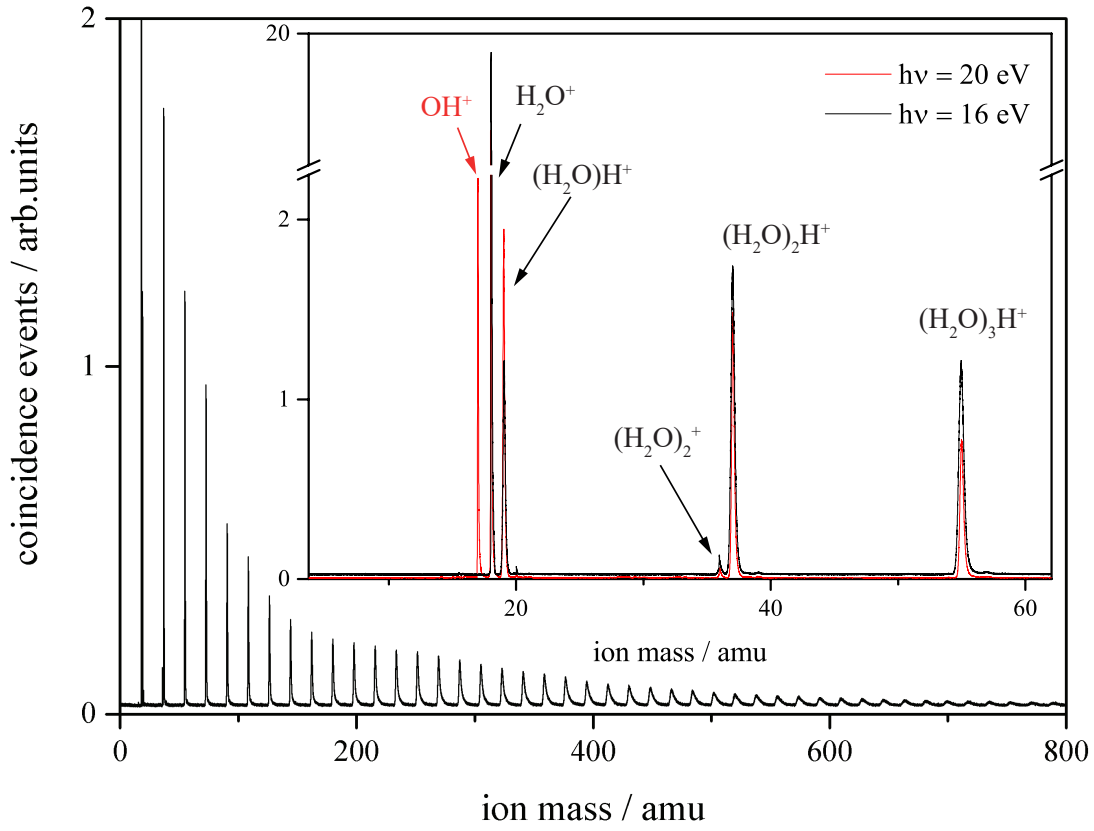

Figure 4.5: Representative mass spectra of water clusters. The peaks in the main figure correspond to protonated water clusters, except for the smallest clusters. The inset shows the low mass range, recorded at 16 and 20 eV photon energies. At 20 eV there is a significant signal observable at 17 amu.

longer than the relevant experimental timescales, such evaporation processes do not influence the experiment.

Deviation from this general fragmentation behavior is observed for the smallest clusters. A small amount of intact, unfragmented water dimer is observed in the mass spectrum at 36 amu. Furthermore, the water monomer stays intact because proton transfer cannot occur in this case. However, for photon energies above 18 eV the water monomer fragments, and an ion mass peak at 17 amu (OH^+) appears in the mass spectrum (Figure 4.5). A comparison of the photoelectron spectra recorded for the mass channels 17 amu and 18 amu at 22 eV photon energy is shown in Figure 4.6. The spectrum recorded for mass channel 18 shows bands corresponding to ionization from the $1b_1$ orbital, the $3a_1$ orbital and the $1b_2$ orbital. The vibrational structures of the bands are not resolved in our measurements. A

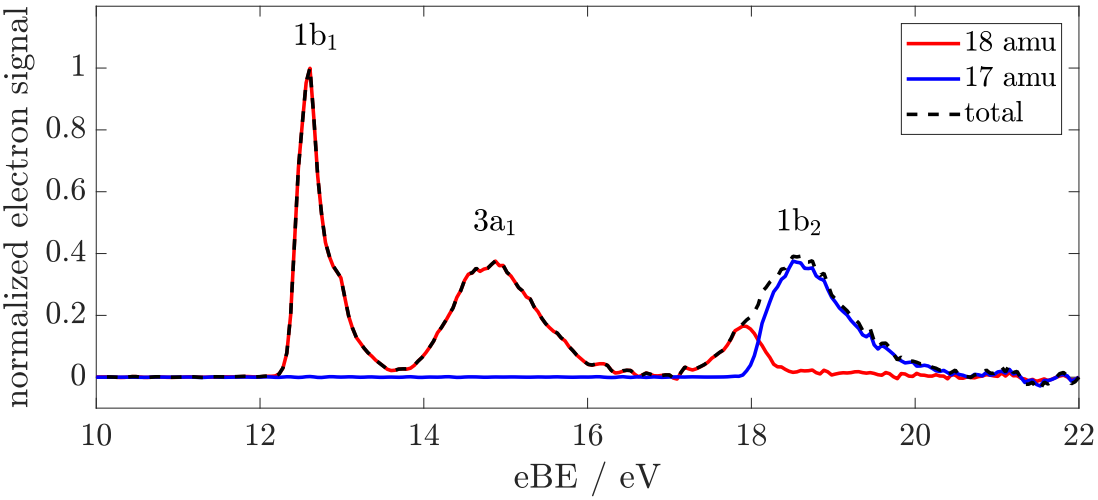

Figure 4.6: Photoelectron spectra of the H_2O monomer recorded for mass channels 17 amu (blue line) and 18 amu (red line). The sum of the two channels (black dashed line) represents the total photoelectron spectrum of the water monomer recorded at 22 eV photon energy.

brief inspection of the spectrum recorded for an ion mass of 18 amu shows that the $1b_2$ band maximum at ∼18 eV is significantly lower than the 18.6-18.8 eV reported in previous studies.[5,118,119] Previous studies also report ionization cross sections for the $1b_2$ band to be similar to those of the $3a_1$ band. However, our spectrum for ion mass 18 amu shows significantly lower intensity for the $1b_2$ band. The explanation for this difference lies in the photoelectron spectrum recorded for mass channel 17 amu. This spectrum shows a single, asymmetric peak with a maximum at ∼18.6 eV and a longer tail towards high electron binding energies. This band corresponds to ionization from the $1b_2$ orbital accompanied by some vibrational excitation, leading to the fragmentation of the water monomer cation. Note that the $1b_2$ orbital has σ-bonding character. Hence the ionization from this orbital reduces the bond order, and therefore destabilizes the chemical bond. The sum of the spectra of both mass channels (black dashed line in Figure 4.6) agrees well with spectra in literature.[5,118,119] The band positions for the monomer are determined as 12.6 eV for the $1b_1$ band, 14.8 eV for the $3a_1$ band and 18.6 eV for the $1b_2$ band. The fragmentation pattern, i.e. the onset of the band in mass channel 17 amu around ∼18 eV agrees well with data reported by Bodi et al.[129] (onset 17.9-18.0 eV) and a value of 18.1 eV reported by Brundle et al.[118] The high binding energy cut off of the $1b_2$ band in mass channel 18 amu around 18.2 eV

also agrees well with the value determined by Bodi et al. of ∼18.12 eV.[129]

A similar behavior is observed for the water dimer. Here only a small fraction of the water dimer cations stays intact and is detected in the mass channel at 36 amu. Most cations fragment and form protonated water monomers H_2OH^+ with an ion mass of 19 amu. The photoelectron spectra recorded for the two different ion masses are compared in Figure 4.7 for a photon energy of 18 eV. For increasing photon energy the signal in mass channel 36 amu decreases even further, relative to mass channel 19. The spectrum for mass channel 36 shows a single band corresponding to photoelectrons ionized from the HOMO of the water dimer without significant vibrational excitation of the cation. This highest occupied molecular orbital $(1b_1)_D$ is essentially the $1b_1$ orbital of the water molecule which donates the hydrogen for the hydrogen bond[127,130](Figure 4.8). Contributions from the other molecular orbitals are essentially contained in the electron spectrum recorded for ion mass 19 amu. The signal at electron binding energies below 13 eV in the spectrum recorded for mass channel 19 amu most likely corresponds to ionization from the $(1b_1)_D$ orbital accompanied by vibrational excitation of the cation. This assignment is supported by calculations by Kamarchik et al.[127] The onset of the signal for mass 19 amu, as well as the high binding energy cut off of the signal in mass channel 36 amu agrees well with data reported by Bodi et al.[129]

4.3.2 Photoelectron spectra of water clusters (n>2)

Photoelectron spectra for different cluster sizes are shown in Figure 4.9. For increasing cluster size, the photoelectron bands broaden and shift towards lower eBE values. Example velocity map images after reconstruction are displayed in Figure 4.10 and show the band broadening very clearly. The eBE shift, corresponding to a slight increase of the image radii, can hardly be seen without reconstruction and energy calibration. The extracted peak positions are shown in Figure 4.11, and tabulated in appendix A.1. Typical uncertainties are estimated to be 0.1 eV for the $1b_1$ and $1b_2$ bands, and 0.2 eV for the $3a_1$ band. The $3a_1$ band positions appear to be less systematic than for the other orbitals, which is due to the broad flat peak shape of the band, making the determination of the band position more difficult. Band positions for the $1b_1$ bands as a function of the average cluster size were previously reported by Barth et al.[122] Although their binding energy data (shown in green in Figure 4.11) agrees well with ours, it has to be

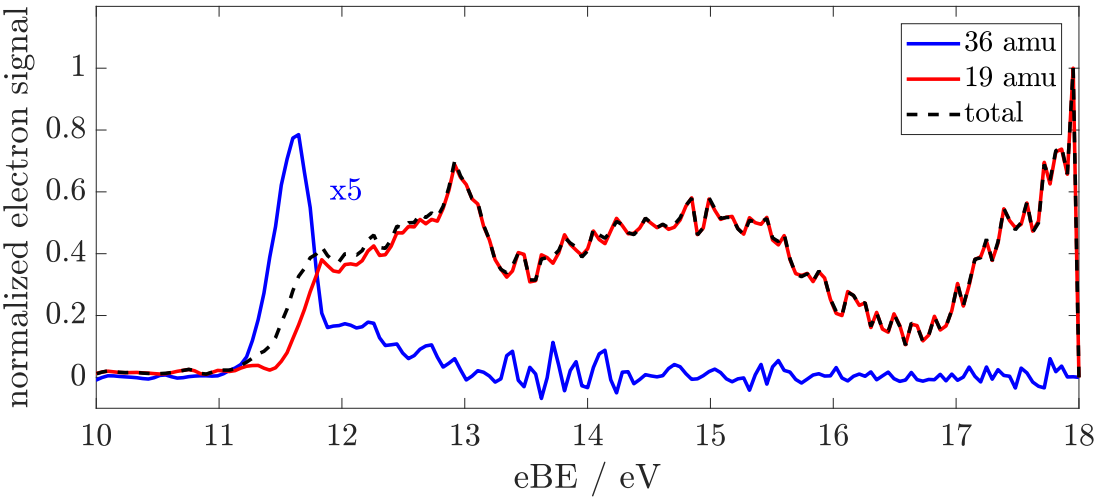

Figure 4.7: Photoelectron spectra of $(H_2O)_2$ recorded for mass channels 19 amu (red line) and 36 amu (blue line). The sum of the two channels (black dashed line) represents the total photoelectron spectrum of the water dimer recorded at 18 eV photon energy. Note that the signal in mass channel 36 (blue line) is scaled by a factor of 5 for better visibility.

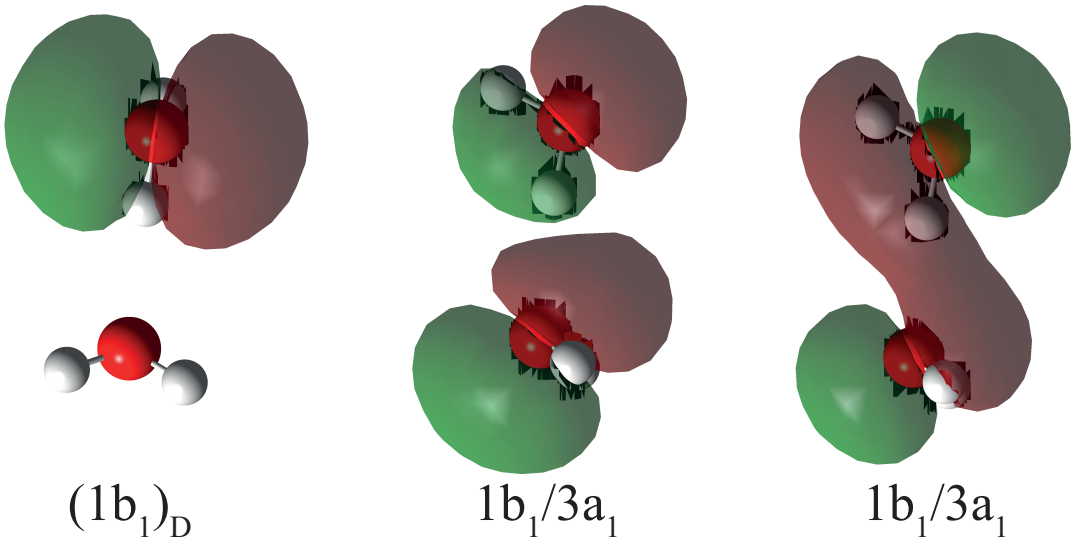

Figure 4.8: Schematic representation of the three highest lying orbitals of the water dimer.

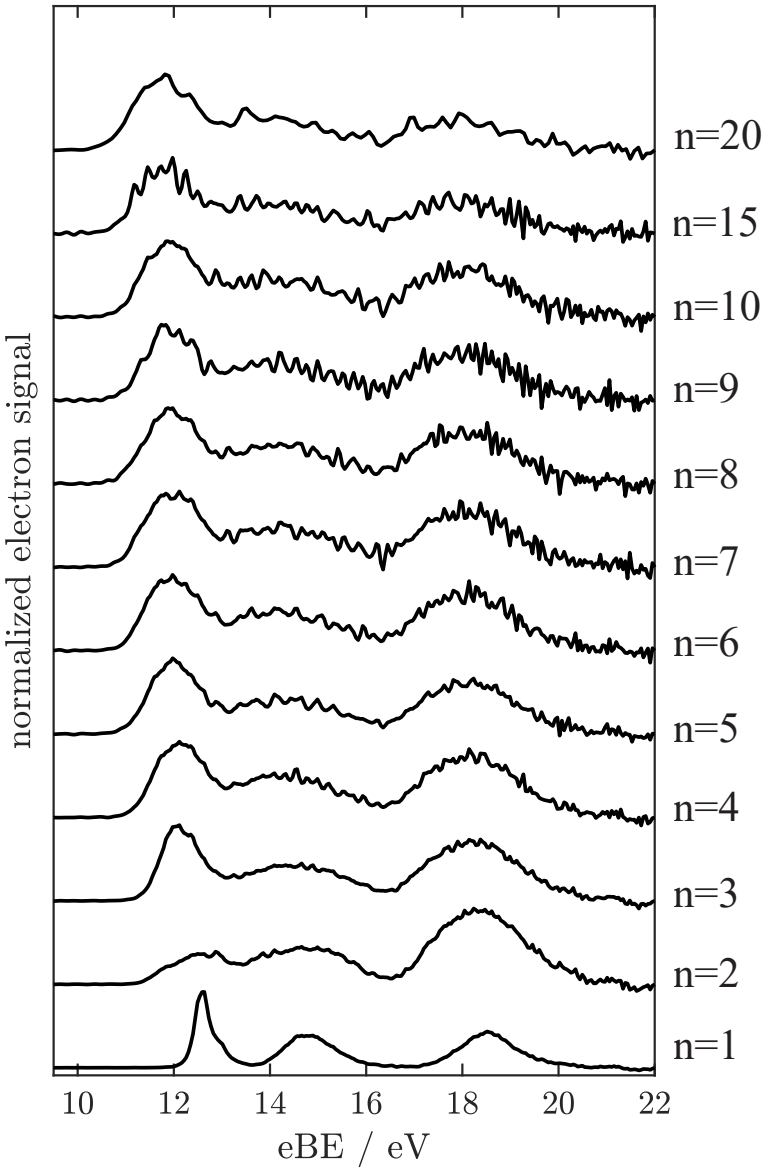

Figure 4.9: Photoelectron spectra of $(H_2O)_n$ clusters of sizes $1 \leq n \leq 20$, recorded at 22 eV photon energy.

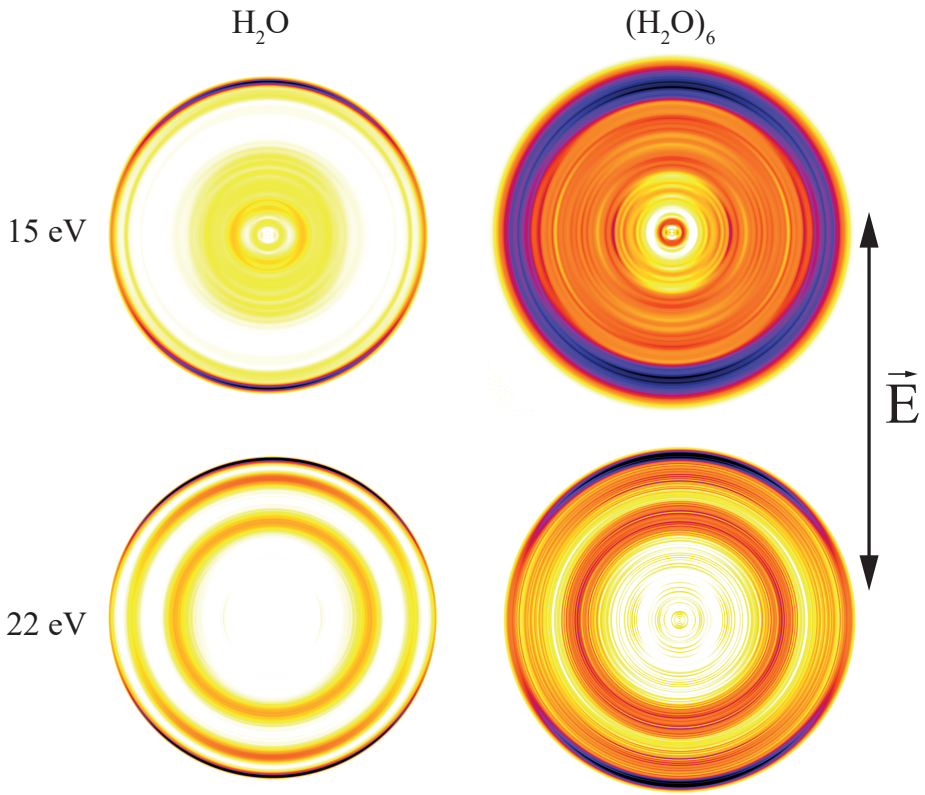

Figure 4.10: Reconstructed photoelectron velocity map images of the water monomer and the water hexamer recorded at 15 eV and 22 eV photon energies.

noted that their measurements were performed on size distributions and not on single cluster sizes. Furthermore, the average cluster sizes were estimated with empirical scaling laws[92] rather than determined experimentally as in the present work. The trend in the band positions for the $1b_1$ orbital with cluster size is similar to the trend reported by Belau *et al.*[125] for ion appearance energies of protonated cluster cations (red circles in Figure 4.11). For all three orbitals the electron binding energy determined from our measurements is still about 0.5 eV above the binding energy value reported for the liquid bulk from liquid jet photoelectron spectroscopy[5] (black dashed line in Figure 4.11). This behavior agrees reasonably with expectations. As discussed in section 4.1, a significant part of the decrease in electron binding energy from the gas phase towards the bulk is caused by the polarization of the medium. It is expected that molecules on the surface of

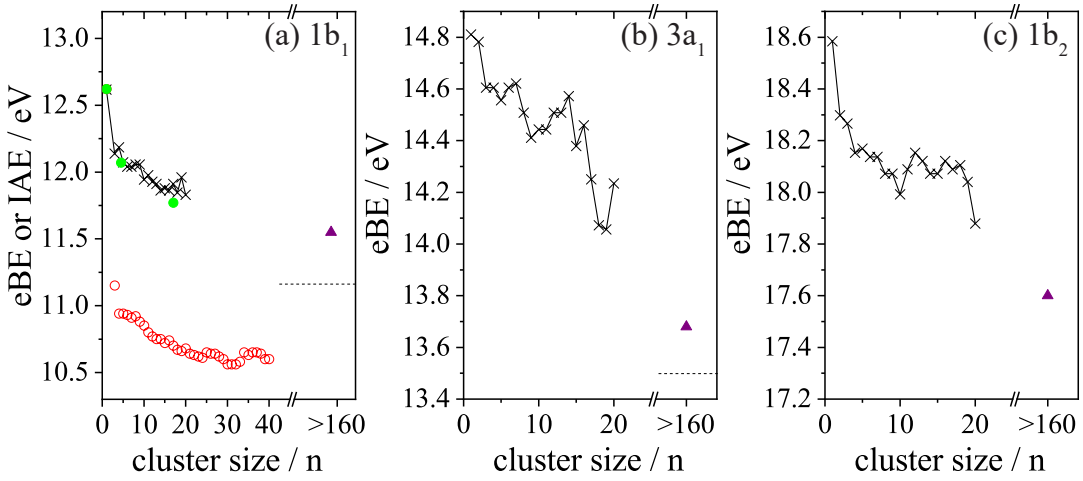

Figure 4.11: Band positions as a function of cluster size. The dashed lines indicate bulk values,[5] the red circles are ion appearance energies from,[125] the violet triangles indicate values for large clusters $\langle n \rangle > 160$,[120] and the green circles indicate data measured by Barth et al.[122] for size distributions with average size determined by scaling laws. Reprinted figure with permission from [117].

a cluster do not experience bulk like polarization effects, and therefore the binding energy of small clusters ($n \leq 20$, Figure 4.11) is not expected to be close to the bulk values. For comparison, the binding energy data reported for large clusters ($n > 160$) by Björneholm and coworkers[120] has not yet reached bulk values either (purple triangles in Figure 4.11). The cluster size reported for this measurement is only estimated as "large", since the scaling laws used for the estimation cannot be used for their experimental conditions.

The discussed polarization effect is an important difference between gas phase water molecules and very small clusters and larger or bulk systems. However it is not the only relevant effect on the measured eBE values. The decrease in electron binding energies is most likely a combination of the stabilization of the cationic state due to polarization and changes to the initial electron wave function of the neutral cluster due to interactions between the molecular orbitals of the individual water molecules.[117]

4.3.3 Photoelectron anisotropies of water monomer and clusters

A comparison between the photoelectron anisotropies determined for the water monomer from our data and previously published data[30,62,83,119] can be seen in Figure 4.12. The data is shown as a function of the photon energy for all three valence orbitals, and is also tabulated in appendix A.2. The β parameters from our work agree reasonably well with previous data.[62,119] Fluctuations that are visible in the data reported by Truesdale et al.[62] are not reproduced in our data. Also the data published by Banna et al.[119] do not show such fluctuations, which makes it likely that they arise from measurement artefacts. The photoelectron anisotropy parameters decreases pronouncedly towards the ionization threshold. For high photon energies, the β parameters seem to converge to an asymptotic value.

Cluster size dependent β parameters for the three valence orbitals as a function of the electron kinetic energies are provided in Figure 4.13 and in appendix A.2, including uncertainties. The only literature values for photoelectron anisotropies of water clusters were reported by Zhang et al.[30] They report β parameters for clusters with an estimated average cluster size of $\langle n \rangle = 58$ for a photon energy of 40 eV. Although the cluster size and the photon energy of their measurement is slightly outside of the range of our experiment their data is shown as green triangles (empty triangles for monomer data, filled triangles for cluster data) in Figure 4.13.

For the $1b_1$ and $3a_1$ orbitals, the β parameters decrease with increasing cluster size for the smallest clusters, i.e. from n=1 to n$\sim$6. This decrease is due to significant modification of the electronic wave functions of the neutral water molecule and the the cation due to changes of the molecular environment.

Upon condensation the molecular orbitals of the individual molecules start to overlap and interact with each other. Qualitatively one can say the molecular orbitals become more complicated by this interaction, meaning the orbital symmetry decreases (see also Figure 4.4). Also the orbitals contain more nodal planes and need higher l contributions for an accurate description. In this picture it makes sense that the β parameters for the water dimer $(1b_1)_D$ orbital (red crosses in panel (a) of Figure 4.13) are very similar to those determined for the water monomer.

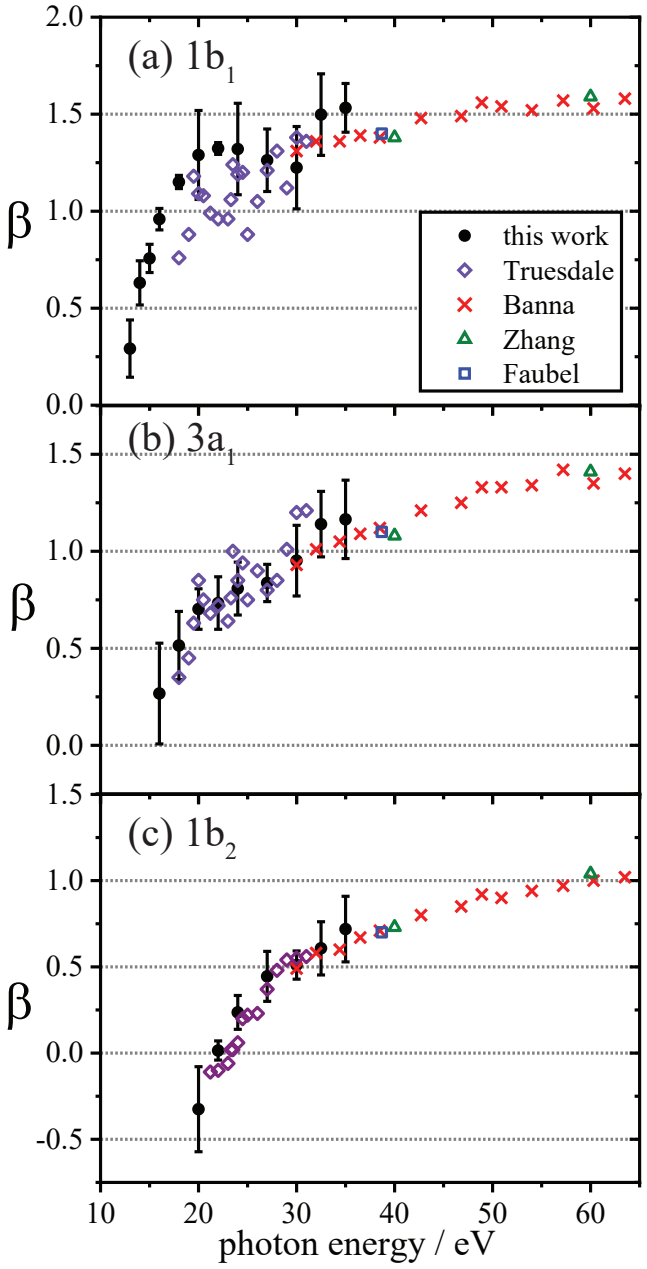

Figure 4.12: β parameters for the valence orbitals of the water monomer as a function of photon energy from this work and previous studies by Truesdale et al.,[62] Banna et al.,[119] Faubel et al.[83] and Zhang et al.[30] Reprinted figure with permission from [117].

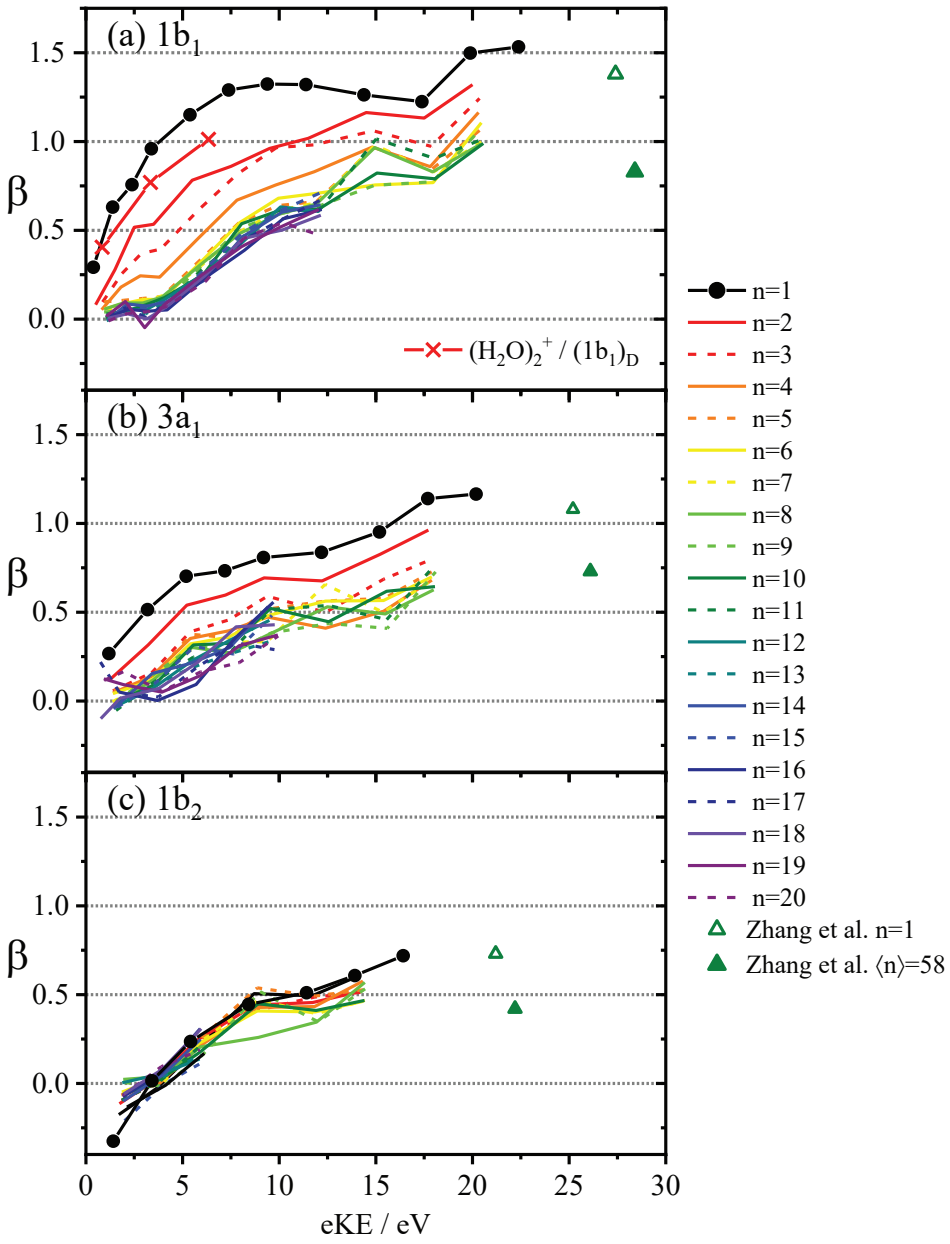

Figure 4.13: β parameters for the valence orbitals of water clusters as a function of the electron kinetic energy. n gives the number of molecules per cluster.

The $(1b_1)_D$ orbital, displayed schematically in Figure 4.8, is basically a slightly perturbed water $1b_1$ orbital that has, for symmetry reasons, no major interactions with other orbitals. In addition to the changes of the initial electronic wave function, the ion core potential, by which the outgoing photoelectron is scattered changes upon condensation as well. While the ion core potential of an isolated water cation is rather well described by the Coulomb potential of a point charge, this is no longer true as soon as the electron hole can delocalize over several molecules in a cluster. Both these effects tend to reduce the photoelectron anisotropy, i.e. the magnitude of the β parameter. For the $1b_2$ band the measured β parameters do not change significantly with the cluster size (Figure 4.13 (c)). The observed fluctuations are within the experimental uncertainty. This can be explained by the fact that this energetically low-lying σ-bonding orbital is not influenced as strongly as the other orbitals by changes of the environment. A contribution of electron transport scattering to the decrease of anisotropy of the $1b_1$ and the $3a_1$ bands can be excluded due to the very small cluster sizes considered here. Furthermore a contribution from electron transport scattering would also lead to a decrease of the anisotropy parameters of the $1b_2$ band, which is not observed. Therefore these β parameters can be considered to be genuine,[117] i.e. unaffected by the electron transport scattering.

Another important result of Figure 4.13 is the fact that the anisotropy parameters for clusters with $n \geq 6$ do not show a further decrease with increasing cluster size, neither for the $1b_1$ nor for the $3a_1$ band. This convergence is even more clearly visible in Figure 4.14, where the β parameters for a few photon energies are displayed as a function of the cluster size. This remarkable convergence indicates that the character of the electronic wave function of the neutral and the cationic state does not change significantly over this size range. If the neutral and cationic electronic states of small water clusters up to 20 molecules can be described by a unit of only $\sim$6 molecules, it seems plausible that the photoelectron anisotropies measured for those clusters would not change further. This in turn indicates that the photoionization process of larger water clusters can be completely described, with respect to the β parameter, by a short range scattering potential given by a unit of only six molecules. The cluster size of six molecules coincides with the smallest water clusters that form real 3D structures rather than quasi-planar ring structures.[131,132] This is also the smallest cluster, for which water molecules have

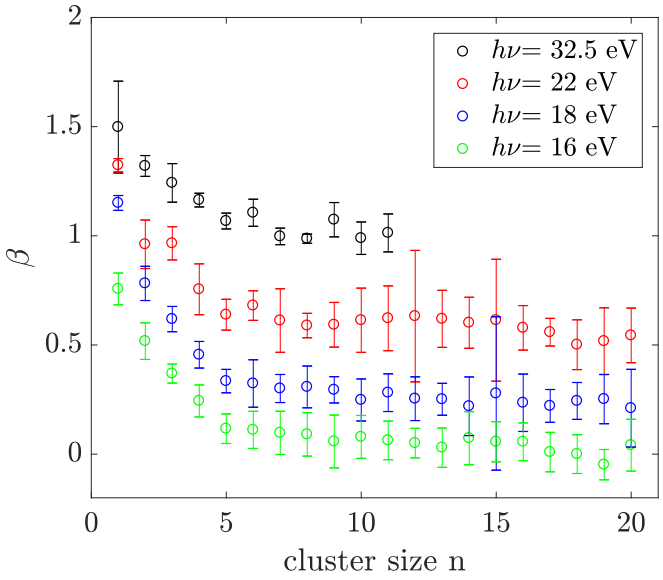

Figure 4.14: convergence of β parameters for $1b_1$ orbital of water clusters as a function of cluster size for selected photon energies.

three hydrogen bonding partners. This comes close to liquid water, where one expects on average 4 binding partners per water molecule in a tetrahedral motif. In ring structures every water molecule is involved in only two hydrogen bonds. The stability of the β parameter for clusters with between 6 and 20 molecules makes it plausible to use the converged β value of the water hexamer as the genuine β parameter for larger clusters and the liquid bulk. As shown in the following section, the further decrease of photoelectron anisotropy between the converged water hexamer value and values measured for liquid jet experiments is an effect of only electron transport scattering (section 2.2).

4.3.4 Photoelectron anisotropy for the liquid bulk

Liquid bulk photoelectron anisotropies were calculated using the genuine β parameters from the water hexamer and the transport scattering model described in section 2.2.3. The liquid jet geometry is explained in section 2.2.3.2. The starting points of the electron trajectories including the genuine kinetic energies and spatial distributions were also described in 2.2.3.3. The genuine PAD is taken from the converged water hexamer β values discussed in the previous section. Individual calculations were performed for all photon energies for which we obtained water hexamer data.

For comparison, a second calculation was performed in which the water gas phase β parameters (Figure 4.12, our data and reference [119]) were used to define the genuine angular distribution for the simulation. A third calculation was performed, using water gas phase elastic scattering cross sections[74] because a previous study[30] suggested that elastic gas phase scattering is sufficient to describe scattering in the condensed phase. As discussed in section 2.2.3.1, the elastic scattering cross sections of gas phase water are about a factor of 20 larger than those for liquid water. This leads to strongly increased scattering probabilities. In this calculation also the water monomer PAD was used for the trajectory starting points. The predicted anisotropy from the three approaches are summarized in Figure 4.15 in red, while experimental cluster or gas phase data is shown in black. Single green and blue symbols show experimental data obtained from liquid micro jet measurements by Nishitani et al.[82] and Faubel et al.[83]

As one intuitively expects, the results show that a lower input anisotropy leads to a lower predicted anisotropy for the liquid jet measurement. The predictions from the genuine hexamer anisotropies ($\beta^{n=6}_{liquid}$, red open diamonds) are lower than the predictions from the monomer β parameters ($\beta^{n=1}_{liquid}$, red open circles). It can be seen that the differences between the two predictions are more significant, the greater the difference between the genuine input values is. This means the results of the two calculations show greater differences for the $1b_1$ band than for the $3a_1$ band, and no difference at all for the $1b_2$ band, where hexamer and monomer anisotropies are almost identical. At very low electron kinetic energies, where the experimental monomer and hexamer values lie closer together, the predicted liquid β parameters are also very similar. The third calculation performed, using elastic gas phase scattering cross sections and the monomer β parameter as an input, predicts basically isotropic photoemission ($\beta^{elastic}_{liquid}$, red open stars) for a liquid jet. The small positive values that remain for $\beta^{elastic}_{liquid}$ are a geometric effect of the interaction of the light with the liquid jet.[117] This is caused by an improved coupling of light polarized along the liquid jet direction as compared to light polarized perpendicular to the jet. The improved coupling leads to an increased light intensity, and consequently an increased electron yield for the parallel polarization. This increased electron yield for one polarization results directly in more detected electrons and therefore a slightly positive β value. This effect can be considered an artefact of the experimental measurements of β parameters for a

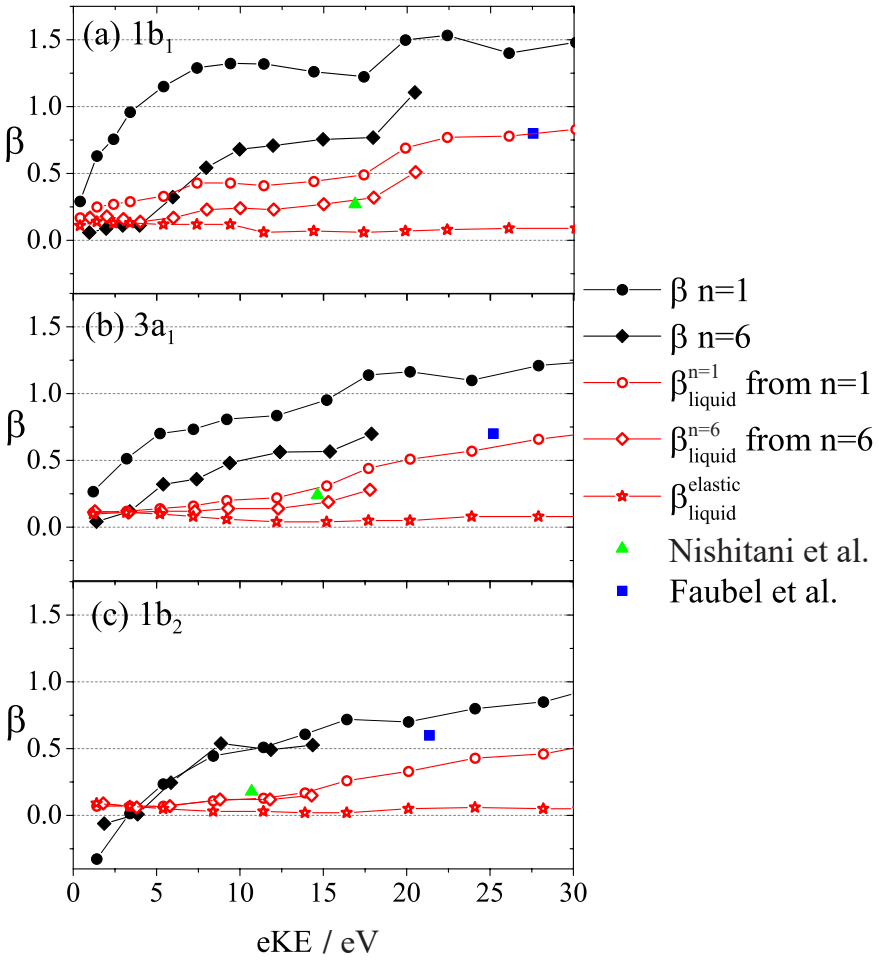

Figure 4.15: Predictions of liquid jet photoemission anisotropies using the hexamer and monomer β parameters as input.

liquid jet. However, it can simply be included in the calculations, by scaling the number of simulated electron trajectories with the light intensity within the liquid jet. Experimentally this effect could be excluded by measuring with constant polarization and liquid jet orientation, but varying the detection direction. For geometrical reasons, it is however, not possible to detect electrons parallel to the liquid jet direction. Also very small angles between the liquid jet direction and the detection direction are difficult to realize.

The β parameters measured experimentally by Nishitani et al.[82] at a photon energy of 29.5 eV (green triangles) are in very good agreement with our predictions from the hexamer anisotropies $\beta^{n=6}_{liquid}$. The experimental anisotropies reported by Faubel *et al.*[83] at a photon energy of 38.7 eV (blue squares) lie outside the energy range that was covered by our experiments. Using the measured anisotropies by Banna et al. however, our predictions starting from the gas phase monomer anisotropy $\beta^{n=1}_{liquid}$ was extended to values high enough to allow a comparison with this data as well. The $\beta^{n=1}_{liquid}$ prediction seems to agree with the $1b_1$ and $3a_1$ anisotropies reported by Faubel within our uncertainties, while the predicted values for the $1b_2$ band seem to lie below the value reported by Faubel. Agreement between $\beta^{n=1}_{liquid}$ and the measurements by Faubel seems to be fortuitous. A microjet of liquid water in vacuum is always surrounded by water vapor, due to its high vapor pressure. Selective photoionization of the liquid jet without photoionization of the water vapor is not possible. Therefore, the water vapor contributes significantly to the photoelectron signal. The bands of the gas phase and the liquid bulk spectrum overlap partially, making it difficult to extract anisotropies for the liquid bulk that are not influenced by the gas phase signal. Especially in the range of the $3a_1$ and the $1b_2$ bands, there is significant overlap of the gas phase and the liquid phase spectra. Careful data post-processing procedures make it possible to subtract the gas phase contribution from the liquid bulk signal to obtain a more or less pure liquid bulk spectrum including anisotropies. While Nishitani et al. use a rather elaborate peak fitting approach to separate the two contributions, Faubel et al. do not mention any signal subtractions. Since the gas phase photoelectron spectrum is more anisotropic than that of the bulk, the remaining gas phase contributions may cause artificially high β parameters in the measurements reported by Faubel et al.

The transport scattering model assumes that the difference between the pho-

toelectron anisotropy of a water hexamer cluster and the anisotropy of liquid bulk water are given purely by electron transport scattering. The photoelectron anisotropy of a molecule is, however, also influenced by the Coulomb interaction of the photoelectron with the remaining ion core. This interaction changes from a water hexamer to the liquid bulk since additional water molecules add to the dielectric screening of the ion core potential. Such a dielectric screening effect is not included in the model, and a quantitative estimation of the effect is difficult. Qualitatively, the interaction of the photoelectron with the ion core reduces the anisotropy. Therefore, including dielectric screening would reduce the Coulomb interaction and increase the predicted anisotropies. Since the magnitude of this effect is unknown, we are unable to determine whether this would decrease the agreement of our predictions with Nishitani or improve the agreement with Faubel.

4.4 Conclusion

The experimental data presented in this chapter show that the photoelectron anisotropy of water clusters containing between 6 and 20 molecules is equal to the photoelectron anisotropy of the water hexamer. This convergence indicates that the photoionization process of small water clusters up to 20 molecules can be readily described by the initial electronic wave function and a short-range scattering potential defined by the water hexamer. Six water molecules as minimum necessary cluster size to observe convergence of the β parameters coincides with the minimal cluster sizes for which 3D cluster structures are formed. This cluster size can also be considered as a first solvation shell of a water molecule. The stability of the photoelectron anisotropy and underlying electronic character between cluster sizes of 6 and 20 molecules suggests that the main difference between the anisotropy of those clusters and the liquid bulk is given by electron transport scattering. Consequently it follows that the anisotropy parameter of the hexamer can be used as the genuine anisotropy parameter of the liquid bulk. Simulations of liquid bulk photoelectron anisotropies including those transport scattering effects are in reasonable agreement with liquid bulk measurements.[82,83] Small differences between the experiment and model are explained by either gas phase signal contributions or the lack of polarization screening in the model. Furthermore the simulations show that gas phase scattering cross sections are not suitable to de-

scribe electron transport in the liquid bulk, as previously suggested.

Overall it can be summarized that the two step model (see Figure 4.16), assuming a genuine contribution from the local photoionization process and a transport scattering contribution, seems to be very successful in the description of the photoelectron anisotropies for liquid water. This approach offers the first quantitative description of the effect of electron scattering on condensed phase photoelectron anisotropies. In the next chapter, the same approach will be tested for large water clusters. One focus will be on whether electron transport scattering can be described by the same model for clusters and the liquid bulk.

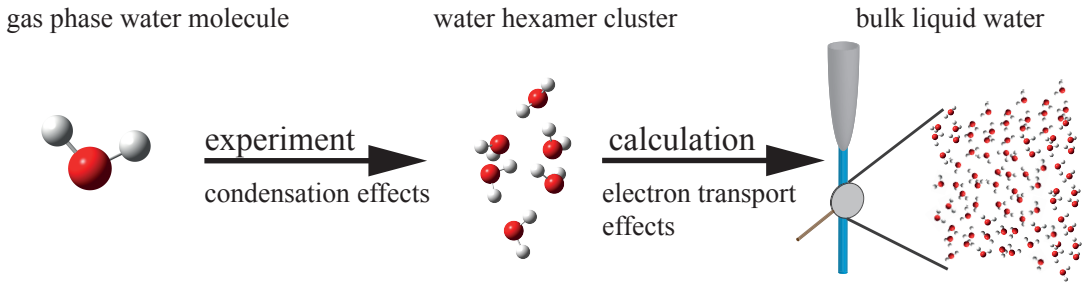

Figure 4.16: Schematic representation of the two step model separating condensation effects on the photoelectron anisotropy from electron transport scattering effects.

Chapter 5
Electron scattering in large water clusters

The work presented in this chapter has been published.[133] Thomas Gartmann and Sebastian Hartweg contributed to the published work equally. While Thomas Gartmann worked more on building and characterizing the setup as well as developing the data acquisition routines, Sebastian Hartweg worked more on the data evaluation and simulations. Both were equally involved in performing the experimental measurements.

5.1 Introduction

As discussed in Chapter 4, the genuine photoelectron anisotropy can be described by an entity of only six molecules, while the further decrease of the anisotropy to the liquid bulk value can be attributed to electron transport scattering with liquid bulk scattering parameters (see the detailed scattering model discussed in section 2.2.3). This chapter will focus on how the decrease in photoelectron anisotropy from the hexamer value towards the bulk evolves as a function of cluster size. We are particularly interested in clarifying whether or not transport scattering in large clusters can be described by condensed phase scattering parameters, as is the case for liquid bulk. For this purpose we will measure photoelectron velocity map images of water clusters of different sizes. The experiments are combined with calculations using the genuine anisotropies determined in Chapter 4 and different models for the electron transport scattering. The comparison between the scattering calculations and the experimental values can answer the question

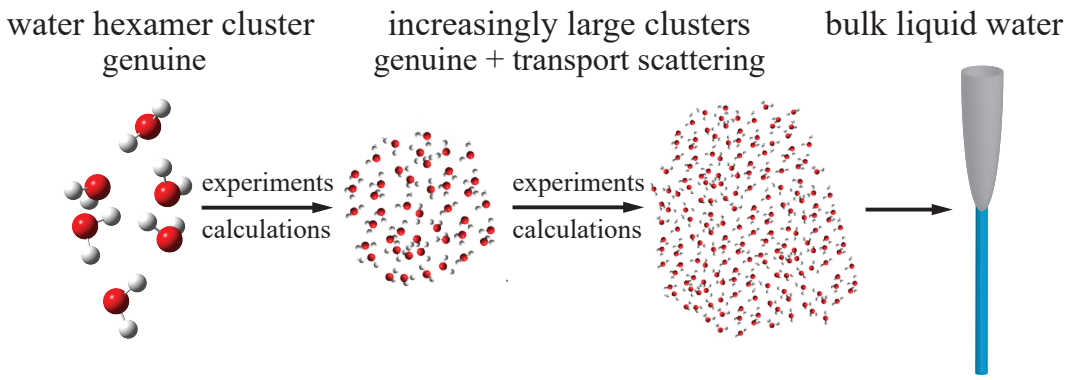

Figure 5.1: Schematic of using larger clusters to study the decrease of photoelectron anisotropy from the genuine value determined for the water hexamer to the liquid bulk value. This decrease is exclusively due to electron transport scattering.

how electron scattering in water clusters compares to electron scattering in the liquid bulk. This is schematically depicted in Figure 5.1. This combination of calculations and experiments can also provide information on the smallest cluster size at which first effects of electron transport scattering become apparent. This onset of electron transport scattering also gives the maximum system size up to which photoelectron spectra are not influenced by electron transport scattering.

5.2 Experimental and theoretical methods

5.2.1 Experiments and data analysis

Coincidence methods, which allow to record size-resolved photoelectron velocity map images, become increasingly difficult for larger clusters. The main problem is that the extraction of photoions and photoelectrons typically occurs perpendicular to the molecular beam direction. For heavier photoions the increased flight times lead to a greater displacement of the photoions on the ion detector in the molecular beam direction (Figure 3.8). This holds true if all neutral clusters in the molecular beam initially travel with the same velocity, and if the extraction field does not significantly influence the velocity in the molecular beam direction, (Figure 3.7). There exist technical methods to circumvent those problems and to build coincidence experiments working for larger clusters (larger ion detectors, higher extraction voltages, or pulsed extraction fields), however we are not aware

of the existence of such an experimental setup at a synchrotron user facility.

Generally, full size resolution is less important for large clusters because the anisotropy parameters and the electron binding energies are expected to change less strongly with cluster size than for the smallest clusters. Therefore a setup as discussed in section 3.1 was used to perform photoelectron velocity map imaging measurements on cluster ensembles. Experimental cluster size distributions were recorded with mass spectrometry and the Na-doping technique before and after each photoelectron VMI measurement. This allowed us to assign an average cluster size to each VMI measurement.

An EL-valve with a trumpet shaped nozzle was used as a cluster source. The gas mixture was prepared by flowing neon or helium with pressures between 1.6 and 13 bar over a liquid water reservoir. For neat water expansions the gas line was closed. Reservoir temperatures were chosen between 60°C and 170°C corresponding to water partial pressures between ∼0.2 and ∼7.8 bar. The tubing between the reservoir and the valve and the valve itself, were kept at a temperature that was 5°C and 10°C higher than the reservoir temperature, respectively. The EL-valve was operated at a repetition rate of 500 Hz. The laser (HHG laser) was operated at a repetition rate of 1000 Hz. Only the signal generated by every other laser shot, i.e. every laser shot coinciding with a cluster pulse being emitted from the cluster source, was detected by the MCP gate and the CMOS camera. Operation of the electron detection at a rate of 1000 Hz was not possible because of the too long fluorescence time of the phosphor screen.

5.2.1.1 Determination of average cluster sizes

Sodium-doped mass spectra were recorded after single photon ionization with 280 nm light from the OPA. Photoions were extracted with extraction voltages up to 25 kV and the typical voltage ratios specified in section 3.1.6. To retrieve relative abundances for the clusters of different sizes, the individual mass peaks were integrated and corrected for the doping and ionization efficiencies as explained in section 2.3.5. The average cluster size was then determined as a weighted average. The cluster sizes determined before and after the VMI measurements typically varied by less than 10%. It should be noted here that the high harmonic light source in general would have allowed to record mass spectra without using the sodium doping technique. Because of the comparatively low photon flux of the

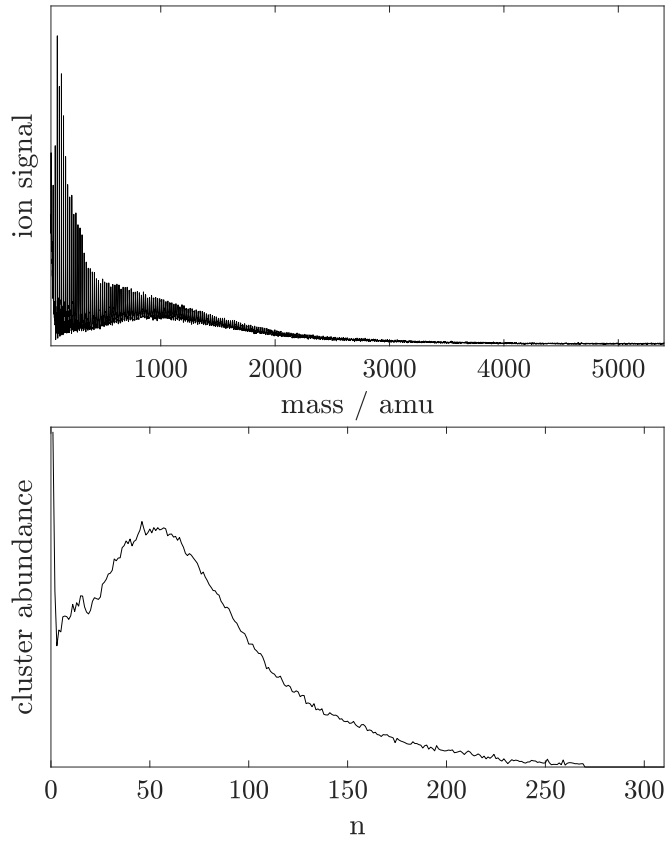

Figure 5.2: Top panel: Mass spectrum of sodium doped water clusters. Bottom panel: Cluster size distribution after peak integration and correction procedure described in section 2.3.5.

EUV radiation it is, however, more convenient to use the sodium doping method for cluster sizing.

5.2.1.2 VMI measurements

For the photoelectron VMI measurements, the cluster beam was photoionized using high harmonic radiation of 26.35 eV, 20.15 eV and 13.95 eV (17th, 13th and 9th harmonic of 1.55 eV) from the HHG source described in section 3.1.4. VMI images were reconstructed with the pBasex algorithm and the kinetic energy spectra were calibrated using the water gas phase $1b_1$ band. A series of test measurements showed that the resulting VMI images did not depend on whether the Na oven was on or off. To save time, most VMI measurements were then performed while the Na oven was on. Two different kinds of background subtractions were performed. First, a background recorded with physically blocked molecular beam

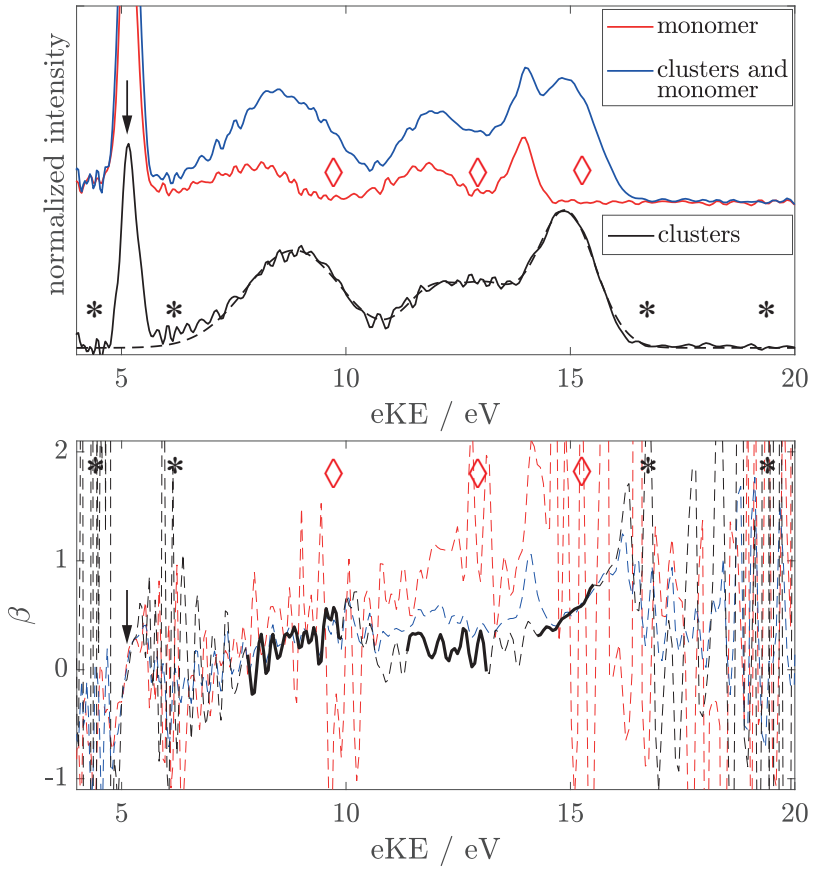

Figure 5.3: Top panel: Photoelectron spectra of the water monomer (red), of clusters ($\langle n \rangle = 144$) with a significant monomer contribution (blue) and of clusters after subtraction of the monomer contribution (black). The black dashed line in the top panel shows the least squares fit of 4 Gaussian bands to the spectrum (see text). Regions with low signal levels are indicated with asterisks and diamonds. Bottom panel: β traces corresponding to the spectra in the top panel. The full black line indicates over which energy range the β trace was averaged to obtain β values for the three valence bands. The additional peak above 5 eV eKE (labeled by the arrow) arises from photoionization of the neon (used as carrier gas) 2p orbital. The regions of high noise in the β traces (labeled by asterisks and diamonds) correspond to regions of very low photoelectron signal.

("laser-only") was subtracted. This mainly suppresses effects due to radiation that is scattered in the setup, including for example electrons created by photoionization of the extraction optics or chamber walls by scattered light. A second background subtraction was performed to subtract water monomer contributions, that partially overlap with the cluster spectra (see Figure 5.3). This step is necessary in order to extract photoelectron anisotropies and peak positions for only clusters, without gas phase contributions. Whenever possible, this background subtraction was performed for the raw photoelectron images before reconstruction. In some cases, after slight realignment of the laser beam or molecular beam, this subtraction of the raw data was not possible due to minor shifts of the image center. In those cases the subtraction was performed on reconstructed and calibrated photoelectron spectra and β traces. The subtraction of the spectra is straightforward. For the subtraction of the β traces, one needs to consider the respective signal levels at a given eKE:

$$\beta_{\mathrm{c}}(\mathrm{eKE}) = \frac{I_{\mathrm{c+m}}(\mathrm{eKE}) \cdot \beta_{\mathrm{c+m}}(\mathrm{eKE}) - a \cdot I_{\mathrm{m}}(\mathrm{eKE}) \cdot \beta_{\mathrm{m}}(\mathrm{eKE})}{I_{\mathrm{c+m}}(\mathrm{eKE}) - a \cdot I_{\mathrm{m}}(\mathrm{eKE})} \tag{5.1}$$

$I(\mathrm{eKE})_{(\mathrm{m})}$ and $I(\mathrm{eKE})_{(\mathrm{c+m})}$ denotes the photoelectron signal of the pure monomer and of clusters and monomer, respectively. For the data recorded at 20.15 eV, the subtraction was performed using a fitted monomer trace. This was necessary due to the low signal to noise ratios of typical water monomer electron images. Due to the upscaling of a low signal to noise image before subtraction, the noise is disproportionately increased in the final result. Note that the additional peak around 5 eV in the photoelectron spectra shown in Figure 5.3 (labeled by the arrow) arises from the photoionization of neon, which was used as carrier gas in this measurement.

After monomer subtraction, four Gaussian bands were fitted to the cluster spectrum (see Figure 5.3). Two Gaussians for the $1b_1$ and $1b_2$ bands, and two Gaussians of equal width and intensity for the broad $3a_1$ band. The binding energies of the individual bands were extracted as the fitted band positions. For the $3a_1$ band, the mean of the two positions of the double peak was used. The fitted peak widths were not further interpreted, but were used to determine the energy range (fitted FWHM) over which the β traces were averaged to extract average β-values for the $1b_1$ and $1b_2$ bands. For the $3a_1$ band, the β trace was

not averaged over the full FWHM. Instead, the averaged energy range was cut at the peak position of the energetically higher-lying Gaussian peak. This was done to avoid averaging in the energy range, where the $3a_1$ band overlaps with $1b_1$ band (see solid black lines in the bottom panel of Figure 5.3). Note that the regions marked with the black asterisks and red diamonds show strong noise in the β traces only due to almost zero signals in the corresponding photoelectron spectra. For some spectra with low signal levels, monomer subtraction could not be performed reliably. In these cases, only a β parameter for the cluster $1b_1$ band was extracted since this cluster band does not overlap with the monomer band. Binding energies were not extracted for those spectra.

5.2.2 Simulations

Scattering calculations were performed using cluster geometries as described in section 2.2.3.2. The simulated VMI images were evaluated in the same manner as the experimental images, i.e. the calculated raw images were reconstructed using the pBasex algorithm. The resulting speed distributions were fitted with the same model as the experimental spectra and β parameters were averaged over the same energy range, as for the experimental data. For comparison with the cluster data, we also performed simulations for liquid microjets. As mentioned in section 2.2.3.2, β parameters determined for liquid jets depend on the light coupling efficiencies for the two different polarization directions used. Since this effect does not occur in cluster measurements, we have corrected the liquid jet calculations accordingly. As for the clusters, the simulated liquid jet photoelectron spectra were fitted with four Gaussian bands to determine the energy range for averaging the β parameters.

Four different sets of scattering parameters (models ((i)-(iv))) were used for the simulation of transport scattering in clusters. They describe transport scattering using liquid bulk electron scattering cross sections (model (i)), gas phase electron scattering cross sections (model (ii)) and two different sets of intermediate scattering cross sections (models (iii) and (iv)). The parameter sets for the four models differ in the total scattering cross sections for different processes, but assume the same density of scatterers. The angular dependence and energy loss characteristics of all individual scattering processes were identical to the condensed phase model.

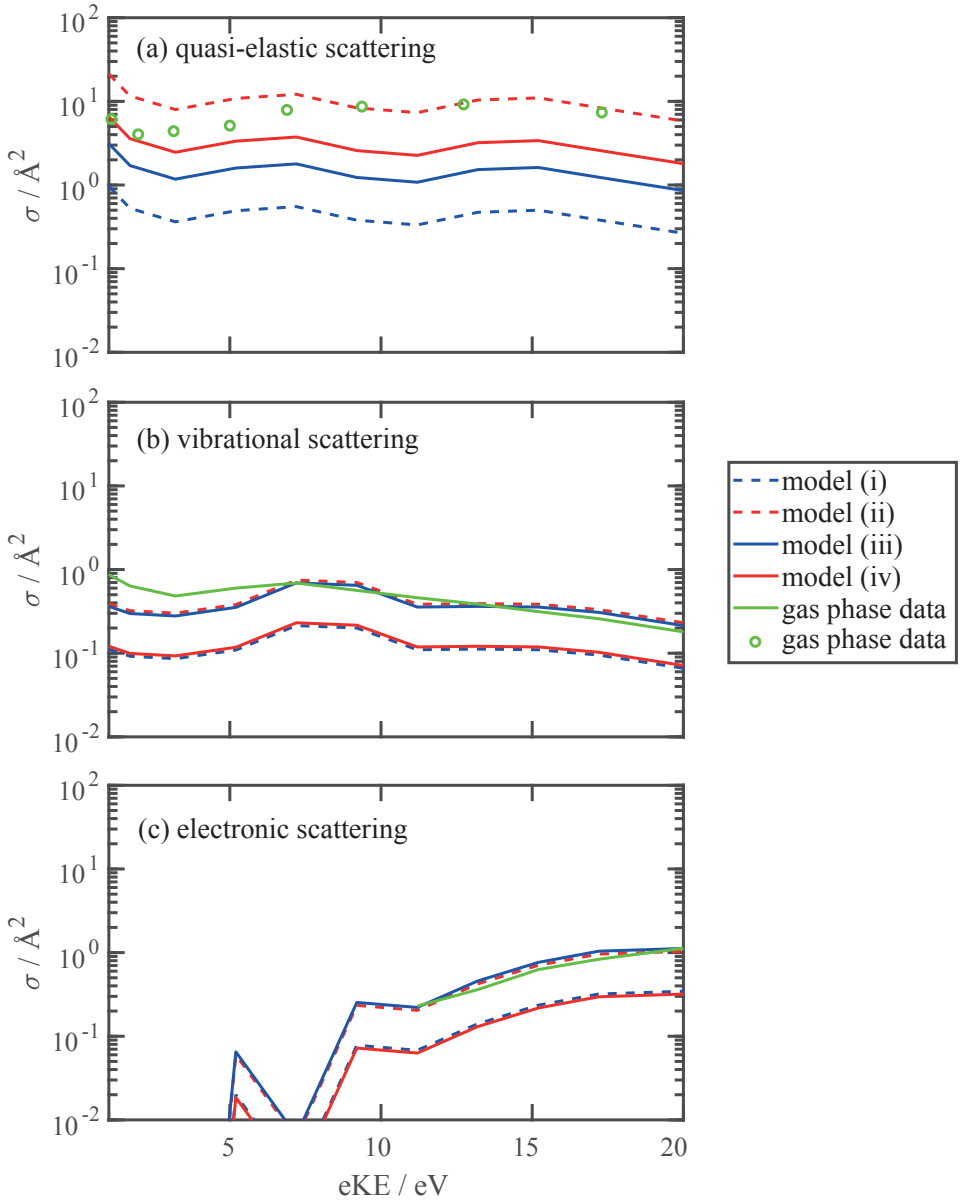

Figure 5.4: Total electron scattering cross sections for the parameters sets (i)-(iv). The gas phase data is taken (green circles) or derived (green lines) from Itikawa and Mason[74] (see text). Reproduced from reference [133] with permission from the PCCP owner societies.

Model (i) liquid bulk scattering parameters: The first set of scattering parameters represent the situation in the condensed phase. They are discussed in detail in section 2.2.3.1. The dashed blue lines in Figure 5.4 show the corresponding absolute scattering cross sections for the quasi-elastic scattering, the vibrational scattering and the electronic scattering as a function of the electron kinetic energy.

Model (ii) gas phase scattering parameters: The second model describes electron scattering with cross sections for gas phase water. The scattering cross sections for isolated water molecules are significantly higher than for the liquid. Gas phase electron scattering cross sections have been reviewed and summarized by Itikawa and Mason[74] for a wide energy range and many different scattering processes. However, no uniform parametrization exists for all processes. To be able to use these scattering parameters in our calculations, we have thus used the scattering parameters of model (i) and scaled the total cross sections, so that they agree with the corresponding total gas phase values, for quasi-elastic, vibrational and electronic scattering. The three scaling factors were chosen such that the scaled total scattering cross sections agree with the values reported by Itikawa and Mason, for kinetic energies of ∼10 eV. The dashed red lines in Figure 5.4 show the corresponding total cross sections.

Quasi-elastic scattering in the gas phase is described by isotropic momentum transfer cross sections determined by Yousfi et al.[74,134] Classical momentum transfer corresponds to the excitation of a translational motion. In the condensed phase, this can be compared to the excitation of a phonon-like intermolecular vibration. The momentum transfer cross sections for gas phase molecules also contain contributions from unresolved rotational excitations. The closest condensed phase analog to a rotational excitation of a water molecule is the excitation of a librational motion in the condensed phase. As mentioned in section 2.2.3.1, we refer to those intermolecular vibrational and librational movements as phonon modes. To compare the liquid bulk quasi-elastic cross sections to the gas phase momentum transfer cross sections, the sum of the isotropic components of all phonon related scattering and the elastic scattering for the liquid was calculated:

$$\sigma_{\text{total}}^{\text{quasi-elastic}}(\text{eKE}) = \sum_i (1 - \gamma_i) \cdot \sigma_i(\text{eKE}), \tag{5.2}$$

where the sum runs over all four considered phonon modes and the elastic scattering cross section. The total quasi-elastic scattering cross section of the liquid $\sigma_{\text{total}}^{\text{quasi-elastic}}(\text{eKE})$ (shown in Figure 5.4(a) as a blue dashed line) is then scaled with a factor of 20 to agree with the momentum transfer cross sections from Itikawa and Mason.[74] In Figure 5.4 (a) the data by Itikawa and Mason is shown as green circles, while the scaled cross sections are shown as a red dashed line. This scaling factor of 20 for the quasi-elastic scattering is applied to the total scattering cross sections of all elastic and phonon scattering processes, leaving the angular dependence unchanged.

For vibrational scattering in the gas phase, Itikawa and Mason report two cross sections: one for scattering on the excitation of the bending mode and another one for scattering on the stretching modes. These two cross sections are summed to obtain a total vibrational scattering cross section. For this purpose, the data had first to be interpolated onto a common kinetic energy axis. The interpolated, summed vibrational scattering cross section is shown in Figure 5.4 (b) as green line. The liquid bulk data include five different vibrational scattering processes, some of which are combination excitations. The five different scattering cross sections are summed to obtain the total vibrational scattering cross section (dashed blue line in Figure 5.4 (b)). A scaling factor of 3.5 was determined to obtain agreement between the scaled total vibrational scattering cross section of the liquid and the gas phase data. This scaled total vibrational cross section used for model (ii) is shown by the red dashed line in Figure 5.4 (b).

For the scattering on electronic excitations, the single total scattering cross section for the liquid phase (dashed blue line in Figure 5.4 (c)) is compared to the sum of the two dominating electronic processes in the gas phase (green line in Figure 5.4). Those two processes are electron (impact) ionization, and excitation channels leading to the dissociation of a H radical. As can be seen from Figure 5.4 (c), those processes have a significant contribution only above 10 eV kinetic energy. From the comparison between the liquid and gas phase data, we determine a scaling factor of 3. The resulting total cross section of model (ii) for electronic excitation is shown as dashed red line in Figure 5.4 (c).

Model (iii) intermediate scattering parameters for clusters: One significant difference between an isolated molecule and the condensed phase is the

dielectric properties of the environment. The interaction of an electron with the scattering potential scales with the dielectric constant ($1/\epsilon$) of the medium. The scattering cross sections thus scale as $1/\epsilon^2$. Clusters, even with a few hundred molecules, are not well described by the bulk dielectric constant. The limited system size is expected to reduce the dielectric constant, thus increasing the electron scattering cross sections compared to the liquid bulk. Model (iii) simulates the effect of a reduced dielectric constant on the electron scattering by considering the limiting case of no dielectric screening at all. For this purpose, the total scattering cross sections of model (i) are scaled by the square of the dielectric constant at optical frequencies ${\epsilon_{\text{optical}}}^2 \approx 1.8^2 = 3.24$. The resulting cross sections are depicted in Figure 5.4 (a-c) as blue solid lines. A comparison of the scattering cross sections of model (iii) with the models (i) and (ii) shows that for the vibrational and electronic cross sections model (iii) agrees well with the gas phase scattering cross sections of model (ii). The quasi-elastic scattering cross sections of model (iii), however, are much closer to those of the liquid bulk (model (i)). This indicates that for vibrational and electronic scattering processes the dielectric screening might be the dominating difference between the liquid bulk and gas phase water, while for quasi-elastic scattering processes additional factors may need to be considered.

Model (iv) intermediate scattering parameters for clusters: One further effect of the limited system size in clusters concerns the quasi-elastic scattering. In the gas phase, excitations of translational and rotational motions contribute significantly to the quasi-elastic scattering of electrons. In the condensed phase, these excitations corresponds to the excitation of phonons. In clusters of a few hundred molecules, these phonon modes may strongly differ from the liquid bulk in number and frequency. Thus it is well possible that the quasi-elastic scattering cross sections for clusters differ from those of the liquid bulk. Model (iv) considers this possibility as a limiting case by taking electron scattering cross sections for the gas phase, and adding the effect of dielectric screening. For this purpose the total cross sections of model (ii) are scaled by the factor $1/\epsilon^2_{\text{optical}} \approx 1/3.24$. The resulting cross sections are displayed in Figure 5.4 (a-c) as red solid lines. Within this model, the vibrational and electronic scattering cross sections agree well with the original liquid water electron scattering cross sections, while the quasi-elastic scattering cross sections are closer to those of the gas phase.

5.3 Results and discussion

5.3.1 Size-dependent electron binding energies

The differences between monomer and cluster binding energies

$$\Delta\text{eBE} = \text{eBE}_{\text{monomer}} - \text{eBE}_{\text{cluster}} \tag{5.3}$$

are shown in Figure 5.5 as a function of $\langle n \rangle^{-(1/3)}$, which is proportional to the inverse cluster radius $1/r$. Therefore, pure polarization screening for the electron binding energy would lead to a straight line between the infinite bulk ($\langle n \rangle^{-(1/3)} = 0$) and the isolated molecule ($\langle n \rangle^{-(1/3)} = 1$). The extracted electron binding energy values are also summarized in Table A.3 in the appendix. The eBE data of the large clusters (black dots in Figure 5.5) continues the trend already observed in section 4.3.2 for the small clusters (green diamonds in Figure 5.5). The eBE data for the $3a_1$ and the $1b_2$ bands extracted from the fitted photoelectron spectra show a less clear trend than the $1b_1$ data. These two bands are more affected by the monomer signal subtraction procedure than is the $1b_1$ band. The extracted values for them are thus more sensitive to incomplete or over subtraction of the monomer spectrum. Overall our data agrees reasonably well with previous cluster eBE data (red crosses) reported by others.[30,120–122,124] For the $1b_1$ and the $3a_1$ most of the previously reported electron binding energy shifts seem to lie slightly higher than those determined in this work. This deviation may be due to the inaccuracy in the estimation of the average cluster size using scaling laws in all of the previous works. Furthermore, cluster size distributions may not always be well described by an average cluster size. The shape and width of a distribution may also have an influence on the measured electron binding energy. For all three orbitals the obtained eBE shifts seem to deviate from the straight line connecting the isolated molecule and the infinite bulk. This indicates a deviation from the behavior expected from a pure polarization screening model. Possible contributions to the evolution of the binding energies with increasing cluster size include changes to the initial state energy, final state polarization screening as well as electron kinetic energy loss due to inelastic electron scattering.

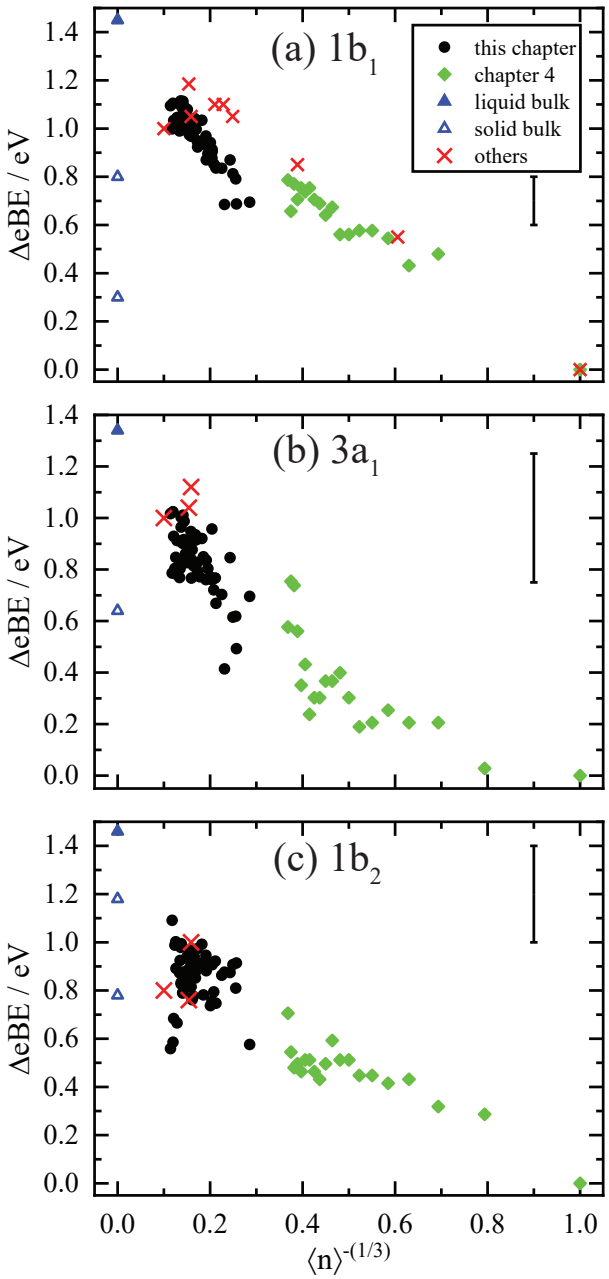

Figure 5.5: Electron binding energy shifts $\Delta eBE = eBE_{\text{monomer}} - eBE_{\text{cluster}}$ as a function of the cluster size. Typical uncertainties are given by the error bars on the right side of each panel. Black circles: data from this Chapter, green diamonds: data from Chapter 4, red crosses: data from references [30, 120–122, 124]. Open and filled blue triangles: Solid and liquid bulk data from reference [5]. Reproduced from reference [133] with permission from the PCCP owner societies.

5.3.2 Size-dependent anisotropy parameters

Figure 5.6 shows β parameters for the three valence orbitals measured at photon energies of 26.35 eV (panels (a)-(c)), and 20.15 eV (panels (d)-(f)). Anisotropy parameters for the $1b_1$ orbital measured at 13.95 eV are shown in Figure 5.7. For 13.95 eV photon energy the lower lying orbitals are not accessible anymore. The blue dashed lines in Figures 5.6 and 5.7 are simulations using liquid bulk scattering parameters (model (i)). The anisotropy parameters are also summarized in Table A.4 in the appendix. For almost all measurements, the photoelectron anisotropies show a pronounced decrease with increasing cluster size. Only for the $1b_2$ band measured at 20.15 eV (Figure 5.6 (f)) and the $1b_1$ band measured at 13.95 eV photon energy (Figure 5.7) the decrease in anisotropy is hardly observable. This is because even for the smallest clusters photoemission is nearly isotropic, as observed for the hexamer data in Chapter 4. For comparison, the corresponding hexamer values are shown in Figure 5.6 and Figure 5.7 as black squares. The low anisotropies measured already for very small clusters at those photon energies, are a consequence of the low electron kinetic energies, below 3 eV for the $1b_1$ band at 13.95 eV photon energy and below 2 eV for the $1b_2$ band at 20.15 eV. For the $1b_2$ band measured at 20.15 eV photon energy the small decrease in anisotropy is represented by an increase in the β parameter since its value for the smallest water clusters is negative at low kinetic energies.

In general, the absolute decrease of the β parameter is smaller if the genuine anisotropy is smaller. Similar to the eBE shifts discussed above, the data for the $1b_1$ bands shows the clearest trends. This is partly because the data is less prone to imperfect monomer subtraction. A further factor is that the trends are clearer for higher anisotropy parameters.

For the $1b_1$ band, the β parameters determined for the smallest clusters with $\langle n \rangle \approx 50$ agree well with the water hexamer values. This indicates that there is no significant effect of transport scattering for clusters smaller than $\langle n \rangle \approx 50$ molecules. A comparison with the PADs reported by Zhang et al.[30] is not useful here since their measurements were performed at significantly higher photon energies. However it is noted that they reported a decrease in the anisotropy parameter from a cluster distribution with an estimated average cluster size of $\langle n \rangle \approx 50$ to a distribution with an estimated average size of $\langle n \rangle \approx 80$. They attributed part of this decrease to arise from elastic electron scattering in the clusters.

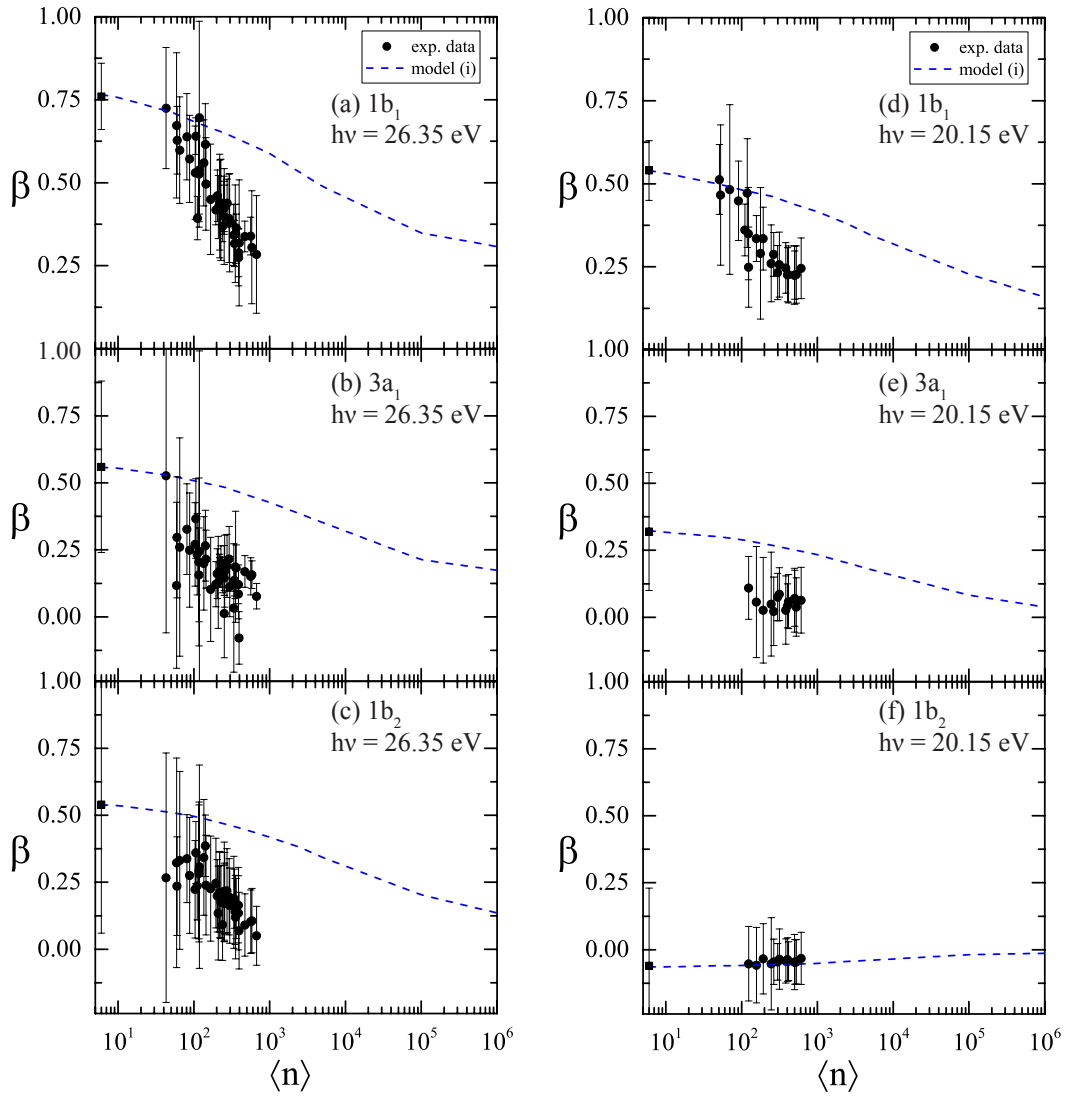

Figure 5.6: Experimental anisotropy parameters determined at photon energies of 26.35 eV (a)-(c) and 20.15 eV (d)-(f) for the three valence orbitals as a function of the average cluster size. The blue dashed lines show the results of the scattering calculations for clusters, using the liquid bulk scattering parameters (model (i)).

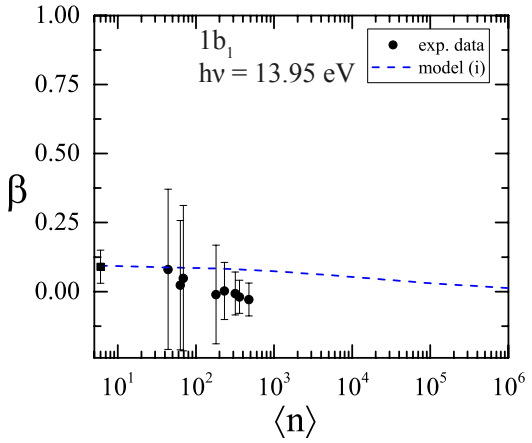

Figure 5.7: Experimental anisotropy parameters determined at a photon energy of 13.95 eV for the $1b_1$ orbital as a function of the average cluster size. The blue dashed line shows the result of scattering calculations for clusters, using the liquid bulk scattering parameters (model (i)).

The comparison of the experimental cluster data with the simulations for electron scattering as in the liquid bulk (model(i), blue dashed lines in Figures 5.6 and 5.7) show significant disagreement. The decrease observed in the experiments is much steeper than the decrease predicted by the simulations. While the experiments basically reach bulk-like β parameters for clusters containing a few hundred molecules, the simulations predict bulk-like values for droplets containing $\sim 10^6$ water molecules. This disagreement between simulations and experiments is less pronounced for the measurements showing quasi-isotropic emission already for small clusters. The observed discrepancy indicates that the calculations using liquid bulk scattering parameters (model (i)) are not suitable to describe electron transport scattering in water clusters with less than 1000 molecules. Considering the absolute differences between the simulation and the experimental data, one finds that the disagreement is strongest for the largest measured clusters. Naively, one may have assumed the liquid bulk description to fit best for the largest clusters. Obviously, larger electron scattering cross sections are needed to explain the pronounced decrease of the experimental β parameters over the studied cluster size range.

As the following arguments show, we can exclude other experimental factors as the origin of the reduced photoelectron anisotropies. Extracted β parameters for the water monomer, as well as for carrier gas photoelectron bands can be used

as a benchmark for the experimental setup and data evaluation. Table 5.1 gives a comparison of such anisotropy parameters extracted from our measurements with values from Chapter 4, and from literature.[135,136] The fact that the values agree well excludes a general problem with the experimental setup and the data evaluation.

Too high charge densities in the ionization region after photoionization are known to decrease the measured anisotropy parameters. Larger clusters were in general created using higher gas pressures and higher water partial pressures. This results in higher gas and cluster densities in the ionization region, and thus, for constant photon flux, in an increased charge density for larger clusters. This increase in charge density with increasing cluster size could in principle lead to a too strong decrease of the photoelectron anisotropy with cluster size. However, such space charge effects could be excluded here by studying the laser fluence dependence of the photoelectron images. It was found that a significant decrease of the photon flux, (i.e. a reduced charge density in the ionization region) did not affect the obtained anisotropies in any way. With the low achievable photon fluxes of the high harmonic light source, we never observed a reduction of experimental anisotropies that could be attributed to space charge effects.

A second type of space charge effects may arise from charges created in the molecular beam prior to photoionization. Under some molecular beam conditions, there was a background observed in the mass spectrum that was assigned to charges created by the impact of clusters on metal surfaces (e.g. the extraction optics). The high molecular beam velocities of expansions with helium and neon carrier gas results in high kinetic energies of the clusters, that are sufficient to ionize stainless steel surfaces. The work function of stainless steel is ∼4.4 eV. Assuming cluster velocities of 500 and 1000 m/s for expansions seeded in neon and helium, respectively, cluster sizes of n≈200 and n≈50 molecules would suffice to ionize the

	$h\nu$	$1b_1$	$3a_1$	$1b_2$	Ne 2p	He 1s
this chapter	26.35 eV	1.27(16)	0.87(12)	0.25(13)	0.14(8)	1.89(16)
Chapter 4	27 eV	1.26(16)	0.84(10)	0.45(14)		
literature[135]	26.86 eV				0.12±0.05	1.96±0.14

Table 5.1: Comparison of water monomer and carrier gas (neon and helium) β values determined from typical images on the used setup, with data recorded as described in Chapter 4 and values reported by Dehmer et al.[135]

repeller plate. To ascertain that such space charges do not influence the anisotropy measurements, an additional data set was recorded avoiding such background signals by employing a larger repeller hole and larger sodium oven entrance and exit holes. The β parameters recorded with this modified setup agreed perfectly with the original setup. Therefore, it was concluded that the strong decrease of the anisotropy parameters is not due to any space charge effects.

Another possible problem may be the determination of the cluster size distribution and the determination of the average cluster sizes. As discussed in section 2.3.3, the ionization probability of a cluster scales with its volume, and therefore with the number of molecules it contains. As a consequence of this size dependence, even a very small number of very large clusters could in principle significantly influence the photoelectron spectrum and the obtained anisotropy parameters. The problem here is that such very large clusters would be too heavy to be efficiently detected by the MCP detector. In fact, xenon expansions containing such very large particles were reported in a study using single pulse x-ray diffraction at a free electron laser.[137] Although such large clusters have not been detected in expansions of water seeded in rare gases, the possible presence of such large clusters cannot be excluded without further considerations. The possible size and abundance of such very large water particles contributing to the photoelectron signal is limited to a narrow range, which is determined by the following arguments: Too small particles on the one hand would not produce low enough β parameters to explain the experimental findings (see dashed blue lines in Figure 5.6). On the other hand, too large particles would produce shadowing effects in the photoelectron images.

Shadowing effects[15] occur in photoelectron images of very large clusters and aerosols due to a combination of significant light attenuation within the particle and electron scattering. The light attenuation within the particle is caused by absorption and depends on the complex index of refraction of the medium and the particle size. For water clusters with up to a few thousand molecules, we find that the light intensity distribution within the clusters is homogeneous at all photon energies considered here. For much larger particles, the light intensity is attenuated as it propagates through the particle, which leads to an inhomogeneous light intensity distribution as exemplified in Figure 5.8 (a). As a consequence of the inhomogeneous light distribution, the spatial photoionization probability

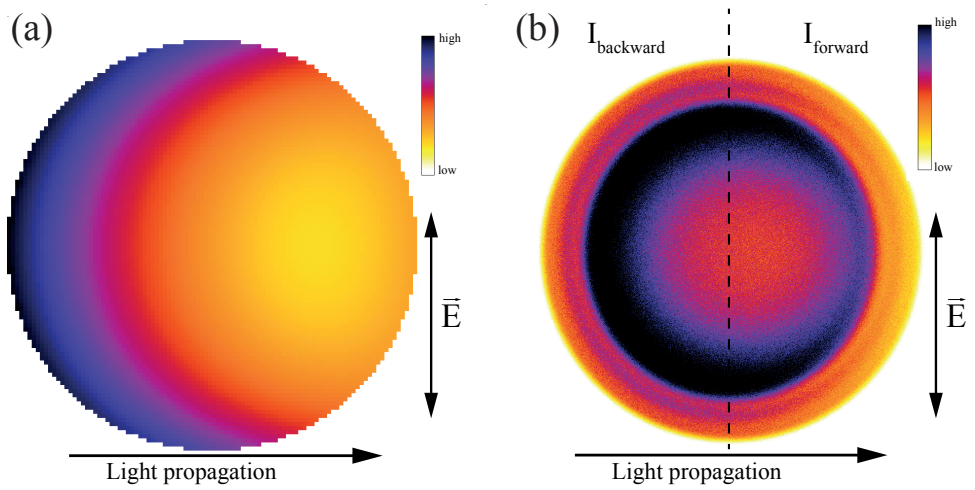

Figure 5.8: Example of shadowing for 26.35 eV photon energy and a particle of 10^6 water molecules. (a) shows the light intensity in the equatorial plane of a large water particle. (b) shows the simulated VMI image (model (i)) corresponding to such a particle. The forward/backward asymmetry is created as a combination of the distribution of the light intensity and electron scattering. Adapted from reference [133] with permission from the PCCP owner societies.

distribution in the particle also becomes inhomogeneous. This means that more electrons are created in regions of higher light intensity than in regions of lower light intensity. Scattering of the electrons after photoionization makes it more likely that an electron escapes from the water droplet into the vacuum at a location close to its origin, rather than traveling all the way to the far side of the droplet before escaping. Therefore, some of the light intensity's inhomogeneity is retained in the photoelectron image, due to the electron scattering. An example of a shadowed, simulated photoelectron image of large water particles, containing 10^6 molecules, photoionized with 26.35 eV photons is shown in Figure 5.8 (b). Shadowing effects in an photoelectron image can be characterized by the ratio α of the electron intensities in the forward and the backward half of the photoelectron image $\alpha = I_{\text{backward}}/I_{\text{forward}}$. The experimental photoelectron images recorded in this work do not show shadowing, i.e. $\alpha \approx 1.0$. To narrow down the size range and abundance in which such large clusters would have to be present in our experiments to explain the strong decrease of the β parameters without showing shadowing, additional scattering calculations were performed. Simulated images Im were calculated as superpositions of two photoelectron images $\text{Im}(\langle n \rangle)$ and $\text{Im}(n_{\text{large}})$. $\text{Im}(\langle n \rangle)$ is a simulated image, that corresponds to a cluster size distribution with an average

cluster size $\langle n \rangle = 500$. $\mathrm{Im}(n_{\mathrm{large}})$ is a simulated electron image for very large particles containing n_{large} molecules. Note that the latter would have very low detection probabilities in our mass spectrometry measurements and thus most likely remain undetected. The superposition is calculated as

$$\mathrm{Im} = p_{\langle n \rangle} \cdot \langle n \rangle \cdot \mathrm{Im}(\langle n \rangle) + p_{\mathrm{large}} \cdot n_{\mathrm{large}} \cdot \mathrm{Im}(n_{\mathrm{large}}), \tag{5.4}$$

where $p_{\langle n \rangle}$ and p_{large} are the normalized abundances of clusters and large particles ($p_{\langle n \rangle} + p_{\mathrm{large}} = 1$). The superposition is additionally weighted by the factors $\langle n \rangle$ and n_{large}, to account for the strongly increased ionization probability of the larger particles. The size of the large water particles was varied between n_{large}=50'000 and n_{large}=10^6 molecules. The resulting images Im were reconstructed and evaluated in the same manner as the experimental images and β parameters and the shadowing ratios α were determined. To judge whether a given combination of large particle size and large particle abundance could explain the low experimental anisotropy parameters, the β parameters and the α ratios of the simulated images are compared to a typical experimental image with ${\beta_{\mathrm{exp}}}^{\langle n \rangle = 500} = 0.34 \pm 0.06$ and $\alpha \approx 1.0$.

Typical results for combinations of large particle sizes and abundances are summarized in Table 5.2. On the one hand, it can be seen that for too small values of n_{large} or too low abundances p_{large} the resulting β parameter is too high ($\beta > 0.4$) to explain the low anisotropy of the experimental image. On the other hand a too large particle size n_{large} or too high abundances p_{large} lead to significant shadowing effect with $\alpha > 1.1$. Nevertheless, there is a combination of n_{large} between 50'000 and 100'000 molecules in an abundance of $p_{\mathrm{large}} > 5\%$ that would explain the low anisotropy parameters, without showing significant shadowing effects. Experimentally, the β parameters show a rather smooth decrease with the measured average cluster size. For this trend to be explained by a small abundance of very large particles, their abundance would need to scale nicely with the measured average cluster size. It seems more likely, that the abundance of such large particles would depend on the expansion conditions used (different temperatures, carrier gases, water partial pressures), rather than showing a smooth trend with the measured cluster size. Since this dependence on expansion conditions is, however, not observed, it can be concluded that effects due to low abundances of very large water particles are rather unlikely.

$\langle n \rangle$	$p_{\langle n \rangle}/\%$	n_{large}	$p_{\text{large}}/\%$	β_{calc}	α_{calc}
500	90.0	50'000	10.0	0.40	1.010
500	95.0	50'000	5.0	0.42	1.009
500	99.0	50'000	1.0	0.51	1.006
500	90.0	100'000	10.0	0.36	1.028
500	95.0	100'000	5.0	0.38	1.026
500	99.0	100'000	1.0	0.45	1.019
500	95.0	250'000	5.0	0.32	1.16
500	99.0	250'000	1.0	0.37	1.14
500	99.5	250'000	0.5	0.42	1.12
500	99.9	250'000	0.1	0.54	1.05
500	99.0	500'000	1.0	0.34	1.15
500	99.5	500'000	0.5	0.37	1.14
500	99.9	500'000	0.1	0.49	1.08

Table 5.2: Example calculations for anisotropy parameters β and shadowing ratios α of size distribution containing small abundances of very large clusters.

It seems much more likely, that the electron scattering in water clusters cannot be described by the same scattering parameters as in the liquid bulk. This will be discussed in the following, using scattering calculations for the models (i)-(iv), with a focus on the $1b_1$ data.

Figure 5.9 shows the anisotropy parameters measured for the $1b_1$ band at different photon energies together with the simulations for the different scattering models. The calculations using the liquid bulk scattering cross sections (model(i)) are shown as dashed blue lines, while the red dashed lines show the results for model (ii), i.e. scattering parameters corresponding to isolated, gas phase molecules. The two models show significantly different behavior. As discussed before, model (i) results in only a weak absolute decrease in β for clusters with less than 1000 molecules. The liquid bulk anisotropy (blue triangle) is reached at much larger cluster sizes. On the contrary, for model (ii) the much higher scattering cross sections lead to a strong decrease of β for already very small clusters with less than 100 molecules. After this initial decrease the anisotropies stay almost constant. The scattering cross sections are in fact so high that the simulated water hexamer value could not be fixed to the experimental value from Chapter 4, without using input values exceeding the physical limit of $\beta = 2.0$. Except for the measurement at 13.95 eV photon energy with $\beta \approx 0$ for all cluster sizes, neither model agrees with the experimental data.

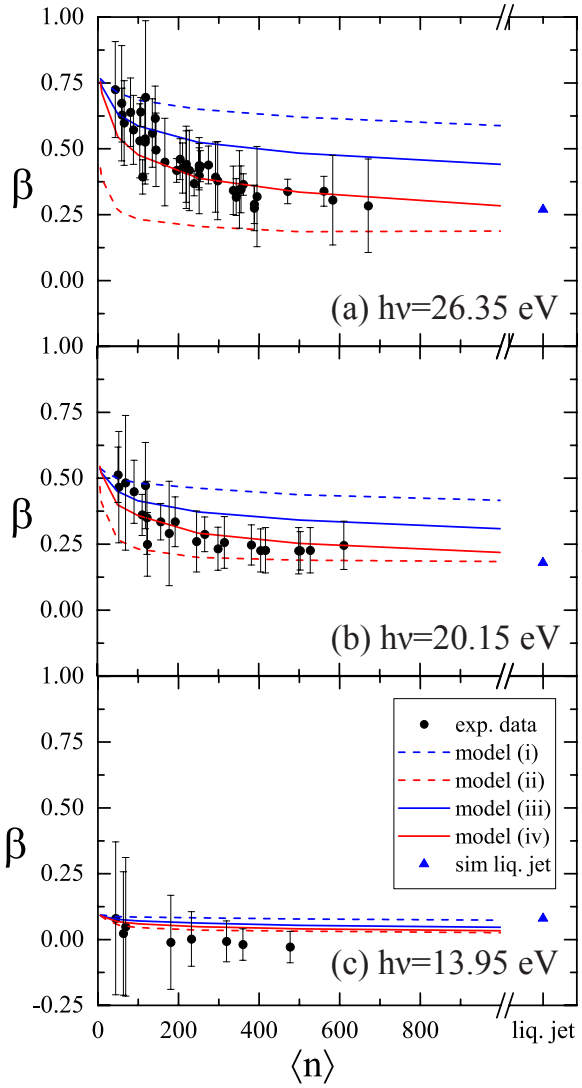

Figure 5.9: β parameters of the $1b_1$ band for ionization with different photon energies. The black circles show experimental data. The dashed lines show simulations using liquid bulk and gas phase scattering parameters (models (i) and (ii)), while the solid lines show simulation results for the intermediate scattering cross sections (model (iii) and (iv)). The blue triangles indicates simulations for a liquid jet using model (i), which are corrected for light coupling effects. Reproduced from reference [133] with permission from the PCCP owner societies.

The results for scattering cross sections in between the gas phase values and the liquid bulk values (models (iii) and (iv) are shown as solid red and blue lines. The agreement of these calculations with the experimental data is much better. It seems plausible that clusters behave as an intermediate case between the liquid bulk and the gas phase. Model (iv), i.e. water gas phase scattering cross sections scaled to account for dielectric screening, seems to agree best with the experimental data. This might indicate that there is a rather strong effect due to non-bulk behavior of phonon-like low frequency intermolecular vibrations. However, the treatment of dielectric screening for model (iii) and (iv) is rather crude and differences between model (iii) and (iv) should not be over interpreted. Furthermore, both models represent limiting cases that are not expected to perfectly reproduce the experimental data, but rather give a qualitative understanding of the situation. The most likely explanation includes aspects from both models. The dielectric properties and the phonon modes of water clusters do not correspond to those of the liquid or gaseous water, and may show a dependence on the cluster size. Also a dependence on the position within the cluster cannot be excluded.

In all models (i-iv), the electron mean free path is constant throughout a given water cluster, i.e. not dependent on the position in the cluster. Furthermore, all models (i)-(iv), assume electron scattering cross sections to be independent of the cluster size. A more detailed picture may require cluster size dependent electron scattering cross sections to account for cluster size dependent dielectric properties and intermolecular vibrational modes. At an unknown, probably very large cluster size, the scattering parameters are assumed to converge to the bulk scattering parameters. However, in the present study we could not identify the cluster size for which convergence to bulk scattering behavior is reached. The only interpretation that can be made from models (iii) and (iv) at this point is that a set of scattering cross sections in between the bulk liquid and the gas phase scattering cross sections can explain the experimentally observed decrease in the anisotropy parameters, while neither the gas phase nor the condensed phase cross sections reproduce the experimental data.

Another effect that might contribute to the decrease of the photoelectron anisotropies is crystallization. Previous studies[138,139] have reported that clusters can become partly crystalline at cluster sizes between 200 and 400 molecules, depending on the cluster temperature. Which effect such a partial crystallization

would have on the electron scattering processes is unknown. To the best of our knowledge, there are no scattering cross sections reported for crystalline water ice. Furthermore, it is unclear how the long-range order of a partly crystalline cluster would affect the genuine anisotropy value. The occurrence of crystallization in clusters is reported[138] to depend strongly on the cluster temperature. Although the cluster temperature in our experiment is not well known there was a wide variety of different expansion conditions used in our experiments, thus presumably also resulting in a rather wide variety of cluster temperatures. Therefore, it seems unlikely that crystallization effects would produce the smooth decrease of β with cluster size that is observed experimentally, without showing differences between different expansion conditions.

For the sake of completeness, Figure 5.10 shows the comparison of the experimentally measured β parameters with the calculations for the four different models. For these bands, the better agreement of models (iii) and (iv) as compared to models (i) and (ii) is less clear. This is partly due to the large uncertainties of the data. The calculated anisotropies for models (iii) and (iv) in parts (a) and (c) of the figure, seem to be slightly higher than the experimental values. The same holds true for the $3a_1$ band data in at 20.15 eV in part (b) of the figure. This slight deviation may be explained by the significant uncertainties in the experimentally determined water hexamer β parameters for those two bands (see error bars in Figure 5.6). Note that these uncertainties do not directly affect the calculations using the scattering parameters of model (ii) because for this parameter set the calculations could not be fixed at the experimental water hexamer value. The data measured at 20.15 eV photon energy shows also no significant decrease because the emission is already isotropic for the smallest clusters.

5.4 Conclusion

The anisotropy parameter β of neutral water clusters has been shown to be a sensitive measure of electron scattering in the low kinetic energy range (<20 eV), where electron scattering is dominated by elastic, phonon and vibrational scattering. With increasing cluster size, an unexpectedly sharp trend towards more isotropic photoemission was found. Already for clusters with less than 1000 water molecules, the anisotropy reaches values expected for the liquid bulk. This

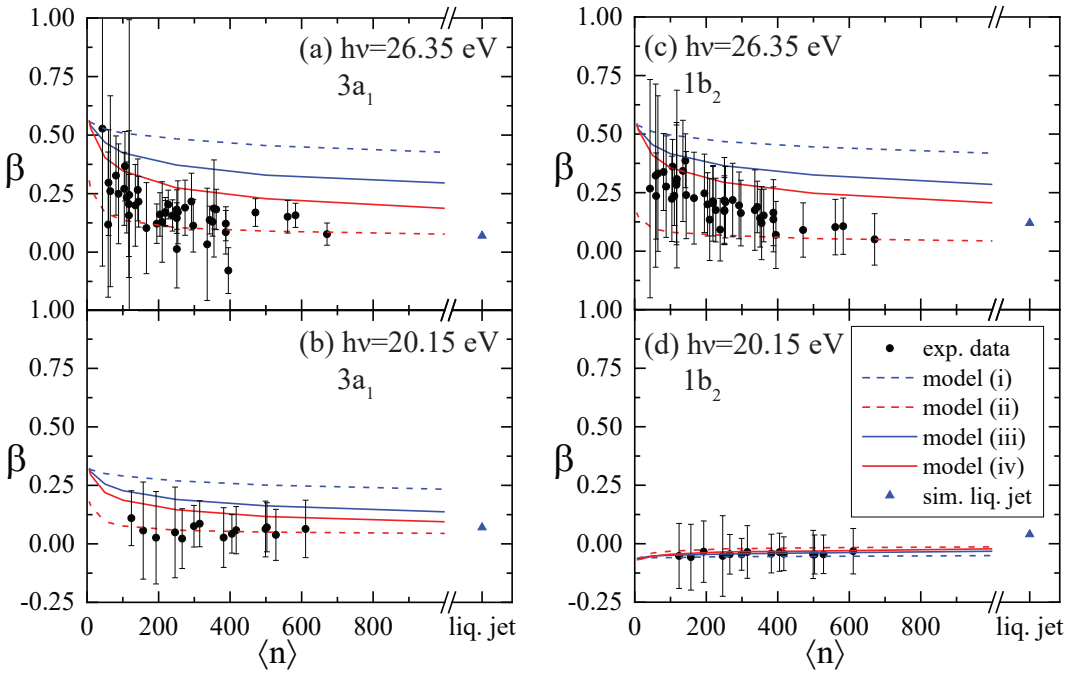

Figure 5.10: β parameters of the $3a_1$ and $1b_2$ bands for ionization at different photon energies. The dashed lines show simulations using liquid bulk and gas phase scattering parameters (models (i) and (ii)), while the solid lines show simulation results for the intermediate scattering cross sections of model (iii) and (iv). The blue triangles indicates simulation for the liquid jet, using model (i), which are corrected for the polarization dependence of the light coupling. Adapted from reference [133] with permission from the PCCP owner societies.

behavior was explained by cluster specific electron scattering because neither gas phase nor liquid bulk scattering cross sections can reproduce the evolution of β with the cluster size. The cluster data can be qualitatively explained by intermediate scattering cross sections with values that lie in between the gas phase and the liquid bulk scattering parameters. Other explanations including undetectable very large water clusters or crystallization effects, seem rather unlikely. A more thorough, quantitative interpretation of the data would probably need to consider other factors than dielectric screening of the scattering potentials. In particular, a dependence of the scattering cross sections on the position within the cluster might be necessary, to account for differences in surface and bulk behavior. Without substantial theoretical effort, such advanced models are however not realizable. Nevertheless, the data presented here may serve as an incentive for further theoretical and experimental work on low energy electron scattering in

water clusters.

Chapter 6
Non-metal to metal transition in sodium-doped clusters

Part of the work presented in this chapter has been published.[98]

6.1 Introduction

The transition from non-metallic to metallic alkali metal ammonia bulk solutions, accompanied by the famous color change from blue to bronze solutions, occurs in the concentration range between 1 and 10 mole percent sodium (mole percent metal, MPM) (see Figure 1.2). This rather famous transition has been studied using many different experimental techniques. Experiments include visual inspection of the solutions,[140] electrical resistance and conductivity measurements,[39,40,141,142] Hall effect measurements,[143] and neutron diffraction.[144] So far photoelectron spectra of bulk sodium ammonia solutions have not been reported. However, Häsing[145] and Aulich[146] reported photoelectron yield curves. Such experiments measure the photoelectron current as a function of the excitation wavelength, and are thus not directly comparable to photoelectron spectra. Despite extensive studies, a completely consistent model for the transition to the metallic state (TMS) in sodium ammonia solutions is yet to be established.

Clusters doped with single sodium atoms (single-doped clusters) have previously served as model systems in photoelectron studies of electron solvation.[48,49,147] In this study, we aim to use sodium doped ammonia clusters of varying compositions as model systems for sodium ammonia solutions over a wide concentration range. It is easier to perform photoelectron spectroscopy on doped clusters than on

bulk solutions. Furthermore, variation of the cluster size, in addition to changing the number of sodium atoms, provides new insight. Varying the cluster size allows for the determination of a minimum system size for which a TMS can occur. The onset of metallic behavior at a certain cluster size is an effect that has been often studied for clusters of metal atoms.[148–151] However, it is important to differentiate the behavior of such metal clusters from the TMS in alkali ammonia solutions. In typical metal clusters, metallic or non-metallic behavior is often dominated by electronic shell structures and shell closures. Therefore it is possible to find metallic behavior for a certain cluster size, and non-metallic behavior after only adding one further atom. Such strong effects of "magic" cluster sizes are not expected for mixed sodium ammonia clusters. In addition to multiply-doped ammonia solutions, we chose to study sodium doped dimethyl ether (DME) clusters. Liquid bulk DME does not dissolve sodium in any measurable amount. Therefore there is no TMS reported for bulk DME solutions.

6.2 Experiment, data analysis and models

6.2.1 Experimental conditions

This study uses photoelectron VMI measurements on distributions of neutral sodium-doped clusters to investigate the concentration dependent electronic structure of the clusters. The cluster distributions are characterized using time-of-flight mass spectrometry. The mass spectra do not only hold information on the cluster sizes but also on the number of sodium atoms in a given cluster. The setup used for the experiments is described in section 3.1. Photoionization using 266 nm (4.67 eV) laser pulses, and detection of electrons or ions was performed at a repetition rate of 20 Hz. Clusters were produced using supersonic expansions using a Parker valve. Neat ammonia was expanded with backing pressures of between 3 and 5.5 bar. To produce DME clusters, between 0.6 and 5.9 bar of DME seeded in 3.9-6.1 bar of helium was expanded. The experiments on dimethyl ether were performed with fully deuterated (d_6)-DME, which was necessary to distinguish multiply-doped DME clusters in the mass spectra. Note that the masses of DME (46 amu) and of sodium (23 amu) result in almost perfect overlap between peaks corresponding to $Na_m(DME)_n$ and $Na_{m+2}(DME)_{n-1}$, which would limit the

information obtained on the doping ratio. To vary the sodium concentration for a given cluster size distribution, the temperature of the sodium oven was changed. Before setting the oven temperature to the desired value for each measurement, a mass spectrum at low oven temperatures was recorded. This single-doped mass spectrum was used to verify that the neutral undoped size distributions used to create more highly concentrated samples did not vary over the course of the measurements, i.e. over several days. Corrections of the cluster size distributions to obtain a neutral undoped size distribution from the sodium doped mass spectrum are not necessary for the data discussed in this chapter. Such corrections (see for example in Chapter 5) are only necessary for VMI measurements of undoped clusters. In this chapter both VMI and mass spectrometry is performed on Na-doped clusters using the same photon energy. Therefore the ions mass distribution corresponds to the exact cluster size distribution that is probed in the photoelectron VMI measurements. Since the mass spectra do not offer sufficient resolution to determine relative abundances for all possible cluster compositions $Na_m(solv)_n$, simulations for the doping efficiencies were performed. The basis for these simulations is the Poisson collision statistics discussed in section 2.3.1. The exact procedure to obtain a sodium concentration will be discussed in 6.2.2. Electron velocity map images were reconstructed using the MEVIR algorithm (section 2.1.2.3).

6.2.2 Estimation of metal concentration

According to the Poisson model, it is in principle sufficient to calculate the average number of sodium atoms $\langle m \rangle$ as a function of the cluster size n, to determine the average sodium concentration of a doped cluster. $\langle m \rangle$ can be calculated according to Equation 2.30 and scales roughly as $n^{2/3}$. For small clusters $\langle m \rangle$ is typically smaller than 1 since there is a significant probability for a small cluster to remain undoped. Single UV photons, however, do not ionize undoped solvent clusters, i.e. our experiment does not detect them, neither in the mass spectrum, nor in the electron image. This means that we have to calculate $\langle m \rangle$ from

$$\langle m \rangle_{\mathrm{UV}}(n) = \frac{\sum_{m>0} m P_m(n)}{\sum_{m>0} P_m(n)}. \tag{6.1}$$

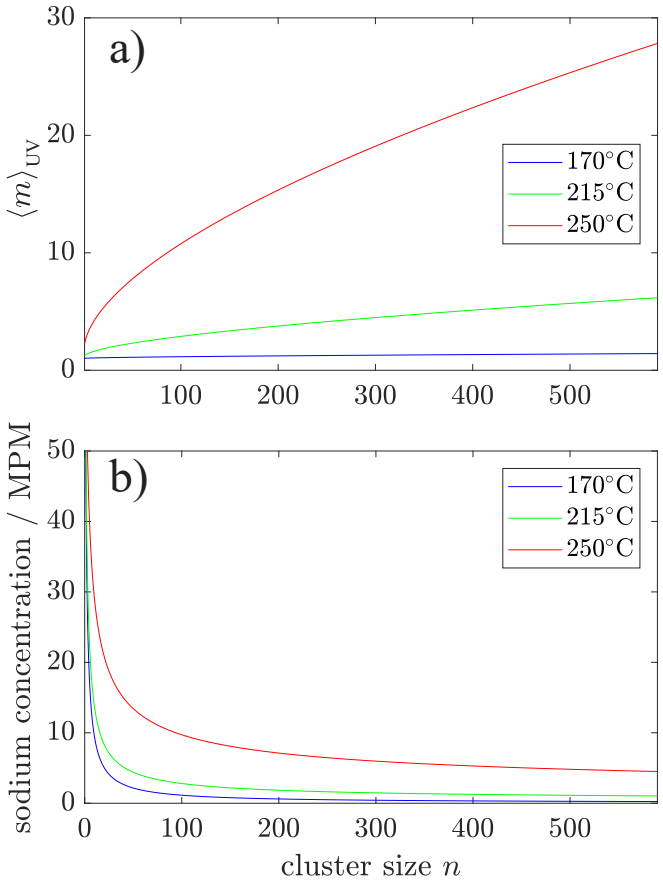

Figure 6.1: a) Average number of sodium atoms in a cluster of size n detected in the experiment for different oven temperatures. b) Expected sodium concentration in mole-percent metal, calculated from the cluster size n and the average number sodium atoms $\langle m \rangle_{\mathrm{UV}}$.

$P_m(n)$ is the probability to dope a cluster of n molecules with m sodium atoms. $\langle m \rangle_{\mathrm{UV}}(n)$ is shown for some oven temperatures in Figure 6.1 (a). Note that $\langle m \rangle_{\mathrm{UV}}(n)$ does not fall below a value of 1 for any cluster size. The average sodium concentration for a given cluster size can be calculated as a mole fraction by dividing $\langle m \rangle_{\mathrm{UV}}(n)$ by $n + \langle m \rangle_{\mathrm{UV}}(n)$. A subsequent multiplication by 100 gives the concentration in MPM (see also Equation 2.41). To obtain an average sodium concentration for the whole cluster distribution, and not only for certain cluster sizes as in Figure 6.1 (b), the sodium concentration is averaged over the full cluster size distribution. Averaging over the size distribution is described by Equation 2.42. However, instead of the undoped size distribution $P(n)$ we chose to use the integrated peak intensity I_{UV} from the single sodium doped mass spectrum, scaled

with an additional factor of $\sqrt{n}$ (see Figure 6.2). The change from the undoped distribution $P(n)$ to the doped distribution I_{UV} (recorded under single-doping conditions) is motivated by the exclusion of undoped clusters. I_{UV} describes the size distribution that is probed under single-doping conditions in the experiment. The additional scaling factor of $\sqrt{n}$ is introduced to account for the increase of the size dependence of the ionization efficiency at higher oven temperatures. As discussed in section 2.3.3, the ionization probability is proportional to the number of sodium atoms in a cluster. While the $\langle m \rangle_{\mathrm{UV}} \approx 1$ for all cluster sizes at low oven temperatures (see blue curve in Figure 6.1 (a)), it shows a pronounced size dependence at higher oven temperatures. This averaging procedure also reduces the influence of the smallest clusters on the estimated concentration. These very small clusters can have unreasonably high sodium concentrations, as can be seen in the example of $Na(NH_3)_2$, which corresponds to a sodium ammonia solution of 33 MPM. A more accurate description than the one explained here could have been obtained from multiplying the determined $\langle m \rangle (n)$ for each temperature with $P(n)$. For reasons of simplicity this was not done. Furthermore, one should keep in mind that the obtained sodium concentrations are only a rough estimate since the model does not include a detailed description of the sticking of sodium atoms to clusters. Also evaporation of solvent molecules from clusters after multiple collisions with sodium atoms would need to be treated for a detailed determination of the concentration. Figure 6.1 and Figure 6.2 show data for a distribution of ammonia clusters with $\langle n \rangle \approx 160$, which will be discussed in more detail in section 6.3.2. The estimated average sodium concentration for this distribution as a function of the oven temperature is shown in Figure 6.3. The region between the dashed lines indicates an uncertainty estimated from the width of the Poisson distribution.

6.2.3 Ab initio calculations

Vertical ionization energies for clusters containing two sodium atoms (double-doped clusters) were calculated on the basis of density functional theory[152,153] (DFT). DFT relies on the fact that the electronic energy of a molecule is fully described by its electron density. The functional $E[\rho(\vec{r})]$, which connects the electron density $\rho(\vec{r})$ to the energy E, is not known exactly. Nevertheless, many approximate functionals are available. We used the ωB97xD functional[154–156] which is a hybrid functional including corrections for long-range correlations and disper-

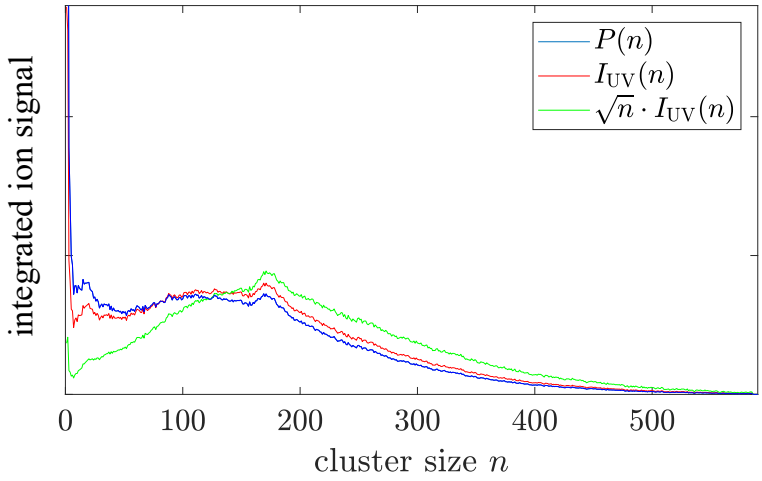

Figure 6.2: Comparison between the measured integrated sodium doped mass spectrometry signal I_{UV}, the undoped cluster size distribution $P(n)$, and the scaled version $\sqrt{n}I_{\mathrm{UV}}$ used to account for the cluster size dependent ionization efficiency.

sion interactions. The empirical dispersion correction[157] is particularly important since we consider weakly bound systems with a significant contribution of van der Waals interactions. We used the comparatively small basis set 6-31+G*[158] for our calculations. Calculations applying the same method and basis set were previously performed for single-doped clusters.[48,49] Tests against higher levels of theory showed that the method produces reliable results for sodium doped clusters. In this work we performed calculations on double-doped ammonia clusters $Na_2(NH_3)_n$ with $n \leq 30$ and on double-doped DME clusters $Na_2(DME)_n$ with $n \leq 18$. In a first step, geometry optimizations were performed for neutral clusters. Next, single point calculations were performed for ions with the optimized neutral structures. The vertical ionization energy was calculated as the difference of these two energies, corrected for the difference between the calculated and experimental values of the ionization energy of the sodium atom. It is clear that theoretical results on clusters of less than 30 molecules including 2 sodium atoms cannot accurately represent the situation in a large, multiply-doped solvent cluster. However, these calculations may still offer a rough idea of the situation and trends present in larger clusters.

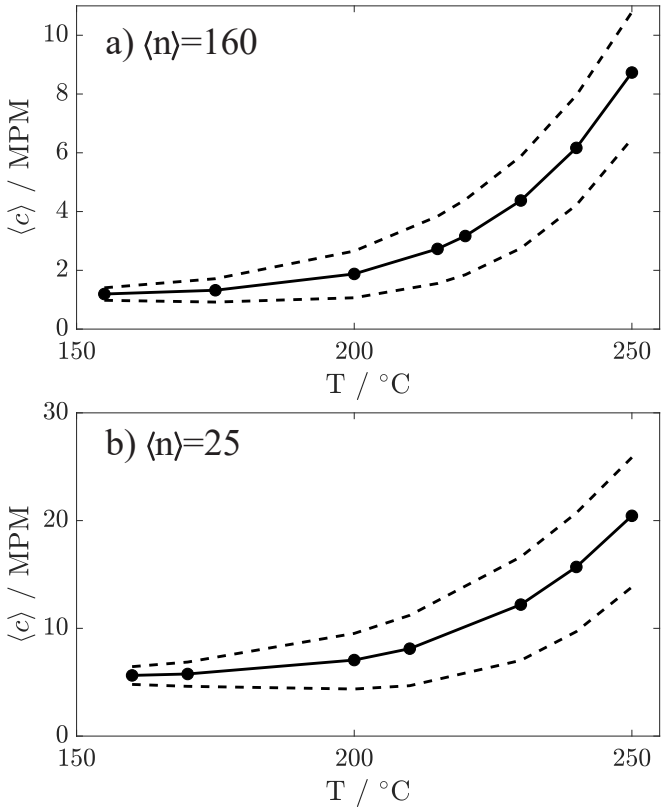

Figure 6.3: Average sodium concentration as a function of the temperature, with estimated uncertainty for two different size distributions of ammonia clusters. The average cluster sizes $\langle n \rangle$ for the two distributions are 160 (a) and 25 (b) molecules.

6.3 Results

6.3.1 Small Na-doped ammonia clusters

6.3.1.1 Mass spectrometry

A set of mass spectra, recorded for a distribution of small ammonia clusters at different oven temperatures is shown in Figure 6.4. The average cluster size recorded under single-doping conditions is 25 molecules. The indicated sodium concentrations were estimated as explained in section 6.2.2. The mass spectra at low oven temperatures show well resolved individual peaks, corresponding to clusters containing a single sodium atom. For increasing oven temperatures, additional peaks appear in the mass spectra that are shifted from the single-doped peaks in steps of 6 amu towards higher masses (panel (b) in Figure 6.4). These peaks correspond to

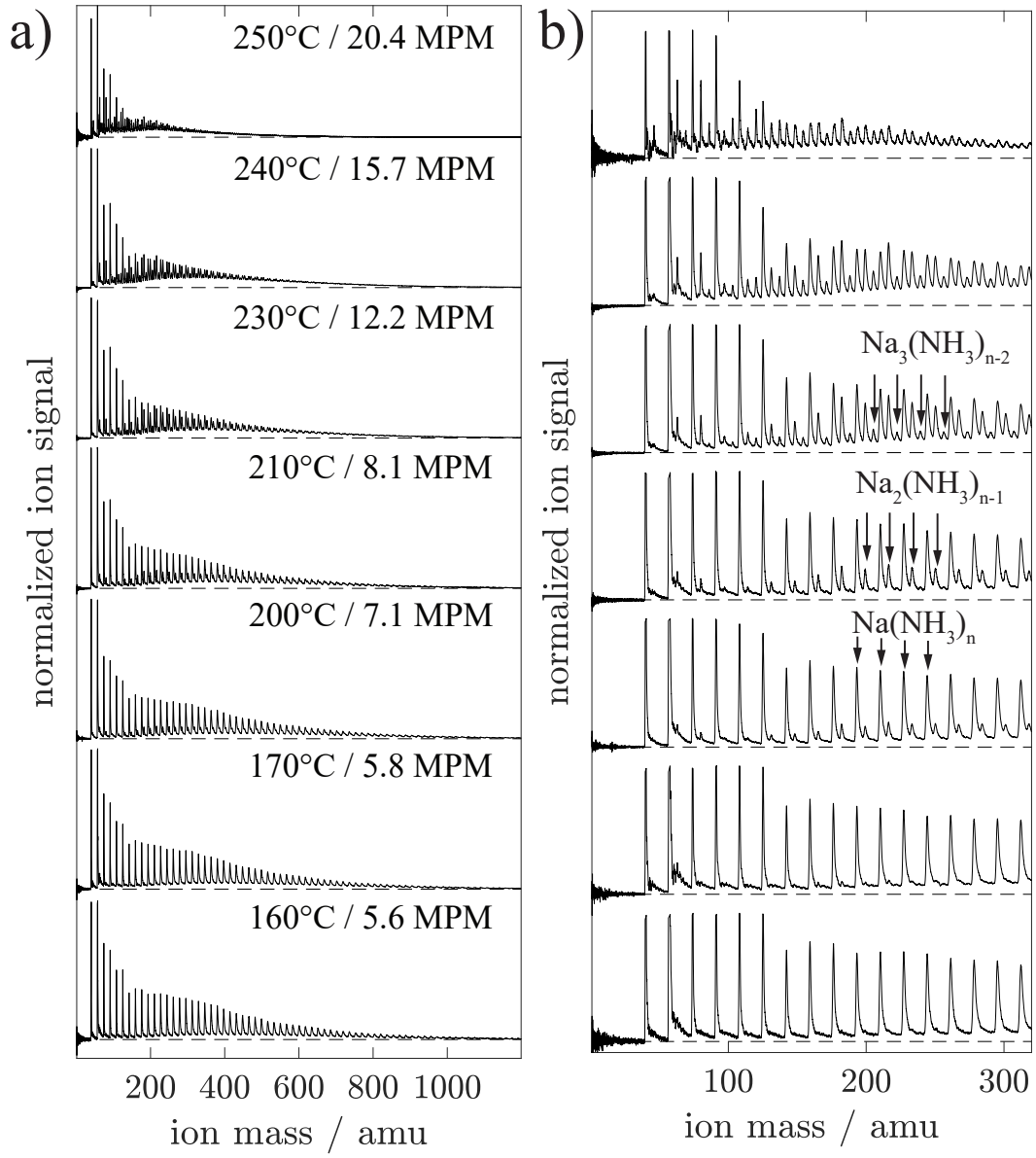

Figure 6.4: Mass spectra of small sodium doped ammonia clusters ($\langle n \rangle \approx 25$) recorded at different oven temperatures. (a) Overview over the full size distribution. The oven temperatures and the estimated sodium concentrations are indicated. The sodium doped monomer and dimer peaks (at 40 amu and 57 amu) are cut at a certain intensity to better display the peaks at higher masses. (b) Zoomed view on the low mass range to visualize the successive appearance of multiply-doped clusters. The lowest mass peaks are cut at a certain intensity to better view the peaks at higher masses.

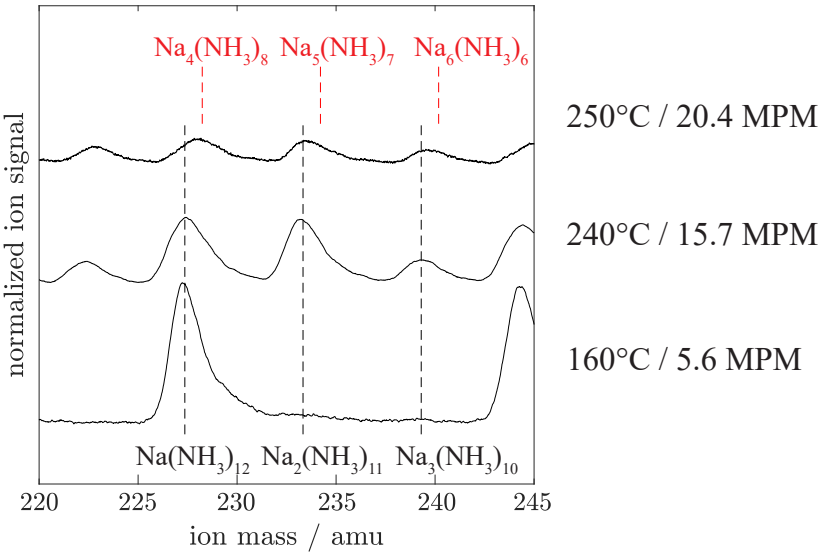

Figure 6.5: Detailed view of the low mass range for the mass spectra recorded at oven temperatures of 160°C , 240°C and 250°C . The dashed black lines indicate peak positions expected for single-, double- and triple-doped ammonia clusters. The dashed red lines indicate peak positions expected for ammonia clusters doped with four to six sodium atoms.

clusters containing 2, 3 and more sodium atoms. For larger clusters the mass peaks are broader, leading to significant overlap between them. This creates the impression of a non-zero baseline of the mass spectrum, and results in the loss of resolved cluster peaks for the larger masses at higher oven temperature. At the highest oven temperature (250°C) it seems as if the cluster size distribution is slightly shifted towards smaller clusters, likely an effect of cluster evaporation. Note that in Figure 6.4 the intensity of the lowest masses is cut at a certain value on the intensity axis. In the overview spectra shown in panel (a), the monomer and dimer peaks are cut; in panel (b) peaks up to the hexamer are cut. A more detailed view of a small mass range of some mass spectra is shown in Figure 6.5. This detailed view shows that at oven temperature of 160°C only single sodium doped clusters are visible, while the mass spectrum at 240°C is dominated by single-, double- and triple-doped clusters. At an oven temperature of 250°C a slight broadening and shift towards higher masses can be observed. This shift is in agreement with the presence of clusters doped with more than three sodium atoms. The mass resolution of the setup is not sufficient to resolve the peaks corresponding to $Na_m(NH_3)_n$ and $Na_{m+3}(NH_3)_{n-4}$, and a separation of $\sim$1 amu. Even at oven temperatures be-

low 250°C clusters containing more than three sodium atoms may be present since the mass peaks are broad enough to contain contributions of such highly doped clusters.

6.3.1.2 Photoelectron VMI

The photoelectron spectra of the cluster distributions discussed in the previous section are shown in Figure 6.6. Some representative photoelectron VMI images before reconstruction are shown in Figure 6.7. The spectrum at the lowest sodium oven temperature, i.e. at single-doping conditions, contains two main bands. An intense one with a band maximum at 2.7 eV and a much less intense one with a band maximum at 3.7 eV. A very weak signal (labeled with an asterisk) is found at an electron binding energy of 4.3 eV. With increasing oven temperature the band located at 3.7 eV (labeled B_{surf}) increases significantly in intensity, until it becomes more intense than the band located at 2.7 eV (labeled B_{solv}). Also, the weak band at 4.3 eV increases slightly in intensity. The binding energies of 4.3 eV and 3.7 eV are in good agreement with values reported by West et al.[48] for the sodium doped ammonia monomer and dimer. It seems plausible, that the weak band at 4.3 eV is due to the sodium doped monomer. The slight increase in intensity with increasing oven temperature agrees with the general trend in doping probability with the increasing sodium vapor pressure. The weak band at 3.7 eV at low oven temperature may be explained by the sodium doped ammonia dimer. However, the strong increase with increasing oven temperature seems to be too pronounced to be caused by the increase in the sodium doped dimer. The band B_{solv} shows a slight shift towards higher electron binding energies for oven temperatures above 230°C (12.2 MPM). This minor shift towards higher binding energies could be explained by the slight reduction of the cluster size due to cluster evaporation, which is observed in the corresponding mass spectra.

6.3.2 Large Na-doped ammonia clusters

6.3.2.1 Mass spectrometry

Mass spectra of large sodium doped ammonia clusters recorded at different sodium oven temperatures are shown in Figure 6.8. Part (a) of the figure shows again the overview over the full size distribution, while part (b) shows the low mass range.

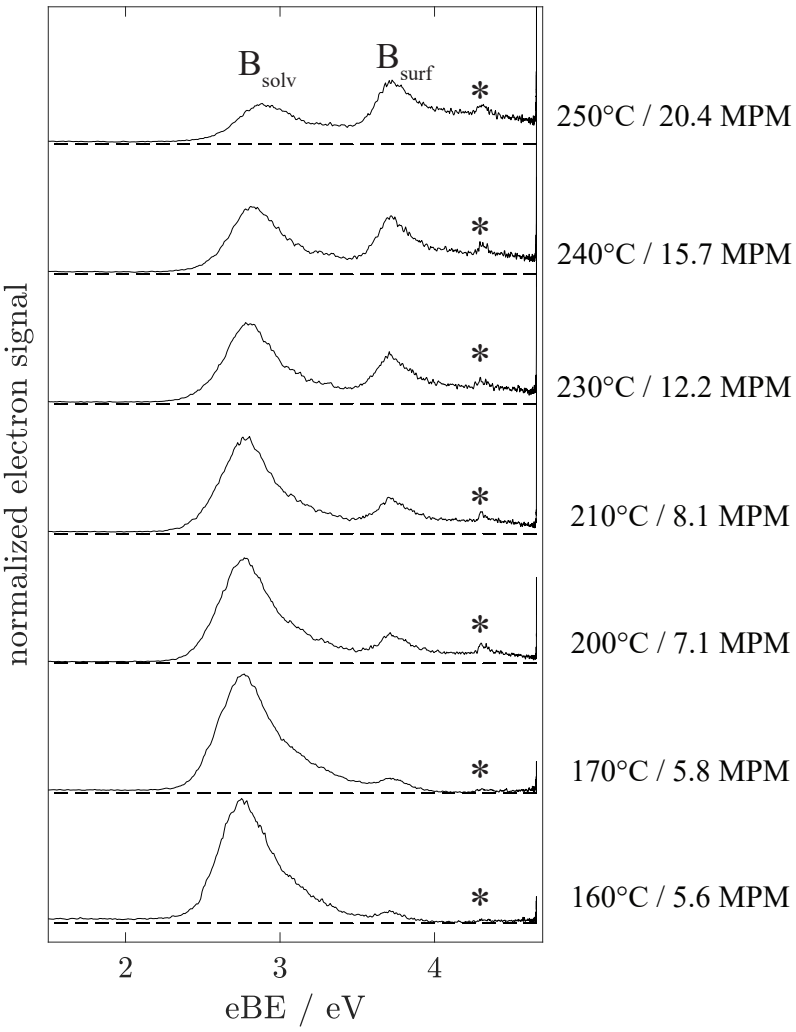

Figure 6.6: Photoelectron spectra of small Na-doped ammonia clusters. The oven temperatures and estimated sodium concentrations are indicated.

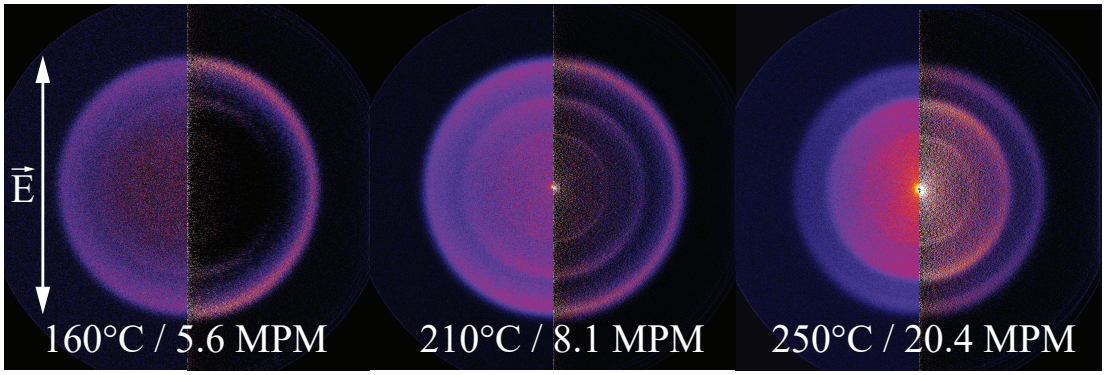

Figure 6.7: Raw (left image halves) and reconstructed (right image halves) velocity map images for different sodium oven temperatures, corresponding to different sodium concentrations.

The average cluster size was determined under single-doping conditions (at 160°C) to be $\langle n \rangle$=160 molecules. The zoomed in view of the low mass range shows that the area that appears black in the overview mass spectra actually consists of well resolved individual peaks. As the oven temperature increases, the maximum mass for which individual peaks are still resolvable decreases significantly. For example, at the lowest oven temperature there are resolved cluster peaks up to ∼4000 amu, whereas at 220°C peaks are only resolved up to ∼2000 amu. This loss of resolved peaks can be attributed to the increase in overlapping peaks of an increasing fraction of multiple-doped clusters. At the highest oven temperature of 250°C the shape of the mass spectrum changes significantly and shifts towards smaller clusters. Note that this change is an effect of the high doping ratio, and not a change of the undoped size distribution, which is the same for all measurements shown. It can be seen that the maximum cluster size detected in the mass spectra at different temperatures remains almost constant, and does not decrease significantly for higher temperatures. The zoomed in view of the low mass range shows again the successive appearance of double- and triple-doped clusters for increasing oven temperatures. At the highest oven temperature there are also mass peaks corresponding to small bare sodium clusters Na_j with $j \leq 17$ (marked by arrows) visible in the mass spectrum. A detailed view of a small mass range is given in Figure 6.9 for the highest oven temperatures. As already observed for the smaller ammonia clusters, there is a slight shift towards higher masses in the mass spectrum that can be explained by the presence of clusters that contain more than three sodium atoms. The peak positions at 250°C indicate the presence of

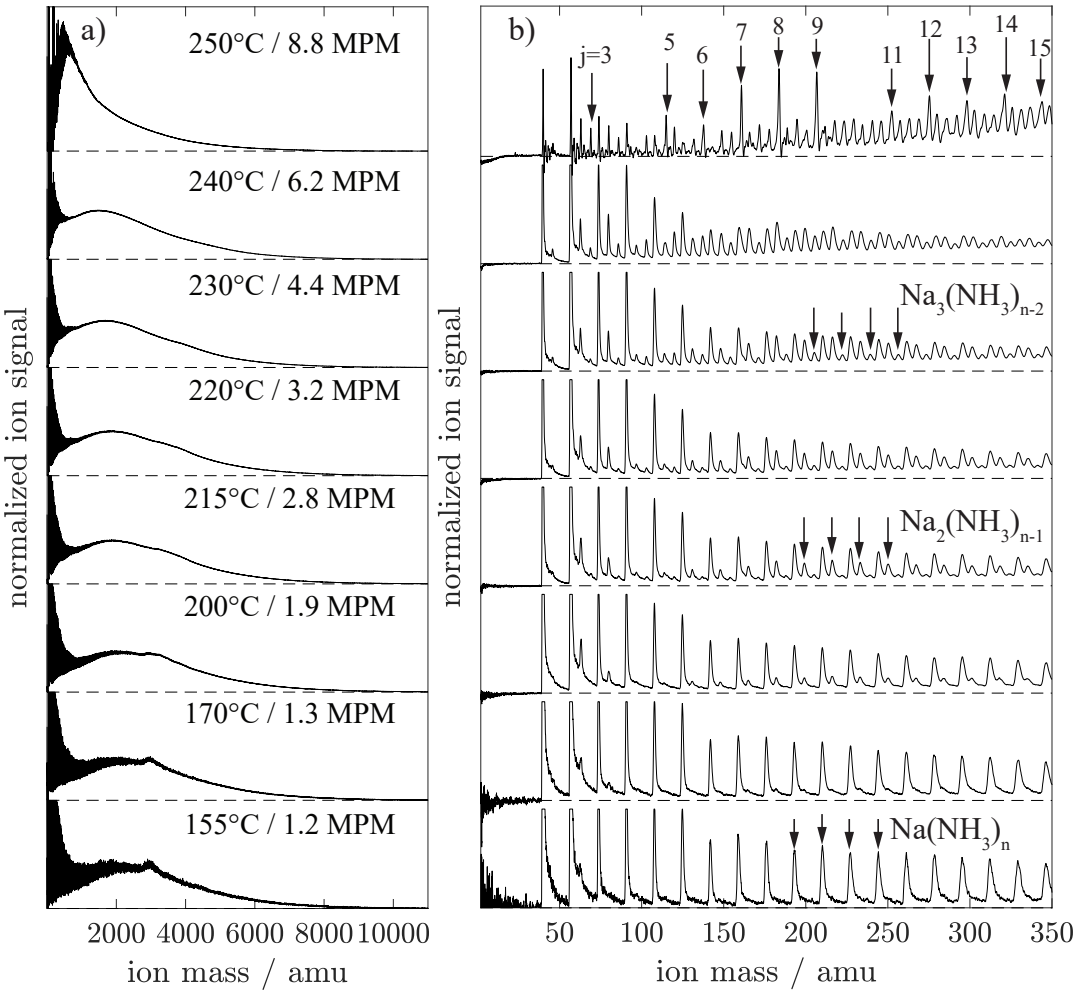

Figure 6.8: Mass spectra of large ($\langle n \rangle$=160) sodium doped ammonia clusters recorded at different oven temperatures. (a) Overview over the full size distribution. The oven temperature and estimated sodium concentration is indicated. The peaks at low masses are cut at a certain intensity to better view the peaks at higher masses. (b) Zoomed in view of the low cluster masses. The peaks at the lowest masses are cut at a certain intensity in order do obtain an overview of the whole mass range.

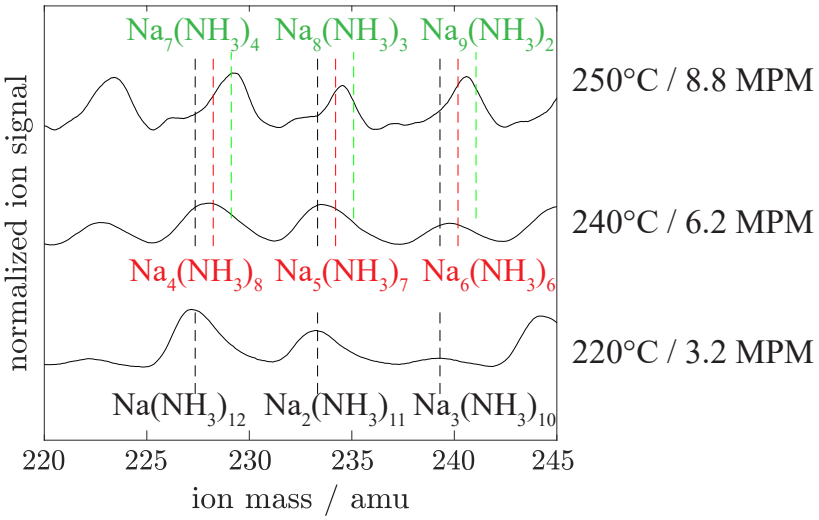

Figure 6.9: Detailed view of a low mass range of the mass spectra recorded at high oven temperatures. The slight shifts of individual peaks towards higher masses with increasing oven temperatures indicates the presence of highly doped clusters.

up to 9 sodium atoms in a cluster. The fact that bare sodium clusters with up to $j = 17$ atoms are detected, indicates that similar numbers of sodium atoms are likely also be present in ammonia clusters. This assumption is also supported by the predicted number of sodium atoms per cluster (see Figure 6.1).

6.3.2.2 Photoelectron VMI

The photoelectron spectra of the larger sodium doped ammonia clusters are shown in Figure 6.10. For the single-doped case, i.e. the spectrum recorded at 155°C , the spectrum consists of a single broad band with a maximum at a electron binding energy of 2.5 eV (labeled B_{solv}). Compared to the previously discussed smaller sodium ammonia clusters (section 6.3.1.2), this main band appears slightly shifted towards lower electron binding energies, which is in agreement with the increased cluster size.[48,49,108,123] A second photoelectron band is not observed at low oven temperatures. However, similar to the small cluster case, an additional band at higher binding energies around 3.5 eV (labeled B_{surf}) grows into the spectrum with increasing oven temperatures. Along with the increase in intensity, the band maximum of B_{surf} shifts slightly towards higher binding energies. The band maximum and onset of B_{solv} does not change with the oven temperature up to 240°C . Only the shape of the band slightly changes. At 250°C oven temperature B_{solv} changes

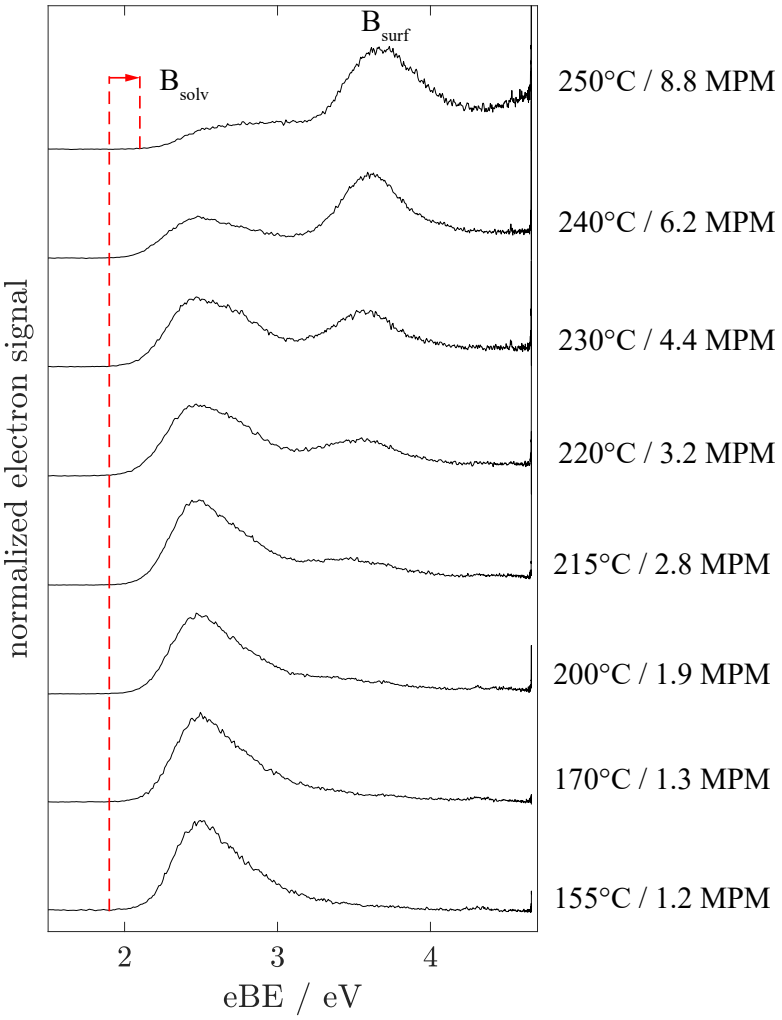

Figure 6.10: Photoelectron spectra of large sodium-doped ammonia clusters, recorded at the indicated oven temperatures. Estimated sodium concentrations are given as well.

pronouncedly. Its shape does not show a maximum anymore, but forms a broad plateau and the onset of the peak is significantly shifted towards higher electron binding energies (indicated by the red vertical lines).

6.3.3 Small Na-doped dimethyl ether clusters

6.3.3.1 Mass spectrometry

Mass spectra of small sodium doped DME clusters recorded at different sodium oven temperatures are shown in Figure 6.11. The average cluster size was determined under single-doping conditions to be $\langle n \rangle \approx$40 molecules. The most apparent change with increasing oven temperature is the loss of resolved peaks. This is due to the increase in partially overlapping peaks corresponding to multiply-doped clusters. It is important to note, that the loss of resolved peaks is not accompanied by a reduction of overall ion signal. Nevertheless, there is a shift towards smaller cluster sizes observed above 230°C oven temperature. Figure 6.11 (b) shows that above 230°C there are small bare sodium clusters with less than 5 atoms visible (labeled with arrows). Figure 6.12 shows a more detailed view of the mass spectra at selected oven temperatures. Part (a) of the figure shows clearly how the space in between the single-doped cluster peaks is filled up by multiply-doped cluster peaks. Part (b) shows no strong changes in the doping ratios between 240°C and 260°C oven temperature. The use of the deuterated dimethyl ether allows to distinguish clusters containing up to 7 sodium atoms in the recorded mass spectra.

6.3.3.2 Photoelectron VMI

Photoelectron spectra recorded for the cluster distributions discussed above are shown in Figure 6.13. Similar to the cases of ammonia clusters discussed in sections 6.3.1 and 6.3.2, the spectrum for the single-doped case is dominated by a single band (labeled B_{solv}). In the present case B_{solv} is located at 1.35 eV for low oven temperature. For increasing oven temperature, the most pronounced changes are the appearance and increasing intensity of an additional band B_{surf} at higher electron binding energy. B_{surf} appears for 200°C oven temperature at 2.65 eV, and shifts towards 3 eV for higher oven temperatures. Additionally, above 250°C there is a shoulder (marked with asterisks) developing on the high binding energy side of B_{surf}. At oven temperatures above 230°C the intensity of B_{solv} decreases signifi-

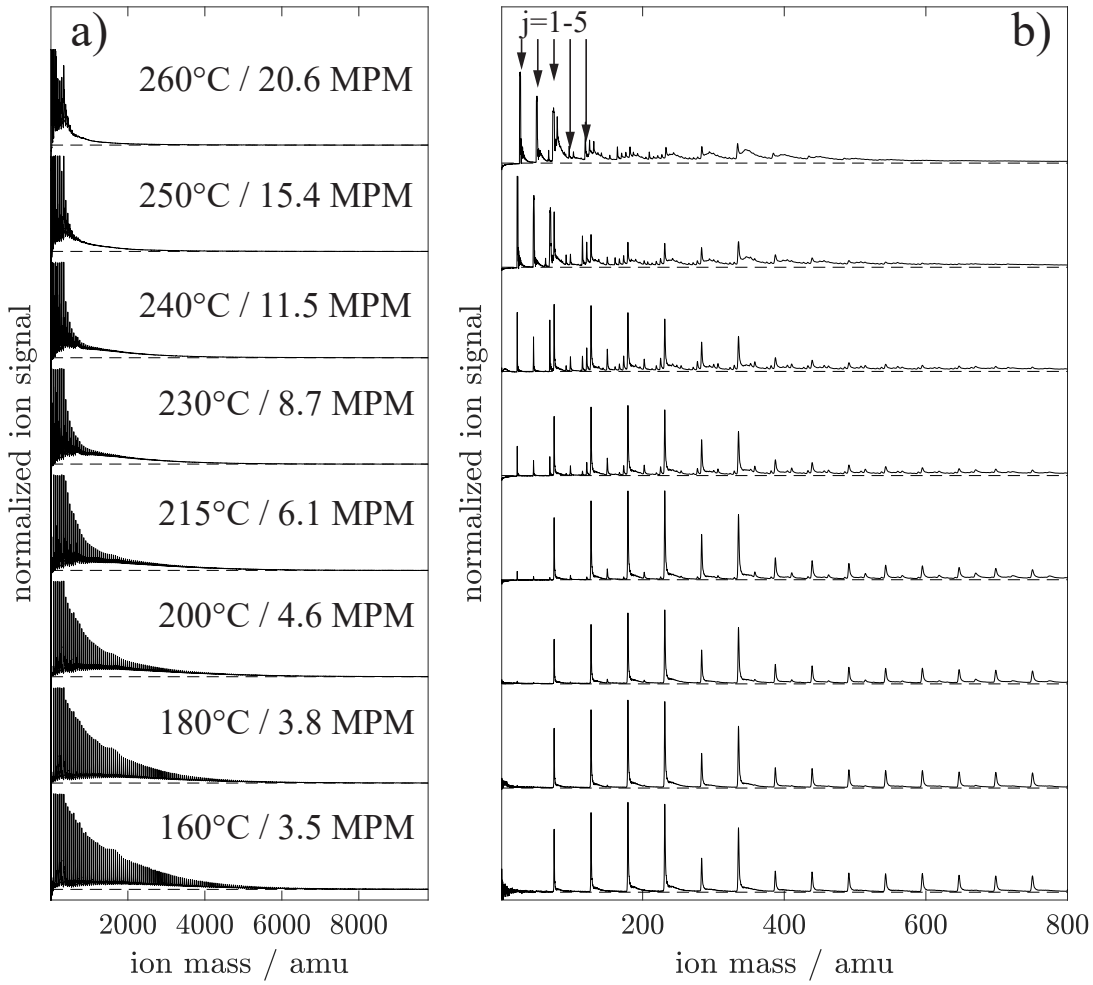

Figure 6.11: Mass spectra of small sodium doped DME clusters recorded at different oven temperatures. (a) Overview over the full size distribution. The oven temperature and sodium concentration are indicated. The peaks at the smallest cluster masses are not shown in their full intensity, but cut at a certain value on the y axis. (b) Zoomed in view on the low mass range, showing the increase in multi-doped peaks.

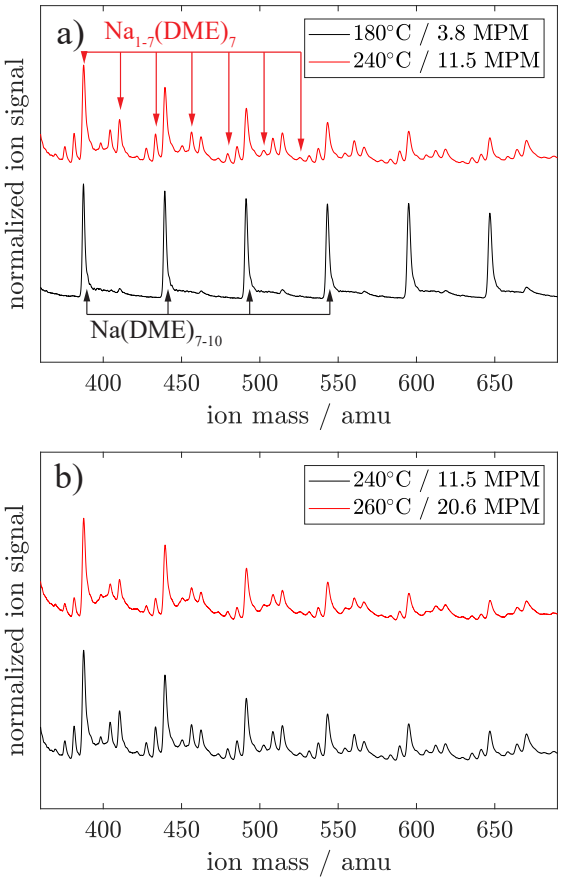

Figure 6.12: Detailed view of the low mass range of the mass spectra recorded at high oven temperatures. (a) Comparison of a mass spectrum dominated by single-doped clusters (180°C) with a mass spectrum of highly-doped clusters (240°C). Single-doped (d_6)-DME cluster peaks are spaced by 52 amu, while DME clusters of a given size, doped with an increasing number of sodium atoms are observed with a spacing of 23 amu. (b) Comparison of highly-doped cluster mass spectra recorded at 240°C and 260°C . The mass spectra show no pronounced change over this temperature range.

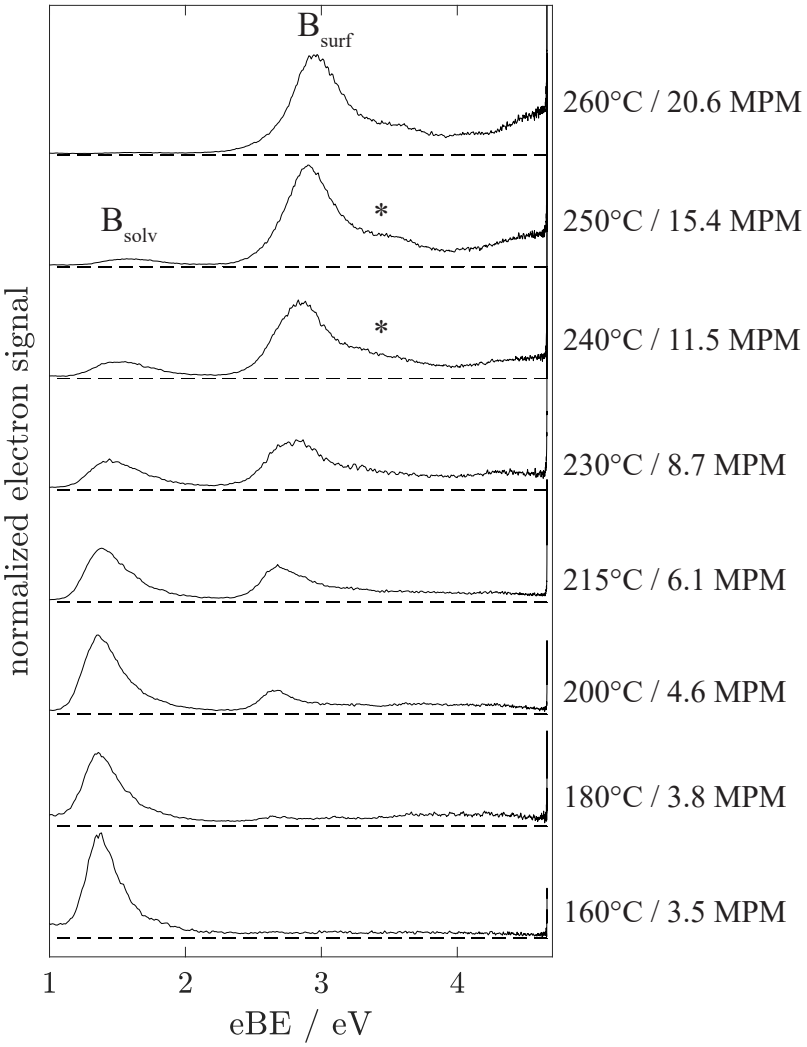

Figure 6.13: Photoelectron spectra of small sodium doped DME clusters. Oven temperatures and estimated sodium concentrations are indicated.

cantly until the band vanishes completely at 260°C . This decrease is accompanied by a shift of its band maximum towards higher electron binding energies. This slight shift is in agreement with the reduction of cluster size due to evaporation, which was observed in the mass spectra.

6.3.4 Large Na-doped dimethyl ether clusters

6.3.4.1 Mass spectrometry

Mass spectra of large sodium doped DME clusters, recorded for different oven temperatures are shown in Figure 6.14. Under single-doping conditions the average cluster size is determined to be $\langle n \rangle = 100$ molecules. For increasing oven temperature the resolved peaks are lost due to the appearance of overlapping peaks of multiply-doped clusters. For oven temperatures above 235°C there seems to be a slight shift towards smaller cluster sizes that is increased for oven temperatures above 260°C . It is observed that for high oven temperatures the maximum cluster size decreases significantly. The reason for this shift towards smaller clusters is most likely evaporation of DME molecules from the clusters. Starting from 260°C the mass spectra show contributions of bare sodium clusters with up to at least 21 atoms. At 280°C the mass spectrum is dominated by bare sodium clusters of up to 50 atoms. Although the peaks corresponding to the bare sodium clusters are the most clearly visible ones in the mass spectrum, it still can be assumed that many clusters still contain a significant amount of DME. A careful inspection of Figure 6.15 (c) shows partly resolved peaks in between the bare sodium cluster peaks. It should be noted here, that the bare sodium clusters are formed within solvent clusters, followed by evaporation of the solvent. They cannot form directly from the sodium oven. A detailed view of selected mass spectra in Figure 6.15 shows again the evolution from single-doping conditions to highly-doped clusters to the case where the mass spectrum is dominated by bare sodium clusters. An unambiguous assignment of all mass peaks for the highly doped cases above 250°C is difficult, but it seems that at 260°C (see Figure 6.15) we can resolve up to $\sim$9 sodium atoms in a DME cluster.

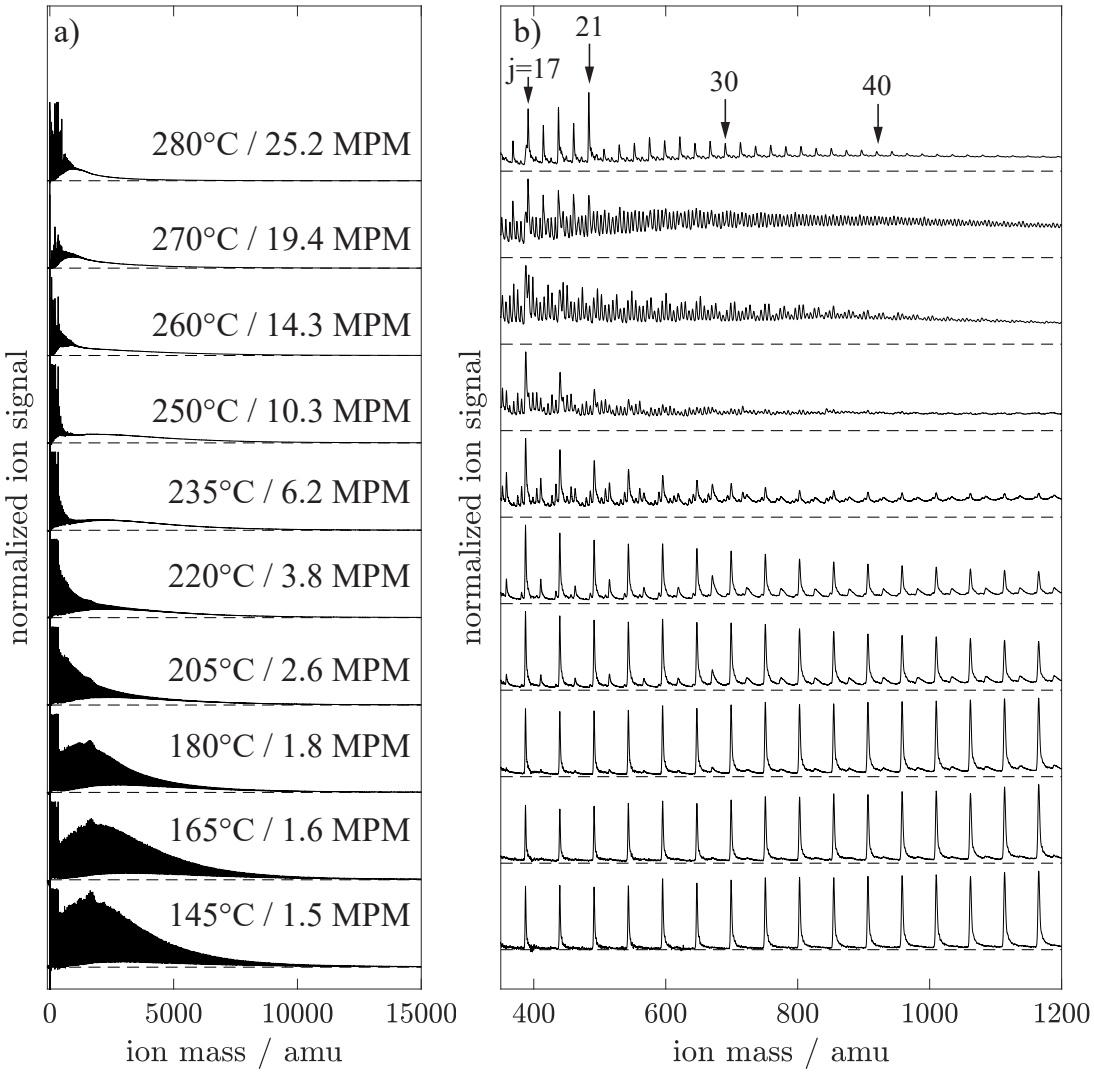

Figure 6.14: Mass spectra of large sodium doped DME clusters recorded at different oven temperatures. (a) Overview over the full size distribution. The oven temperature and estimated sodium concentration is indicated. The low mass peaks are cut at a certain intensity to better visualize the whole mass range. (b) Zoomed in view of the low mass range, visualizing the increasing number of peaks corresponding to multiply-doped clusters.

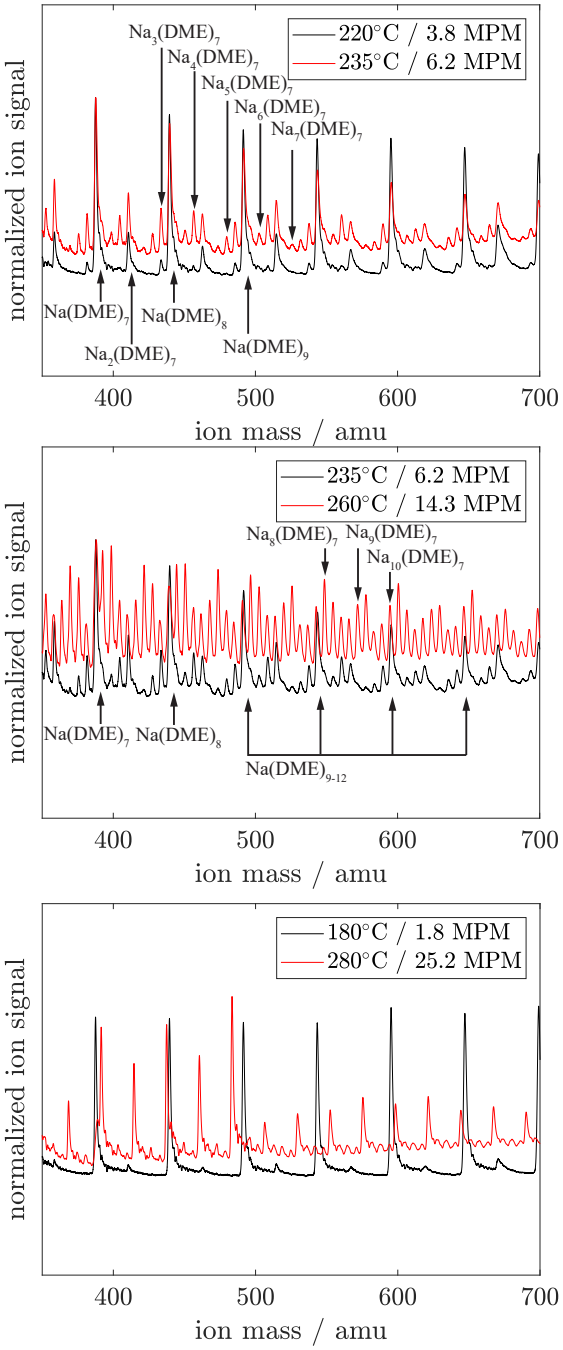

Figure 6.15: Detailed view of the low mass range of the mass spectra recorded at different oven temperatures. (a) Comparison between mass spectrum dominated by single- and double-doped clusters (220°C) to mass spectrum with clusters doped with up to 7 sodium atoms (235°C). (b) Further increase of doping ratios up to oven temperatures of 260°C . (c) At 280°C the mass spectrum is dominated by bare sodium clusters.

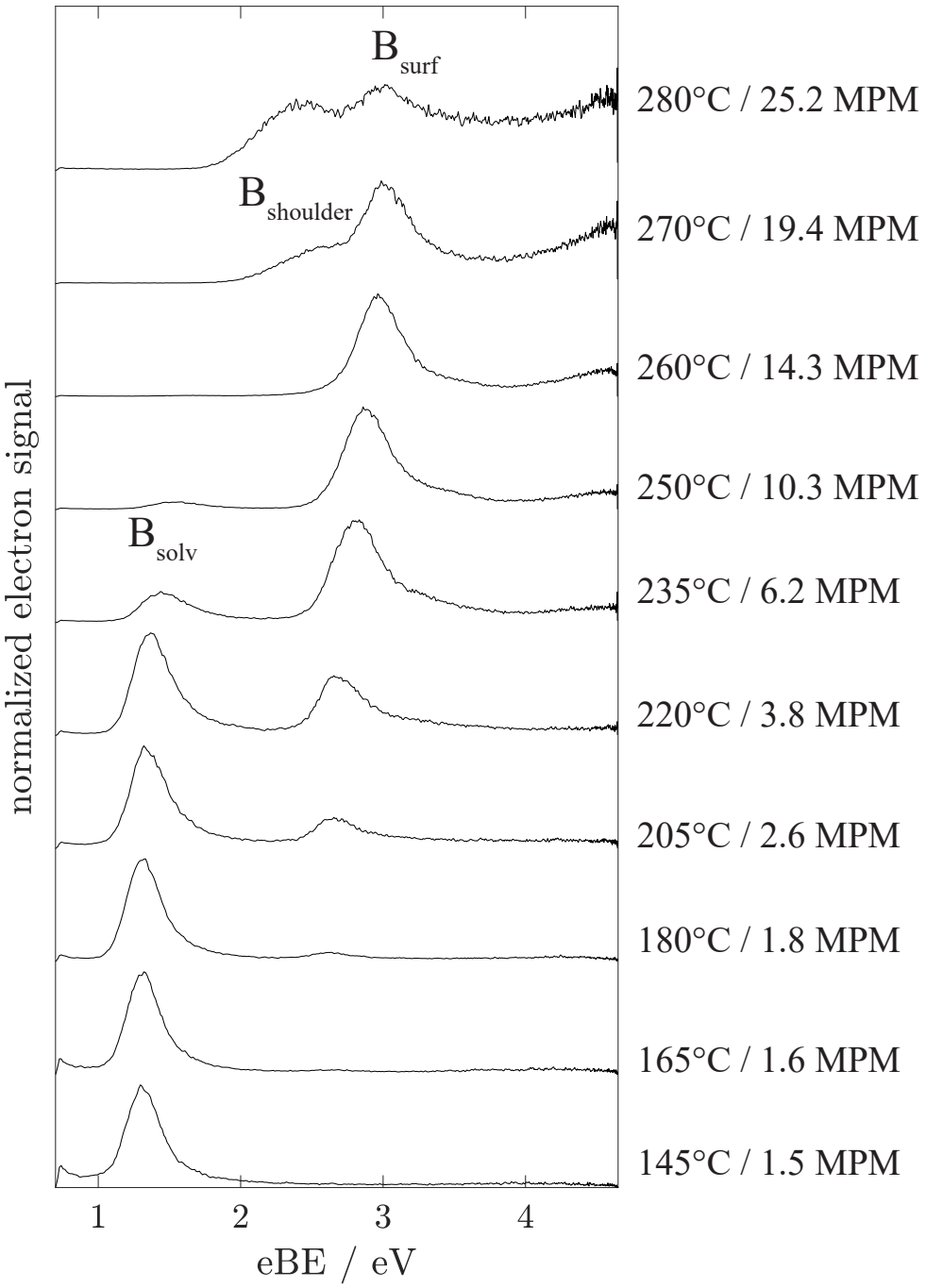

Figure 6.16: Photoelectron spectra of large sodium doped DME clusters. The oven temperatures and estimated sodium concentrations are indicated.

6.3.4.2 Photoelectron VMI

The photoelectron spectra for the large sodium doped DME cluster distribution recorded at different oven temperatures is shown in Figure 6.16. Under single-doping conditions, i.e. at the lowest oven temperature, the spectrum contains a single band with a maximum at 1.3 eV electron binding energy. This band (labeled B_{solv}) lies at a slightly lower eBE than the corresponding band for the smaller DME clusters. This is in agreement with the overall trend to lower electron binding energies for larger clusters. For increasing oven temperatures there is an additional band growing into the spectrum at higher electron binding energies. We label this band B_{surf}. At an oven temperature of 180°C, B_{surf} first appears at 2.6 eV and then shifts towards 3 eV for higher oven temperatures. B_{solv} decreases in intensity for increasing oven temperature, until it vanishes completely at 260°C . At 235°C and 250°C B_{solv} shifts slightly towards higher electron binding energies, which is in agreement with a slight reduction of the cluster size due to evaporation. At 260°C the spectrum consists of the single band B_{surf}. At 270°C this band develops a pronounced shoulder towards lower electron binding energies, resembling the situation for large ammonia clusters at the highest oven temperatures. At 280°C this shoulder grows into a broad peak with a maximum around 2.4 eV.

6.4 Results from ab initio calculations

The geometry optimization for neutral, double-doped, ammonia clusters $Na_2(NH_3)_n$ results in cluster geometries that can be grouped into three structural motifs. Figure 6.17 shows as an example three different motifs of the $Na_2(NH_3)_{20}$ cluster. In the first two structures ((a) and (b) of the figure) both sodium atoms are solvated internally in the cluster. The both structures mainly differ in the distance between the two sodium atoms. The first structure (a) can be basically described as a solvated sodium dimer, with a Na-Na separation of ~ 3 Å. The second structure (b) seems to be better described by two individually solvated sodium atoms. This is also reflected by a larger Na-Na distance of typically $\sim$7 Å, and the fact that there is typically an ammonia molecule located in between the sodium atoms. For both structures, the doubly occupied HOMO separated from the sodium atoms and located on the surface of the cluster. This is in agreement with the situation in single-doped clusters, where the electron was also found to be located at the

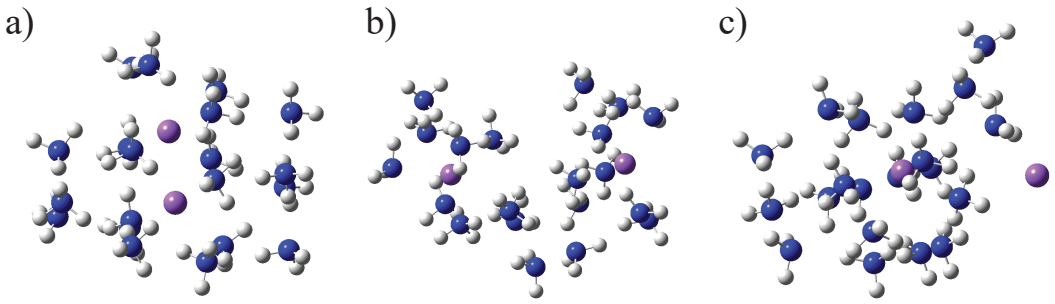

Figure 6.17: Three different types of motifs found during the geometry optimizations. Panel (a) shows a solvated sodium dimer, (b) shows two individually solvated sodium atoms and (c) one internally solvated and one surface bound sodium atom

cluster surface.[48,49] In contrast to the first two structural motifs, the third type of structure (Figure 6.17 (c)) contains one sodium atom that is bound at the cluster surface. In this case, the doubly occupied HOMO is an s-like orbital located on sodium atom at the surface. The calculated vertical ionization energies for the double-doped ammonia clusters are provided in Figure 6.18 together with the results for single-doped clusters from West et al.[48] The vertical ionization energies of the structures with only internally solvated sodium atoms agree quite well with those of single-doped clusters. The clusters with surface sodium atoms, however, show a significantly higher vertical ionization energy. This is in good agreement with the previous findings of West et al.[48] They found that the vertical ionization energy is much more influenced by the location of the sodium atom (or ion) than by the location of the electron. Furthermore, they did not find evidence of an onset of internal solvation of the solvated electrons in clusters. It is therefore unclear whether and at which cluster size a solvated electron in a sodium doped clusters starts to become internally solvated. The labels eBE_{solv} and eBE_{surf} are used to distinguish structures showing internally solvated sodium atoms from structures showing a sodium atom on the cluster surface.

For DME no optimized structures showed two truly internally solvated sodium atoms. It is possible, that more molecules are required to internally solvate two sodium atoms in DME clusters. Note, that the calculations for sodium doped DME clusters did not converge as easily as for the ammonia case. Possible reasons for that are the increased number of atoms per molecule and the presence of many shallow minima due to the weaker interactions between DME molecules. There

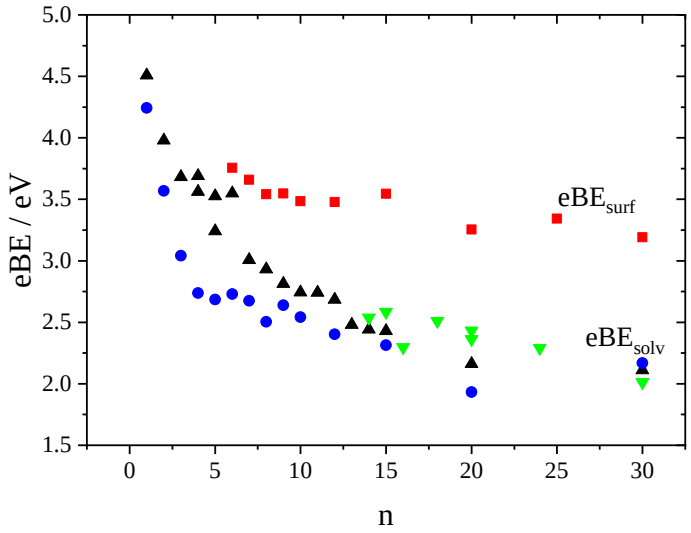

Figure 6.18: Electron binding energies calculated from DFT as a function of the cluster size. Blue circles show data on single-doped NH_3 clusters from West et al.[48] Red squares show data on double-doped NH_3 clusters with one partially solvated sodium atom located at the cluster surface (Figure 6.17 (c)). Black and green triangles show data for double-doped NH_3 clusters, with two internally solvated sodium atoms (Figure 6.17 (a) and (b)). The data shown in green corresponds to cluster structures with a larger separation between the sodium atoms (Figure 6.17 (b)). The figure is reproduced from reference [98] with permission.

were still two different structural motifs for DME, albeit the distinction between them is slightly less clear than in the case of ammonia. As an example, Figure 6.19 shows two structures found for $Na_2(DME)_{15}$. The structure on the left side of the figure shows a surface bound sodium atom, similar to the case in sodium doped ammonia clusters. The second structure contains a sodium atom which is also located on the cluster surface, but seems to be embedded slightly more in the solvent. In both cases the doubly occupied HOMO is an s-like orbital located on the sodium atom at the surface. Figure 6.20 compares vertical ionization energies for the optimized structures with those for single-doped clusters by West et al.[48] It is observed that both structures have vertical ionization energies higher than those reported for the single-doped clusters of similar size. This agrees with the observations for surface sodium atoms in ammonia clusters. However, in the DME case, the slightly more solvated sodium atoms show electron binding energies which are higher than those for the less solvated sodium atoms. Since the energies of the

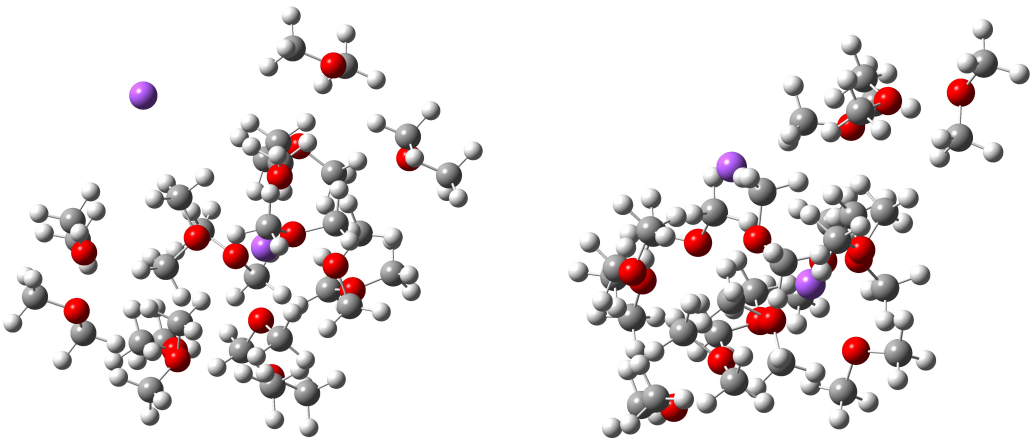

Figure 6.19: Two structural motifs found for double-doped DME clusters.

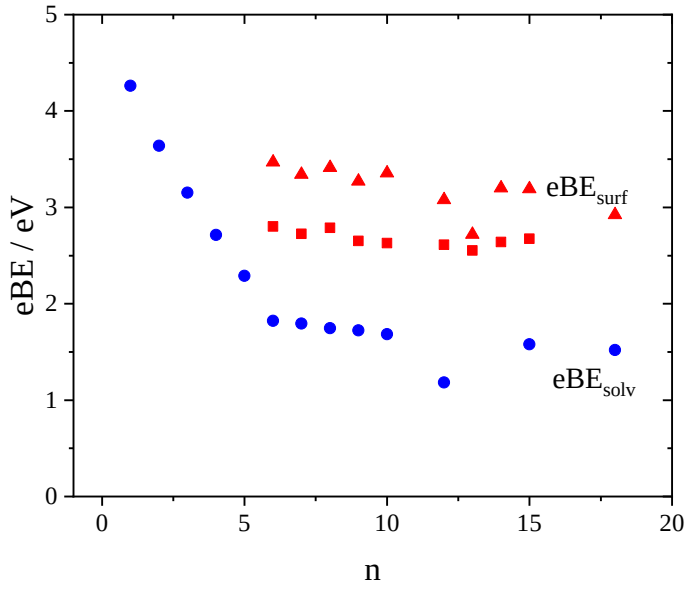

Figure 6.20: Electron binding energies calculated from DFT as a function of the cluster size. Blue circles show data on single-doped DME clusters from West et al.[48] Red squares and triangles show data for double-doped DME clusters with one partially solvated sodium atom located at the cluster surface (Figure 6.19 (a)). The triangles correspond to the structure with the slightly more solvated sodium(Figure 6.19 (b)).

two neutral structures are similar, this higher ionization energy can be explained by less stable ionic structure. This can be understood by considering the close arrangement of the DME molecules around the partially negatively charged sodium atom in the neutral structure. This arrangement is not optimal for the neutral sodium atom, which is created upon ionization of the cluster. The labels eBE_{solv} and eBE_{surf} are again used to distinguish sodium atoms on the cluster surface from internally solvated sodium atoms. In this case however, the only structures showing exclusively internally solvated sodium atoms are the single-doped structures from West et al.[48]

6.5 Discussion

6.5.1 Low and high binding energy features in the PES

Most photoelectron spectra discussed in section 6.3 consist of the two main bands B_{solv} and B_{surf}. In the PES we have labeled the band located at lower electron binding energy as B_{solv} and the band at higher electron binding energy as B_{surf}. Experimental binding energies corresponding to the band maxima of the B_{solv} bands have been extracted under single-doping conditions and are summarized and compared to literature values in Table 6.1. It can be seen that our values agree well with previously reported data. B_{solv} is assigned to photoemission from a sodium atom solvated internally in a cluster, i.e. the ionization of an solvated electron that is separated from the sodium atom. This assignment is supported by ab initio calculations on double-doped ammonia clusters discussed in section 6.4, as well as by previous theoretical and experimental work on single-doped clusters. We find that over a wide range of oven temperatures and sodium concentrations the band

	this work		literature[48]	
substance	$\langle n \rangle$	eBE_{solv} / eV	$\langle n \rangle$	eBE_{solv} / eV
NH_3	25	∼2.7	20	2.69±0.1
NH_3	160	∼2.5	170	2.54±0.11
DME	40	∼1.35	48	1.42±0.16
DME	100	∼1.3	90	1.44±0.16

Table 6.1: Comparison of binding energy positions for single-doped clusters to literature values. Slight deviations can be attributed to different procedures in the size determination.

B_{solv} does not change significantly. The similarity between the DFT results on single-doped clusters and those on double-doped clusters with internally solvated sodium atoms predicts this behavior. This indicates that the photoelectron spectrum of sodium ammonia clusters does not depend on the sodium concentration, as long as the sodium atoms are internally solvated and separated from their valence electron. For sodium-doped DME clusters there were no structures found with more than one internally solvated sodium atom. Nevertheless, it is likely that for large enough clusters more than one sodium atom can be internally solvated in a DME cluster. Furthermore it is assumed that such a cluster with several internally solvated sodium atoms would show electron binding energies similar to the single-doped clusters. Therefore, we also assign the band B_{solv} for the DME clusters to internally solvated sodium atoms that separate from their valence electron.

The band B_{surf} is assigned to sodium atoms with doubly occupied HOMO s-orbital, located at the surface of the clusters. This assignment is supported by the DFT calculations on double-doped DME and ammonia clusters (see Figure 6.18 and Figure 6.20) that give electron binding energies in good agreement with the experimental B_{surf} band. The increase in relative intensity of B_{surf} can be explained by the assumption that only a certain number of sodium atoms can be internally solvated in a cluster of a given size. B_{surf} can be seen as a cluster or confinement effect that only occurs due to the limited system size and large surface area. As such, it is not expected to occur in bulk, and has not been reported for bulk solutions. The cluster-equivalent of the TMS in bulk is therefore expected to manifest itself as a strong change of the feature B_{solv} rather than in a change of B_{surf}.

6.5.2 Strong changes in electronic structure at high sodium concentration

For small ammonia and DME clusters (Figures 6.6 and 6.13) there were no striking changes found for the band B_{solv} for increasing sodium concentration. The main change in the PES is the appearance and increase in the intensity of B_{surf}. The only change to B_{solv} is a decrease in relative intensity and a slight shift towards higher electron binding energies, occurring for the highest oven temperatures for which B_{solv} is observed. This slight shift in electron binding energy is in agreement with the observed shift towards smaller clusters caused by evaporation of

solvent molecules. For large sodium doped ammonia and DME clusters in contrast, stronger changes in the photoelectron spectra are found (Figures 6.10 and 6.16). For NH_3, B_{solv} transforms from a peak to a broad plateau with an onset shifted towards higher electron binding energies at an oven temperature of 250°C (Figure 6.10). For large DME clusters, the situation is somewhat different. B_{solv} vanishes completely at a temperature of 260°C , so that the spectrum consists of a single band B_{surf}. At 270°C a new shoulder appears in the PES on the low eBE side of B_{surf}. In both cases, i.e. for large ammonia and large DME clusters, the changes of the PES at high oven temperatures indicate strong changes to the electronic structure of the clusters. The shoulder arising for the highly doped DME clusters and the plateau occurring for the highly doped ammonia clusters are compared to each other in Figure 6.21. Although there are some similarities between the two spectra, the differences predominate. It is difficult to compare the overall shape of the two features and the onsets of the two spectra differ. In the sodium case the onset of the spectrum is at 2.1 eV, whereas in the case of DME is around 1.8 eV. In both cases, the changes to the PES occur for cluster distributions that already show contributions of bare sodium clusters in the mass spectra. For smaller clusters, where only much smaller bare sodium clusters are observed, no such strong changes to the PES occur. This may be seen as an indication of a connection between the occurrence of large bare sodium clusters and the changes to the PES. Therefore, it is useful to have a closer look at the amount and cluster sizes of bare sodium clusters, Na_j, present in the individual cases. Figure 6.22 compares the mass spectra of large $Na_m(NH_3)_n$ for the two highest oven temperatures of 240°C and 250°C. The red dotted lines indicate masses of bare sodium clusters Na_j, with $7 \leq j \leq 19$. The mass spectrum recorded at 240°C shows no evidence of bare sodium cluster larger than $j = 3$. In contrast, the mass spectrum recorded at 250°C shows peaks clearly corresponding to bare sodium clusters with $j = 7, 8, 9$ and $j = 12, 13, 14$. Bare sodium clusters with up to 19 atoms are not clearly visible, but are indicated by deviations of the peak shapes at the positions where a sodium cluster peak would be expected. However, the mass spectrum is still dominated by clusters containing ammonia molecules. Figure 6.23 shows the mass spectra of large $Na_m(DME)_n$ clusters over the oven temperature range, where the shoulder appears. The red dotted lines indicate masses of bare sodium clusters Na_j with $9 \leq j \leq 21$. It can be seen that at 260°C and 270°C there are similar amounts

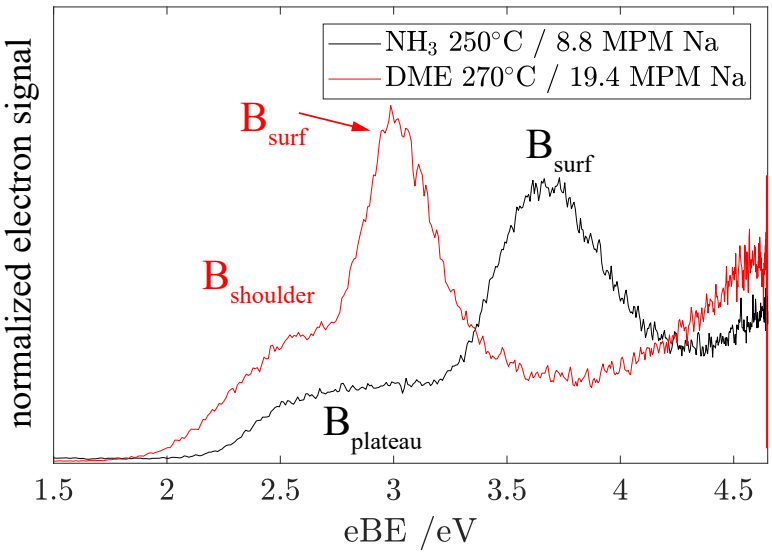

Figure 6.21: Photoelectron spectra of ammonia clusters containing 8.8 MPM sodium and of DME clusters containing 19.4 MPM sodium (see Figures 6.10 and 6.16).

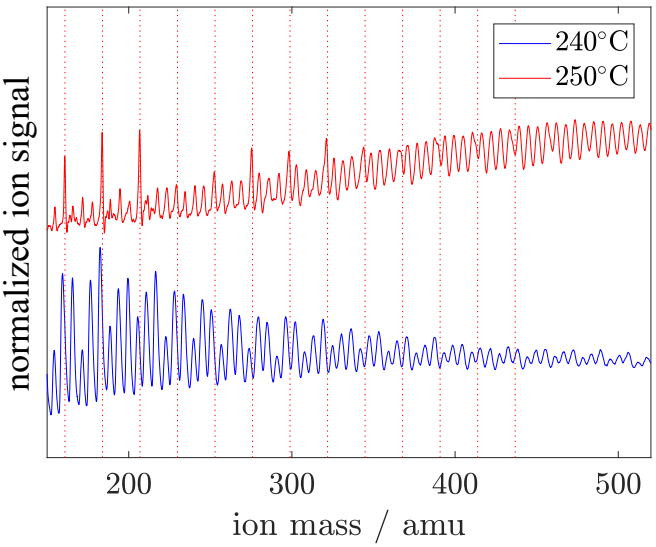

Figure 6.22: Comparison of the mass spectra recorded at 240°C and 250°C oven temperatures for large NH_3 clusters. Red dotted lines show masses of bare sodium clusters Na_j with $7 < j < 19$. While at 250°C there are sodium cluster with $j \leq 17$ present, there are no sodium clusters with $j > 3$ found at 240°C .

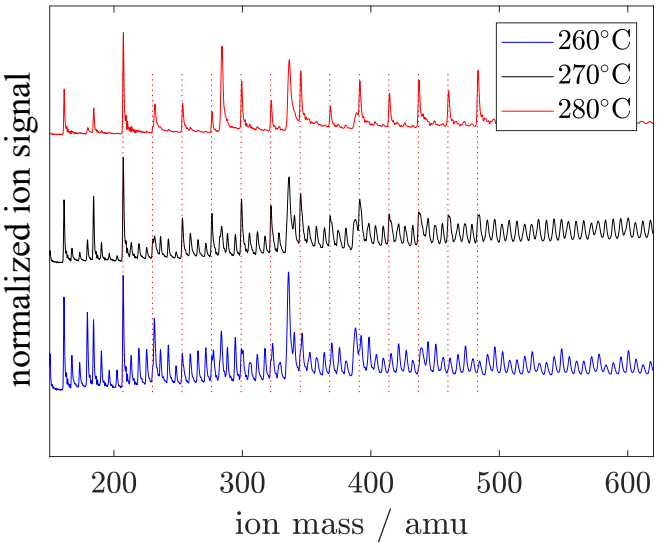

Figure 6.23: Comparison of the mass spectra recorded between 260°C and 280°C oven temperatures for large DME clusters. The red dotted lines indicate positions of bare sodium clusters Na_j with $9 < j < 21$. The mass spectra at 260°C and 270°C show indications of the presence of bare sodium clusters with $j < 17$ and $j < 19$ respectively. The mass spectrum at 280°C is dominated by bare sodium clusters with $j < 50$.

of sodium clusters visible in the mass spectra. In contrast to these small differences the amount and size of bare sodium clusters changes drastically at 280°C. For 280°C basically all resolved peaks correspond to bare sodium clusters, with maximum cluster sizes of $j = 50$ atoms. Nevertheless, there are still significant contributions from clusters containing DME molecules, although their peaks are not resolved. It seems unlikely that the shoulder in the PES appearing at 270°C is caused by bare sodium clusters since bare sodium clusters are already present at 260°C, where there is no such shoulder observed in the PES. Furthermore, at 260°C in the case of DME clusters there are more and larger bare sodium clusters present than in the case of ammonia clusters at 250°C .

Furthermore, the PES of bare sodium clusters are known and do neither agree with the observed shoulder in the sodium DME spectra nor with the plateau in the sodium ammonia spectra. For sodium clusters Na_j with $j \leq 21$ atoms ionization threshold are reported to be above 3.3 eV.[159,160] Even for large sodium nanoparticles photoionization thresholds are reported to be at 2.6 eV,[161] which is still significantly above our measured onset. Therefore, the bare sodium clusters ob-

served in the mass spectra cannot explain the strong changes to the PES. However, one may consider the presence of sodium clusters solvated in DME and ammonia. It is very likely that there is a significant amount of clusters, actually consisting of sodium clusters with a few solvent molecules added. This assumption can be made since the bare sodium clusters are actually formed by solvent evaporation from highly-doped solvent clusters. Such solvated sodium clusters are expected to show lower electron binding energies than bare sodium clusters. This effect can be thought of in a similar way as the lowering of the ionization potential of a single sodium atom upon solvation, and is not related to a transition to a metallic state. The fact that the photoelectron threshold is lower in the highly doped DME clusters than in the case of highly doped ammonia clusters would agree with the expectations since the same trend is observed for single sodium atoms. The decrease in ionization energy upon solvation of a sodium atom is stronger for DME than for ammonia.[48]

Comparing the PES of the large sodium doped DME clusters at the highest oven temperatures (Figure 6.24) shows that the shoulder changes further. It develops into a peak, increases in intensity and shifts towards lower electron binding energies. This contradicts an explanation including solvated sodium clusters. The increase in oven temperature, increases the estimated sodium concentration, via the collision probability in the model discussed in section 6.2.2. Including the effect of solvent evaporation, which becomes more important for higher oven temperature, would even increase this effect of increasing sodium concentration. In reverse, this means the solvation of the sodium clusters would decrease, leading to an increase in the electron binding energy. The observed trend is, however, the opposite. Therefore the presence of solvated sodium clusters does also not explain the observed changes in the PES for high oven temperatures.

In the case of the large sodium doped ammonia clusters the two highest sodium oven temperatures correspond to estimated sodium concentrations of 8.8 MPM and 6.2 MPM (see Figure 6.10). This is roughly the same concentration range in which the TMS is observed for bulk solutions. Häsing et al.[145] reported concentration dependent photoelectron thresholds for bulk sodium ammonia solutions. For dilute solutions of 0.83 MPM he reported a photoelectron threshold of 1.42 eV that shifts to values in between 1.5 eV and 1.6 eV for metallic solutions between 10 MPM and 16 MPM. While the absolute values of the thresholds do not agree with our

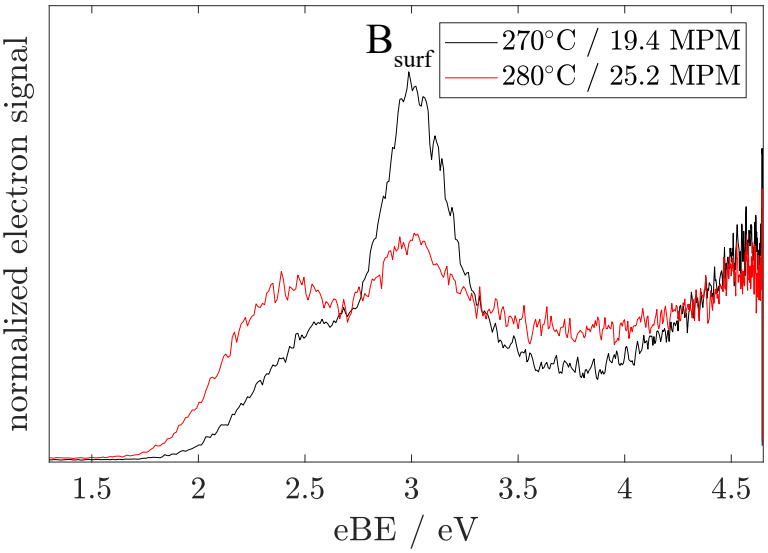

Figure 6.24: Photoelectron spectra of DME clusters containing 19.4 and 25.2 MPM sodium. At higher sodium concentration, the onset of the shoulder shifts towards lower electron binding energies and the shoulder changes to a more peak-like shape.

spectra, the overall shift observed is in the same energy range of 0.2 eV. Note that the absolute value is not expected to be the same, since Häsing was working on bulk solutions and not on nanoscale clusters. This means our experimental data indicates strong changes in the electronic structure of sodium ammonia clusters that do agree with an interpretation as the cluster-equivalent of the TMS in bulk sodium ammonia solutions. Nevertheless, it is not possible to give a final proof for this interpretation from our data alone.

In the case of large DME clusters the situation is more complicated because there is no bulk data to compare to, due to the insolubility of sodium in bulk DME. As a consequence, there is also no TMS in bulk sodium DME solutions. However, it is well known that in clusters it is possible to create supersaturated solutions. Whether it is possible to enforce a transition to a metallic state by confining increasing amounts of sodium atoms to a DME cluster is unclear. The lack of bulk data and theoretical predictions make it impossible at this stage to provide a final interpretation of the spectral changes in highly-doped DME clusters

6.6 Conclusion

Cluster measurements provide a route to study concentration dependent photoelectron spectra of sodium ammonia solutions. The same approach can be used for other alkali metals or solvents. For bulk solutions such measurements are still difficult due to the high vapor pressure of the solvents and the limited solubility in bulk. The observed strong changes in the PES of large, highly concentrated sodium ammonia clusters are in agreement with an assignment to a cluster analog of the TMS observed in bulk systems. The fact that similar effects could not be observed for cluster distributions with less than 160 molecules average cluster size provides an estimate for a minimum system size for which this phase transition can be observed. This is an intriguing result, since such system sizes are no longer completely out of the size range accessible by modern ab initio calculations. A final proof, however, of the interpretation as the cluster-analog of the TMS in bulk cannot be provided by cluster spectroscopy alone. A new and complementary approach to the photoelectron spectroscopy of sodium ammonia solutions is followed by researchers at the Fritz Haber Institute in Berlin. Initiated by our work, their study tries to use the liquid microjet technique for sodium ammonia solutions. A first important step is already taken, i.e. the step of performing photoelectron spectroscopy on a liquid jet of ammonia.[100]

The observation of an additional shoulder $B_{shoulder}$ for very high oven temperatures in large sodium DME clusters poses more questions. Since bulk DME does not dissolve sodium in any substantial amount, no similar effects were reported for bulk systems containing sodium and DME. At this point, we can thus not provide a final interpretation of the appearance of this shoulder at high sodium concentrations for DME clusters.

6. NON-METAL TO METAL TRANSITION IN SODIUM-DOPED CLUSTERS

Chapter 7
Magnetic selection of neutral sodium-doped clusters

7.1 Introduction

In bulk sodium ammonia solutions, spin pairing of solvated electrons occurs in a concentration range between 0.1 and 1 MPM.[38,45–47] It is unclear at which concentrations similar effects occur in clusters. It is expected that the concentration at which spin pairing occurs in small clusters depends on the system size. Note that at a given single cluster size only discrete values for the sodium concentration can be realized. A sodium concentration as low as 0.1 MPM can only be realized for clusters containing more than 1000 solvent molecules. The lowest average sodium concentration produced in chapter 6 was estimated to be 1.2 MPM. Although these clusters were all single-doped, the concentration is already in the range where bulk solutions show spin-paired solvated electrons. Nevertheless, these clusters contain single solvated electrons and cannot form spin pairs. As soon as the number of sodium atoms is increased from one to two, there is the possibility to either have electrons in spin paired singlet states or in unpaired triplet states. It is unclear whether it is possible to distinguish these singlet and triplet states by photoelectron spectroscopy, however, it should be feasible to distinguish the states via their magnetic properties.

The Zeeman effect describes the splitting of atomic or molecular levels in the presence of a static magnetic field. This splitting can be quantitatively described

by the potential energy

$$V_{\text{Zeeman}} = -\vec{\mu} \cdot \vec{B}, \tag{7.1}$$

given by the scalar product of the magnetic field $\vec{B}$ and the magnetic moment of an atom $\vec{\mu}$ given by

$$\vec{\mu} = -\frac{\mu_B \left(g_l \vec{L} + g_S \vec{S} \right)}{\hbar}. \tag{7.2}$$

μ_B is the Bohr magneton and g_l and g_S are the gyromagnetic ratios for the total orbital angular momentum $\vec{L}$ and the total spin angular momentum $\vec{S}$, respectively. $\hbar$ is the reduced Planck constant. Neglecting the contribution of the electron orbital angular momentum $\vec{L}$, the potential energy is given as

$$V_{\text{Zeeman}} = \frac{\mu_B g_S}{\hbar} \vec{S} \cdot \vec{B}. \tag{7.3}$$

Equation 7.3 is correct for the case of a sodium atom in its electronic ground state, because $\vec{L} = 0$ in this case. For a solvated electron in a sodium doped cluster, this is still a good approximation because the electron has mostly s-character. If the magnetic field responsible for the splitting is spatially inhomogeneous the particle will experience a force. This force caused by the inhomogeneous potential is defined as the negative gradient of the potential, i.e.

$$\vec{F} = \nabla \left(\vec{\mu} \cdot \vec{B} \right) = -\frac{\mu_B g_S}{\hbar} \nabla \left(\vec{S} \cdot \vec{B} \right) = -\mu_B g_S m_S \begin{pmatrix} \frac{\mathrm{d}B}{\mathrm{d}x} \\ \frac{\mathrm{d}B}{\mathrm{d}y} \\ \frac{\mathrm{d}B}{\mathrm{d}z} \end{pmatrix}. \tag{7.4}$$

Equation 7.4 assumes that at each position the spin quantization axis is parallel to the magnetic field, and that the spin component along this quantization axis can take values of $\hbar m_S$. For a molecular cluster containing a single sodium atom the total electron spin $S = 1/2$ and m_S can take values of $\pm 1/2$, corresponding to a high-field-seeking ($m_S = -1/2$) and a low-field-seeking ($m_S + 1/2$) state on which the force acts in direction of the increase and the decrease of the magnetic field, respectively. There is no force acting on a double-doped cluster in a singlet state, with $S = 0$ and $m_S = 0$. A double-doped cluster in a triplet state with $S = 1$ has three magnetic sub-levels described by $m_S = \pm 1, 0$. The levels with $m_S = \pm 1$ are again high-field-seeking ($m_S = -1$) and low-field-seeking ($m_S = +1$), while the state with $m_S = 0$ does not experience any force.

In this chapter we will describe a magnetic deflector for the study of sodium-doped clusters. It is similar to the one used in the famous experiment by Otto Stern and Walther Gerlach with which they proved the directional quantization of the electron spin.[162] Deflection of clusters using magnetic fields has been performed before.[163–168] However, these previous studies of magnetic properties were performed on metal clusters and not on non-covalently bound systems. Similar to the question of metalicity discussed in the previous chapter, the magnetic properties of such small metal clusters are governed by magic cluster sizes, and the addition or subtraction of just one atom can drastically change the properties of the cluster. The situation in solvent clusters containing solvated electrons is different from that since we do not expect such special effects for certain numbers of solvent molecules. Note that also electric fields can be used to deflect clusters according to their polarizabilities.[169–171] A magnetic deflection experiment for sodium-doped clusters coupled to a photoelectron VMI spectrometer and an ion TOF mass spectrometer may provide new insights into the spin pairing of solvated electrons. The present work reports on the first steps towards such an experiment. One of the future aims is to clarify whether one can distinguish singlet and triplet states, i.e. paired or unpaired solvated electrons, in photoelectron VMI measurements. Already the use of a magnetic deflector together with cluster mass spectrometry may provide insights on whether double-doped clusters are in singlet or triplet states. This may for example answer the question of the cluster size dependence of spin pairing effects in clusters, and how the corresponding concentrations compare to bulk data.

In this chapter we will describe the design and characterization of a magnetic deflection experiment for sodium-doped solvent clusters.

7.2 Design and experimental setup

7.2.1 Design process

The deflector was designed in collaboration with Alon Luski and professor Edvardas Narevicius at the Weizmann Institute of Science in Israel. The group from Weizmann Institute simulated the magnetic fields in the deflector, machined the parts of the deflector and designed and built most of the electronic circuits used to

operate the deflector. All other work, including incorporating the deflector into our setup and the theoretical and experimental characterization of the performance of the deflector, was performed in our group. The final design of the deflector and the experimental setup will be discussed in section 7.2.2. The performance expected from theory will be described in section 7.3, and the experimental characterization will be discussed in section 7.4.

7.2.2 Deflector and experimental setup

7.2.2.1 Deflector setup

The assembled deflector is 21 cm long (see Figure 7.1). The magnetic fields are created by three electromagnets (Figure 7.2), which are each 7 cm long and mounted onto a liquid-cooled cold plate made from aluminum (Figure 7.3). Each electromagnet consists of a metal body on which a coil, made from 15 turns of kapton insulated copper wire, is mounted. To protect the wires mechanically and to increase heat conduction from the wires to the cooled metal parts the wires are set in epoxy. A CAD drawing of the metal body can be found in Figure B.2 in the appendix B.1. The metal body is machined from magnetic steel. The core of the electromagnet is 5.6 cm long and 2.5 mm wide. At both ends of each electromagnet, the wires are bent upwards, i.e. out of the plane of the coil (see right part of Figure 7.2). In this 7 mm long area on each side of the electromagnets the fields perpendicular to the molecular beam direction will be reduced.

The molecular beam passes right under the cores of the electromagnets in a triangular flight channel that is formed by a 21 cm long pole piece (Figure 7.1). The flight channel is 3.75 mm high vertically, measured from the tip of the triangular cross section to the core of the electromagnetic coil. At the widest point of the triangular cross section, the channel is 5.5 mm wide horizontally. The spacing between the pole piece and the epoxy surface of the coils is 0.9 mm, see also the CAD drawing in B.1. To monitor the temperature of the deflector during operation, a thermocouple is pinched between two of the coils. The original plan was to use cooling water from a closed cycle cooling system to cool the deflector. This water is circulating with 2 bar pressure and has a temperature of 18°C . It turned out during initial testing that this provided insufficient cooling. After a few tests the cooling was switched to a mixture of 30 % glycol in water, circulated

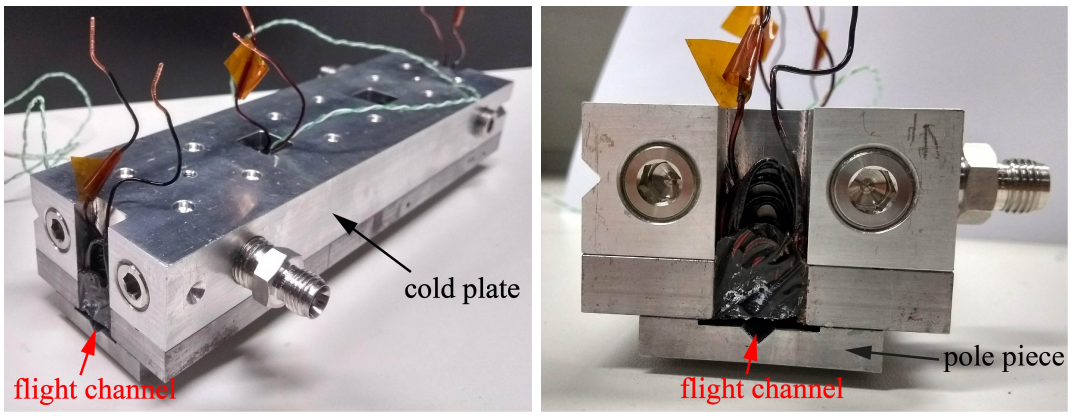

Figure 7.1: Fully assembled deflector. The triangular flight channel is indicated. The additional green-white cable in the left picture is a thermocouple.

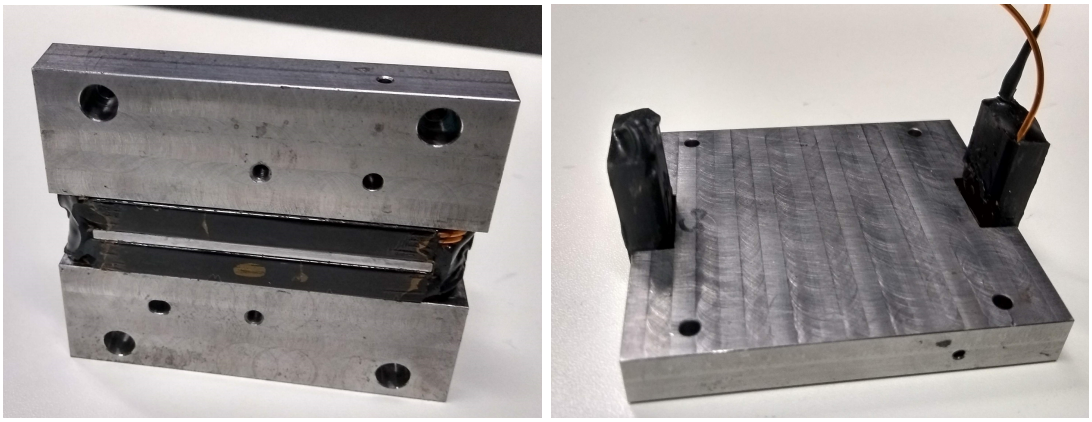

Figure 7.2: Photographs of a bottom (left) and top (right) view of an electromagnet. It is 7 cm long and the wires (not visible under the epoxy) are wound around the 5.6 cm long core and bent upwards at the ends of the electromagnet (right part).

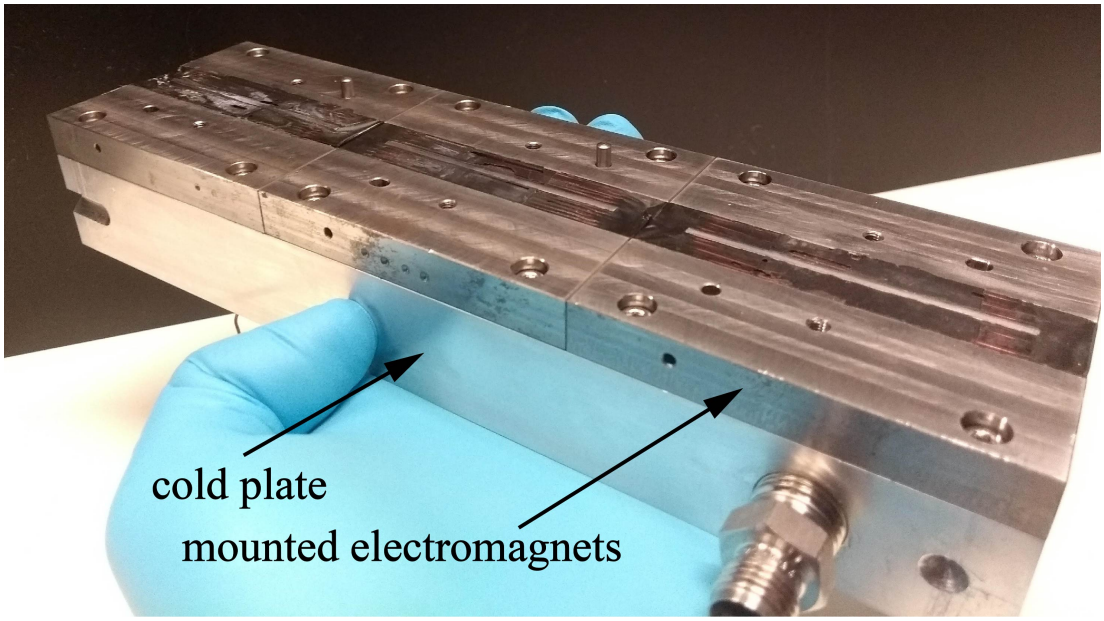

Figure 7.3: Photograph of three coils mounted on the stainless steel cold plate. The coolant connection can be seen in the front on the right side.

by a closed-cycle chiller at -5 °C .

7.2.2.2 Electronic design of the deflector

Continuous operation of a strong electromagnet in vacuum is not possible due to the resistive heating in the coils. Therefore it is necessary to operate the deflector in a pulsed fashion. Figure 7.4 shows a simplified sketch of the electronic circuits to operate the deflector. A full schematic of the surge current generators (SCG) is shown in the appendix B.2. Each electromagnet is driven by an individual SCG. The surge current generators are controlled by trigger pulses that are used to switch thyristors. A thyristor is a bistable switch that can be closed using a trigger pulse and opens again as soon as the current through the switch falls below a threshold value. The charging trigger starts the process of charging the capacitors within the SCGs. After the discharge trigger, the capacitors of the generators are discharged, emitting surge current pulses to the electromagnets of the deflector. The discharge of generators through the inductive coils of the electromagnets results in a negative voltage on the capacitors. This voltage is reset to a slightly positive value by the recovery trigger. A typical trigger pulse scheme is shown in Figure 7.5 and the corresponding course of the voltage on one of the capacitors in the SCGs is

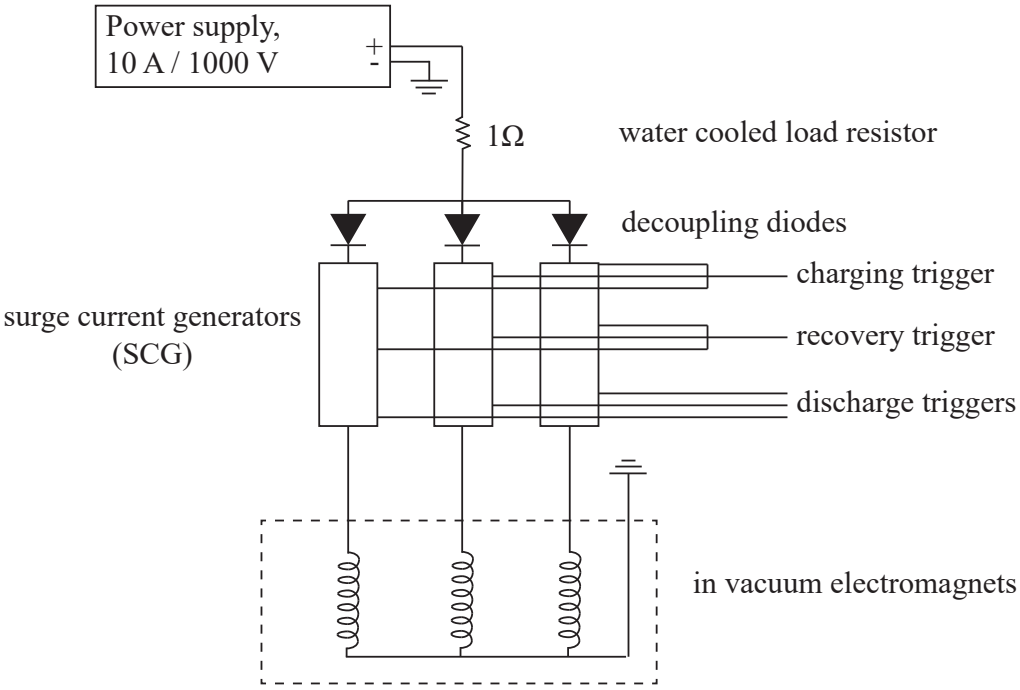

Figure 7.4: Simplified sketch of the electronic circuits used to operate the deflector. Details of the surge current generators are shown in the appendix B.2. Adjustments to the electronic system are discussed in the text.

shown in Figure 7.6. The charging and recovery trigger are supplied to all three surge current generators synchronously. The discharge triggers can be supplied to each SCG with a relative delay, effectively pulsing each electromagnet with a relative delay. The discharge and recovery triggers are single, 20 μs long boxcar voltage pulses, while the charging trigger consists of a series of 30 such pulses delayed by 100 μs each. The use of many charging triggers compensates for a premature opening of the thyristor due to instabilities in the charging current. Such instabilities can occur due to the high power load on the power supply during the charging process. Note that the water cooled 1 Ω resistor in Figure 7.4 is ideally the only resistor in the charging of the capacitors. Therefore, the high resulting charging currents reach the output limit of the power supply. The surge current pulse from the SCG to the electromagnets are designed to be about $\sim$200 μs long pulses with a flat top profile. Running the surge current generators with a 500 V supply voltage produces surge currents of about 1000 A. In reality the pulses do not show perfectly flat tops, but rather have a plateau width of about 180 μs and a FWHM of about 250 μs. Note that the time necessary to charge the SCGs (rising

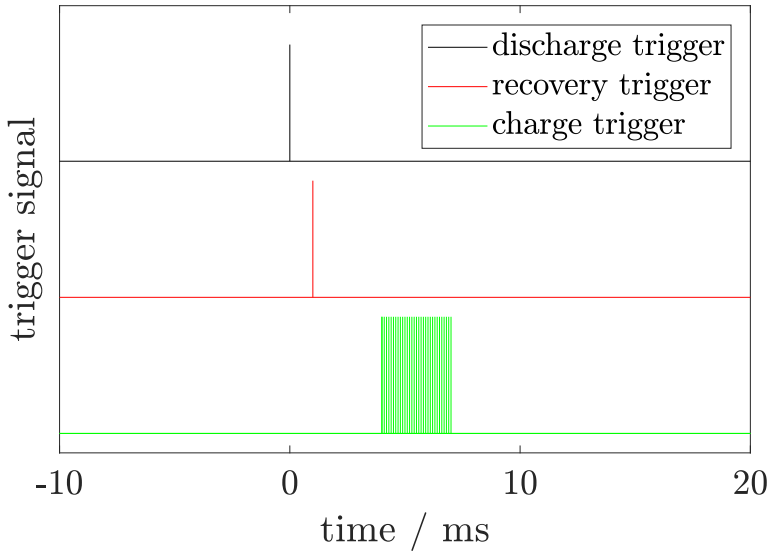

Figure 7.5: Schematic representation of the trigger sequence for the surge current generators. The discharge trigger (black) initiates the surge current pulse, the recovery trigger (red) resets the voltages on the capacitors to a slightly positive value and the charging triggers (green) restart the charging process.

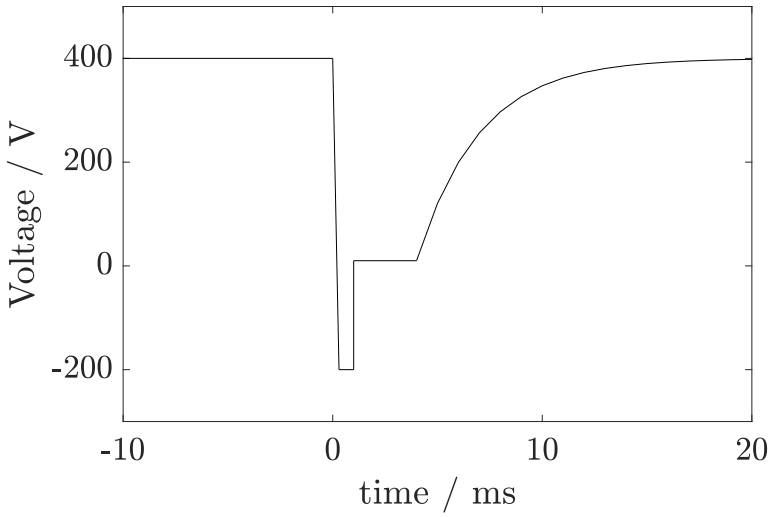

Figure 7.6: Schematic representation of the voltage over one of three capacitors in the surge current generators, for the trigger scheme shown in Figure 7.5. The surge current is emitted during the pronounced voltage drop.

part in Figure 7.6) is strongly dependent on the type of power supply used. In our experiment the power supply used was a TDK-lambda genesis 1000-10, with a maximum output voltage of 1000 V and a maximum output current of 10 A. During the initial testing of the deflector and its electronics it was found, that the high loads on the power supply resulted in unstable charging behavior, related to the current limitations of the power supply. This lead to the situation that the surge current generators were not always reliably charged to the set voltage. This problem was fixed by introducing an additional capacitor circuit before the 1 Ω load resistor, and some additional resistors after the 1 Ω load resistor. These changes reduced the load on the power supply at the cost of slightly increased charging times.

7.2.3 Overall experimental setup

The overall experimental setup is shown schematically in Figure 7.7 (a). The deflector chamber, housing the deflector, elongates the cluster flight path between the sodium oven and the ionization region by about 50 cm, compared to the setup used for the studies discussed in Chapter 6. For simplicity, the first characterization of the deflector was performed using cluster mass spectrometry, rather than photoelectron spectroscopy. Therefore the ion time of flight region was not shielded by a μ-metal and the detector was exchanged for a smaller detector optimized for ion detection. The deflector is mounted on two translation stages to allow exact alignment parallel to the molecular beam. The location of the deflector (Figure 7.7 (b)) is in the front part of the deflector chamber, to leave a 23 cm free-flight region after the deflector. In addition to the skimmer between the source and the oven chamber, a further skimmer (detection skimmer) was introduced between the deflection and the detection chambers. A third skimmer (entrance skimmer) can be mounted in front of the deflector to start the deflection experiment with a well defined molecular beam. During the test measurements different skimmer sizes were used, and experiments were also performed without an entrance skimmer. It was found that the main effect of reduced skimmer sizes is only a signal reduction but no improvement of the cluster deflection. It is clear that the alignment of the deflector relative to the molecular beam is crucial. Experimentally, good alignment was achieved by first aligning the molecular beam through the skimmers without the deflector mounted in the chamber. After that, an alignment laser beam was

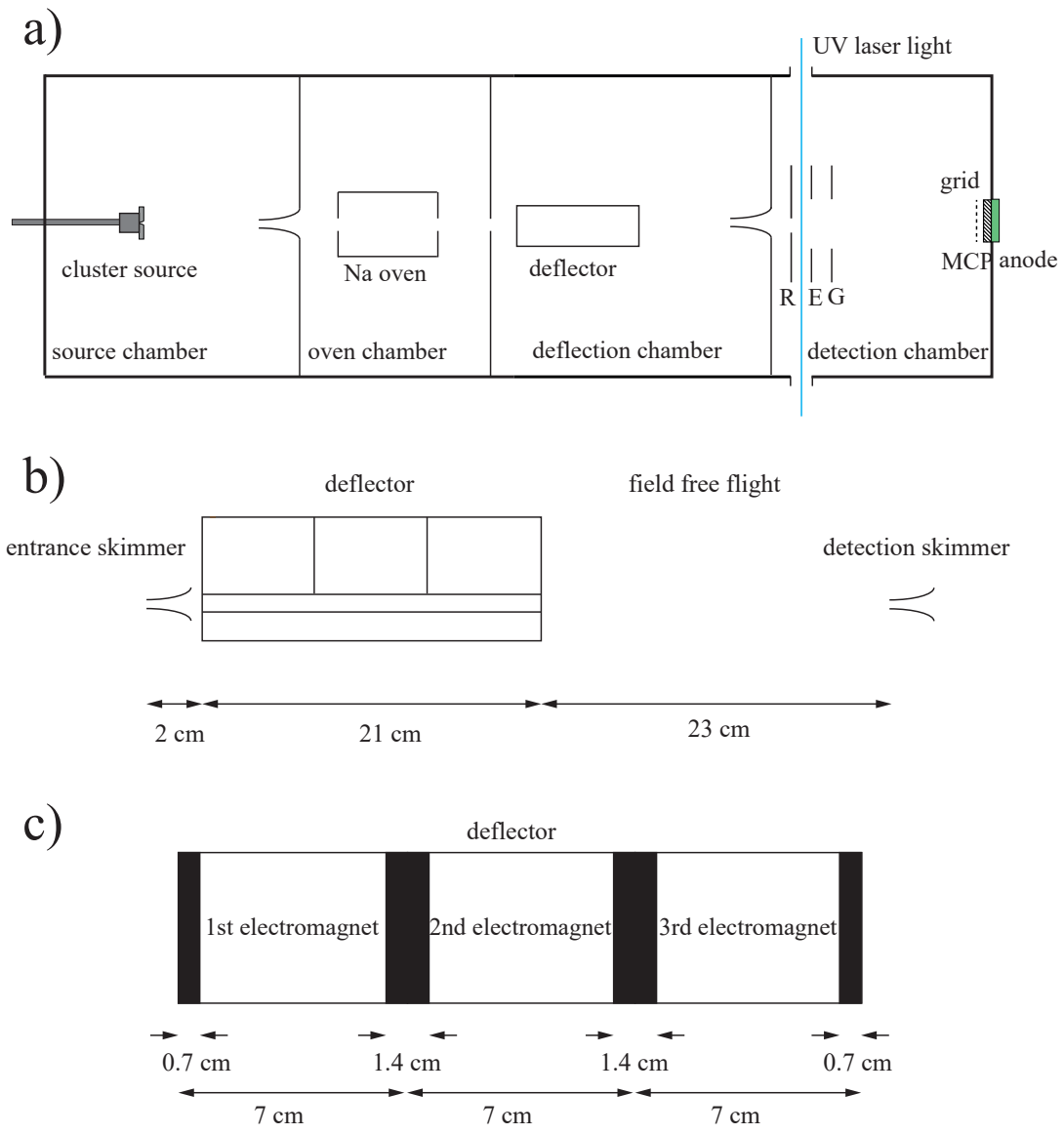

Figure 7.7: a) Schematic representation of the setup. b) Detailed view of the distances in the deflection chamber. c) Detailed view of the deflector. Black regions indicate the areas where the wires of the coils bend upwards, creating a reduced magnetic field.

aligned to the molecular beam path, through the skimmers from the detector side. In a third step, the deflector was mounted and aligned in the deflector chamber in a way so that it did not clip the aligned alignment laser.

Most deflection experiments were performed on sodium-doped ammonia clusters. These clusters were created in a neat continuous expansion of ammonia and doped in a sodium oven. Additional test measurement were performed on sodium doped DME and H_2O clusters. Pulsed expansions using a Parker valve were also tested. Furthermore characterization measurements were also performed on an effusive beam of sodium atoms created directly from the sodium oven, without the use of a supersonic gas expansion. The sodium-doped clusters were photoionized using 266 nm light and the sodium atoms were photoionized using 212 nm light. Photoions were extracted using optimized time-of-flight mass spectrometry settings. Since the magnetic fields in the deflector are switched on for only a short time of $\sim$200 μs, the current pulse needs to be appropriately timed. Therefore, a deflection measurement consists of measurements with different delays between the deflector field pulse and the laser pulse. The relative timing is adjusted by variation of the deflector timing. For each deflector timing a mass spectrum is recorded and the ion signal corresponding to a certain cluster mass is integrated (see Figure 7.8). The ion signal as a function of the deflector timing is given relative to the signal level in a mass spectrum that does not show any deflection, e.g. for a deflector pulse after the laser pulse. This means ion signals without deflection are normalized to one, and ion signals showing deflection lie between one and zero.

7.3 Theoretical characterization of the deflector

7.3.1 Simulations

To predict the performance of the deflector, a molecular dynamics (MD) approach was used to simulate the trajectories of sodium doped clusters through the experimental setup. The force field for the MD simulation is defined by the magnetic field gradients (Figure 7.9), obtained from a Comsol simulation assuming a 2D model of the deflector cross section and a DC current of 1000 A. The magnetic field gradient in the z direction deflects particles in either the positive or negative z direction, depending on m_S. In the center of the flight channel (x=0), the field gradient

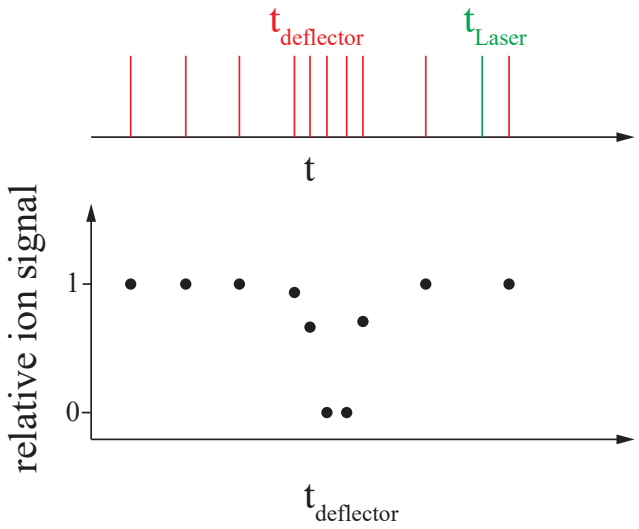

Figure 7.8: Schematic of the measurement procedure. The timing of the deflector is varied relative to the timing of the laser. At each deflector timing the ion signal is recorded.

along the z axis is more or less constant. The magnetic field gradient along the x axis is zero in the center of the flight channel (x=0) and increases in magnitude towards the pole piece. The gradient in x direction acts in a deflecting way on one spin component, while it acts as a focusing element for the other spin component. The forces are only applied to particles in the deflector while the deflector is pulsed. The pulses are defined by 200 μs long boxcar pulses. The amplitude of the forces applied during this pulse are calculated according to Equation 7.4. Figure 7.9 shows the magnetic field gradients corresponding to a current of 1000 A. To simulate the performance of the deflector at reduced current strength, the forces can be scaled by a factor between zero and one. A factor of 0.5 corresponds thereby to a current of 500 A. Outside of the 200 μs time window of the current pulse and outside of the deflector no forces are applied. Furthermore the fields are assumed to be constant along the molecular beam direction. Therefore there are only forces acting perpendicular to the initial molecular beam direction (i.e. in the z and x directions), and these forces do not depend on the position along the molecular beam. Similar to the experiment, the three electromagnets can be pulsed individually with a time delay between the field pulses. The spatial setup of the simulation is displayed in Figure 7.7 (b). The deflector is further divided in sections with high magnetic fields and sections with low magnetic fields on each

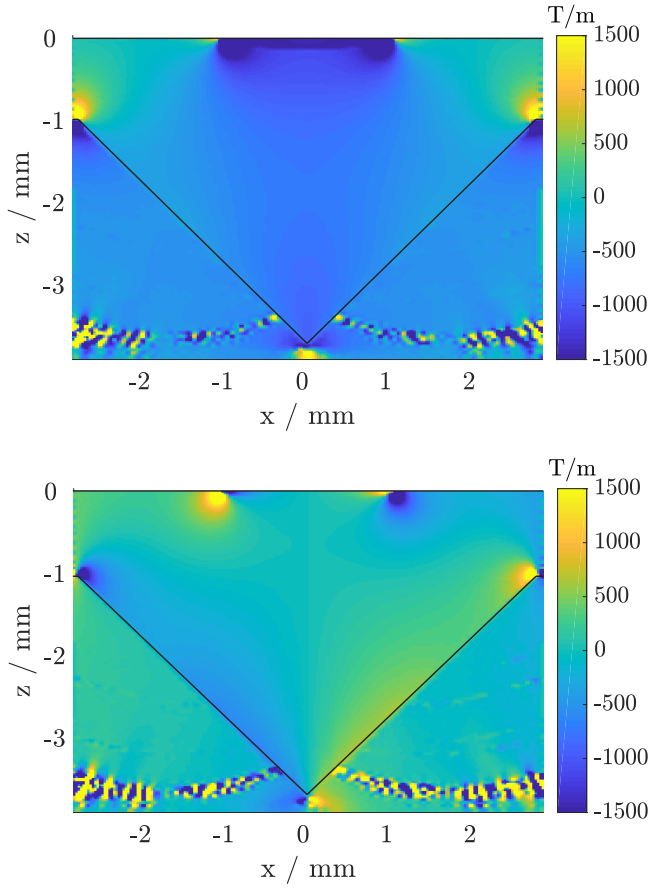

Figure 7.9: z (upper part)and x (bottom part) component of the gradient of the calculated magnetic flux density, within the triangular flight channel. The channel walls are indicated as black lines.

side of each electromagnet (see Figure 7.7 (c) and Figure 7.3). Since it is difficult to estimate the magnetic fields in the region of low magnetic field, we chose a conservative estimate of the performance by setting the fields in these regions (marked black in Figure 7.7 (c)) to zero.

The trajectories are started 2 cm before the deflector. The deflector is 21 cm long and the free-flight region between the deflector exit and the detection skimmer is 23 cm. The starting conditions for the trajectories are defined by the cluster mass, the spatial distribution of the clusters defined by the molecular beam profile and the initial molecular beam velocity. The molecular beam profile is defined as a Gaussian beam, clipped by the entrance skimmer. The molecular beam velocity can either be given as a single cluster velocity, or as convolution of a single velocity with a Maxwell-Boltzmann distribution. The latter was used to account for the effect of a molecular beam velocity distribution of finite width. Particles that collide with the deflector walls are considered "lost". Trajectories of particles that do not collide with the deflector walls end after the second field free region in the plane of the detection skimmer. In the case of a single molecular beam velocity, all particles need the same time to travel from the starting to the detection point. However, in the case of a finite width of the molecular beam velocity distribution, the flight times for different clusters vary. In this case the trajectory starting points are shifted in time, so that all particles arrive at the plane of detection at the same time. This simulates the experimental detection by ionization using a short laser pulse, i.e. only clusters that arrive in the ionization region at the same time can be detected. In the detection plane, the position of the particles is determined to obtain a molecular beam profile. Example beam profiles for a simulation of sodium doped ammonia molecules are shown in Figure 7.10. In the experiment only clusters that are transmitted through the detection skimmer are detected. In the simulations it is sufficient to study the determined molecular beam profiles in the plane of the detection skimmer for the three cases of $m_S = \pm 1/2$ and $m_S = 0$. The number of particles transmitted through a skimmer can be determined as the number of particles that lie within a circle of a given radius in the beam profile. Some example circles corresponding to typical skimmer sizes are drawn on top of the beam profiles in Figure 7.10. In Figure 7.11 the ion signal, i.e. the fraction of particles transmitted through a skimmer, is shown as a function of the skimmer size for the three molecular beam profiles shown in Figure 7.10. To obtain

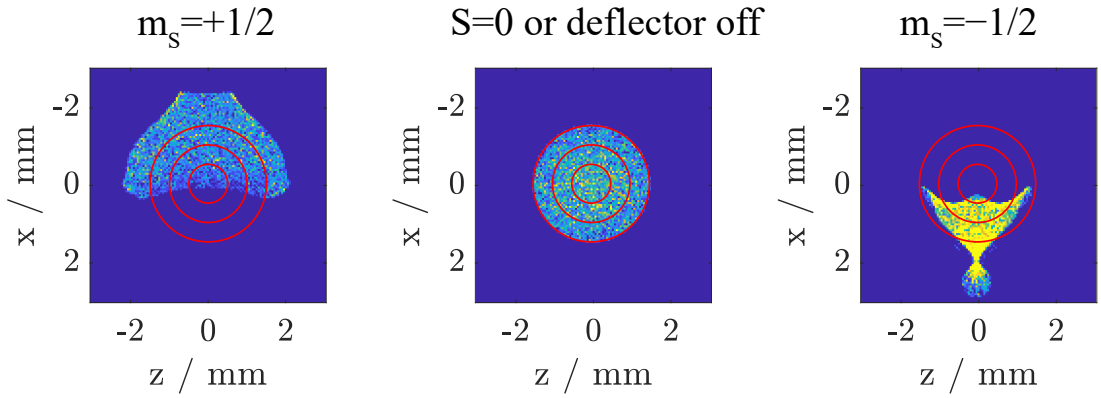

Figure 7.10: Simulated profile of a molecular beam consisting of sodium doped ammonia molecules, deflected with a imperfect deflector timing. The profile is calculated 23 cm after the exit of the deflector, in the plane of the detection skimmer. Red circles indicate typical skimmer diameters of 1, 2 and 3 mm diameters.

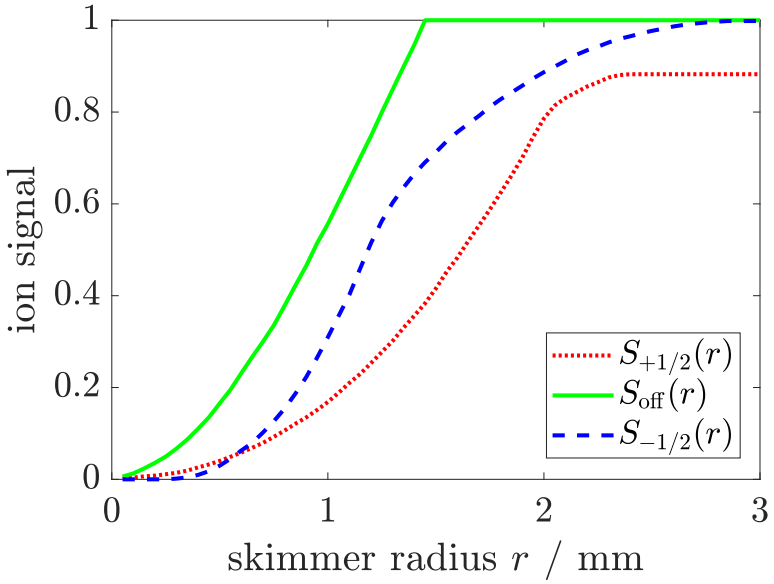

Figure 7.11: Example for evaluated deflection simulation. A relative signal of $S_{+1/2}(r)/S_0(r) = 0.4$ means that one expects a relative signal reduction to 40% of the initial signal when operating the deflector.

relative ion signals (bottom part of Figure 7.8) from the simulated ion signals in Figure 7.11 we have to divide the curves labeled as $S_{\pm 1/2}(r)$ by the curve $S_{\text{off}}(r)$. The resulting curve gives the ion signal relative to the case of no deflection for all possible skimmer sizes. Choosing the skimmer radius corresponding to the experimental setup gives the predicted experimental signal for the chosen settings.

7.3.2 Predicted performance of deflector

7.3.2.1 Effect of cluster size

Simulation results for $Na(NH_3)_n$ for n=1,5,10 are shown in Figures 7.12 to 7.14. The figures show the beam profiles simulated in the plane of the detection skimmer for different deflector delays. The bottom parts of the figures show the calculated relative ion signal as a function of the deflector timing for a skimmer diameter of 2 mm. The simulations for the different cluster masses assume a molecular beam velocity of 1000 m/s and magnetic fields corresponding to a current of 850 A. The three electromagnets were pulsed simultaneously with a pulse length of 200 μs. Comparison between the three figures shows decreasing deflection for increasing masses, which is expected. For the sodium doped monomer, $NaNH_3$, the simulations predict complete deflection, i.e. a signal decrease to zero, for both spin components. This complete deflection is found over a range of deflector timings of 300 μs. For deflector timings outside this 300 μs time window, the expected signal increases back to one, indicating no deflection at all. For $Na(NH_3)_5$ we find almost complete deflection for both spin components, but only for a narrow window of deflector timings. This indicates, that for heavier clusters the deflector timing needs to be near to its optimal value to achieve good deflection. For $Na(NH_3)_{10}$ at the given settings, only weak deflection can be achieved for one spin component. The spin component which is deflected towards the tip of the triangular cross section of the flight path is not deflected significantly. This is an effect of the geometry of the fields created. For some combinations of deflector timing, cluster mass and skimmer radius, this effect can also lead to an increase in signal (relative signal >1), since there are some slight focusing effects towards the tip of the triangular shape. Note that for the used 2 mm skimmer diameter, even in the case of non magnetic particles, not all simulated particles pass through the skimmer. Since we cannot experimentally distinguish between the two magnetic components in the mass spectrometric detection, we will discuss the average deflection of the two components. This means we will discuss the average of the black and the red curves in Figures 7.12-7.14.

Figure 7.12: Simulated molecular beam profiles for $NaNH_3$ for different deflector timings, at the position of the detection skimmer. All profiles show a range of ±3 mm around the center of the detection skimmer. The signal traces in the bottom panel assume a detection skimmer of 2 mm diameter.

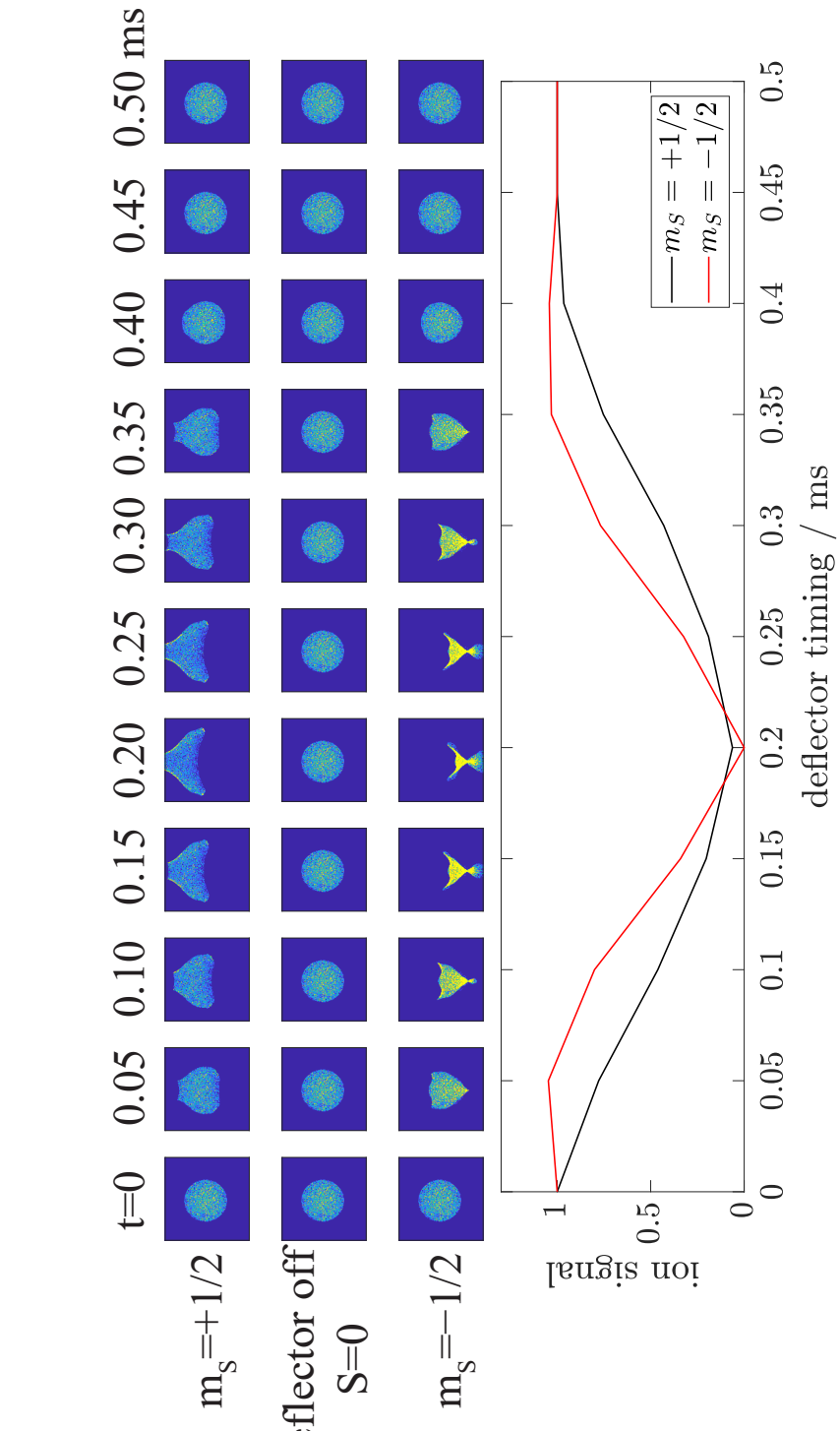

Figure 7.13: Simulated molecular beam profiles for $Na(NH_3)_5$ for different deflector timings, at the position of the detection skimmer.All profiles show a range of ±3 mm around the center of the detection skimmer. The signal traces in the bottom panel assume a detection skimmer of 2 mm diameter.

Figure 7.14: Simulated molecular beam profiles for $Na(NH_3)_{10}$ for different deflector timings, at the position of the detection skimmer.All profiles show a range of ±3 mm around the center of the detection skimmer. The signal traces in the bottom panel assume a detection skimmer of 2 mm diameter.

7.3.2.2 Effect of molecular beam velocity

The effect of the molecular beam velocity on the deflection of clusters is shown in Figure 7.15. The force field was scaled to correspond to a current of 850 A, and the individual magnets were pulsed simultaneously. It is observed that for slower molecular beams more cluster deflection is achieved. The higher flight time of slower molecular beams results in a longer residence time in the deflector, which results in a higher velocity perpendicular to the molecular beam direction. In addition, the longer flight time between the deflector and the detection skimmer further increases the achieved displacement perpendicular to the molecular beam direction. Also at slower molecular beam velocities the deflection is less sensitive to the exact setting of the deflector timing. For molecular beams faster than 1000 m/s complete deflection is only achievable for the smallest clusters.

If the flight time through the deflector exceeds the length of the current pulse (i.e 200 μs) a delay between the current pulses in the individual electromagnets can improve the observed deflection. Typical flight times through the 21 cm long deflector for different molecular beam velocities are given in Table 7.1. Figure 7.16 compares the deflection for a $Na(NH_3)_{10}$ cluster traveling at a velocity of 700 m/s with and without a delay of 100 μs between successive electromagnets. It is observed that this 100 μs delay can increase the obtained deflection in this case from 75% to 100%.

7.3.2.3 Effect of field strength

As discussed in section 7.1 the forces acting on the clusters in the deflector are proportional to the magnetic field gradients, which are proportional to the magnetic fields, which in turn are proportional to the amplitude of the current pulses through the electromagnets. Simulations, corresponding to running the deflector with reduced current pulses were performed using different scaling factors for the

velocity v / ms^{-1}	flight time t / μs
700	300
1000	210
1300	162

Table 7.1: Flight times of clusters with typical velocities through the 21 cm long deflector. The current pulses through the electromagnets are 200 μs long.

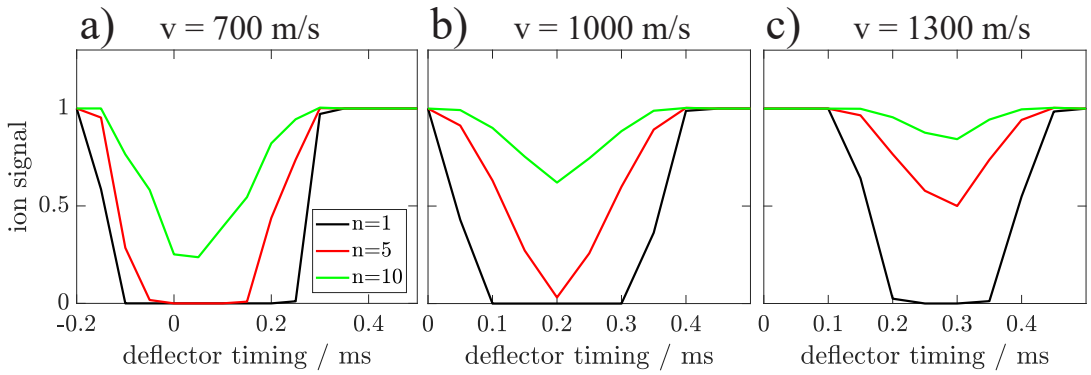

Figure 7.15: Dependence of deflection behavior on molecular beam velocity. Faster molecular beams reduce the time of flight needed to pass the deflector and therefore reduce the deflection. Results are shown for clusters of n=1 (black), n=5 (red) and n=10 (green) ammonia molecules.

force fields. The results of these simulations are summarized in Figure 7.17. These simulations were performed assuming a molecular beam traveling at 1000 m/s, and the electromagnets were pulsed with a delay of 50 μs. It is observed that a force field corresponding to reduced currents reduces the achieved deflection significantly. The reduction of the achieved deflection with decreasing fields is more severe for larger clusters. The sodium doped ammonia monomer should still be completely deflected by fields corresponding to currents below 600 A.

7.3.2.4 Effects of skimmer size and alignment

Inaccuracies in the alignments of the molecular beam through the deflector may have a significant effect on the deflection behavior as well. There are many possible deviations from perfect alignment, of which we will only discuss a few here. Assuming perfect alignment of the molecular beam with respect to the skimmers of the experiment, it is still possible that the deflector is not perfectly aligned onto the molecular beam axis. This would result in a slight offset of the molecular beam within the deflector. This would lead to a reduction in the observed deflection since the gradient of the magnetic field are strongest in the center of the flight channel through the deflector. Such a misalignment would most likely also be accompanied by significantly reduced signal levels because the deflector would block parts of the molecular beam. Another kind of inaccuracy can be the imperfect position of a skimmer. For the source or entrance skimmer this would only have

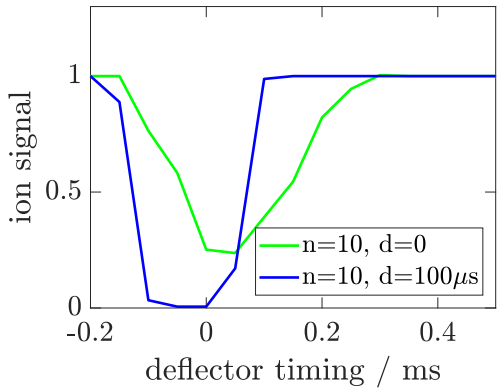

Figure 7.16: Comparison of the simulated deflection of $Na(NH_3)_{10}$ traveling at a molecular beam velocity of 700 m/s. While in the case without delay between the individual coils the maximum achieved deflection is 75%, 100% deflection can be achieved for a 100 μs delay between successive coils.

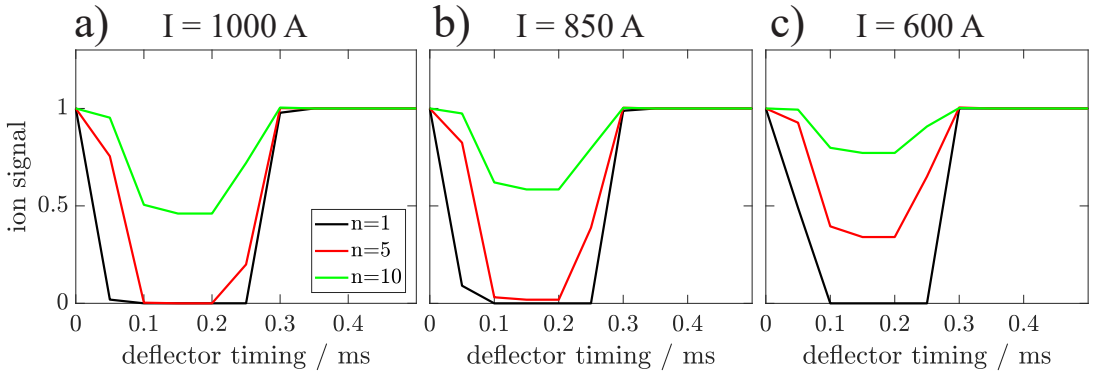

Figure 7.17: Dependence of deflection behavior on the driving current, for three different cluster sizes.

a reduction of the signal levels as a consequence. For the detection skimmer this could, however, strongly influence the deflection behavior. Consider for example the molecular beam profiles shown in Figures 7.12-7.14. A displacement of the detection skimmer away from the center of the images (away from perfect alignment) can have a variety of different effects on the obtained deflection behavior.

Also the size of the detection skimmer can be expected to have a strong effect on the achieved deflection. As example the effect of different skimmer diameters on the deflection of a $Na(NH_3)_{10}$ cluster traveling with 1000 m/s is shown in Figure 7.18. The applied forces correspond to a current of 1000 A, and the consecutive magnets are pulsed with a delay of 50 μs. It is found that reducing the skimmer diameter from 2 mm to 0.5 mm increases the deflection from 55% to 87%. Note that the total signal scales in first approximation with the square of the skimmer radius. Therefore the improvement of the expected deflection comes at the cost of reduced signal levels for smaller skimmers.

7.3.2.5 Summary

The simulations predict that deflection of single-doped ammonia clusters for $n \leq 10$ molecules is possible with the designed deflector. Deflection is expected to work best for slow molecular beams with velocities below 1000 m/s. The delays between the pulses of successive electromagnets need to be optimized for a given molecular beam velocity. For larger clusters above $\sim$100 amu in mass, deflection is expected to be difficult to achieve if the molecular beams travel at 1000 m/s or faster, or if currents of 1000 A cannot be achieved experimentally. For clusters with masses below $\sim$100 amu complete deflection should also be possible for such imperfect conditions.

7.4 Experimental characterization

7.4.1 Repetition rate and data acquisition times

In the current setup the deflector can be operated at a repetition rate of 2 Hz, using currents of up to 850 A. The limitation of the repetition rate has currently two reasons. The first one is the time needed to finish the charging of the surge current generators. This charging time was slightly elongated by the modifications of the

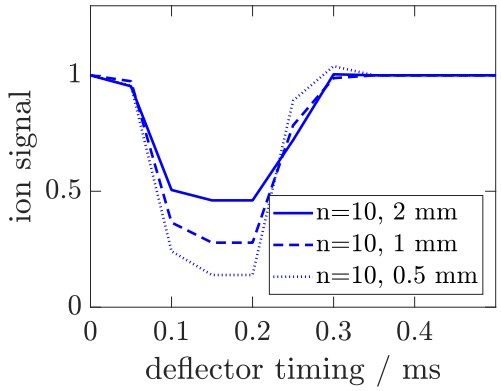

Figure 7.18: Effect of the skimmer size on the deflection of $Na(NH_3)_{10}$ traveling at 1000 m/s. The deflector was simulated with a 1000 A current and the delay between coils was 50 μs. Skimmer sizes in the legend are given as diameters.

electronic setup that were necessary to reduce the peak load on the power supply. The heating of the electromagnets is the second factor limiting the repetition rate. The deflector temperature as a function of the used current amplitude is shown in Figure 7.19. While cooling the deflector with water glycol mixture at -5°C running the deflector with a repetition rate of 2 Hz and currents of 800 A heats the electromagnets to 55°C , operating the deflector at higher temperatures does not seem reasonable. Working at higher deflector temperatures could potentially lead to outgassing of the epoxy or damage to the electromagnets. Higher temperatures also lead to an increase in the resistivity of the electromagnetic coils and therefore to further increased heat production. Furthermore it is unclear whether the measured temperature is close to the temperature of the hottest parts of the deflector. Therefore the measurement is only an estimate of the temperature of the copper wires.

A repetition rate of 2 Hz limits the data acquisition considerably. The mass spectra discussed in Chapter 6 were averaged for 2000 laser shots at 20 Hz. The deflector setup works with significantly lower signal levels, and therefore reduced signal to noise ratios. The main reason for the reduced signal levels is the increased distance between the cluster source and the ionization region. Furthermore, the repeated skimming of the molecular beam and possibly clipping of the molecular beam on the deflector contribute as well to the signal reduction. Therefore it would be desirable to average the mass spectra for at least 2000 laser shots as well. However, at 2 Hz repetition rate this measurement would take more than 15

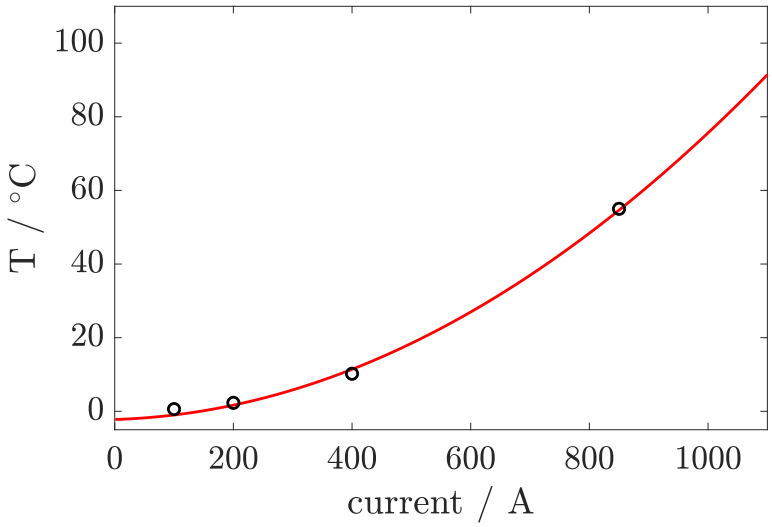

Figure 7.19: Dependence of the deflector temperature on the current. Temperatures are measured with a thermocouple in between two of the electromagnetic coils. The red solid lines shows a quadratic fit to the measured data values.

minutes per mass spectrum. Bearing in mind that an effective characterization of a set of parameters requires the measurement of many mass spectra, such long data acquisition times are problematic. To be able to cover a sufficient parameter range in a useful time, we chose to reduce the signal to noise ratio in the mass spectra by reducing the number of averaged laser shots to 500. This trade off reduced the measurement time to about 4 minutes per mass spectrum but increases the relative uncertainty in the ion signals.

7.4.2 Deflection of an effusive sodium beam

Test measurements were performed on an effusive beam of sodium atoms, produced by the sodium oven at 265°C . Photoionization was performed with a 212 nm laser pulse and ions were detected in a time of flight mass spectrometer. The velocity distribution of sodium atoms follows a Maxwell-Boltzmann distribution (see Figure 7.20), and for 265°C the most likely velocity is around 625 m/s. Since the sodium atom is lighter than sodium doped clusters, good deflection is expected for sodium atoms traveling at a single well defined velocity, even at low magnetic fields. For a broad velocity distribution this is no longer the case. The experimental deflection results for zero delay between the pulses in the individual electromagnets

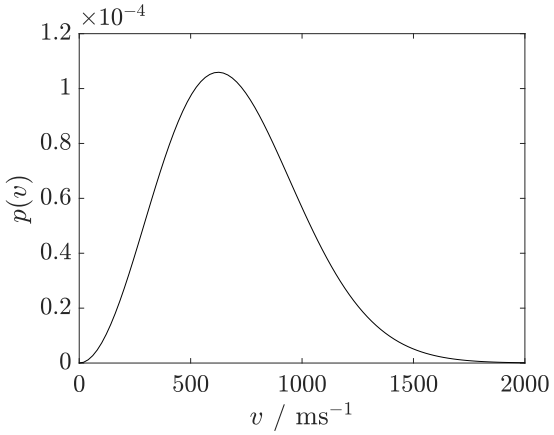

Figure 7.20: Maxwell-Boltzmann distribution for sodium atoms at 265°C .

and varying field strengths are compared to simulations in Figure 7.21. Only partial deflection of the sodium beam was observed. This partial deflection is also reproduced by the simulations, which agree well with the experimental measurements. The reason why the signal cannot be deflected completely is the broad velocity distribution. The effect of the broad velocity distribution can be understood by considering two sodium atoms traveling at 500 m/s and 1000 m/s, respectively. Note that these are not extreme velocities in the distribution shown in Figure 7.20. The deflector entry is about 44 cm away from the ionization region. This means the atom traveling at 1000 m/s enters the deflector 440 μs before being ionized by the laser pulse. At this time, the atom traveling at 500 m/s has already left the 21 cm long deflector. Therefore, there is no timing (assuming zero delay between the coils) at which the electromagnets could deflect both atoms. The increase in deflection with increasing current (or magnetic field strength) can be understood as a reduction of the time necessary to significantly accelerate a sodium atom. To clarify this effect we have also measured deflection for different delays between the electromagnets. The results of these measurements are shown together with corresponding simulations in Figure 7.22. The simulations are generally in good agreement with the measurements. The slightly worse deflection that the simulations predict for the case of a 90 μs delay lies within the uncertainties of the measurements. The blue symbols in the bottom right plot of Figure 7.22 shows the signals for the sodium dimer, obtained from integrating the corresponding peak in the mass spectra. There is no deflection expected in this case since the sodium dimer has a singlet (diamagnetic) ground state. This data set gives an impression

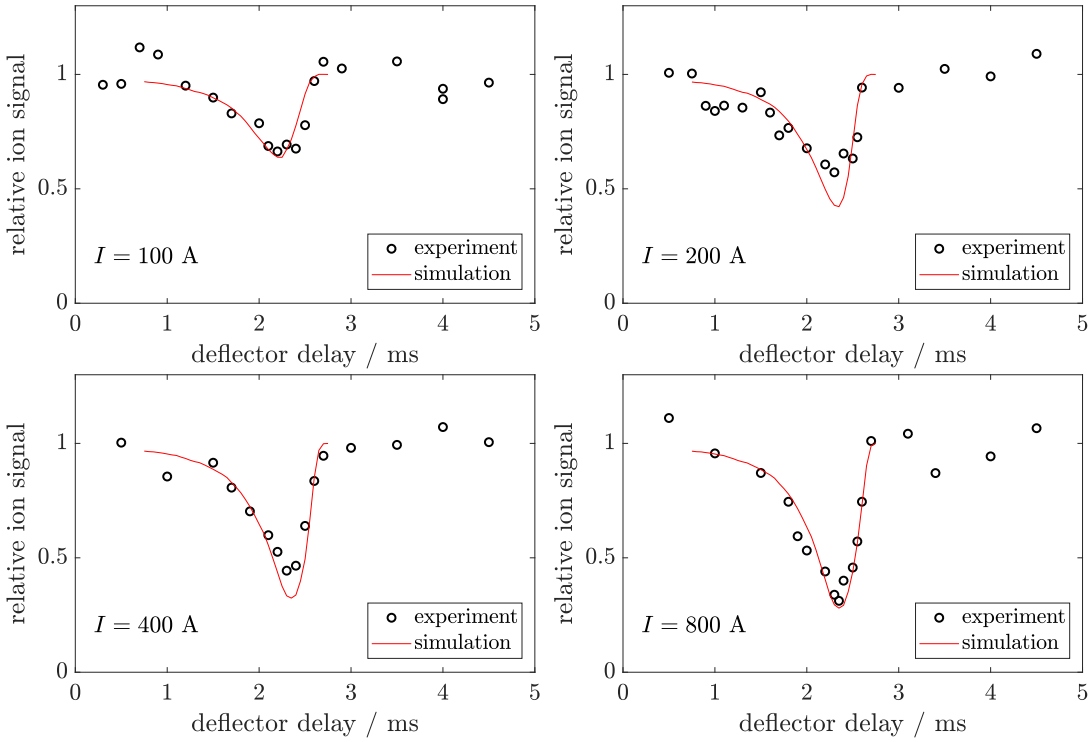

Figure 7.21: Deflection curves for effusive sodium beams with different current settings and zero delay between the pulses in consecutive electromagnets. Black circles show experimental measurements, while the red curve shows simulations.

of the uncertainties of the measurements. Note that it is possible that the dimer signal is less stable over time than the sodium atom signal since it may be more sensitive to slight fluctuation of the conditions in the sodium oven.

To further verify that all electromagnets of the deflector were working as intended, deflection experiments were also performed using each electromagnet individually. The results are shown in Figure 7.23. The labeling as first, second and third electromagnet increasing along the molecular beam propagation direction, meaning the atoms enter the deflector at the first electromagnet, and exit from the third electromagnet.

It is observed that not all three coils perform equally well in the deflection experiments, and the simulation predict the same behavior. The deflection increases along the molecular beam direction from the first electromagnet to the third one. This is again an effect of the molecular beam velocity distributions. Particles of different velocities that are ionized in the ionization region at a given time have left (or entered) a given part of the deflector at different times. This spread in time in-

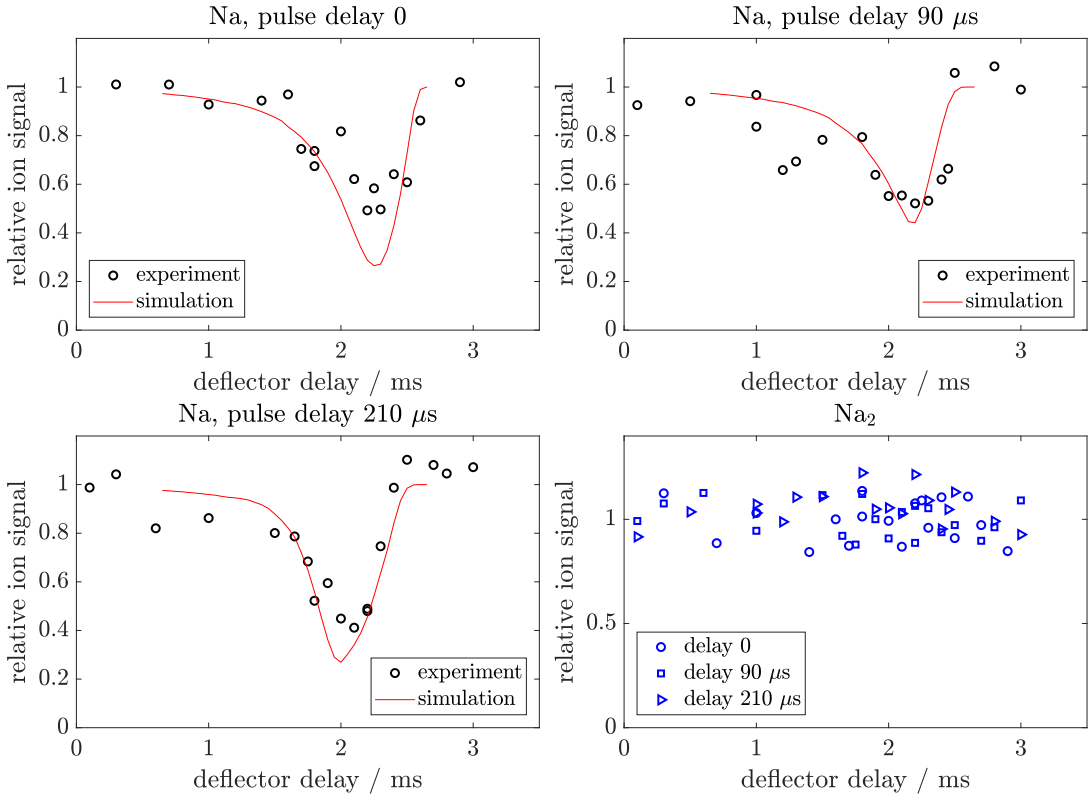

Figure 7.22: Measurements and simulations of the deflection of an effusive Na beam for different delays between the field pulses in the electromagnets.

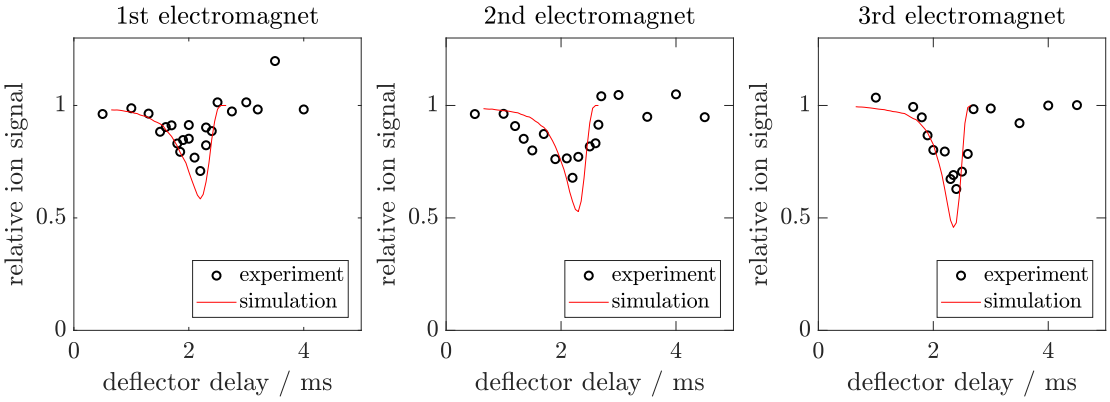

Figure 7.23: Deflection of an effusive sodium beam with a single deflector magnet.

creases the longer the distance between the deflector part and the ionization region becomes, leading to the fact that a 200 μs field pulse in the third electromagnet can deflect a larger range of velocities from the velocity distribution than the same pulse in the first electromagnet. In summary, in all cases the incomplete deflection of sodium atoms can be attributed to effects of the broad velocity distribution and not to a deficiency of the deflector.

7.4.3 Deflection of sodium-doped clusters

Results for the deflection of the smallest sodium doped ammonia clusters $NaNH_3$ and $Na(NH_3)_2$ are shown in Figure 7.24. The experiments were performed for different delays between the successive electromagnets, which were operated with current pulses of 850 A. While about 60% of the $NaNH_3$ clusters can be deflected, the effect on the $Na(NH_3)_2$ signal is much weaker. The maximum deflection for the different delays is similar. It seems as if the shape and width of the dips observed in the ion signal changes with the delay between the electromagnets. Considering the uncertainty of the data, it is not possible to quantify these differences reliably. For clusters larger than the sodium doped dimer no deflection was observed. Test measurements using sodium-doped DME clusters did show similar results: For the sodium-doped monomer NaDME some small amount of the signal was deflected, but for larger clusters no effect of the deflector was observed. Test measurements for water clusters did not show significant deflection. This was attributed to a too high molecular beam velocity caused by an expansion of water seeded in helium. In the cluster case it is more difficult to perform meaningful simulations because the cluster velocity distribution is not known accurately. The incomplete deflection and the shape of the ion signals as a function of the deflector timing resemble those measured and simulated for the effusive sodium beam. However, in the case of clusters there may be other effects involved than only the molecular beam velocity, as will be discussed later. To compare the cluster case to the sodium measurements (Figure 7.23), deflection experiments using single electromagnets were performed. These results are shown in Figure 7.25. The single magnet deflection experiments show no significant deflection with the first magnet and increasing deflection for the second and the third magnet. This effect seems to be even more pronounced than for the effusive beam of sodium atoms (Figure 7.23). The similarities between the cluster deflection and the deflection of sodium atoms seem to indicate that the

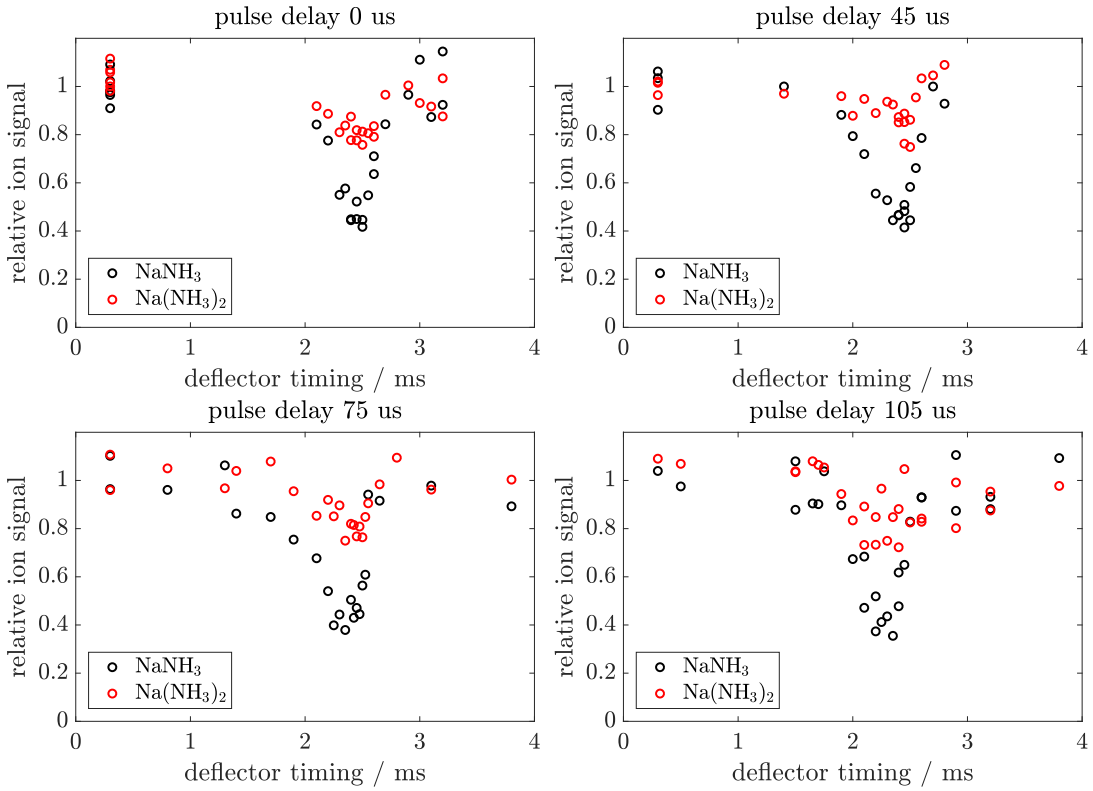

Figure 7.24: Deflection of $NaNH_3$ (black) and $Na(NH_3)_2$ (red) for different delays between individual magnets. The deflector magnets were operated with a current of 850 A.

explanation for the incomplete deflection of the small clusters might also be a broad velocity distribution. To further clarify this aspect, we have considered possible velocity distributions of small sodium-doped ammonia clusters. For this purpose it is necessary to make several assumptions about the doping process. As discussed in section 2.3, it is very unlikely to dope a single ammonia molecule directly. It is more likely that $NaNH_3$ is formed via the collision of a larger cluster with a sodium atom and subsequent evaporation of the additional ammonia molecules:

$$(NH_3)_n + Na \longrightarrow Na(NH_3)_n{}^* \longrightarrow NaNH_3 + (n\text{-}1)\,NH_3$$

For simplicity, we assume $NaNH_3$ is exclusively formed from collisions of the ammonia trimer $(NH_3)_3$ with sodium atoms:

$$(NH_3)_3 + Na \longrightarrow Na(NH_3)_3{}^* \longrightarrow NaNH_3 + 2\,NH_3$$

Furthermore we assume that the collision needs to be with sodium atoms traveling exactly in the molecular beam direction (Figure 7.26 (a)). Collisions with sodium

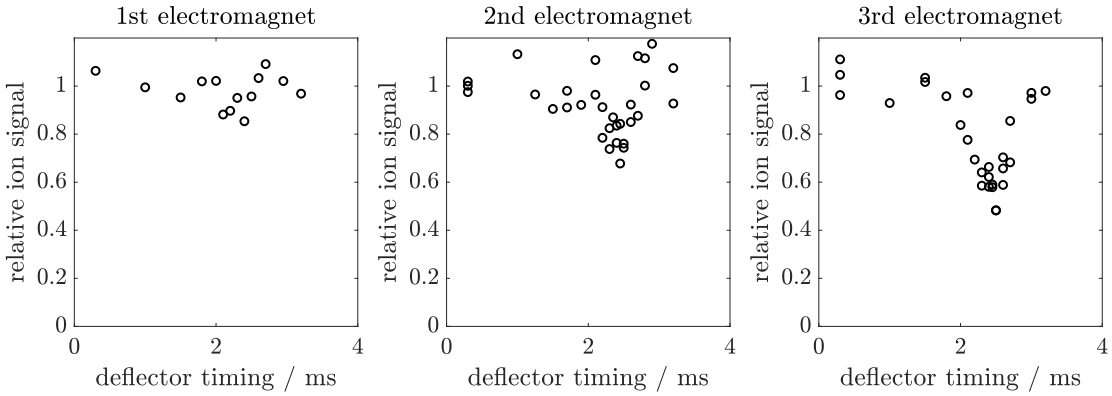

Figure 7.25: Deflection of $NaNH_3$ using the individual electromagnets of the deflector.

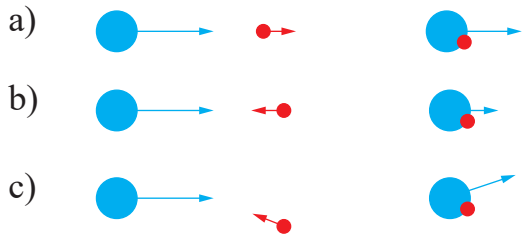

Figure 7.26: Example collisions between sodium atoms and small ammonia clusters. (a) Collisions with sodium atoms with a velocity component perpendicular to the ideal molecular beam direction (c) are not taken into account due to a small acceptance angle of the deflector. Collisions with sodium atoms traveling in the opposite molecular beam direction are excluded in a first approach due to low sticking probabilities.

atoms traveling in the opposite molecular beam direction (Figure 7.26 (b)) are for now excluded due to the higher collision energy that presumably leads to a reduced sticking probability. Collisions with sodium atoms that do not travel exactly on the molecular beam axis will lead to doped clusters that do not travel exactly along the ideal molecular beam axis anymore (Figure 7.26 (c)). These clusters will be excluded for now as well since the maximum angle at which a doped cluster can travel from the oven to still enter the deflector is about $\pm 1°$. If we assume that there is no further momentum transfer occurring during the evaporation of the two ammonia molecules, we can calculate the velocity distribution resulting for the $NaNH_3$ clusters using the laws of momentum conservation. For this purpose we use the thermal velocity distribution for the sodium atoms (v_{Na}) and an initial molecular beam velocity v_{mb}=800 m/s before doping and calculate the resulting velocity as

$$v_{\mathrm{NaNH_3}} = \frac{v_{\mathrm{Na}} m_{\mathrm{Na}} + v_{\mathrm{mb}} m_{(\mathrm{NH_3})_3}}{m_{\mathrm{Na(NH_3)_3}}} \tag{7.5}$$

The result is shown as the full red line in the center graph of Figure 7.27. The simulated deflection resulting from such a velocity distribution can be seen in the right graph of the same figure as the full red line. For this velocity distribution, the model predicts complete deflection. The additional curves in the center and right graph of Figure 7.27 show further broadened velocity distributions and the deflection resulting for them. These simulations do not represent detailed assumptions about the doping process, but are used to illustrate the effect of even broader velocity distributions in the case of $NaNH_3$. It can be seen that the deflection decreases with increasing width of the velocity distributions but is still around 80% for the broadest distribution shown. If one also takes into account collisions between clusters and sodium atoms that travel in exactly the opposite direction of the molecular beam, the resulting velocity distribution for the $NaNH_3$ would become bimodal with a second slower part (see examples in Figure 7.28). Additionally, one may consider additional formation channels for $NaNH_3$ possibly taking into account larger initial clusters like $(NH_3)_4$ or $(NH_3)_5$. Such formation paths can still be considered plausible. In Figure 7.28 example velocity distributions, arising for $NaNH_3$ produced from doping of $(NH_3)_n$ clusters with $2 \leq n \leq 5$ are shown, taking into account the of collisions shown in Figure 7.26 (a) and (b). However, since we lack detailed knowledge on which of the channels ($2 \leq n \leq 5$, collision types (a) and (b) in Figure 7.26) contributes to which degree, further simulations

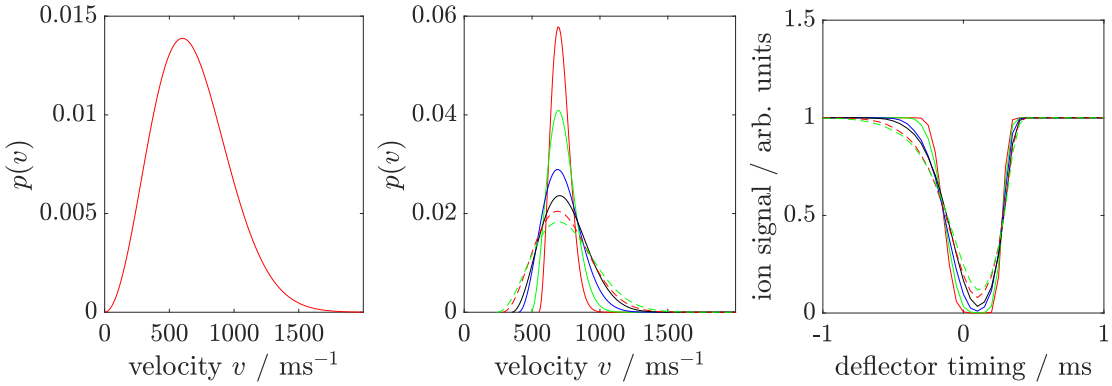

Figure 7.27: Maxwell-Boltzmann velocity distribution of Na vapor at 250°C (left). The full red line in the center graph shows the velocity distribution resulting from a collision of ammonia trimer traveling at 800 m/s with sodium atoms following the distribution on the left. The full red line in the right panel shows the deflection expected for the cluster velocity distribution shows as the full red line in the center graph. Additional curves in the center panel and the right panel show the effect of an additionally broadened cluster velocity distribution.

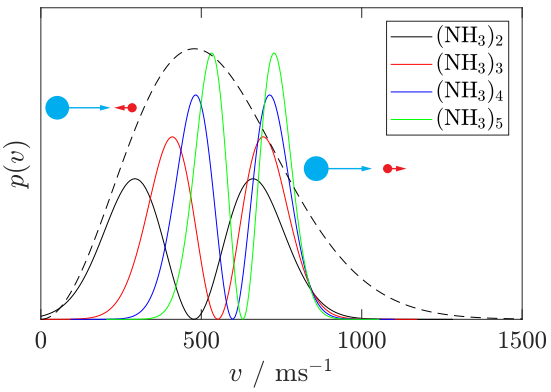

Figure 7.28: Bimodal velocity distributions resulting from collision of clusters of different sizes with a thermal distribution of sodium atoms. The distributions take into account collisions with sodium atoms traveling in or against the molecular beam direction, see Figure 7.26. The dashed black line shows schematically a broad velocity distribution created from weighted superposition of the different production channels.

of the velocity distributions would be highly speculative. It seems plausible, that the resulting velocity distribution of $NaNH_3$ can be similarly broad as the one for the effusive sodium beam, as indicated by the distribution shown as black dashed line in Figure 7.28. It thus seems possible that the incomplete deflection of sodium-doped clusters is at least partially caused by broad velocity distributions. This does however not explain why slightly larger clusters, i.e. larger than the dimer are not deflected at all. Since these clusters should be formed from larger initial undoped clusters, their velocity distributions would intuitively be expected to be narrower.

The cluster velocity distribution, however, is likely not the only relevant factor to consider. Another aspect are the already mentioned evaporation processes. If clusters evaporate too slowly after a collision with a sodium atom, this evaporation may not yet be finished when the clusters enter the deflector. This means, if larger clusters (e.g. with an initial $n > 10$) are still evaporating while they travel through the deflector or after the deflector, new $NaNH_3$ could be formed during or after the deflection. Those clusters would naturally experience less deflection since they had a higher mass during the deflector pulse. Such effects could also lead to an increased performance of the third electromagnet as compared to the first two magnets, since it can be assumed that the evaporation rate decreases along the molecular beam direction. To further investigate this possibility, an additional chamber was introduced to the setup, further elongating the distance between the sodium oven and the deflector by 20 cm. The idea was, that this increase in flight path could suffice to finish all relevant evaporation processes. However, the increased distance had no positive effect on the deflection of the clusters. The general signal levels decreased significantly leading to an increased uncertainty in the determined signal levels.

A further possible explanation for reduced deflection is the relaxation of the magnetic polarization. Transitions between the two spin states $m_S = \pm 1/2$, while the cluster travels through the deflector field would also reduce the achievable deflection. In such a case the cluster would first be accelerated in one direction and then in the other, strongly reducing the final displacement perpendicular to the molecular beam. Within the molecular beam, there are no collision between different clusters. This isolation of the clusters increases the relaxation times drastically. However, there are still processes that can lead to spin relaxation. One such exam-

ple is the spin rotational interaction, coupling the electron spin to the rotational movement of the cluster. Furthermore, the vibrational modulation of the hyperfine interaction can lead to relaxation. A quantitative theoretical estimation of these relaxation times is not really possible. An experimental estimation may become possible, as soon as other experimental uncertainties can be excluded.

7.5 Conclusion and outlook

A deflector for paramagnetic clusters, designed in collaboration between our group and the group of Edvardas Narevicius at the Weizmann Institute of Science in Israel, was incorporated into our experimental setup and characterized theoretically as well as experimentally. Test experiments on effusive beams of atomic sodium showed that the deflector worked as intended, and that the simulated and measured performance agree quantitatively. The deflection of sodium-doped clusters was less successful than expected. Only the smallest clusters $NaNH_3$ and $Na(NH_3)_2$ could be partially deflected, while no deflection was observed for any larger clusters. The most likely explanations for the deviation of the experiments from the simulations are broad cluster velocity distributions and magnetic relaxation. The broad velocity distributions are caused by doping the ammonia clusters via collisions with sodium atoms in a pickup cell. These pickup and following evaporation processes are, at least for the smallest clusters, not yet well understood. It is conceivable that the doping process does not only broaden the velocity distribution, but also results in possible collisions between clusters because after the doping process not all clusters are traveling with the same velocity anymore. Magnetic relaxation processes are certainly present, but it is unclear on which timescales they occur. At the moment it is not possible to tell how much both processes contribute to the reduction of the achieved deflection. Consequently, it is at the moment not possible to estimate magnetic relaxation times from our experimental data.
An experimental improvement that is currently being planned may be able to resolve this issue. A laser ablation source for the production of sodium doped clusters will produce sodium ammonia clusters without relying on molecular collisions in a pick up cell. Such an expansion is expected to circumvent ambiguities associated with the doping process (broad velocity distributions and cluster evaporation), and may therefore improve the observed deflection significantly. This might allow

for an estimation of magnetic relaxation times from experimental measurements. Also, an improvement of the limited repetition rate of 2 Hz is planned by improving the design of the deflector cooling system and the electronics. Furthermore, future experiments using lithium doped clusters instead of sodium doped cluster are planned, which would slightly reduce the cluster masses.

Chapter 8
Conclusion and outlook

In Chapters 4 and 5 we describe studies on low-energy electron scattering in water clusters by angle-resolved photoelectron spectroscopy of clusters of various sizes. As the cluster size increases, a photoelectron has an increasing probability of being scattered elastically or inelastically during its transport through the cluster. This creates a trend towards more isotropic photoemission with increasing cluster size caused by electron transport scattering. However, when comparing photoemission anisotropies between the gas and condensed phase, electron transport scattering is not the only effect reducing the photoemission anisotropies. The photoionization process itself, depending on the short range scattering potential created by the molecular environment, influences the photoemission anisotropies as well. In Chapter 4 we introduced the idea that the photoionization process itself can be described separately from electron transport by a genuine anisotropy. The genuine anisotropy describes the photoelectron angular distribution of photoelectrons in liquid water, before any transport scattering event has occurred. In Chapter 4 this genuine anisotropy was determined by fully size-resolved photoelectron velocity map imaging of water clusters with up to 20 molecules. It was found that with increasing cluster size the anisotropy decreases quickly up to a cluster size of six molecules and then converges. This surprisingly small cluster of six molecules corresponds to the smallest water cluster that forms a 3D structure, instead of quasi-planar ring structures. This converged water hexamer anisotropy was taken as the genuine anisotropy to describe the photoionization process in liquid water and large water clusters. Furthermore, the determined genuine anisotropy was used in the detailed scattering model developed in our group[12,14,15](see section 2.2) to predict the photoelectron anisotropy for liquid bulk water. Experimental

data on liquid water agree well with our predictions.[82]

The approach of separating the contributions to the photoelectron angular distribution into a genuine anisotropy and the decrease caused by electron transport scattering was shown to be successful. Furthermore it is possible to determine genuine anisotropy values from measurements on water clusters that are so small that electron transport scattering does not yet occur. Whether this two-step model is transferable to electron scattering in other liquids remains to be shown.

Chapter 5 reports on the effect of low-energy electron transport scattering in angle-resolved photoelectron spectroscopy of larger water clusters with average cluster sizes below 1000 molecules. The same detailed scattering model as for condensed (liquid, amorphous) water was employed to calculate the decrease of the photoelectron anisotropy with cluster size. The experimentally observed anisotropy decreased more pronouncedly than predicted by the model, and reached bulk-like values already for cluster sizes of only a few hundred molecules. To understand the observed differences between the model and the experiments, simulations using different sets of scattering parameters were performed. It was found that neither liquid (or amorphous solid) bulk nor gas phase scattering cross sections can explain the experimentally observed behavior. However, intermediate scattering cross sections between the condensed phase and the gas phase values explain the observed decrease of the anisotropy with cluster size qualitatively. Two possible reasons for cluster specific electron scattering behavior are a reduced dielectric constant, resulting in a reduced dielectric screening of the scattering potentials, and differences in the intermolecular vibrational modes. The cluster size at which water clusters show bulk-like electron scattering behavior could not yet be determined.

Overall it has been shown that electron scattering during the photoionization process can be separated from electron transport scattering. The transport scattering part in liquid bulk water is appropriately described by the scattering model with liquid bulk scattering parameters. Such transport scattering simulations may also be used to retrieve genuine properties (eBE and anisotropies) for species in solutions,[12] which are otherwise not accessible. For measurements of solutes dissolved in smaller clusters one has to account for the possibility of increased electron scattering effects compared with the liquid bulk. How significant this effect can be, in particular for photoelectron angular distributions, has been shown in Chapter 5. Our simple model of intermediate scattering parameters can hardly be expected to

describe all effects of electron scattering in clusters quantitatively. But this concept offers a first qualitative understanding of increased electron scattering effects in clusters.

The low-energy electron scattering work on clusters will be extended to different compounds. In an upcoming beamtime at the DESIRS beamline of SOLEIL synchrotron, fully size-resolved photoelectron angular distributions of small ammonia clusters at various electron kinetic energies will be recorded. An intriguing question is whether the two-step model used for water can be generalized to other substances. It is yet unclear whether the quick convergence to a genuine anisotropy is a unique property of water clusters, or a more general behavior of clusters of small molecules. This study could help to understand which parameters influence the short range scattering potential and how important the H-bond network is in the convergence to bulk-like behavior.

Chapter 6 and 7 deal with the concentration dependence of electron solvation in sodium-doped clusters. We presented angle-resolved photoelectron spectra of clusters of ammonia and dimethyl ether containing varying amounts of sodium. Furthermore the number of solvent molecules, i.e. ammonia and DME, was varied over a wide range. For small double-doped clusters $Na_2(NH_3)_n$ and $Na_2(DME)_n$ DFT calculations for vertical ionization energies were performed. With the results of the DFT calculations, we could assign the two main bands in the PES. A first band (B_{solv}) corresponds to internally solvated sodium ions and solvated electrons that are separated from the sodium ion. A second band (B_{surf}) was assigned to electrons in a doubly occupied orbital located on a sodium atom at the surface of the cluster. The positions and widths of both bands seem not to depend significantly on the sodium concentration, but their relative intensities change with sodium concentration. The intensity of B_{surf} relative to B_{solv} increases with increasing sodium concentration. For large ammonia clusters at high sodium concentration we reported characteristic changes in the photoelectron spectra. The estimated sodium concentrations for these clusters fall into the range where the bulk solutions show the famous transition to the metallic state (TMS).[38] The observed changes for sodium-doped ammonia clusters are in agreement with an assignment to a cluster-equivalent of the TMS, although our data cannot provide a final proof for this interpretation.

For the DME clusters doped with large amounts of sodium, pronounced changes

are observed in the PES. These changes are more difficult to explain than in the case of ammonia because sodium is insoluble in bulk DME, and consequently, there is no TMS reported for those systems. Due to the insolubility of sodium in bulk DME it is clear that the sodium doped DME clusters represent significantly over-saturated solutions. It is unclear what kind of processes can occur in such systems, and more studies are needed to analyze the observed behavior.

Overall it can be said that sodium-doped solvent clusters offer a path to study concentration dependent photoelectron spectra of nanoscale solutions of sodium in high vapor pressure liquids. Such measurements using liquid jets of ammonia are challenging, but seem feasible, considering recent developments.[100] For DME such measurements in liquid jets will not be possible due to the mentioned insolubility. The limited system size used in our studies offers the possibility to estimate a minimum system size of 100-200 solvent molecules for which the TMS in sodium ammonia solutions occurs. This is an intriguing result, since those system sizes are within the reach of modern ab initio calculations.

The long-term goal of the work presented in Chapter 7 is the study of concentration dependent magnetic properties of small sodium ammonia clusters and the distinction of spin paired and unpaired solvated electrons in the photoelectron spectra. To realize this goal, a Stern-Gerlach type deflector was developed in collaboration with the Narevicius group at the Weizmann Institute in Israel. Such a deflector can be used to deflect solvent clusters containing single sodium atoms. Furthermore clusters containing two sodium atoms can be deflected at least partially, if the electrons are unpaired, i.e. in a triplet state. Even using mass spectrometry, such a deflector would therefore allow to determine whether a certain double-doped cluster, $Na_2(NH_3)_n$, is in a triplet state or in a singlet state. So far, the designed deflector was incorporated into our setup and characterized both experimentally and theoretically. For the deflection of an effusive beam of thermal sodium atoms, the achieved deflection agrees quantitatively with simulations, and confirms the expected performance of the deflector. Due to the broad velocity distribution of the sodium atoms (T=260°C), the short magnetic field pulse in the deflector can only be timed to deflect a part of the sodium beam. Test measurements have also been performed for sodium doped clusters. Even for the smallest sodium-doped cluster $NaNH_3$ only partial deflection was observed. For clusters containing more than two ammonia molecules no deflection could be observed. The simula-

tions by contrast, predict essentially complete deflection for single-doped clusters of $n < 10$ solvent molecules, assuming a narrow velocity distribution of the clusters. The most likely explanation for the difficulties with the cluster deflection is the broadening of the cluster velocity distribution in the course of the doping process. For the smallest clusters the doping process in a pickup cell is not well understood and several production channels are possible, including evaporation of solvent molecules from larger clusters. Those different production channels result in clusters of different velocities, thus reducing the overall deflection that can be achieved. A second factor possibly limiting the achievable deflection is the magnetic relaxation of clusters. While a theoretical estimate of the timescale of those relaxation processes is difficult, one might estimate these relaxation times from cluster deflection experiments once other ambiguities are excluded. Further experimental developments are needed and planned to achieve the goal of studying magnetic properties and spin pairing effects in sodium-doped solvent clusters.

For the deflector project, most ambiguities arise from the doping process, that is not well understood for small clusters. Future plans include the replacement of the doping process by laser ablation for cluster formation. This will allow for the creation of sodium-doped clusters with a narrower velocity distribution, which are probably easier to deflect.

As an extension of the sodium-doped cluster work, we plan to study concentration dependent photoelectron velocity map images of clusters doped with lithium atoms instead of sodium atoms. First experiments with lithium-doped DME clusters have already been performed.[147] It is also planned to study the TMS for different solvents like methylamine.[172] The extension of the studies presented in Chapter 6 to different alkali metals and solvents might enable the observation of the TMS under different conditions (i.e. concentrations, temperatures etc.), and thus substantiate our yet tentative assignment of the spectral changes accompanying the TMS.

References

[1] J. V. Coe, A. D. Earhart, M. H. Cohen, G. J. Hoffman, H. W. Sarkas, and K. H. Bowen, "Using cluster studies to approach the electronic structure of bulk water: Reassessing the vacuum level, conduction band edge, and band gap of water," *The Journal of Chemical Physics*, vol. 107, no. 16, pp. 6023–6031, 1997.

[2] T. Goulet, A. Bernas, C. Ferradini, and J.-P. Jay-Gerin, "On the electronic structure of liquid water: Conduction-band tail revealed by photoionization data," *Chemical Physics Letters*, vol. 170, no. 5, pp. 492–496, 1990.

[3] C. Adriaanse, J. Cheng, V. Chau, M. Sulpizi, J. VandeVondele, and M. Sprik, "Aqueous redox chemistry and the electronic band structure of liquid water," *Journal of Physical Chemsitsry Letters*, vol. 3, no. 23, pp. 3411–3415, 2012.

[4] M. Faubel, B. Steiner, and J. P. Toennies, "Photoelectron spectroscopy of liquid water, some alcohols, and pure nonane in free micro jets," *The Journal of Chemical Physics*, vol. 106, no. 22, pp. 9013–9031, 1997.

[5] B. Winter, R. Weber, W. Widdra, M. Dittmar, M. Faubel, and I. V. Hertel, "Full valence band photoemission from liquid water using euv synchrotron radiation," *Journal of Physical Chemistry A*, vol. 108, no. 14, pp. 2625–2632, 2004.

[6] R. Seidel, S. Thürmer, and B. Winter, "Photoelectron spectroscopy meets aqueous solution: Studies from a vacuum liquid microjet," *The Journal of Physical Chemistry Letters*, vol. 2, no. 6, pp. 633–641, 2011.

[7] B. Winter and M. Faubel, "Photoemission from liquid aqueous solutions," *Chemical Reviews*, vol. 106, no. 4, pp. 1176–1211, 2006.

[8] B. Winter, "Liquid microjet for photoelectron spectroscopy," *Nuclear Instruments and Methods in Physics Research Section A: Accelerators, Spectrometers, Detectors and Associated Equipment*, vol. 601, no. 1, pp. 139 – 150, 2009.

[9] B. Winter, E. F. Aziz, U. Hergenhahn, M. Faubel, and I. V. Hertel, "Hydrogen bonds in liquid water studied by photoelectron spectroscopy," *The Journal of Chemical Physics*, vol. 126, no. 12, p. 124504, 2007.

[10] F. Buchner, A. Nakayama, S. Yamazaki, H.-H. Ritze, and A. Lübcke, "Excited-state relaxation of hydrated thymine and thymidine measured by liquid-jet photoelectron spectroscopy: Experiment and simulation," *Journal of the American Chemical Society*, vol. 137, no. 8, pp. 2931–2938, 2015.

[11] S. Ghosal, J. C. Hemminger, H. Bluhm, B. S. Mun, E. L. D. Hebenstreit, G. Ketteler, D. F. Ogletree, F. G. Requejo, and M. Salmeron, "Electron spectroscopy of aqueous solution interfaces reveals surface enhancement of halides," *Science*, vol. 307, no. 5709, pp. 563–566, 2005.

[12] D. Luckhaus, Y. I. Yamamoto, T. Suzuki, and R. Signorell, "Genuine binding energy of the hydrated electron," *Science Advances*, vol. 3, no. 4, p. e1603224, 2017.

[13] A. T. Shreve, T. A. Yen, and D. M. Neumark, "Photoelectron spectroscopy of hydrated electrons," *Chemical Physics Letters*, vol. 493, no. 4, pp. 216 – 219, 2010.

[14] M. Goldmann, J. Miguel-Sanchez, A. H. C. West, B. L. Yoder, and R. Signorell, "Electron mean free path from angle-dependent photoelectron spectroscopy of aerosol particles," *Journal of Chemical Physics*, vol. 142, no. 22, p. 8, 2015.

[15] R. Signorell, M. Goldmann, B. L. Yoder, A. Bodi, E. Chasovskikh, L. Lang, and D. Luckhaus, "Nanofocusing, shadowing, and electron mean free path in the photoemission from aerosol droplets," *Chemical Physics Letters*, vol. 658, pp. 1–6, 2016.

[16] S. Amanatidis, B. L. Yoder, and R. Signorell, "Low-energy photoelectron transmission through aerosol overlayers," *The Journal of Chemical Physics*, vol. 146, no. 22, p. 224204, 2017.

[17] M. Michaud and L. Sanche, "Total cross-sections for slow-electron (1-20 eV) scattering in solid H_2O," *Physical Review A*, vol. 36, no. 10, pp. 4672–4683, 1987.

[18] M. A. Huels, B. Boudaïffa, P. Cloutier, D. Hunting, and L. Sanche, "Single, double, and multiple double strand breaks induced in dna by 3-100 eV electrons," *Journal of the American Chemical Society*, vol. 125, no. 15, pp. 4467–4477, 2003.

[19] E. Alizadeh, T. M. Orlando, and L. Sanche, "Biomolecular damage induced by ionizing radiation: The direct and indirect effects of low-energy electrons on dna," *Annual Review of Physical Chemistry*, vol. 66, no. 1, pp. 379–398, 2015.

[20] Y.-I. Suzuki, K. Nishizawa, N. Kurahashi, and T. Suzuki, "Effective attenuation length of an electron in liquid water between 10 and 600 eV," *Physical Review E*, vol. 90, p. 010302, 2014.

[21] H. Shinotsuka, B. Da, S. Tanuma, H. Yoshikawa, C. J. Powell, and D. R. Penn, "Calculations of electron inelastic mean free paths. xi. data for liquid water for energies from 50 eV to 30 keV," *Surface and Interface Analysis*, vol. 49, no. 4, pp. 238–252, 2016.

[22] G. Olivieri, K. M. Parry, C. J. Powell, D. J. Tobias, and M. A. Brown, "Quantitative interpretation of molecular dynamics simulations for x-ray photoelectron spectroscopy of aqueous solutions," *The Journal of Chemical Physics*, vol. 144, no. 15, p. 154704, 2016.

[23] R. L. Kurtz, N. Usuki, R. Stockbauer, and T. E. Madey, "Measurements of electron attenuation lengths in condensed molecular solids," *Journal of*

Electron Spectroscopy and Related Phenomena, vol. 40, no. 1, pp. 35 – 58, 1986.

[24] J. C. Ashley, "Interaction of low-energy electrons with condensed matter - stopping powers and inelastic mean free paths from optical-data," *Journal of Electron Spectroscopy and Related Phenomena*, vol. 46, no. 3, pp. 199–214, 1988.

[25] A. Akkerman and E. Akkerman, "Characteristics of electron inelastic interactions in organic compounds and water over the energy range 20-10'000 eV," *Journal of Applied Physics*, vol. 86, no. 10, pp. 5809–5816, 1999.

[26] D. Emfietzoglou and H. Nikjoo, "The effect of model approximations on single-collision distributions of low-energy electrons in liquid water," *Radiation Research*, vol. 163, no. 1, pp. 98–111, 2005.

[27] M. Michaud, A. Wen, and L. Sanche, "Cross sections for low-energy (1-100 eV) electron elastic and inelastic scattering in amorphous ice," *Radiation Research*, vol. 159, no. 1, pp. 3–22, 2003.

[28] C. J. Tung, T. C. Chao, H. W. Hsieh, and W. T. Chan, "Low-energy electron interactions with liquid water and energy depositions in nanometric volumes," *Nuclear Instruments & Methods in Physics Research Section B-Beam Interactions with Materials and Atoms*, vol. 262, no. 2, pp. 231–239, 2007.

[29] N. Ottosson, M. Faubel, S. E. Bradforth, P. Jungwirth, and B. Winter, "Photoelectron spectroscopy of liquid water and aqueous solution: Electron effective attenuation lengths and emission-angle anisotropy," *Journal of Electron Spectroscopy and Related Phenomena*, vol. 177, no. 2, pp. 60 – 70, 2010.

[30] C. Zhang, T. Andersson, M. Förstel, M. Mucke, T. Arion, M. Tchaplyguine, O. Björneholm, and U. Hergenhahn, "The photoelectron angular distribution of water clusters," *Journal of Chemical Physics*, vol. 138, no. 23, p. 234306, 2013.

[31] F. Blanco, A. Muñoz, D. Almeida, F. F. da Silva, P. Limão-Vieira, and G. García, "Clustering and condensation effects in the electron scattering

cross sections from water molecules," *International Journal of Mass Spectrometry*, vol. 365, pp. 287–294, 2014.

[32] S. Thürmer, R. Seidel, M. Faubel, W. Eberhardt, J. C. Hemminger, S. E. Bradforth, and B. Winter, "Photoelectron angular distributions from liquid water: Effects of electron scattering," *Physical Review Letters*, vol. 111, p. 173005, 2013.

[33] S. M. Pimblott, J. A. LaVerne, and A. Mozumder, "Monte carlo simulation of range and energy deposition by electrons in gaseous and liquid water," *Journal of Physical Chemistry*, vol. 100, no. 20, pp. 8595–8606, 1996.

[34] H. Tomita, M. Kai, T. Kusama, and A. Ito, "Monte carlo simulation of physicochemical processes of liquid water radiolysis," *Radiation and Environmental Biophysics*, vol. 36, no. 2, pp. 105–116, 1997.

[35] M. Dingfelder, D. Hantke, M. Inokuti, and H. G. Paretzke, "Electron inelastic-scattering cross sections in liquid water," *Radiation Physics and Chemistry*, vol. 53, no. 1, pp. 1 – 18, 1998.

[36] R. Shimizu and D. Ze-Jun, "Monte carlo modelling of electron-solid interactions," *Reports on Progress in Physics*, vol. 55, no. 4, pp. 487–531, 1992.

[37] J. M. Thomas, P. P. Edwards, and V. L. Kuznetsov, "Sir Humphry Davy: Boundless chemist, physicist, poet and man of action," *ChemPhysChem*, vol. 9, no. 1, pp. 59–66, 2008.

[38] E. Zurek, P. P. Edwards, and R. Hoffmann, "A molecular perspective on lithium–ammonia solutions," *Angewandte Chemie International Edition*, 2009.

[39] C. A. Kraus, "Solutions of metals in non-metallic solvents; i. general properties of solutions of metals in liquid ammonia.," *Journal of the American Chemical Society*, vol. 29, no. 11, pp. 1557–1571, 1907.

[40] C. A. Kraus and W. W. Lucasse, "The resistance-temperature coefficient of concentrated solutions of sodium in liquid ammonia," *Journal of the American Chemical Society*, vol. 44, no. 9, pp. 1941–1949, 1922.

[41] G. E. Gibson and W. L. Argo, "The absorption spectra of the blue solutions of sodium and magnesium in liquid ammonia," *Physical Review*, vol. 7, pp. 33–48, 1916.

[42] A. J. Birch, "117. reduction by dissolving metals. part i," *Journal of the Chemical Society (Resumed)*, pp. 430–436, 1944.

[43] P. P. Edwards, "The electronic properties of metal solutions in liquid ammonia and related solvents," in *Advances in Inorganic Chemistry and Radiochemistry* (H. Emeléus and A. Sharpe, eds.), vol. 25 of *Advances in Inorganic Chemistry and Radiochemistry*, pp. 135 – 185, Academic Press, 1982.

[44] D. Holton and P. Edwards, "Metals in non-aqueous solvents," *Chemistry in Britain*, vol. 21, no. 11, p. 1007, 1985.

[45] N. W. Taylor and G. N. Lewis, "The paramagnetism of "odd molecules"," *Proceedings of the National Academy of Sciences of the United States of America*, vol. 11, no. 16576892, pp. 456–457, 1925.

[46] E. Huster, "The solutions of sodium in liquid ammonia, magnetism, thermal expansions, condition of dissolved sodium," *Annalen Der Physik*, vol. 33, no. 6, 1938.

[47] S. Freed and N. Sugarman, "The magnetic susceptibilities of metals dissolved in liquid ammonia," *The Journal of Chemical Physics*, vol. 11, no. 8, pp. 354–360, 1943.

[48] A. H. C. West, B. L. Yoder, D. Luckhaus, C. M. Saak, M. Doppelbauer, and R. Signorell, "Angle-resolved photoemission of solvated electrons in sodium-doped clusters," *Journal of Physical Chemistry Letters*, vol. 6, no. 8, pp. 1487–1492, 2015.

[49] A. H. C. West, B. L. Yoder, D. Luckhaus, and R. Signorell, "Solvated electrons in clusters: Magic numbers for the photoelectron anisotropy," *The Journal of Physical Chemistry A*, vol. 119, no. 50, pp. 12376–12382, 2015.

[50] T. Zeuch and U. Buck, "Sodium doped hydrogen bonded clusters: Solvated electrons and size selection," *Chemical Physics Letters*, vol. 579, pp. 1–10, 2013.

[51] I. Dauster, M. A. Suhm, U. Buck, and T. Zeuch, "Experimental and theoretical study of the microsolvation of sodium atoms in methanol clusters: differences and similarities to sodium-water and sodium-ammonia," *Physical Chemistry Chemical Physics*, vol. 10, no. 1, pp. 83–95, 2008.

[52] A. Damascelli, Z. Hussain, and Z.-X. Shen, "Angle-resolved photoemission studies of the cuprate superconductors," *Reviews of Modern Physics*, vol. 75, no. 2, pp. 473–541, 2003.

[53] A. Damascelli, "Probing the electronic structure of complex systems by arpes," *Physica Scripta*, vol. 2004, no. T109, p. 61, 2004.

[54] A. T. J. B. Eppink and D. H. Parker, "Velocity map imaging of ions and electrons using electrostatic lenses: Application in photoelectron and photofragment ion imaging of molecular oxygen," *Review of Scientific Instruments*, vol. 68, no. 9, pp. 3477–3484, 1997.

[55] K. L. Reid, "Photoelectron angular distributions," *Annual Review of Physical Chemistry*, vol. 54, no. 1, pp. 397–424, 2003.

[56] R. N. Cooper, J. Zare, *Photoelectron Angular Distributions*, vol. XIc of *Lectures in Theoretical Physics*, pp. 317–337. New York: Gordon and Breach, Science Publishers, 1969.

[57] J. Cooper and R. N. Zare, "Angular distribution of photoelectrons," *Journal of Chemical Physics*, vol. 48, no. 2, p. 942, 1968.

[58] D. W. Chandler and P. L. Houston, "Two-dimensional imaging of state-selected photodissociation products detected by multiphoton ionization," *Journal of Chemical Physics*, vol. 87, no. 2, pp. 1445–1447, 1987.

[59] H. Helm, N. Bjerre, M. J. Dyer, D. L. Huestis, and M. Saeed, "Images of photoelectrons formed in intense laser fields," *Physical Review Letters*, vol. 70, no. 21, pp. 3221–3224, 1993.

[60] P. Kruit and F. H. Read, "Magnetic field paralleliser for 2pi electron-spectrometer and electron-image magnifier," *Journal of Physics E: Scientific Instruments*, vol. 16, no. 4, pp. 313–324, 1983.

[61] J. Eland, "Experimental methods," in *Photoelectron Spectroscopy (Second Edition)* (J. ELAND, ed.), pp. 30 – 66, Butterworth-Heinemann, second edition ed., 1984.

[62] C. M. Truesdale, S. Southworth, P. H. Kobrin, D. W. Lindle, G. Thornton, and D. A. Shirley, "Photoelectron angular distributions of h2o," *The Journal of Chemical Physics*, vol. 76, no. 2, pp. 860–865, 1982.

[63] M. G. White, R. A. Rosenberg, G. Gabor, E. D. Poliakoff, G. Thornton, S. H. Southworth, and D. A. Shirley, "Time-of-flight photoelectron spectroscopy of gases using synchrotron radiation," *Review of Scientific Instruments*, vol. 50, no. 10, pp. 1268–1273, 1979.

[64] A. T. J. B. Eppink, S. Wu, and B. J. Whitaker, *Reconstruction methods*, pp. 65–112. Imaging in molecular dynamics, Cambridge: Cambridge University Press, 2003.

[65] S. Manzhos and H.-P. Loock, "Photofragment image analysis using the onion-peeling algorithm," *Computer Physics Communications*, vol. 154, no. 1, pp. 76–87, 2003.

[66] G. M. Roberts, J. L. Nixon, J. Lecointre, E. Wrede, and J. R. R. Verlet, "Toward real-time charged-particle image reconstruction using polar onion-peeling," *Review of Scientific Instruments*, vol. 80, no. 5, p. 053104, 2009.

[67] C. Bordas, F. Paulig, H. Helm, and D. L. Huestis, "Photoelectron imaging spectrometry: Principle and inversion method," *Review of Scientific Instruments*, vol. 67, no. 6, pp. 2257–2268, 1996.

[68] V. Dribinski, A. Ossadtchi, V. A. Mandelshtam, and H. Reisler, "Reconstruction of abel-transformable images: The gaussian basis-set expansion abel transform method," *Review of Scientific Instruments*, vol. 73, no. 7, pp. 2634–2642, 2002.

[69] G. A. Garcia, L. Nahon, and I. Powis, "Two-dimensional charged particle image inversion using a polar basis function expansion," *Review of Scientific Instruments*, vol. 75, no. 11, pp. 4989–4996, 2004.

[70] B. Dick, "Inverting ion images without abel inversion: maximum entropy reconstruction of velocity maps," *Physical Chemistry Chemical Physics*, vol. 16, no. 2, pp. 570–580, 2014.

[71] E. P. Wigner, "Lower limit for the energy derivative of the scattering phase shift," *Physical Review*, vol. 98, no. 1, pp. 145–147, 1955.

[72] D. Field and L. B. Madsen, "Time delays in cold elastic scattering," *The Journal of Chemical Physics*, vol. 118, no. 4, pp. 1679–1683, 2003.

[73] R. Bourgain, J. Pellegrino, S. Jennewein, Y. R. P. Sortais, and A. Browaeys, "Direct measurement of the wigner time delay for the scattering of light by a single atom," *Optics Letters*, vol. 38, no. 11, pp. 1963–1965, 2013.

[74] Y. Itikawa and N. Mason, "Cross sections for electron collisions with water molecules," *Journal of Physical and Chemical Reference Data*, vol. 34, no. 1, pp. 1–22, 2005.

[75] K. Jung, T. Antoni, R. Muller, K. H. Kochem, and H. Ehrhardt, "Rotational excitation of N_2 , CO and H_2O by low-energy electron collisions," *Journal of Physics B: Atomic and Molecular Physics*, vol. 15, no. 19, p. 3535, 1982.

[76] G. Seng and F. Linder, "Vibrational excitation of polar molecules by electron impact. ii. direct and resonant excitation in H_2O," *Journal of Physics B: Atomic and Molecular Physics*, vol. 9, no. 14, p. 2539, 1976.

[77] T. W. Shyn, S. Y. Cho, and T. E. Cravens, "Vibrational-excitation cross sections of water molecules by electron impact," *Physical Review A*, vol. 38, no. 2, pp. 678–682, 1988.

[78] A. A. A. El-Zein, M. J. Brunger, and W. R. Newell, "Excitation of vibrational quanta in water by electron impact," *Journal of Physics B: Atomic, Molecular and Optical Physics*, vol. 33, no. 22, p. 5033, 2000.

[79] A. El-Zein, M. J. Brunger, and W. R. Newell, "Resonance phenomena in electron impact excitation of the fundamental vibrational modes of water," *Chemical Physics Letters*, vol. 319, no. 5, pp. 701–707, 2000.

[80] H. C. Straub, B. G. Lindsay, K. A. Smith, and R. F. Stebbings, "Absolute partial cross sections for electron-impact ionization of H_2O and D_2O from threshold to 1000 eV," *The Journal of Chemical Physics*, vol. 108, no. 1, pp. 109–116, 1998.

[81] W. Kedzierski, J. Derbyshire, C. Malone, and J. W. McConkey, "Isotope effects in the electron impact break-up of water," *Journal of Physics B: Atomic, Molecular and Optical Physics*, vol. 31, no. 24, p. 5361, 1998.

[82] J. Nishitani, C. W. West, and T. Suzuki, "Angle-resolved photoemission spectroscopy of liquid water at 29.5 eV," *Structural Dynamics*, vol. 4, no. 4, p. 044014, 2017.

[83] M. Faubel, K. R. Siefermann, Y. Liu, and B. Abel, "Ultrafast soft x-ray photoelectron spectroscopy at liquid water microjets," *Accounts of Chemical Research*, vol. 45, no. 1, pp. 120–130, 2012.

[84] B. T. Draine and P. J. Flatau, "Discrete-dipole approximation for scattering calculations," *Journal of the Optical Society of America A*, vol. 11, no. 4, pp. 1491–1499, 1994.

[85] H. DeVoe, "Optical properties of molecular aggregates. i. classical model of electronic absorption and refraction," *The Journal of Chemical Physics*, vol. 41, no. 2, pp. 393–400, 1964.

[86] H. DeVoe, "Optical properties of molecular aggregates. ii. classical theory of the refraction, absorption, and optical activity of solutions and crystals," *The Journal of Chemical Physics*, vol. 43, no. 9, pp. 3199–3208, 1965.

[87] M. A. Yurkin and A. G. Hoekstra, "The discrete-dipole-approximation code adda: Capabilities and known limitations," *Journal of Quantitative Spectroscopy and Radiative Transfer*, vol. 112, no. 13, pp. 2234–2247, 2011.

[88] H. Hayashi and N. Hiraoka, "Accurate measurements of dielectric and optical functions of liquid water and liquid benzene in the vuv region (1–100 eV) using small-angle inelastic x-ray scattering," *The Journal of Physical Chemistry B*, vol. 119, no. 17, pp. 5609–5623, 2015.

[89] B. L. Yoder, J. H. Litman, P. W. Forysinski, J. L. Corbett, and R. Signorell, "Sizer for neutral weakly bound ultrafine aerosol particles based on sodium doping and mass spectrometric detection," *Journal of Physical Chemistry Letters*, vol. 2, no. 20, pp. 2623–2628, 2011.

[90] J. H. Litman, B. L. Yoder, B. Schlappi, and R. Signorell, "Sodium-doping as a reference to study the influence of intracluster chemistry on the fragmentation of weakly-bound clusters upon vacuum ultraviolet photoionization," *Physical Chemistry Chemical Physics*, vol. 15, no. 3, pp. 940–949, 2013.

[91] S. Schütte and U. Buck, "Strong fragmentation of large rare gas clusters by high energy electron impact," *International Journal of Mass Spectrometry*, vol. 220, no. 2, pp. 183–192, 2002.

[92] C. Bobbert, S. Schütte, C. Steinbach, and U. Buck, "Fragmentation and reliable size distributions of large ammonia and water clusters," *European Physical Journal D*, vol. 19, no. 2, pp. 183–192, 2002.

[93] C. Huang, V. V. Kresin, A. Pysanenko, and M. Fárník, "Water cluster fragmentation probed by pickup experiments," *The Journal of Chemical Physics*, vol. 145, no. 10, p. 104304, 2016.

[94] J. Lengyel, A. Pysanenko, V. Poterya, J. Kočišek, and M. Fárník, "Extensive water cluster fragmentation after low energy electron ionization," *Chemical Physics Letters*, vol. 612, pp. 256–261, 2014.

[95] J. Lengyel, A. Pysanenko, P. Rubovič, and M. Fárník, "Sodium doping and reactivity in pure and mixed ice nanoparticles," *The European Physical Journal D*, vol. 69, no. 12, p. 269, 2015.

[96] B. Schläppi, J. J. Ferreiro, J. H. Litman, and R. Signorell, "Sodium-sizer for neutral nanosized molecular aggregates: Quantitative correction of size-dependence," *International Journal of Mass Spectrometry*, vol. 372, pp. 13–21, 2014.

[97] J. E. Sansonetti, "Wavelengths, transition probabilities, and energy levels for the spectra of sodium," *Journal of Physical and Chemical Reference Data*, vol. 37, no. 4, pp. 1659–1763, 2008.

[98] S. Hartweg, A. H. C. West, B. L. Yoder, and R. Signorell, "Metal transition in sodium–ammonia nanodroplets," *Angewandte Chemie International Edition*, vol. 55, no. 40, pp. 12347–12350, 2016.

[99] W. Weyl, "Ueber metallammonium-verbindungen," *Annalen der Physik*, vol. 197, no. 4, pp. 601–612, 1864.

[100] T. Buttersack, P. E. Mason, R. S. McMullen, T. Martinek, K. Brezina, D. Hein, H. Ali, C. Kolbeck, C. Schewe, S. Malerz, B. Winter, R. Seidel, O. Marsalek, P. Jungwirth, and S. E. Bradforth, "Valence and core-level x-ray photoelectron spectroscopy of a liquid ammonia microjet," *Journal of the American Chemical Society*, vol. 141, no. 5, pp. 1838–1841, 2019.

[101] S. Vongehr, S.-C. Tang, and X.-K. Meng, "Collision statistics of clusters: from poisson model to poisson mixtures," *Chinese Physics B*, vol. 19, no. 2, 2010.

[102] J. K. Fink and L. Leibowitz, "Thermodynamic and transport properties of sodium liquid and vapor," report, Argonne National Lab, 1995.

[103] A. Bondi, "van der waals volumes and radii," *The Journal of Physical Chemistry*, vol. 68, no. 3, pp. 441–451, 1964.

[104] P. W. Forysinski, P. Zielke, D. Luckhaus, J. Corbett, and R. Signorell, "Photoionization of small sodium-doped acetic acid clusters," *The Journal of Chemical Physics*, vol. 134, no. 9, p. 094314, 2011.

[105] I. Gilmore and M. Seah, "Ion detection efficiency in sims:: Dependencies on energy, mass and composition for microchannel plates used in mass spectrometry," *International Journal of Mass Spectrometry*, vol. 202, no. 1, pp. 217 – 229, 2000.

[106] P. Zielke, P. W. Forysinski, D. Luckhaus, and R. Signorell, "Adiabatic ionization potential of acetic acid and torsional dynamics of its cation," *The Journal of Chemical Physics*, vol. 130, no. 21, p. 211101, 2009.

[107] P. W. Forysinski, P. Zielke, D. Luckhaus, and R. Signorell, "Pfi-zeke photoelectron spectrum of CH_2F_2, ionisation potential and ionic fragmentation ap-

pearance potentials," *Physical Chemistry Chemical Physics*, vol. 12, no. 13, pp. 3121–3130, 2010.

[108] B. L. Yoder, A. H. C. West, B. Schlappi, E. Chasovskikh, and R. Signorell, "A velocity map imaging photoelectron spectrometer for the study of ultrafine aerosols with a table-top vuv laser and na-doping for particle sizing applied to dimethyl ether condensation," *Journal of Chemical Physics*, vol. 138, no. 4, p. 12, 2013.

[109] M. Ferray, A. L. Huillier, X. F. Li, L. A. Lompre, G. Mainfray, and C. Manus, "Multiple-harmonic conversion of 1064 nm radiation in rare gases," *Journal of Physics B: Atomic, Molecular and Optical Physics*, vol. 21, no. 3, p. L31, 1988.

[110] F. Frassetto, C. Cacho, C. A. Froud, I. C. E. Turcu, P. Villoresi, W. A. Bryan, E. Springate, and L. Poletto, "Single-grating monochromator for extreme-ultraviolet ultrashort pulses," *Optics Express*, vol. 19, no. 20, pp. 19169–19181, 2011.

[111] F. Frassetto, P. Miotti, and L. Poletto, "Grating configurations for the spectral selection of coherent ultrashort pulses in the extreme-ultraviolet," *Photonics*, vol. 1, no. 4, pp. 442–454, 2014.

[112] W. Li, S. D. Chambreau, S. A. Lahankar, and A. G. Suits, "Megapixel ion imaging with standard video," *Review of Scientific Instruments*, vol. 76, no. 6, p. 063106, 2005.

[113] W. C. Wiley and I. H. McLaren, "Time-of-flight mass spectrometer with improved resolution," *Review of Scientific Instruments*, vol. 26, no. 12, pp. 1150–1157, 1955.

[114] G. A. Garcia, B. K. C. de Miranda, M. Tia, S. Daly, and L. Nahon, "Delicious III: A multipurpose double imaging particle coincidence spectrometer for gas phase vacuum ultraviolet photodynamics studies," *Review of Scientific Instruments*, vol. 84, no. 6, p. 1, 2013.

[115] X. F. Tang, G. A. Garcia, J. F. Gil, and L. Nahon, "Vacuum upgrade and enhanced performances of the double imaging electron/ion coincidence end-

station at the vacuum ultraviolet beamline desirs," *Review of Scientific Instruments*, vol. 86, no. 12, p. 8, 2015.

[116] L. Nahon, N. de Oliveira, G. A. Garcia, J.-F. Gil, B. Pilette, O. Marcouille, B. Lagarde, and F. Polack, "Desirs: a state-of-the-art vuv beamline featuring high resolution and variable polarization for spectroscopy and dichroism at soleil," *Journal of Synchrotron Radiation*, vol. 19, no. 4, pp. 508–520, 2012.

[117] S. Hartweg, B. L. Yoder, G. A. Garcia, L. Nahon, and R. Signorell, "Size-resolved photoelectron anisotropy of gas phase water clusters and predictions for liquid water," *Physical Review Letters*, vol. 118, no. 10, p. 103402, 2017.

[118] C. R. Brundle and D. W. Turner, "High resolution molecular photoelectron spectroscopy. ii. water and deuterium oxide," *Proceedings of the Royal Society of London. Series A, Mathematical and Physical Sciences*, vol. 307, no. 1488, pp. 27–36, 1968.

[119] M. S. Banna, B. H. McQuaide, R. Malutzki, and V. Schmidt, "The photoelectron spectrum of water in the 30 to 140 eV photon energy range," *The Journal of Chemical Physics*, vol. 84, no. 9, pp. 4739–4744, 1986.

[120] O. Björneholm, F. Federmann, S. Kakar, and T. Möller, "Between vapor and ice: Free water clusters studied by core level spectroscopy," *Journal of Chemical Physics*, vol. 111, no. 2, pp. 546–550, 1999.

[121] G. Öhrwall, R. F. Fink, M. Tchaplyguine, L. Ojamäe, M. Lundwall, R. R. T. Marinho, A. N. de Brito, S. L. Sorensen, M. Gisselbrecht, R. Feifel, T. Rander, A. Lindblad, J. Schulz, L. J. Sæthre, N. Mårtensson, S. Svensson, and O. Björneholm, "The electronic structure of free water clusters probed by auger electron spectroscopy," *Journal of Chemical Physics*, vol. 123, no. 5, p. 054310, 2005.

[122] S. Barth, M. Ončák, V. Ulrich, M. Mucke, T. Lischke, P. Slavíček, and U. Hergenhahn, "Valence ionization of water clusters: From isolated molecules to bulk," *Journal of Physical Chemistry A*, vol. 113, no. 48, pp. 13519–13527, 2009.

[123] R. Signorell, B. L. Yoder, A. H. C. West, J. J. Ferreiro, and C.-M. Saak, "Angle-resolved valence shell photoelectron spectroscopy of neutral nano-sized molecular aggregates," *Chemical Science*, vol. 5, no. 4, pp. 1283–1295, 2014.

[124] L. Partanen, M.-H. Mikkela, M. Huttula, M. Tchaplyguine, C. Zhang, T. Andersson, and O. Björneholm, "Solvation at nanoscale: Alkali-halides in water clusters," *Journal of Chemical Physics*, vol. 138, no. 4, p. 044301, 2013.

[125] L. Belau, K. R. Wilson, S. R. Leone, and M. Ahmed, "Vacuum ultraviolet (vuv) photoionization of small water clusters," *Journal of Physical Chemistry A*, vol. 111, no. 42, pp. 10885–10886, 2007.

[126] F. Dong, S. Heinbuch, J. J. Rocca, and E. R. Bernstein, "Dynamics and fragmentation of van der waals clusters: $(H_2O)_n$, $(CH_3OH)_n$, and $(NH_3)_n$ upon ionization by a 26.5 eV soft x-ray laser," *The Journal of Chemical Physics*, vol. 124, no. 22, p. 224319, 2006.

[127] E. Kamarchik, O. Kostko, J. M. Bowman, M. Ahmed, and A. I. Krylov, "Spectroscopic signatures of proton transfer dynamics in the water dimer cation," *The Journal of Chemical Physics*, vol. 132, no. 19, p. 194311, 2010.

[128] P. A. Pieniazek, J. VandeVondele, P. Jungwirth, A. I. Krylov, and S. E. Bradforth, "Electronic structure of the water dimer cation," *The Journal of Physical Chemistry A*, vol. 112, no. 27, pp. 6159–6170, 2008.

[129] A. Bodi, J. Csontos, M. Kallay, S. Borkar, and B. Sztaray, "On the protonation of water," *Chemical Science*, vol. 5, no. 8, pp. 3057–3063, 2014.

[130] B. Wang, W. Jiang, X. Dai, Y. Gao, Z. Wang, and R.-Q. Zhang, "Molecular orbital analysis of the hydrogen bonded water dimer," *Scientific Reports*, vol. 6, p. 22099, 2016.

[131] R. J. Saykally and D. J. Wales, "Pinning down the water hexamer," *Science*, vol. 336, no. 6083, pp. 814–815, 2012.

[132] D. J. Wales and M. P. Hodges, "Global minima of water clusters $(H_2O)_n$, $n \leq 21$, described by an empirical potential," *Chemical Physics Letters*, vol. 286, no. 1-2, pp. 65–72, 1998.

[133] T. E. Gartmann, S. Hartweg, L. Ban, E. Chasovskikh, B. L. Yoder, and R. Signorell, "Electron scattering in large water clusters from photoelectron imaging with high harmonic radiation," *Physical Chemistry Chemical Physics*, vol. 20, no. 24, pp. 16364–16371, 2018.

[134] M. Yousfi and M. D. Benabdessadok, "Boltzmann equation analysis of electron-molecule collision cross sections in water vapor and ammonia," *Journal of Applied Physics*, vol. 80, no. 12, pp. 6619–6630, 1996.

[135] J. L. Dehmer, W. A. Chupka, J. Berkowitz, and W. T. Jivery, "Wavelength dependence of the photoelectron angular distributions of the rare gases," *Physical Review B*, vol. 12, pp. 1966–1973, 1975.

[136] K. Codling, R. G. Houlgate, J. B. West, and P. R. Woodruff, "Angular distribution and photoionization measurements on the 2p and 2s electrons in neon," *Journal of Physics B: Atomic and Molecular Physics*, vol. 9, no. 5, pp. L83–L86, 1976.

[137] D. Rupp, M. Adolph, L. Flückiger, T. Gorkhover, J. P. Müller, M. Müller, M. Sauppe, D. Wolter, S. Schorb, R. Treusch, C. Bostedt, and T. Möller, "Generation and structure of extremely large clusters in pulsed jets," *The Journal of Chemical Physics*, vol. 141, no. 4, p. 044306, 2014.

[138] U. Buck, C. C. Pradzynski, T. Zeuch, J. M. Dieterich, and B. Hartke, "A size resolved investigation of large water clusters," *Physical Chemistry Chemical Physics*, vol. 16, no. 15, pp. 6859–6871, 2014.

[139] G. Torchet, P. Schwartz, J. Farges, M. F. de Feraudy, and B. Raoult, "Structure of solid water clusters formed in a free jet expansion," *The Journal of Chemical Physics*, vol. 79, no. 12, pp. 6196–6202, 1983.

[140] P. D. Schettler and A. Patterson, "Liquid-liquid phase separation in alkali metal-ammonia solutions. i. lithium, potassium, rubidium, with new data on sodium," *The Journal of Physical Chemistry*, vol. 68, no. 10, pp. 2865–2869, 1964.

[141] A. J. Birch and D. K. C. MacDonald, "Metal-ammonia solutions," *The Journal of Chemical Physics*, vol. 16, no. 7, pp. 741–741, 1948.

[142] P. Chieux and M. J. Sienko, "Phase separation and the critical index for liquid–liquid coexistence in the sodium–ammonia system," *The Journal of Chemical Physics*, vol. 53, no. 2, pp. 566–570, 1970.

[143] D. S. Kyser and J. C. Thompson, "Measurement of the hall effect in metal—ammonia solutions," *The Journal of Chemical Physics*, vol. 42, no. 11, pp. 3910–3918, 1965.

[144] J. C. Wasse, S. Hayama, S. Masmanidis, S. L. Stebbings, and N. T. Skipper, "The structure of lithium–ammonia and sodium–ammonia solutions by neutron diffraction," *The Journal of Chemical Physics*, vol. 118, no. 16, pp. 7486–7494, 2003.

[145] J. Häsing, "Die lichtelektrischen Eigenschaften der Lösungen von Natrium in flüssigem Ammoniak," *Annalen der Physik*, vol. 429, no. 7, pp. 509–533, 1940.

[146] H. Aulich, B. Baron, P. Delahay, and R. Lugo, "Photoelectron emission by solvated electrons in liquid ammonia," *The Journal of Chemical Physics*, vol. 58, no. 10, pp. 4439–4443, 1973.

[147] J. V. Barnes, B. L. Yoder, and R. Signorell, "Magic numbers for the photoelectron anisotropy in li-doped dimethyl ether clusters," *The Journal of Physical Chemistry A*, vol. 123, no. 12, pp. 2379–2386, 2019.

[148] B. v. Issendorff and O. Cheshnovsky, "Metal to insulator transitions in clusters," *Annual Review of Physical Chemistry*, vol. 56, no. 1, pp. 549–580, 2005.

[149] O. C. Thomas, W. Zheng, S. Xu, and K. H. Bowen, "Onset of metallic behavior in magnesium clusters," *Physical Review Letters*, vol. 89, p. 213403, 2002.

[150] A. Aguado, A. Vega, A. Lebon, and B. von Issendorff, "Insulating or metallic: Coexistence of different electronic phases in zinc clusters," *Angewandte Chemie International Edition*, vol. 54, no. 7, pp. 2111–2115, 2014.

[151] G. L. Gutsev, C. A. Weatherford, B. R. Ramachandran, L. G. Gutsev, W.-J. Zheng, O. C. Thomas, and K. H. Bowen, "Photoelectron spectra and

structure of the Mn_n^- anions (n = 2–16)," *The Journal of Chemical Physics*, vol. 143, no. 4, p. 044306, 2015.

[152] P. Hohenberg and W. Kohn, "Inhomogeneous electron gas," *Physical Review*, vol. 136, pp. B864–B871, 1964.

[153] W. Kohn and L. J. Sham, "Self-consistent equations including exchange and correlation effects," *Physical Review*, vol. 140, pp. A1133–A1138, 1965.

[154] J.-D. Chai and M. Head-Gordon, "Long-range corrected hybrid density functionals with damped atom–atom dispersion corrections," *Physical Chemistry Chemical Physics*, vol. 10, pp. 6615–6620, 2008.

[155] J.-D. Chai and M. Head-Gordon, "Systematic optimization of long-range corrected hybrid density functionals," *The Journal of Chemical Physics*, vol. 128, no. 8, p. 084106, 2008.

[156] A. D. Becke, "Density-functional thermochemistry. v. systematic optimization of exchange-correlation functionals," *The Journal of Chemical Physics*, vol. 107, no. 20, pp. 8554–8560, 1997.

[157] S. Grimme, "Semiempirical GGA-type density functional constructed with a long-range dispersion correction," *Journal of computational chemistry*, vol. 27 15, pp. 1787–99, 2006.

[158] R. Ditchfield, W. J. Hehre, and J. A. Pople, "Self-consistent molecular-orbital methods. ix. an extended gaussian-type basis for molecular-orbital studies of organic molecules," *The Journal of Chemical Physics*, vol. 54, no. 2, pp. 724–728, 1971.

[159] M. M. Kappes, M. Schär, U. Röthlisberger, C. Yeretzian, and E. Schumacher, "Sodium cluster ionisation potentials revisited: Higher-resolution measurements for Na_x (x<23) and their relation to bonding models," *Chemical Physics Letters*, vol. 143, no. 3, pp. 251 – 258, 1988.

[160] A. Herrmann, S. Leutwyler, E. Schumacher, and L. Wöste, "On metal-atom clusters iv. photoionization thresholds and multiphoton ionization spectra of alkali-metal molecules," *Helvetica Chimica Acta*, vol. 61, no. 1, pp. 453–487, 1978.

[161] K. Wong, G. Tikhonov, and V. V. Kresin, "Temperature-dependent work functions of free alkali-metal nanoparticles," *Physical Review B*, vol. 66, p. 125401, 2002.

[162] W. Gerlach and O. Stern, "Der experimentelle nachweis der richtungsquantelung im magnetfeld," *Zeitschrift für Physik*, vol. 9, no. 1, pp. 349–352, 1922.

[163] U. Rohrmann, S. Schäfer, and R. Schäfer, "Size- and temperature-dependent magnetic response of molecular cage clusters: Manganese-doped tin clusters," *The Journal of Physical Chemistry A*, vol. 113, no. 44, pp. 12115–12121, 2009.

[164] A. Diaz-Bachs, L. Peters, R. Logemann, V. Chernyy, J. M. Bakker, M. I. Katsnelson, and A. Kirilyuk, "Magnetic properties of Co-doped Nb clusters," *Physical Review*, vol. 97, p. 134427, 2018.

[165] T. M. Fuchs and R. Schäfer, "Double Stern-Gerlach experiments on $Mn@sn_{12}$: Refocusing of a paramagnetic superatom," *Physical Review A*, vol. 98, p. 063411, 2018.

[166] J. P. Bucher, D. C. Douglass, P. Xia, B. Haynes, and L. A. Bloomfield, "Magnetic deflection of neutral metal clusters in a beam," *Zeitschrift für Physik D Atoms, Molecules and Clusters*, vol. 19, no. 4, pp. 251–254, 1991.

[167] I. M. Billas, A. Châtelain, and W. A. de Heer, "Magnetism from the atom to the bulk in iron, cobalt, and nickel clusters," *Science*, vol. 265, no. 5179, pp. 1682–1684, 1994.

[168] M. B. Knickelbein, "Nickel clusters: The influence of adsorbates on magnetic moments," *The Journal of Chemical Physics*, vol. 116, no. 22, pp. 9703–9711, 2002.

[169] l. Carrera, M. Mobbili, and E. Marceca, "Electric susceptibility of sodium-doped water clusters by beam deflection," *The Journal of Physical Chemistry A*, vol. 113, no. 12, pp. 2711–2714, 2009.

[170] S. Schäfer, B. Assadollahzadeh, M. Mehring, P. Schwerdtfeger, and R. Schäfer, "Structure and electric properties of Sn_N clusters (n = 6-20) from

combined electric deflection experiments and quantum theoretical studies," *The Journal of Physical Chemistry A*, vol. 112, no. 48, pp. 12312–12319, 2008.

[171] S. Schäfer, S. Heiles, J. A. Becker, and R. Schäfer, "Electric deflection studies on lead clusters," *The Journal of Chemical Physics*, vol. 129, no. 4, p. 044304, 2008.

[172] M. G. DeBacker, E. B. Mkadmi, F. X. Sauvage, J.-P. Lelieur, M. J. Wagner, R. Concepcion, J. Kim, L. E. H. McMills, and J. L. Dye, "The lithium-sodium-methylamine system: does a low-melting sodide become a liquid metal?," *Journal of the American Chemical Society*, vol. 118, no. 8, pp. 1997–2003, 1996.

Glossary

amu	atomic mass unit
ARPES	angle-resolved photoelectron spectroscopy
Basex	basis set expansion
CCD	charge-coupled device
CMOS	complementary metal-oxide-semiconductor
DDA	discrete dipole approximation
DME	dimethyl ether
eBE	electron binding energy
eKE	electron kinetic energy
EL-valve	Even-Lavie valve
EUV	extreme ultraviolet
FWHM	full width at half maximum
HHG	high harmonic generation
HOMO	highest occupied molecular orbital
i^2pepico	double imaging photoelectron photoion coincidence
IR	infrared
MPM	mole-percent metal
OPA	optical parametric amplifier
PBasex	polar basis set expansion
PAD	photoelectron angular distribution
PES	photoelectron spectrum
PID	proportional-integral-derivative
PSD	position sensitive detector
SCG	surge current generator
SFG	sum frequency generation
SPI	single photon ionization
TMS	transition to the metallic phase
TOF	time of flight
UV	ultraviolet
VMI	velocity map imaging
VUV	vacuum ultra violet

Appendix A
Additional tables

A.1 Electron binding energies of small water clusters

n	$1b_1$	$3a_1$	$1b_2$
1	12.62	14.81	18.58
2	-	14.78	18.30
3	12.14	14.60	18.27
4	12.19	14.60	18.15
5	12.07	14.56	18.17
6	12.04	14.60	18.14
7	12.04	14.62	18.14
8	12.06	14.51	18.07
9	12.06	14.41	18.07
10	11.94	14.44	17.99
11	11.98	14.44	18.09
12	11.93	14.51	18.15
13	11.91	14.51	18.12
14	11.86	14.57	18.07
15	11.88	14.38	18.07
16	11.86	14.46	18.12
17	11.91	14.25	18.09
18	11.85	14.07	18.10
19	11.96	14.06	18.04
20	11.83	14.23	17.88

Table A.1: Electron binding energies for the valence orbitals of water clusters with $1 \leq n \leq 20$. Typical uncertainties are 0.1 eV for the $1b_1$ and $1b_2$ bands and 0.2 eV for the $3a_1$ band.

A.2 Anisotropy parameters of small water clusters

n=1	**$1b_1$**		**$3a_1$**		**$1b_2$**	
hν / eV	β	$\sigma(\beta)$	β	$\sigma(\beta)$	β	$\sigma(\beta)$
13	0.29	0.15				
14	0.63	0.11				
15	0.76	0.07				
16	0.96	0.06	0.27	0.26		
18	1.15	0.03	0.51	0.18		
20	1.29	0.23	0.7	0.1	-0.33	0.25
22	1.32	0.03	0.73	0.14	0.01	0.06
24	1.32	0.24	0.81	0.14	0.24	0.1
27	1.26	0.16	0.84	0.1	0.45	0.14
30	1.22	0.21	0.95	0.18	0.51	0.08
32.5	1.5	0.21	1.14	0.17	0.61	0.15
35	1.53	0.13	1.16	0.2	0.72	0.19
n=2	**$1b_1$**		**$3a_1$**		**$1b_2$**	
hν / eV	β	$\sigma(\beta)$	β	$\sigma(\beta)$	β	$\sigma(\beta)$
13	0.08	0.20				
14	0.28	0.08				
15	0.52	0.08				
16	0.53	0.09	0.12	0.17		
18	0.78	0.08	0.32	0.11		
20	0.86	0.09	0.54	0.13	-0.18	0.18
22	0.96	0.11	0.60	0.11	-0.02	0.08
24	1.02	0.13	0.69	0.08	0.19	0.13
27	1.16	0.22	0.68	0.17	0.51	0.20
30	1.13	0.16	0.83	0.28	0.49	0.22
32.5	1.32	0.05	0.96	0.13	0.61	0.12
...	...		...		...	

n=3	**$1b_1$**		**$3a_1$**		**$1b_2$**	
hν / eV	β	$\sigma(\beta)$	β	$\sigma(\beta)$	β	$\sigma(\beta)$
13	0.10	0.20				
14	0.26	0.03				
15	0.37	0.04				
16	0.39	0.05	0.06	0.23		
18	0.62	0.06	0.16	0.12		
20	0.82	0.08	0.39	0.13	-0.11	0.22
22	0.97	0.08	0.46	0.10	0.03	0.10
24	0.98	0.05	0.59	0.15	0.24	0.12
27	1.06	0.15	0.50	0.19	0.44	0.23
30	0.97	0.14	0.69	0.27	0.46	0.14
32.5	1.24	0.09	0.80	0.11	0.52	0.14
n=4	**$1b_1$**		**$3a_1$**		**$1b_2$**	
hν / eV	β	$\sigma(\beta)$	β	$\sigma(\beta)$	β	$\sigma(\beta)$
13	0.05	0.20				
14	0.18	0.06				
15	0.24	0.07				
16	0.24	0.07	0.05	0.23		
18	0.46	0.06	0.14	0.13		
20	0.67	0.07	0.35	0.12	-0.10	0.21
22	0.76	0.12	0.40	0.12	0.01	0.13
24	0.83	0.09	0.47	0.11	0.25	0.13
27	0.97	0.26	0.41	0.34	0.41	0.24
30	0.86	0.16	0.51	0.44	0.49	0.35
32.5	1.16	0.03	0.68	0.08	0.51	0.14
...	...		...		...	

n=5	**1b$_1$**		**3a$_1$**		**1b$_2$**	
hν / eV	β	$\sigma(\beta)$	β	$\sigma(\beta)$	β	$\sigma(\beta)$
13	0.10	0.14				
14	0.11	0.06				
15	0.12	0.07				
16	0.13	0.06	0.06	0.28		
18	0.33	0.05	0.13	0.18		
20	0.54	0.05	0.38	0.17	-0.07	0.22
22	0.64	0.07	0.36	0.16	0.00	0.12
24	0.66	0.08	0.52	0.16	0.21	0.17
27	0.97	0.31	0.56	0.56	0.43	0.25
30	0.85	0.34	0.58	0.13	0.43	0.23
32.5	1.07	0.04	0.73	0.23	0.58	0.16
n=6	**1b$_1$**		**3a$_1$**		**1b$_2$**	
hν / eV	β	$\sigma(\beta)$	β	$\sigma(\beta)$	β	$\sigma(\beta)$
13	0.06	0.16				
14	0.09	0.06				
15	0.11	0.08				
16	0.11	0.09	0.04	0.29		
18	0.32	0.11	0.12	0.18		
20	0.54	0.09	0.32	0.22	-0.06	0.29
22	0.68	0.07	0.36	0.35	0.01	0.17
24	0.71	0.11	0.48	0.22	0.25	0.22
27	0.76	0.10	0.56	0.32	0.54	0.48
30	0.77	0.10	0.57	0.29	0.49	0.14
32.5	1.11	0.06	0.70	0.24	0.53	0.19
...	...		...		...	

n=7	**1b$_1$**		**3a$_1$**		**1b$_2$**	
hν / eV	β	$\sigma(\beta)$	β	$\sigma(\beta)$	β	$\sigma(\beta)$
13	0.06	0.15				
14	0.06	0.07				
15	0.10	0.10				
16	0.13	0.07	0.00	0.23		
18	0.30	0.06	0.11	0.25		
20	0.49	0.08	0.29	0.28	-0.05	0.25
22	0.61	0.15	0.33	0.17	0.03	0.20
24	0.66	0.10	0.33	0.15	0.23	0.20
27	0.98	0.15	0.66	0.81	0.41	0.28
30	0.83	0.13	0.50	0.34	0.40	0.44
32.5	1.00	0.04	0.68	0.21	0.46	0.15

n=8	**1b$_1$**		**3a$_1$**		**1b$_2$**	
hν / eV	β	$\sigma(\beta)$	β	$\sigma(\beta)$	β	$\sigma(\beta)$
13	0.06	0.15				
14	0.09	0.10				
15	0.09	0.10				
16	0.12	0.07	-0.02	0.28		
18	0.31	0.10	0.12	0.27		
20	0.48	0.09	0.30	0.31	-0.05	0.31
22	0.59	0.06	0.27	0.20	0.00	0.19
24	0.65	0.08	0.38	0.16	0.24	0.20
27	0.97	0.15	0.53	0.44	0.47	0.60
30	0.83	0.23	0.49	0.31	0.39	0.18
32.5	0.99	0.02	0.63	0.10	0.47	0.05
...	...		...		...	

n=9	**1b$_1$**		**3a$_1$**		**1b$_2$**	
hν / eV	β	$\sigma(\beta)$	β	$\sigma(\beta)$	β	$\sigma(\beta)$
13	0.04	0.17				
14	0.05	0.10				
15	0.06	0.12				
16	0.09	0.08	0.00	0.31		
18	0.29	0.06	0.16	0.22		
20	0.51	0.12	0.31	0.38	0.02	0.44
22	0.59	0.10	0.27	0.37	0.04	0.34
24	0.63	0.07	0.38	0.27	0.21	0.22
27	0.75	0.19	0.44	0.28	0.26	0.44
30	0.77	0.14	0.41	0.17	0.35	0.13
32.5	1.07	0.08	0.73	0.24	0.57	0.21

n=10	**1b$_1$**		**3a$_1$**		**1b$_2$**	
hν / eV	β	$\sigma(\beta)$	β	$\sigma(\beta)$	β	$\sigma(\beta)$
13	0.03	0.18				
14	0.05	0.11				
15	0.08	0.10				
16	0.12	0.07	-0.01	0.29		
18	0.25	0.10	0.09	0.26		
20	0.54	0.11	0.32	0.32	0.00	0.34
22	0.61	0.15	0.33	0.26	-0.02	0.19
24	0.62	0.03	0.52	0.11	0.16	0.13
27	0.82	0.23	0.45	0.32	0.52	0.28
30	0.79	0.10	0.62	0.23	0.35	0.43
32.5	0.99	0.07	0.64	0.23	0.54	0.16
...	...		...		...	

n=11	**$1b_1$**		**$3a_1$**		**$1b_2$**	
hν / eV	β	$\sigma(\beta)$	β	$\sigma(\beta)$	β	$\sigma(\beta)$
13	0.01	0.15				
14	0.06	0.16				
15	0.06	0.09				
16	0.07	0.10	-0.05	0.30		
18	0.28	0.09	0.11	0.30		
20	0.45	0.10	0.25	0.27	-0.06	0.30
22	0.62	0.15	0.28	0.27	0.03	0.38
24	0.61	0.07	0.51	0.28	0.18	0.29
27	1.01	0.29	0.54	0.78	0.45	0.42
30	0.91	0.03	0.46	0.57	0.41	0.25
32.5	1.01	0.09	0.77	0.46	0.47	0.19

n=12	**$1b_1$**		**$3a_1$**		**$1b_2$**	
hν / eV	β	$\sigma(\beta)$	β	$\sigma(\beta)$	β	$\sigma(\beta)$
13	-0.01	0.13				
14	0.06	0.10				
15	0.05	0.07				
16	0.11	0.17	-0.03	0.27		
18	0.25	0.10	0.07	0.24		
20	0.43	0.11	0.23	0.32	-0.09	0.44
22	0.63	0.30	0.34	0.38	0.01	0.30
24	0.61	0.08	0.45	0.25	0.20	0.22
...	...		...		...	

n=13	**1b$_1$**		**3a$_1$**		**1b$_2$**	
hν / eV	β	$\sigma(\beta)$	β	$\sigma(\beta)$	β	$\sigma(\beta)$
13	0.01	0.15				
14	0.04	0.11				
15	0.03	0.09				
16	0.10	0.08	-0.03	0.34		
18	0.25	0.07	0.09	0.26		
20	0.46	0.11	0.19	0.32	0.00	0.57
22	0.62	0.13	0.27	0.30	0.05	0.42
24	0.61	0.02	0.33	0.40	0.14	0.27

n=14	**1b$_1$**		**3a$_1$**		**1b$_2$**	
hν / eV	β	$\sigma(\beta)$	β	$\sigma(\beta)$	β	$\sigma(\beta)$
13	-0.01	0.12				
14	0.09	0.14				
15	0.07	0.12				
16	0.10	0.09	-0.04	0.32		
18	0.22	0.13	0.16	0.69		
20	0.47	0.21	0.21	0.36	-0.07	0.46
22	0.60	0.12	0.30	0.47	0.03	0.38
24	0.64	0.04	0.53	0.28	0.16	0.25

n=15	**1b$_1$**		**3a$_1$**		**1b$_2$**	
hν / eV	β	$\sigma(\beta)$	β	$\sigma(\beta)$	β	$\sigma(\beta)$
13	-0.01	0.12				
14	0.07	0.18				
15	0.06	0.09				
16	0.06	0.12	-0.04	0.31		
18	0.28	0.35	0.10	0.60		
20	0.49	0.18	0.31	0.45	-0.10	0.36
22	0.61	0.28	0.26	0.36	0.04	0.39
24	0.71	0.22	0.48	0.36	0.25	0.39
...	...		...		...	

n=16	**1b$_1$**		**3a$_1$**		**1b$_2$**	
hν / eV	β	$\sigma(\beta)$	β	$\sigma(\beta)$	β	$\sigma(\beta)$
13	0.01	0.14				
14	0.06	0.16				
15	0.04	0.09				
16	0.05	0.06	0.05	0.22		
18	0.24	0.13	0.00	0.25		
20	0.39	0.13	0.09	0.31	-0.21	0.68
22	0.56	0.14	0.35	0.55	-0.01	0.20
24	0.62	0.09	0.56	0.27	0.12	0.19

n=17	**1b$_1$**		**3a$_1$**		**1b$_2$**	
hν / eV	β	$\sigma(\beta)$	β	$\sigma(\beta)$	β	$\sigma(\beta)$
13.0	0.02	0.16	–	–	–	–
14.0	0.06	0.10	–	–	–	–
15.0	0.01	0.09	0.22	0.43	–	–
16.0	0.08	0.07	0.05	0.31	–	–
18.0	0.22	0.08	0.02	0.16	–	–
20.0	0.44	0.09	0.19	0.16	-0.08	0.33
22.0	0.56	0.06	0.33	0.13	0.06	0.30
24.0	0.67	0.04	0.29	0.13	0.31	0.21

n=18	**1b$_1$**		**3a$_1$**		**1b$_2$**	
hν / eV	β	$\sigma(\beta)$	β	$\sigma(\beta)$	β	$\sigma(\beta)$
13.0	0.01	0.12	–	–	–	–
14.0	0.03	0.16	–	–	–	–
15.0	0.00	0.09	0.12	0.42	–	–
16.0	0.07	0.11	0.09	0.23	–	–
18.0	0.24	0.08	0.05	0.15	–	–
20.0	0.45	0.04	0.14	0.20	-0.07	0.42
22.0	0.50	0.11	0.31	0.34	0.09	0.43
24.0	0.58	0.09	0.37	0.15	0.19	0.19
...	...		...		...	

n=19	**1b$_1$**		**3a$_1$**		**1b$_2$**	
hν / eV	β	$\sigma(\beta)$	β	$\sigma(\beta)$	β	$\sigma(\beta)$
13.0	0.02	0.21	–	–	–	–
14.0	0.10	0.12	–	–	–	–
15.0	-0.05	0.07	0.12	0.43	–	–
16.0	0.08	0.11	0.17	0.34	–	–
18.0	0.25	0.11	0.05	0.21	–	–
20.0	0.41	0.04	0.16	0.29	-0.06	0.30
22.0	0.52	0.15	0.22	0.18	0.08	0.28
24.0	0.62	0.11	0.37	0.16	0.31	0.45
n=20	**1b$_1$**		**3a$_1$**		**1b$_2$**	
hν / eV	β	$\sigma(\beta)$	β	$\sigma(\beta)$	β	$\sigma(\beta)$
13	0.00	0.16				
14	0.02	0.14				
15	0.04	0.11				
16	0.08	0.11	-0.02	0.34		
18	0.23	0.15	0.04	0.53		
20	0.45	0.27	0.37	0.72		
22	0.57	0.21	0.52	0.73		
24	0.47	0.14	0.37	0.50		

Table A.2: Anisotrpoy parameter β for different cluster sizes $1 \leq n \leq 20$ and photon energies. $\sigma(\beta)$ gives the standard deviation of the β parameter over the averaged kinetic energy range.

A.3 Electron binding energy shifts of large water clusters

	$1b_1$		$3a_1$		$1b_2$	
$\langle n \rangle$	ΔeBE / eV	FWHM / eV	ΔeBE / eV	FWHM / eV	ΔeBE / eV	FWHM / eV
43	0.69	1.55	0.7	3.15	0.58	2.56
59	0.69	1.57	0.49	2.08	0.91	2.1
60	0.79	1.65	0.62	2.92	0.81	2.48
65	0.81	1.43	0.62	2.68	0.91	2.25
70	0.87	1.21	0.85	3.33	0.87	2.27
81	0.68	1.84	0.41	2.3	0.88	2.37
88	0.84	1.53	0.7	2.91	0.86	2.55
104	0.84	1.49	0.67	2.87	0.75	2.63
106	0.84	1.48	0.77	2.85	0.92	2.38
111	0.85	1.73	0.72	2.96	0.79	2.58
117	0.9	1.48	0.76	2.87	0.91	2.47
117	0.91	1.45	0.77	2.93	0.91	2.33
118	0.88	1.29	0.98	2.84	0.85	1.91
124	0.94	1.49	0.77	2.91	0.74	2.69
135	0.9	1.4	0.8	2.98	0.91	2.45
142	0.87	1.42	0.84	3.15	0.88	2.33
144	0.97	1.55	0.76	2.66	0.95	2.53
157	0.94	1.38	0.85	2.88	0.78	2.64
166	1.03	1.48	0.92	2.79	0.99	2.79
178	0.95	1.36	0.77	3.12	0.91	2.59
193	0.92	1.3	0.83	2.87	0.9	2.39
195	0.95	1.61	0.79	2.79	0.97	2.61
204	1	1.52	0.91	3.18	0.88	2.79
210	1.01	1.54	0.93	3.23	0.85	2.89
219	1.04	1.52	0.92	2.92	0.92	2.8
219	1.04	1.52	0.91	2.9	0.94	2.77
227	0.97	1.5	0.81	2.94	0.78	2.86
239	0.99	1.51	0.88	3.09	0.76	2.88

246	0.97	1.62	0.77	2.74	0.88	2.72
251	1.01	1.59	0.95	3.22	0.82	2.8
251	1	1.47	0.88	3.03	0.81	2.66
251	1.02	1.58	0.84	2.84	0.91	2.78
254	1.02	1.51	0.88	2.98	0.89	2.82
266	0.97	1.28	0.83	2.92	0.97	2.67
274	1.02	1.51	0.91	3.02	0.89	2.78
292	1.08	1.45	0.9	3.02	0.82	2.91
297	1.04	1.58	0.86	2.73	0.94	2.83
299	1.01	1.43	0.83	3.04	0.86	2.61
315	1.02	1.32	0.86	3.11	0.87	2.57
336	1.09	1.51	0.99	2.62	0.87	2.98
343	1.06	1.58	0.92	2.91	0.86	3.01
351	1.08	1.55	0.91	2.89	0.88	2.99
355	1.11	1.52	1.01	3.11	0.79	3.08
361	1.03	1.56	0.9	2.98	0.79	2.97
382	0.99	1.35	0.83	2.85	0.99	2.66
388	1.1	1.56	1	2.94	0.83	3.31
388	1.09	1.55	0.96	2.96	0.83	3.03
395	1.11	1.46	0.99	2.67	0.98	2.73
405	1.01	1.4	0.8	3	0.92	2.6
417	0.99	1.37	0.77	3.03	0.87	2.71
471	1.05	1.72	0.91	3.06	0.67	3.38
499	1.01	1.32	0.78	3.02	0.89	2.75
503	1.03	1.42	0.85	2.93	1	2.81
528	1.01	1.41	0.8	2.88	0.99	2.87
561	1.03	1.63	0.93	3.14	0.68	3.25
583	1.1	1.38	1.02	3.22	0.59	3.46
611	1	1.44	0.79	2.82	1.09	2.83
671	1.1	1.35	1.02	3.36	0.56	3.38

Table A.3: Fitted band positions and widths (FWHM) for the valence orbitals measured for distributions of water clusters of different average cluster sizes $\langle n \rangle$.

A.4 Anisotropy parameters of large water clusters

hν=26.52 eV	β		
$\langle n \rangle$	$1b_1$	$3a_1$	$1b_2$
43	0.72(18)	0.53(59)	0.27(47)
59	0.67(22)	0.12(31)	0.32(39)
60	0.63(10)	0.30(23)	0.24(18)
64.5	0.60(16)	0.26(41)	0.33(33)
81	0.64(13)	0.33(17)	0.34(16)
87.5	0.57(13)	0.25(21)	0.28(22)
104	0.53(14)	0.27(16)	0.22(18)
106	0.64(6)	0.37(15)	0.36(12)
111	0.39(7)	0.23(15)	0.24(13)
117	0.53(16)	0.21(31)	0.29(26)
117	0.54(16)	0.16(18)	0.28(26)
118	0.68(26)	0.36(56)	0.34(34)
134.5	0.56(13)	0.20(17)	0.34(22)
142	0.62(12)	0.27(13)	0.39(11)
143.5	0.50(14)	0.22(11)	0.24(19)
165.5	0.45(17)	0.10(19)	0.23(20)
194.5	0.42(4)	0.12(8)	0.25(17)
204	0.46(8)	0.16(9)	0.20(14)
210	0.43(10)	0.13(17)	0.13(17)
218.5	0.44(14)	0.17(6)	0.20(16)
218.5	0.42(15)	0.17(5)	0.21(15)
227	0.42(15)	0.20(6)	0.18(14)
238.5	0.37(5)	0.16(7)	0.09(13)
250.5	0.44(8)	0.01(17)	0.22(18)
250.5	0.42(8)	0.18(8)	0.17(14)
251	0.40(14)	0.15(7)	0.17(15)
253.5	0.43(6)	0.17(13)	0.21(15)
273.5	0.44(7)	0.19(12)	0.22(16)
292	0.39(13)	0.22(12)	0.20(14)

297	0.38(15)	0.11(11)	0.16(14)
336	0.34(9)	0.03(24)	0.18(17)
342.5	0.32(7)	0.14(6)	0.19(11)
351	0.35(15)	0.13(6)	0.14(12)
355	0.35(9)	0.19(21)	0.12(16)
360.5	0.36(4)	0.18(9)	0.15(11)
387.5	0.29(7)	0.12(7)	0.16(14)
387.5	0.27(9)	0.09(9)	0.14(14)
395	0.27(16)	-0.11(6)	-0.05(14)
470.5	0.34(5)	0.17(6)	0.09(12)
561	0.34(6)	0.15(7)	0.10(12)
582.5	0.31(17)	0.16(5)	0.11(12)
670.5	0.28(18)	0.08(5)	0.05(11)
hν=20.28 eV		β	
$\langle n \rangle$	$1b_1$	$3a_1$	$1b_2$
50.5	0.51(11)		
53	0.47(21)		
69.5	0.48(26)		
91	0.45(12)		
111	0.36(8)		
119	0.47(16)		
123	0.35(14)		
124	0.25(12)	0.11(12)	-0.05(14)
156.5	0.34(7)	0.06(21)	-0.06(14)
178	0.29(20)		
193	0.33(9)	0.03(20)	-0.03(13)
246	0.26(12)	0.05(19)	-0.05(17)
266	0.29(7)	0.02(13)	-0.05(8)
299	0.23(8)	0.08(9)	-0.05(7)
315	0.26(10)	0.09(10)	-0.04(11)
382	0.25(8)	0.03(13)	-0.04(8)
405	0.23(8)	0.04(8)	-0.04(8)
417	0.23(9)	0.06(10)	-0.04(7)
498.5	0.23(9)	0.06(12)	-0.05(10)

503	0.22(7)	0.07(10)	-0.05(8)
528	0.23(9)	0.04(11)	-0.05(8)
611	0.25(9)	0.06(12)	-0.03(10)
hν=14.04 eV		β	
$\langle n \rangle$	$1b_1$	$3a_1$	$1b_2$
44	0.08(29)		
63	0.02(23)		
69	0.05(26)		
180.5	-0.01(18)		
231.5	0.00(10)		
319	-0.01(8)		
360	-0.02(6)		
477	-0.03(6)		

Table A.4: Ansiotropy parameters β determined for the valence orbitals of large water clusters with different average cluster sizes $\langle n \rangle$ for different photon energies hν. Standard deviations are given in brackets.

Appendix B
Additional Figures

B.1 Mechanical design of the deflector

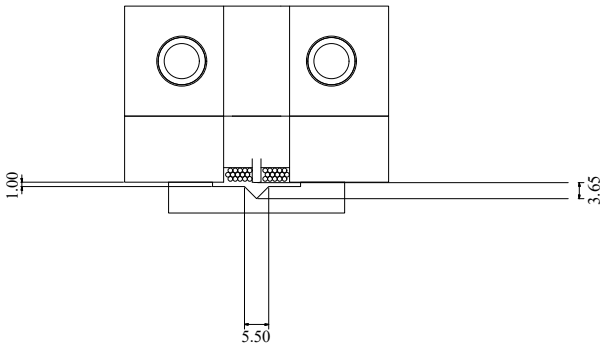

Figure B.1: CAD drawing of the deflector flight channel. Distances are given in mm.

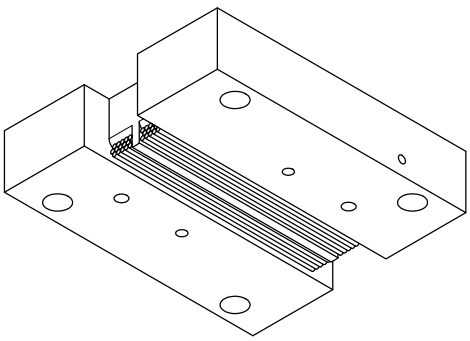

Figure B.2: CAD drawing of single electromagnet of the deflector. Wires are only shown partially.

B.2 Surge current generators

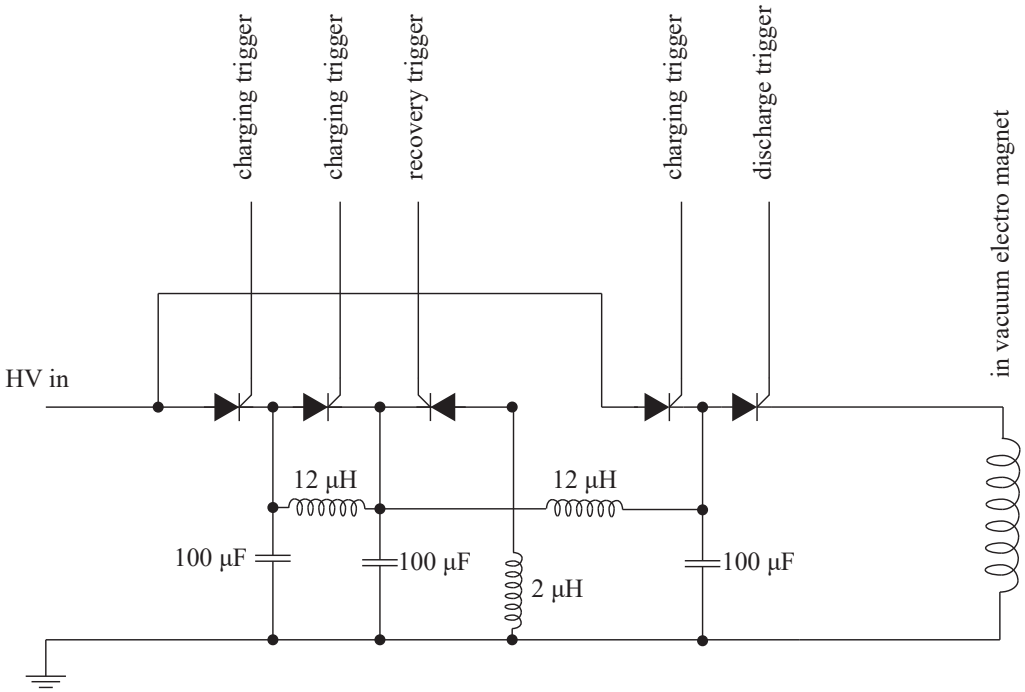

Figure B.3: Electronic scheme of the surge current generators.